



HAL
open science

3D modeling of the Tehran sedimentary basin : impact on seismic risk assessment

Saeid Soltani

► **To cite this version:**

Saeid Soltani. 3D modeling of the Tehran sedimentary basin : impact on seismic risk assessment. Applied geology. Université Grenoble Alpes [2020-..]; International Institute of Earthquake Engineering and Seismology, 2023. English. NNT: 2023GRALU032 . tel-04507703

HAL Id: tel-04507703

<https://theses.hal.science/tel-04507703v1>

Submitted on 17 Mar 2024

HAL is a multi-disciplinary open access archive for the deposit and dissemination of scientific research documents, whether they are published or not. The documents may come from teaching and research institutions in France or abroad, or from public or private research centers.

L'archive ouverte pluridisciplinaire **HAL**, est destinée au dépôt et à la diffusion de documents scientifiques de niveau recherche, publiés ou non, émanant des établissements d'enseignement et de recherche français ou étrangers, des laboratoires publics ou privés.

THÈSE

Pour obtenir le grade de



DOCTEUR DE L'UNIVERSITÉ GRENOBLE ALPES

École doctorale : STEP - Sciences de la Terre de l'Environnement et des Planètes

Spécialité : Sciences de la Terre et de l'Environnement

Unité de recherche : Institut des Sciences de la Terre

Modélisation 3D du bassin sédimentaire de Téhéran : impact sur l'évaluation du risque sismique

3D modeling of the Tehran sedimentary basin: impact on seismic risk assessment

Présentée par :

Saeid SOLTANI

Direction de thèse :

Bertrand GUILLIER

CHARGE DE RECHERCHE, Université Grenoble Alpes

Directeur de thèse

Ebrahim HAGHSHENAS

Professeur,

Co-directeur de thèse

Cécile CORNOU

CHARGÉE DE RECHERCHE, IRD

Co-directrice de thèse

Rapporteurs :

Philippe AGARD

PROFESSEUR DES UNIVERSITÉS, Université Sorbonne

Mehdi ZARE

FULL PROFESSOR, Int. Inst. of Earthquake Enging. & Seism

Thèse soutenue publiquement le 6 octobre 2023, devant le jury composé de :

Bertrand GUILLIER

CHARGE DE RECHERCHE HDR, IRD délégation Sud-Est

Directeur de thèse

Cecile CORNOU

DIRECTRICE DE RECHERCHE, IRD délégation Sud-Est

Co-directrice de thèse

Ebrahim HAGHSHENAS

ASSOCIATE PROFESSOR, Int. Inst. of Earthquake Enging. & Seism

Directeur de thèse

Mehdi ZARE

FULL PROFESSOR, Int. Inst. of Earthquake Enging. & Seism

Rapporteur

Emmanuel CHALJUB

PHYSICIEN, Université Grenoble Alpes

Président

Agathe ROULLE

CHARGÉE DE RECHERCHE, BRGM

Examinatrice

Etienne BERTRAND

DIRECTEUR DE RECHERCHE, Université Gustave Eiffel

Rapporteur

Invités :

Marc Wathelet

CHARGE DE RECHERCHE, Université Grenoble Alpes

Mohammad Tatar

PROFESSEUR, IIEES



Résumé

L'objectif de cette thèse est de parvenir à une compréhension globale des effets de site multidimensionnels dans le bassin de Téhéran. Avec plus de 15 million d'habitants, la zone urbaine de Téhéran est située au nord de l'Iran, dans la zone sismique centrale du massif d'Alborz, qui fait partie de la ceinture orogénique plus large des Alpes et de l'Himalaya. Située sur d'épais dépôts alluviaux, la ville de Téhéran est confrontée à un risque sismique notable, avec une possibilité importante d'effets de site multidimensionnels qui peuvent augmenter les dommages sismiques dans toute la ville de Téhéran. Afin d'améliorer notre compréhension de l'impact des effets multidimensionnels du site sur les mouvements du sol en surface, la première partie de ce manuscrit est consacrée à la construction du premier modèle 3D de la vitesse des ondes de cisaillement à Téhéran en utilisant de nombreuses données géotechniques et géophysiques, principalement dérivées de données de sismiques actives et passives. Le modèle de vitesse 3D qui en résulte indique que la profondeur du socle rocheux varie entre 100 et 900 mètres, avec une augmentation générale de la profondeur du nord-nord-est au sud-sud-ouest du bassin, et présente deux couches de vitesse distinctes: (i) une couche superficielle avec une vitesse diminuant de 950 m/s à 600 m/s du nord-est au sud-ouest, et (ii) une couche plus profonde avec des vitesses atteignant 1300 m/s. Dans la deuxième partie de cette thèse, cette nouvelle structure de vitesse 3D est utilisée pour simuler la réponse sismique 3D pour une onde plane SH à 2 Hz se propageant dans le bassin de Téhéran, en utilisant le code d'éléments spectraux open-source EFISPEC3D. La comparaison entre l'amplification du site obtenue à partir du mouvement du sol synthétique et l'amplification du site "réel" dérivée d'un réseau sismologique temporaire (Haghshenas, 2005) souligne la capacité de la modélisation numérique à reproduire l'amplification du site dans la région du sud de Téhéran. Cependant, notre modèle de vitesse 3D s'avère trop simpliste pour capturer toutes les hétérogénéités existantes, en particulier à proximité de la zone de faille complexe du centre-nord de Téhéran. Enfin, l'analyse de sensibilité souligne (i) que le choix de la station de référence (méthode SSR) a un impact significatif sur l'amplification de site, et (ii) le rôle majeur du contraste d'impédance, par rapport à l'atténuation du matériau, dans l'ajustement de la fonction d'amplification.

Mots clés: Effet de site, Modélisation numérique, Téhéran, Risque sismique, Bassin sédimentaire

Abstract

The objective of this PhD thesis is to achieve a comprehensive understanding of the multi-dimensional site effects in the Tehran basin. With over 15 million residents, the metropolitan urban area of Tehran is situated in northern Iran within the central Alborz seismic zone, which is part of the broader Alps-Himalayan orogenic belt. Located on thick alluvial deposits, Tehran faces a notable seismic risk, with a significant possibility of multi-dimensional site effects that may increase the seismic damages throughout the city of Tehran.

In order to improve our understanding of the impact of multi-dimensional site effects on surface ground motions, the first part of this manuscript is devoted to constructing the first 3D model of shear-wave velocity in Tehran using extensive geotechnical and geophysical data, mainly derived from active and passive seismic data.

The resulting 3D velocity model indicates that the depth of the bedrock varies between 100 and 900 meters, with a general increase in depth from the north-northeast to the south-southwest of the basin, and exhibits two distinct velocity layers: (i) a surface layer with a velocity decreasing from 950 m/s to 600 m/s from the northeast to the southwest, and (ii) a deeper layer with velocities reaching up to 1300 m/s.

In the second part of this thesis, the newly developed 3D velocity structure is used to simulate 3D seismic response for vertically incident SH plane wave up to 2 Hz of the Tehran's basin, using the open-source spectral-element code EFISPEC3D.

Comparison between the site amplification obtained from the synthetic ground motion and the "real" site amplification derived from a temporary seismological network (Haghshenas, 2005) outlines the ability of numerical ground motion to replicate the site amplification in the southern region. However, our 3D velocity model is found to be too simplistic to capture all existing heterogeneities, especially in the vicinity of the complex north-central fault zone in Tehran. Finally, sensitivity analysis outlines (i) that the choice of the reference rock station (SSR method) has a significant impact on site amplification, and (ii) the primary role of impedance contrast compared to material attenuation in adjusting the amplification function.

Keywords: Site effect, Numerical simulation, Tehran, Seismic risk, sedimentary basin

To my family

My parents, my sisters, my niece and nephews

Acknowledgment

Now, the moment has arrived to express my gratitude to everyone who has been a part of my journey. Special appreciation goes to my wonderful supervisors for their guidance and support. In fact, if someone were to ask me about one of the main achievements of my academic journey, my response would be meeting Ebrahim and having the opportunity to work with him. I've learned many things from him, not just about seismology but also about life itself. Thus, I extend my heartfelt gratitude to him, and I hope to continue our collaboration for many years to come. I must also express my gratitude to Bertrand for his kindness and positive attitude. Had he not chosen to visit Iran in 2017, I would never have had the chance to meet him (and the other great people at ISTERRE). I'm so grateful for the opportunity he has provided me and all his support during the PhD. Furthermore, I must thank Cécile for her compassion and mentoring. The first seismology paper I ever read (during my master's) was authored by her, and I had always aspired to meet and collaborate with her one day.

I want to extend my thanks to Etienne Bertrand, Phillipe Agard and Mehdi Zare for kindly agreeing to review this thesis. Their insightful perspectives and interest in my work have been incredibly valuable to me. I would also like to thank the other members of the jury, Emmanuel Chaljub (which I learned a lot about the method through his works), Agathe Roullé, Mohammad Tatar and Marc Wathelet. Thank you for your time and for providing valuable feedback on my work.

I would like to extend my gratitude to Florent DeMartin and all the contributors involved in the EFISPEC3D development, as well as François Lavoué for his invaluable assistance for the last part of thesis. Additionally, I express my thanks to the members of my thesis committee—Emanuel Chaljub, Marc Wathelet, James Hollingworth, and also Pierre Yves Bard for accompanying me throughout this journey.

A special thanks to Kaveh Oghalaei, who has been a constant source of friendship and support for me from the very first day of our friendship until today. Thanks to Alireza, with whom I also shared joyful moments at ISTERRE and beyond throughout these years. And also, warm gratitude to all the wonderful friends at Grenoble and ISTERRE – Leon, Sarvenaz, Jafar, Joshua, Sony, Sara, Najmeh, Neda, Arash, Sayeh and ... - Being with you made life in Grenoble easier and more enjoyable.

I would also like to express my gratitude to all my friends from IIEES – Iman, Navid, Hamed, Homa, Zohreh, Ramin, Mehdi, Maysam, Saeed, Azar and Pariya – for their assistance, the joyful moments we shared at IIEES, and their positive attitudes.

And finally, the moment has arrived to express my deepest gratitude to my family—my parents, Mardali and Balanesa; my sisters, Maryam, Ameneh, Layla, Masoumeh and Tahereh, and my nephews and nieces, Melika, Amirali, Taha, Nora and Amirhossein. Words alone cannot capture the immense sacrifices and support they've given me throughout my life. I thank them from the bottom of my heart, and I am genuinely blessed to have them by my side.

RÉSUMÉ	1
ABSTRACT	3
LIST OF FIGURES	12
LIST OF TABLES	21
GENERAL INTRODUCTION	22
<i>CHAPTER 1</i>	29
1-1 INTRODUCTION	30
1-2 TECTONICS AROUND TEHRAN AND GEOLOGY OF THE BASIN	30
1-2-1 TECTONICS AND FAULTS	30
1-2-2 MORPHOLOGICAL AND STRUCTURAL GEOLOGY	34
1-2-3 TEHRAN'S SEDIMENTARY FORMATIONS	38
1-3 ACTIVE FAULTS IN TEHRAN BASIN	42
1-3-1 LARGE SCALE FAULT	42
1-3-2 MINOR FAULTS	44
1-4 SEISMICITY AROUND TEHRAN	44
1-4-1 HISTORICAL EARTHQUAKES	45
1-4-2 MICROSEISMICITY	48
1-5 STATE OF KNOWLEDGE ABOUT TEHRAN BASIN PROPERTIES	50
1-5-1 GEOTECHNICAL DATA	50
1-5-2 SITE EFFECT IN TEHRAN	50
1-5-3 BEDROCK DEPTH	53
1-6 CONCLUSION	56

CHAPTER 2 57

2-1 INTRODUCTION 58

2-2 SINGLE-STATION METHODS 58

2-2-1 SITE-TO-REFERENCE METHOD (SSR) 58

2-2-1-1 PRINCIPLES AND RETRIEVED INDICATORS 58

2-2-1-2 APPLICATION 59

2-2-1-3 LIMITATION 59

2-2-2 H/V METHOD (NOISE AND EARTHQUAKE) 60

2-2-2-1 PRINCIPLES AND RETRIEVED INDICATORS 61

2-2-2-2 APPLICATION 63

2-2-2-3 LIMITATION 65

2-2-3 ELLIPTICITY OF RAYLEIGH WAVES 66

2-2-3-1 PRINCIPLES AND RETRIEVED INDICATORS 66

2-2-3-2 APPLICATION 69

2-2-3-3 LIMITATION 70

2-3 ARRAY (MULTI-STATION) METHODS 70

2-3-1 PRINCIPLES OF THE METHODS 71

2-3-1-2 THE FK AND RTBF PASSIVE ARRAY METHODS 71

2-3-2 ARRAY GEOMETRY AND RESPONSE 73

2-3-3 PROCESSING AND RETRIEVED RESULTS (DISPERSION CURVE – SIGNED ELLIPTICITY) 74

2-3-3-1 DISPERSION CURVE 74

2-3-3-2 SIGNED ELLIPTICITY 75

2-3-4 ACTIVE ARRAY METHOD: MASW 76

2-3-4-1 PROCESSING AND RETRIEVED RESULTS 76

2-3-4-2 APPLICATION AND LIMITATION 78

2-4 INVERSION 78

2-4-1 PRINCIPLES AND MAIN INVERSION METHODS 79

2-4-2 NEIGHBORHOOD ALGORITHM AND GROUND MODEL PARAMETERIZATION 79

2-4-3 COMBINED INVERSION AND PENETRATION DEPTH 82

2-5 CONCLUSION 83

CHAPTER 3 84

GENERAL INTRODUCTION	85
ABSTRACT	86
INTRODUCTION	88
3-1 TECTONIC, GEOLOGICAL AND GEOPHYSICAL SETTINGS	90
3-1-1 TECTONIC SETTINGS	90
3-1-2 GEOLOGY OF THE TEHRAN'S BASIN	94
3-1-3 STATE OF KNOWLEDGE ON TEHRAN'S BASIN GEOMETRY, BEDROCK DEPTH AND NEAR-SURFACE DEPOSITS	97
3-2 SURFACE WAVE BASE METHODS	98
3-2-1 SINGLE STATION METHODS	98
3-2-2 MULTI-STATION ACTIVE AND PASSIVE SURFACE WAVE METHODS	99
3-2-3 INVERSION	99
3-3 GEOTECHNICAL AND GEOPHYSICAL DATA	100
3-3-1 NEAR SURFACE GEOPHYSICAL AND GEOTECHNICAL DATA	100
3-3-2 SINGLE STATION DATA	101
3-3-3 ACTIVE AND PASSIVE SURFACE WAVE MEASUREMENTS	103
3-4 DATA PROCESSING AND RESULTS	104
3-4-1 NEAR SURFACE STIFFNESS	104
3-4-2 FUNDAMENTAL RESONANCE FREQUENCY	105
3-4-3 SURFACE WAVES DISPERSION ESTIMATES	108
3-4-4 SHEAR-WAVE VELOCITY INVERSION	115
3-5 BUILDING A 3D SHEAR-WAVE VELOCITY MODEL FOR TEHRAN'S BASIN	118
3-6 DISCUSSION AND CONCLUSION	125
3-7 REPRESENTATIVE VS AND VP MODELS FOR SEDIMENTS AND SEISMIC BEDROCK	127
3-7-1 SEISMIC BEDROCK VELOCITY AND UNCERTAINTY IN BEDROCK DEPTH MAP	127
3-7-2 REPRESENTATIVE VELOCITY LAYERING MODEL FOR SEDIMENTS	128
3-7-2-1 COMPARISON BETWEEN 1D RESONANCE FREQUENCIES AND OBSERVED H/V PEAK FREQUENCIES	128

3-7-2-2 SIMPLIFICATION OF THE VS LAYERING IN SEDIMENTS	131
--	-----

3-8 GENERAL CONCLUSION	135
-------------------------------	------------

CHAPTER 4

4-1 INTRODUCTION	137
-------------------------	------------

4-2 NUMERICAL METHODS IN SEISMOLOGY	138
--	------------

4-2-1 INTRODUCTION	138
--------------------	-----

4-2-2 FINITE DIFFERENCE METHOD	139
--------------------------------	-----

4-2-3 STABILITY ANALYSIS	142
--------------------------	-----

4-3 SPECTRAL ELEMENT METHOD	145
------------------------------------	------------

4-3-1 INTRODUCTION	145
--------------------	-----

4-3-2 MATHEMATICAL OVERVIEW OF SEM	145
------------------------------------	-----

4-4 EFISPEC3D	153
----------------------	------------

4-4-1 INTRODUCTION	153
--------------------	-----

4-4-2 MESHING THE TEHRAN'S BASIN DOMAIN	156
---	-----

4-4-2-1 INTRODUCTION	156
----------------------	-----

4-4-2-2 TEHRAN BASIN BORDER	159
-----------------------------	-----

4-4-2-3 TEHRAN MESH GENERATION	159
--------------------------------	-----

4-4-3 INPUTS FOR TEHRAN SIMULATION	162
------------------------------------	-----

4-4-3-1 GENERAL CONFIGURATION (TEH.CFG)	163
---	-----

4-4-3-2 MEDIUM DEPTH AND LAYER'S DEFINITION (TEH.IFI)	166
---	-----

4-4-3-3 SOURCE TIME FUNCTION (TEH.PWF)	167
--	-----

4-4-3-4 RECEIVERS (TEH.FSR)	168
-----------------------------	-----

4-5 PROCESSING AND RESULTS	169
-----------------------------------	------------

4-5-1 NUMERICAL SIMULATION SNAPSHOTS	169
--------------------------------------	-----

4-5-2 TIME-SERIES CROSS-SECTION	171
---------------------------------	-----

4-5-3 COMPARISON BETWEEN SIMULATED AND EXPERIMENTAL F_0 'S	175
--	-----

4-5-4 COMPARISON BETWEEN SIMULATED AND EXPERIMENTAL AMPLIFICATIONS (SSR'S)	177
--	-----

4-5-4-1 NORTHERN REGION	178
-------------------------	-----

4-5-4-2 SOUTHERN REGION	179
-------------------------	-----

4-5-4-3 SOUTHEASTERN REGION	182
4-5-4-4 CONCLUSION	184
4-5-5 SENSITIVITY ANALYSIS	185
4-5-5-1 IMPACT OF THE REFERENCE STATION	186
4-5-5-2 THE EFFECT OF THE QUALITY FACTOR	188
4-5-5-3 THE EFFECT OF BEDROCK S-WAVE VELOCITY	189
4-6 DISCUSSION AND CONCLUSION	191
<hr/>	
<i>CHAPTER 5</i>	196
<hr/>	
5-1 GENERAL CONCLUSION	197
<hr/>	
5-2 PERSPECTIVES AND LIMITATIONS	201
<hr/>	
REFERENCES	203
<hr/>	
APPENDIX A:	216
<hr/>	
APPENDIX B:	217
<hr/>	
APPENDIX C:	226
<hr/>	
APPENDIX D:	228
<hr/>	
APPENDIX E:	240
<hr/>	

List of Figures

- Figure i-1:** Localization of Tehran City. A) Tehran location in the northern part of Iran. B) Tehran province and its counties. The cities with the population over 50000 are shown in this figure. C) Tehran city districts and the comparison between Tehran city border (white) and Tehran basin border (blue)..... **Page 22**
- Figure i-2:** Left: density map of Tehran population (From JICA 2000). Table represents the population density from the latest census (SCI 2016). Right: The building age for 22 Tehran districts..... **Page 23**
- Figure i-3:** Seismic Hazard Map of the Middle East (Giardini et al., 2018). Tehran, located in the center, displays a very strong seismic risk..... **Page 24**
- Figure 1-1:** Left: Active fault map of Iran (from Hessami et al., 2007). Right: Tectonic structure of central Alborz with main faults (black lines) and location of central Alborz's unit (blue text) **Page 32**
- Figure 1-2:** Cross section of Alborz range at the longitude of Tehran (Allen et al., 2003). This cross section is located on figure 1-1-right with a blue line..... **Page 32**
- Figure 1-3:** Schematic diagram displaying the exact definition of piedmont between the mountain and the plain (Parsons & Abrahams, 2009). Piedmont in Tehran is defined from subaerial alluvial boundary (SAB) near the mountain front..... **Page 35**
- Figure 1-4:** Terminology for the Tehran basin definition. A: geological, geomorphological and tectonic map of the piedmont and plain areas. NTF: North Tehran Fault; N.: Niavaran Fault; M.: Mashmodieh or Lavizan Fault; D.: Davoudieh Fault; T.: Tarasht Fault; N.R. F/S: North Ray Fault or escarpment; S.R. F/S: South Ray Fault or escarpment; K F/S: Kahrizak Fault or escarpment. 9 Anticlinal and 2 synclinal traces are also show in this figure (after Knill & Jones, 1968). B: map showing the different zones of Piedmont and plain introduced by Berberian et al. (1985). C: Location of Arathkuh (southern limit of basin) and RudShur Basin, small local depression separated from the Tehran Basin..... **Page 36**
- Figure 1-5:** Synthesis of the stratigraphic sequences of the Tehran basin following Rieben (1955, 1966), Engalenc (1968) and Pedrami (1978) **Page 39**
- Figure 1-6:** Geological cross-section of Tehran alluviums based on Rieben classification and borehole data (JICA & CEST, 2000) **Page 41**
- Figure 1-7:** The latest release of geological map of Tehran basin sediments (after Abbassi and Shabanian,2023) **Page 41**
- Figure 1-8:** Synthesis of the active faults within the Tehran basin. Parchin, Mosha, SorkhehHesar and Firuzeh are out-basin faults but also shown in this figure (from Berberian et al., 1985; Nazari et al., 2010) **Page 44**
- Figure 1-9:** C: Micro seismicity located by the Tehran (IGUT) network between 1996 and 2008 (From Tatar et al., 2012)..... **Page 49**

Figure 1-10: SSR results for temporary network station in Tehran considering JAM as reference station (redrawn from Haghshenas (2005))..... **Page 51**

Figure 1-11: Fazlavi (2015) studies. A) Location of arrays for North-South cross section. B) 2D velocity profiles for Tehran basin (redrawn from Fazlavi 2015))..... **Page 53**

Figure 1-12: Shirzad and Shomali (2013) tomographic results from seismic noise data. A: Rayleigh wave group-velocity tomography map for 1s. period. B: Rayleigh wave group-velocity tomography map for 2 s. period. C: the sensitivity kernel in depth for 1 s. and 2 s. period..... **Page 55**

Figure 2-1: A) The principle of SSR computation, modified after Stiedl et al. (1996). B) The SSR typical results example obtained in Grenoble valley for a 2.5 Ml seismic event occurred 15 km far from the basin comparing to 1D transfer function and H/V noise curve (adapted from Cornou & Bard, 2003))..... **Page 60**

Figure 2-2: A) Correlation between H/V peak frequency (f_0 -H/V) and SSR fundamental frequency (f_0 -SSR) and B) H/V amplitude (A_0 -H/V) and SSR amplitude (A_0 -SSR) for SESAME (2004) sites (adapted from Haghshenas et al., 2008))..... **Page 61**

Figure 2-3: The various steps to retrieve H/V curves from seismic ambient noise recordings (adapted from Bonnefoy-Claudet, 2004))..... **Page 63**

Figure 2-4: (left panel) Amplitude spectra are shown in terms of time and frequency while the maximum value in time on the vertical axis and the corresponding value on the horizontal axes (white points) are extracted. (right panel) For each frequency, the saved ratios are analyzed statistically in a 2D histogram representation (adapted from Poggi et al., 2012))..... **Page 67**

Figure 2-5: (top panel) At a given frequency narrow band f , signal blocks extracted on all three components for each detected zero crossing from negative to positive on the vertical component, the N and E components being phase-shifted by $\pi/2$. (bottom panel) The N and E signals are projected in the azimuth that maximizes the correlation with the vertical component to form the horizontal time blocks. All the vertical and horizontal Signals are then summed, which yields a single vertical and horizontal signal. Next, the ellipticity at frequency f is measured from the energy of these summed signals (adapted from Hobiger, 2011))..... **Page 68**

Figure 2-6: Example of array response from single time window f-k analysis result. The maximum beam power found at $\vec{k} = \vec{k}_0$ is shifted from the center..... **Page 72**

Figure 2-7: (left) Theoretical frequency–wavenumber array responses and (left) the 2D section across an azimuth of the theoretical frequency–wavenumber determining k_{min} (here at 0.04 rad/m) and k_{max} (here at +/- 0.4 rad/m) (adapted from Foti et al., 2018))..... **Page 74**

Figure 2-8: A) ambient noise signals recorded at 8 station simultaneously. B) the array limits (k_{max} , k_{min} , $k_{max}/2$ and $k_{min}/2$) and C) the array geometry..... **Page 75**

Figure 2-9: A) Schematic view of an array analysis output file. For each time windows, slowness (1/phase velocity) can be extracted for Rayleigh and Love waves. For Rayleigh waves, the corresponding ellipticity values can also be determined. B) The manual picking of a dispersion curve (black curve) from the PDF frequency-Rayleigh velocity..... **Page 75**

Figure 2-10: Representation of ellipticity angle (ξ) for different prograde/retrograde values. Ellipticity angle can be varies between $\pm\pi/2$ (adapted from Marano et al., 2012)..... **Page 76**

Figure 2-11: Schematic view of data acquisition for MASW method (adapted from Olafsdottir et al., 2019).....**Page 77**

Figure 2-12: Schematic view of 2D wavefield transformation of A) time-offset (T-X) domain to B) frequency-wavenumber (F-K) domain..... **Page 78**

Figure 2-13: Example of Voronoi cells for a two-dimensional parameter space. A) The first iteration with $n_{s0} = 9$ leads to find the cell with the lowest misfit (cell number 6). B) the cell number 6 is divided to $n_s=7$ new cells to search for minimum misfit for the second iteration..... **Page 80**

Figure 2-14: Example of inversion with parameterization involving two layers with linear increase of Vs with depth over half space. The black Vs profile indicates the theoretical Vs profile while the inverted Vs profiles are indicated in color. The color scale depends on the misfit values (adapted from Renalier, 2010)..... **Page 81**

Figure 2-15: Schematic view of the contribution of each method in the frequency/wavelength domain..... **Page 83**

Figure 3-1: Site amplification (site-to-reference spectral ratio) results of temporary seismological network in Tehran, with JAM as the reference station. The highest amplification values, reaching up to 8, are observed at MOF and SHL stations in south and southwest areas (re-drawn after Haghshenas 2005)..... **Page 90**

Figure 3-2: Tectonic setting of Central Alborz (A) and Tehran region (B). A: Central Alborz with main faults (red lines) and units (in blue), the historical earthquakes with $M_s \geq 6.5$ are displayed in white rectangles (for details, see Berberian and Yeats, 2018). The Tehran city location is displayed in red filled area. B: Faults close and inside the Tehran’s basin: faults over 10 km length (thick red lines) and other important quaternary faults (thin red lines, see Table 3-1 for detail). The three main faults (North Tehran Fault, NTF, Mosha and Parchin) close to Tehran are labelled in red..... **Page 93**

Figure 3-3: A) Tehran’s quaternary sediments in the piedmont and the plain of the Tehran’s basin. Map modified from Abbassi and Shabanian (2023) and Abbassi and Farbod (2009). B) The studied area of the basin for the 3D velocity model (blue line) where the southwestern unrecognizable basin limits are shown by a dash red line..... **Page 96**

Figure 3-4: Figure 4: Distribution of the 197 near surface (seismic refraction profiles) and geotechnical data used in this study (black dots). In background, the representation of the 41 JICA and CEST (2000) soil profiles (see soil profiles description in appendix A, from the softest profile labeled as #1 to the stiffest one labeled as #41)..... **Page 101**

Figure 3-5: Spatial distribution of single station seismic noise measurements used in this study. Dashed rectangles: areas with restricted access..... **Page 103**

Figure 3-6: Location of the 33 seismic noise arrays in Tehran as well as the 13 MASW profiles... **Page 104**

Figure 3-7: Spatial variation of V_{s30} in Tehran inferred from the 197 near surface and geotechnical data (Figure 4)..... **Page 105**

Figure 3-8: H/V curves in Tehran’s basin and their 4 typologies following the SESAME (2004) criteria. A: all the 575 average H/V curves. B: the 159 interpretable average HV curves from which HV peak frequencies have been extracted. C: typical H/V curve with a clear peak allowing the f_0 and A_0 determination. D: example of H/V curve with a broad peak type. E: H/V curve with a low amplitude peak. F: various examples of H/V curves that could not be interpreted. In C, D, E and F, the thick and thin dashed lines indicate the average H/V curve with its uncertainty, respectively. The peak frequency (f_0) is indicated by the arrow..... **Page 107**

Figure 3-9: Spatial distribution of H/V peak frequencies in Tehran’s basin with a hypothetical line (in red) that separates the northeast part of the basin with frequencies higher than 0.5 Hz and the southwest part of the basin with frequencies lower than 0.5 Hz. Dashed rectangle: area with restricted access..... **Page 108**

Figure 3-10: Array processing results at FAR site (A-C) and the extracted dispersion curves and ellipticities of Rayleigh waves with their uncertainty (D-F). A: Probability density function (PDF) of Rayleigh wave phase velocities as a function of frequency for modes R0 and R1. B: PDF of Love waves phase velocities as a function of frequency for the fundamental mode L0. C: PDF of the Rayleigh wave ellipticity angles as a function of frequency for R0 (upper panel) and R1 (lower panel). D: extracted dispersion curves for the fundamental (R0) and first higher mode (R1) of Rayleigh waves. E: extracted dispersion curve for the fundamental mode (L0) of Love waves. F: extracted ellipticity angle curve for the fundamental R0 (upper panel) and first higher mode R1 (lower panel) of the Rayleigh waves. In A and B, the theoretical array resolution limits (black lines), as defined in Wathelet et al. (2008), are indicated: $k_{min}/2$ (dashed line), k_{min} (continuous line), $k_{max}/2$ (dashed line), k_{max} (plain line)..... **Page 111**

Figure 3-11: A- Rayleigh wave phase velocity as a function of wavelength for the different arrays. B: spatial distribution of the phase velocities at 400 m wavelength with a red hypothetical line separating the northeast and the south part of the basin..... **Page 112**

Figure 3-12: The frequency range of dispersion curves and Rayleigh wave ellipticities..... **Page 113**

Figure 3-13: Comparison of ellipticity curves extracted from seismic noise recordings (RayDec method, in blue; Hobiger et al., 2009) with the ellipticity extracted from earthquakes coda recordings (RayDecC method, in red; Aki, 1969; Zeng 2006). The number of earthquakes used is 47, 99, 64, 37 and 42 for AZP, MOF, SHL, FAR and DAR seismological stations (Figure 1), respectively..... **Page 114**

Figure 3-14: Inversion results for ABS (A), FAR (B) and PLC (C) sites. Black curves: Fundamental Rayleigh wave mode (R0) dispersion curve from RTBF processing and related ellipticity curve (including uncertainty). Purple curves: First higher Rayleigh wave mode (R1) dispersion curve from RTBF processing and related ellipticity curve (including uncertainty). Green curves: Fundamental Love wave mode (L0) dispersion curve from RTBF processing (including uncertainty). Blue curves: dispersion curves for R0 mode from MASW processing. Red curves: Rayleigh wave ellipticity angle inferred from RayDec method (including uncertainty). Notice that for PLC array, the ellipticity angle indicated in black corresponds to the ellipticity angle inferred from RayDec assuming a negative sign. In each panel, the forward modeled dispersion and ellipticity curves as well as the shear-wave velocity profiles are indicated in color, gray colors indicating models with the lowest misfit..... **Page 116**

Figure 3-15: Variation of the fundamental Rayleigh wave ellipticity angle as a function of the frequency for various shear-wave velocity contrasts between sediments and seismic bedrock (gray and black curves) at PLC site. The black curve stands for the velocity contrast (values indicated in the figure) leading to a change of the ellipticity angle from negative to positive values for frequencies below 1.4 Hz. The red and green dots, with related uncertainty, correspond to the ellipticity angle inferred from the RayDec method assuming negative or positive angle..... **Page 117**

Figure 3-16: A. Relationship between the fundamental resonance frequency and the seismic bedrock depth in Tehran’s basin. The red line represented the inverse power fitted curve and red dashed lines are the $\pm 50\%$ confidence intervals. B. Comparison of the relationship obtained in Tehran’s basin with other sedimentary basins over the world (adapted from Thabet, 2019)..... **Page 119**

Figure 3-17: Seismic bedrock depth of Tehran obtained from the relationship between the fundamental resonance frequency and the seismic bedrock depth. The red squares indicate the seismic array location. The yellow dots represent the location of used H/V to estimate bedrock. The red line shows the hypothetical border separating the NE and the SW of the basin. The black line indicates the cross sections..... **Page 120**

Figure 3-18: Interpretation of the geophysical (A) and geological (B) AA’ cross section. A: geophysical representation with the inverted Vs profiles (names of the arrays are indicated on the cross-section) and the bedrock depth inferred at single-station sites using the resonance frequency-sediment thickness relationship. The dashed area represents the uncertainty on the seismic bedrock depth fixed to ± 50 m. B: geological interpretation inferred from geophysical data and surface geology. The red question marks correspond to

limited knowledge about the extension of A formation under the southern part of the city. The yellow question marks correspond to the doubt about the bedrock depth shape between NZM and FAR due to the absence of data..... **Page 122**

Figure 3-19: Interpretation of the geophysical (A) and geological (B) BB' cross section. A: geophysical representation with the inverted V_s profiles (names of the arrays are indicated on the cross-section) and the bedrock depth inferred at single-station sites using the resonance frequency-sediment thickness relationship. The dashed area represents the uncertainty on the seismic bedrock depth fixed to +/- 50 m. B: geological interpretation inferred from geophysical data and surface geology. The red question marks correspond to limited knowledge about the extension of A formation under the southern part of the city..... **Page 123**

Figure 3-20: Distribution of shear-wave velocities for A) the surface layer corresponding to B, C or D formation and B) the deep sediment layer corresponding to A formation..... **Page 124**

Figure 3-21: The differences between inverted (blue bars) and interpolated (yellow bars) bedrock depth. Left axis indicates the depth and the right axis indicates relative error that does not exceed about 5%..... **Page 129**

Figure 3-22: Example of SH transfer functions for two sites in north (DAR) and south (FAR) of Tehran. The best misfit profiles are indicated in black on the inversion results (left panel) and the corresponding theoretical SH transfer function are indicated in the right panel..... **Page 129**

Figure 3-23: Fundamental resonance frequencies (f_0) extracted at array sites (black squares) with estimated error (orange lines) and the theoretical f_0 (green square) from 1D transfer function. The red dashed lines represent the array sites at which no f_0 could be extracted from H/V curves..... **Page 130**

Figure 3-24: Tehran Basin map showing the absolute difference between f_0 from the transfer functions and the f_0 extracted from the H/V curves..... **Page 131**

Figure 3-25: Best misfit V_s profile (in black) for two sites in north (DAR) and south (FAR) of Tehran (left panel) and the simplified V_s profile (in red) (left panel), and the corresponding theoretical SH transfer functions for the best misfit V_s profile (in black) and the simplified one (in red, right panel)..... **Page 132**

Figure 3-26: Theoretical f_0 from best misfit V_s profiles (3 or more sedimentary layers, in green) and the simplified one (2 sedimentary layers, in black). The maximum difference between frequencies is less than 0.03 Hz..... **Page 132**

Figure 3-27: Distribution of V_s (black crosses) for the soft layer (A) and the hard layer (B) for the 27 array sites. The red or blue plain lines represent the average velocity from the 27 sites. For the soft layer (A) the dashed lines represent ± 200 m/s and for the hard layer (B) the dashed lines represent ± 250 m/s shear wave velocity **Page 133**

Figure 3-28: Fundamental frequencies (f_0) extracted from array stations (black x) with estimated error (orange bars) and the calculated f_0 (green square) from 1D transfer function for double simplification 1D models. The red dashed lines represent the arrays without f_0 coming from H/V curves..... **Page 134**

Figure 3-29: Evaluation of the errors linked to the simplified Vs model comparing the fundamental frequencies derived from H/V curves and from the 1D simplified Vs layering model. Left panel: scatter plot of f_{0HV} peaks and f_{0TF} extracted from 1D SH transfer functions. The dash line represents the 20% standard deviation. Right panel: the density plot of the relative error between the observed H/V peak frequencies and the theoretical ones..... **Page 134**

Figure 4-1: Illustration of the space-time discretization scheme and elastic wave equation of the FD algorithm (adopted from Igel, 2017)..... **Page 141**

Figure 4-2: left: The numerical phase velocity as a function of the number of grid points for various CFL criteria. As the number of grid points per wavelength increases the correct velocity is recovered (adapted from Igel 2017) Right: an example of left tail shape distorted waveform propagated in space as a result of numerical dispersion caused by deficient number of (grid) points per wavelength (nppw)..... **Page 144**

Figure 4-3: Domain decomposition from the whole domain to “ne” elements, mapping each element to the interval of -1 to 1 (Adapted from Schubert, 2003)..... **Page 147**

Figure 4-4: GLL points between -1 and 1 as a function of the polynomial order N (Adapted from Chaljub, 2000)..... **Page 149**

Figure 4-5: representation of Mass Matrix for 3 element each contains 5 colocation point (Adapted from Igel, 2017)..... **Page 151**

Figure 4-6: representation of Stiffness Matrix for 3 element each contains 5 colocation point (Adapted from Igel, 2017)..... **Page 152**

Figure 4-7: Domain decomposition when space-dependent fields are discretized. Here is an example represented the partitioning volumes for unstructured grids in 3D for volcano simulation (Adapted from Igel, 2017)..... **Page 154**

Figure 4-8: EFISPEC3D workflow (Adapted from EFISPEC tutorial documents)..... **Page 155**

Figure 4-9: A) Basic definition of mesh objects. B) Different types of 3D mesh elements. C) The type of meshing subdivision. Left: conformal and right: non-conformal structured mesh..... **Page 157**

Figure 4-10: Homogenization for velocity profiles. Instead of considering the abrupt changes in velocity between two layers the integral of slowness from $L/2$ to $-L/2$ smoothed the velocity profile. (the figure adapted from EFISPEC3D tutorial documents)..... **Page 158**

Figure 4-11: A) the simulation block for Tehran study shown in Central Alborz region. B) the extracted region, and C) the rotated and translated block for use on simulation..... **Page 160**

Figure 4-12: the snapshot of the mesh that utilized in the simulation..... **Page 162**

Figure 4-13: An example of grid image with correspond values and representation with ESRI ASCII grid file format (Esri, Inc., 2023)..... **Page 166**

Figure 4-14: The 2-layer medium represented at 2D cross section fulfilled the mentioned criteria (Adapted from EFISPEC3D tutorial documents)..... **Page 167**

Figure 4-15: The low pass filter impulse with duration of three seconds and the amplitude spectrum with the maximum target frequency of 2 Hz..... **Page 168**

Figure 4-16: The locations of H/V stations' receivers are represented on the elevation model map of Tehran in local coordinates..... **Page 169**

Figure 4-17: plot A to D represents the wave propagation at four different time points: 3, 5, 10, and 20 seconds after the source was injected. The middle plot displays a 3D velocity structure of Tehran, with red arrows indicating reflected waves from the rocks, blue arrows indicating absorbed waves at the basin boundaries, and yellow arrows pointing wave trapping in the deeper parts of the basin..... **Page 170**

Figure 4-18: An example of time-series for displacement components..... **Page 171**

Figure 4-19: A) Tehran map with the location of two cross section AA' and BB'; B): AA' geological cross-section and C) corresponding velocity seismograms; D) BB' geological cross-section and E) corresponding seismograms..... **Page 172**

Figure 4-20: The Fourier amplitude spectrum for all time-series extracted on both cross sections. A: Map localization of the A-A' and B-B' cross sections. B: Fourier amplitude spectra for A-A'. C: Fourier amplitude spectra for B-B'..... **Page 174**

Figure 4-21: Figure 4-21: A: Scatter plot of f_0 extracted from 3D numerical simulation as a function of H/V peak frequencies observed in Tehran. The dash line represents the 20% standard deviation, the right panel represents density and histogram plot of relative error between the resonance frequencies derived from synthetics and experimental data. B: Spatial distribution of the absolute errors between observed and simulated frequencies..... **Page 176**

Figure 4-22: Different regions considered to compare observed and simulated SSR curves. Each region exhibits almost the same shape of SSR curves..... **Page 177**

Figure 4-23: SSR derived from ground motion synthetics (red lines) and experimental earthquake data (blue lines) at four stations located in the north of Tehran's basin. A: DAR station, B: SUD station, C: TAP station and D: ABM station. For all stations..... **Page 180**

Figure 4-24: SSR derived from ground motion synthetics (red lines) and experimental earthquake data (blue lines) at four stations located in the south of Tehran's basin. A: FAR station, B: MOF station, C: GHP station and D: SHL station. For all stations, the 1D SH transfer function is displayed in green lines..... **Page 181**

Figure 4-25: SSR derived from ground motion synthetics (red lines) and experimental earthquake data (blue lines) at four stations located in the in southeast zone. A: AZP station, B: CAL station and C: TAR station. For all stations, the 1D simulated response is displayed in green lines..... **Page 183**

Figure 4-26: A: Amplification at the fundamental resonance frequency for the experimental and simulated SSR curves. B: ratio between simulated and experimental amplification at the fundamental resonance frequency as a function of experimental resonance frequency..... **Page 184**

Figure 4-27: A: Location of reference JAM station and 17 other possible bedrock reference stations (red plain circles) and the location of DAR and FAR stations in yellow. B: The Fourier amplitude spectra of all reference stations (brown curve for JAM station and light grey curves for the 17 other sites) computed from the surface velocities. C: the experimental SSR (in blue) and simulated SSRs using the 17 reference stations (gray lines) for DAR station. The average SSR using all reference stations including JAM is shown in black while the SSR computed using JAM is indicated in red. D: the experimental SSR (in blue) and simulated SSR (in red) for FAR station. The average SSR using all reference stations including JAM is shown in black while the SSR computing using JAM is indicated in red..... **Page 187**

Figure 4-28: Testing the sensitivity of the SSR results to the quality factor (Q_s). The solid lines represent the simulation results using $Q_s=V_s/10$, while the dashed lines represent the results using $Q_s=V_s/5$. Note that $Q_p=2Q_s$ **Page 188**

Figure 4-29: Testing the sensitivity of the SSR curves to change in the impedance contrast. the experimental SSR (in blue) and simulated SSR (in red), the simulated SSR with bedrock velocity of 3500 m/s (in yellow) and 1D transfer function (in green) for A: DAR station and B: FAR station..... **Page 190**

Figure 4-30: Simulated SSR at H/V experimental measurements location divided into two groups based on fundamental resonance frequencies. Results show that the sites with fundamental resonance frequency below 0.5 Hz located in the southern region exhibit significant 3D site effect..... **Page 193**

Figure 4-31: Interpolated results for f_0 (A) and A_0 (B) in Tehran basin from the simulated SSR at H/V sites..... **Page 194**

List of Tables

Table 1-1: Determination of geotechnical properties based on geological features (inspired from Fakher et al., 2007).....	Page 40
Table 1-2: Tehran’s active faults identified in the Tehran basin from reports done by TDMMO and IIEES.....	Page 43
Table 1-3: Pre-historical, historical and instrumental earthquakes in Tehran region with the magnitude greater than 4.0.....	Page 47
Table 2-1: Parameters of inverse power frequency– thickness relationship for some sedimentary basin around the world.....	Page 64
Table 3-1: Tehran’s active faults with their lengths from Abbassi and Mokhtari (2020). NTF: North Tehran Fault.....	Page 92
Table 3-2: The different parameters used for inversion process.....	Page 110
Table 3-3: For the 6 stations displaying a high H/V amplitude (> 3.5) determination of the velocity in bedrock to change the ellipticity angle from negative to positive. The velocity in the last layer is extracted from the Vs profiles coming from the inversions. The impedance contrast to have sign change varies between 0.42 to 0.48.....	Page 118
Table 3-4: P- and S- wave velocity for the Alborz region for depth shallower than 5 km.....	Page 128
Table 3-5: Relative error for each calculated f_0 from response analysis. The arrays without f_0 from H/V are not presented.....	Page 130
Table 4-1: The different input files requires for 3D wave propagation simulation using EFISPEC3D code.	Page 162
Table 4-2: The layer medium properties of the Tehran simulation.....	Page 166
Table 4-3: The Pearson correlation coefficient between simulated curves before and after the change of bedrock velocity. Negative change indicates that the results have improved following the bedrock velocity modification. the Pearson correlation coefficient ranges from -1 to +1, where -1 indicates a perfect negative correlation, and +1 indicates a perfect positive correlation.....	Page 190

General Introduction

Iran is a country in Western Asia, lying between the latitudes of 25.4 and 39.46 degrees above the equator in the northern hemisphere and 44.2 and 63.19 degrees east of the Greenwich meridian in the eastern hemisphere. Iran covers an area of 1.64 million square kilometers and divided into 31 provinces (SCI, 2016; Figure i-1).

Tehran province is the most populous and influential of Iran's 31 provinces. Because of centralization, 16.60% of Iran's population (13 267 637 inhabitants) lives in Tehran province, which covers only about 1% of the country's land area. Also, due to the massive urbanization, 95% of this population lives in urban area (SCI, 2016).

Tehran city, the capital, with an area of 730 km^2 is home to 872 7510 of these inhabitants (65%) who live in 22 districts. There are also 11 smaller cities in the Tehran province that have populations of more than 100,000 people (SCI, 2016; Figure i-1).

Tehran sedimentary basin comprises a larger area, including some of the nearby smaller cities around Tehran city. It is bounded to the North and East by the city of Tehran in itself. The southern bounds are estimated around 30 kilometers South of the city. However, to the West of the city, the basin limits are not clearly recognizable (Figure i-1).

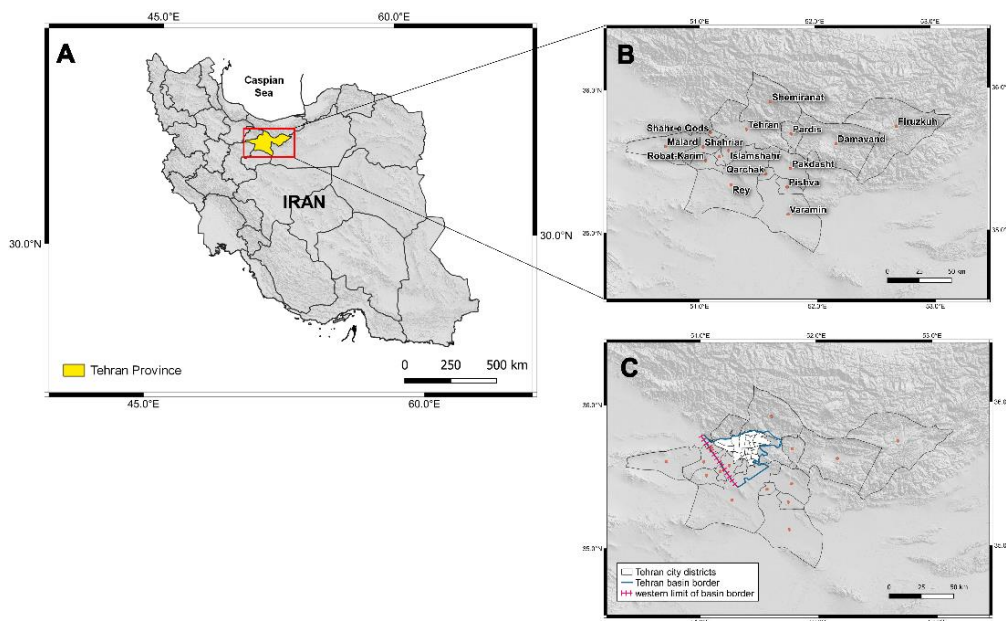


Figure i-1: Localization of Tehran City. A) Tehran location in the northern part of Iran. B) Tehran province and its counties. The cities with the population over 50000 are shown in this figure. C) Tehran city districts and the comparison between Tehran city border (white) and Tehran basin border (blue).

Tehran has an average population density of more than 10 000 people per square kilometer. Meanwhile, population density in some part, such as District 10 near the city center, exceeds 40 000 people per square kilometer, making Tehran one of the world's largest and densest urban centers with a significant seismic hazard (Figure i-2-left).

Because of the population, Tehran also has many buildings. Totally, there are 2 871 996 buildings in Tehran. These buildings comprise different typologies with Steel Frame and Reinforced Concrete which are the two most prevalent typologies, constituting approximately 57% and 34% of the building stock respectively. Among them 58% of Tehran's buildings are low-rise (1-3 floors), 35% mid-rise (4-7 floors), and 7% high-rise (more than 8 floors). According to the JICA and CEST (2000) up to 80% of the buildings in the city center (old core of the city), with the highest population density, are more than 50 years old. These buildings have poor construction systems and no seismic retrofitting in the design life (Figure i-2-right; SCI 2016).

Also, Tehran suffers from remarkable seismic exposure derived from risk elements (Firuzi et al., 2019). The problems are coming both from the density population and probably the impact on the buildings: poor construction management, failure to respect the building codes and the progression of urban fabrics towards hazard zones, but also the traffic management: very congested streets, inefficient highway network, etc. Of course, these elements work as a multiplier of vulnerability of the Tehran city (Amini Hosseini et al., 2009).

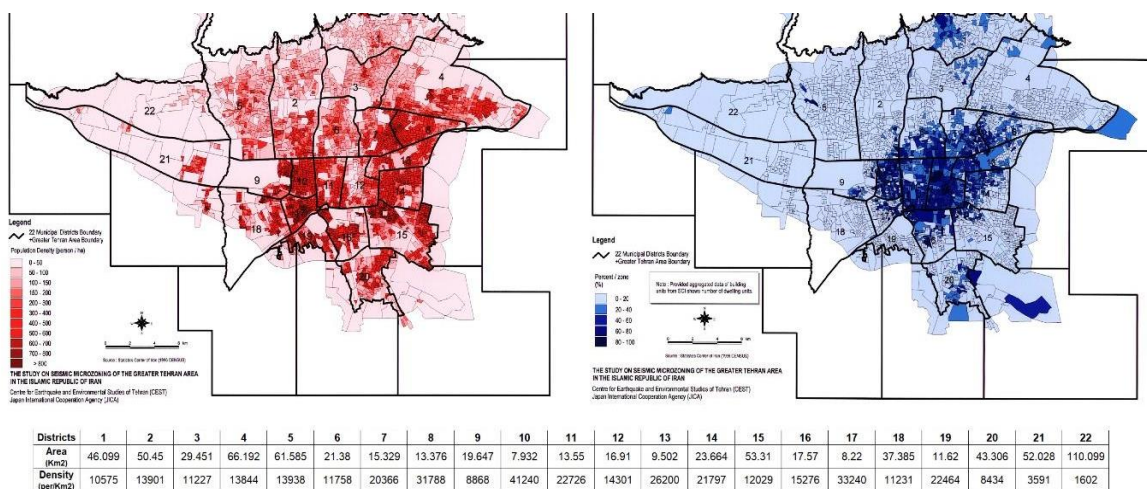


Figure i-2: Left: density map of Tehran population (From JICA 2000). Table below represents the population density from the latest census (SCI 2016). Right: The building age for 22 Tehran districts.

Besides buildings and population, Tehran urban area serves as the hub for many economic activities in Iran, when its economy represents almost 30% of the whole country's GDP (SCI, 2016). It demonstrates again the importance of safety and security against all natural/man-made hazards in Tehran area, and also at national scale as seismic hazard is regarded as the main natural hazard in Tehran in many studies. In fact, the mean value of peak ground acceleration (PGA) with 10% probability of being exceeded in 50 years (corresponding to a mean return period of 475 years) for Tehran is about 0.5 g. Noteworthy, on the ground surface level, the PGA is higher, as local soil deposits in this area amplify the seismic motion (Giardini et al., 2018; Figure i-3).

So, back to the classical definition of seismic risk assessment as a simple convolution of three components including hazard, exposure and vulnerability, Tehran needs detailed studies in all aspects related to earthquake risk in order to enhance people and governmental official preparedness level.

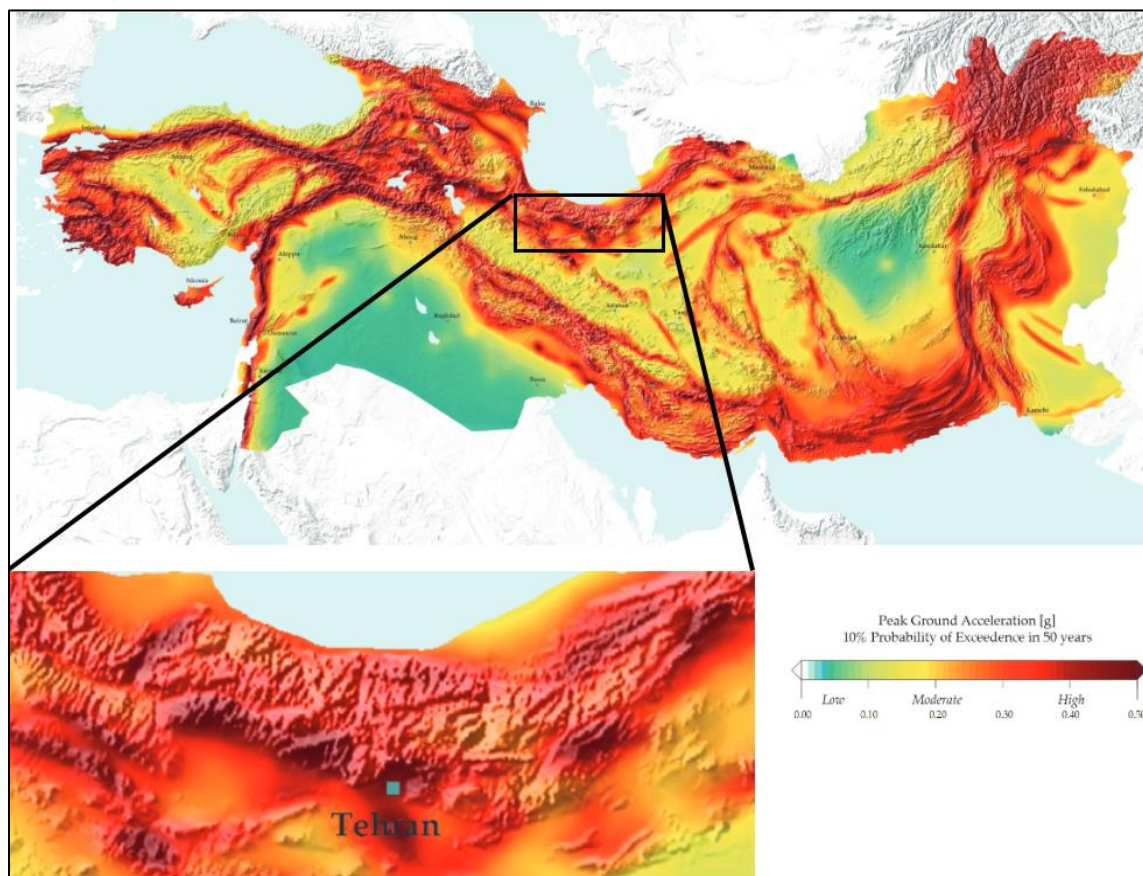


Figure i-3: Seismic Hazard Map of the Middle East (Giardini et al., 2018). Tehran, located in the center, displays a very strong seismic risk.

But this is not the end of story. Site effects which are widely recognized as an important factor of any seismic risk studies has not been considering in the recent assessment of seismic hazard in Tehran.

Site effects refer to the local variations in ground motion characteristics during an earthquake due to variations in the geological and geotechnical properties of the site. In Tehran, the only instrumental site effect study dated back to 2005, when the analysis of earthquakes recorded by a temporary seismological network has approved a large amplification of seismic ground motion, ranging from 4 to 8, over a broad frequency range spanning from very low frequencies around 0.4 Hz up to 1-2 Hz. However, simultaneous analysis of noise recordings yielded contrasting findings. The H/V curves obtained from one hour of ambient noise recordings (extracted at 1 a.m.), exhibited flat responses at the resonance frequencies indicated by earthquakes (by SSR; site to reference method; Haghshenas, 2005). The study suggested two hypotheses for site effect in Tehran based on these observations.

- i) The existence of a low velocity contrast at depth corresponding to a deep bedrock with very thick alluvial deposits that can explain the SSR low frequency amplification and the H/V noise failure. For the latter it is possible that at periods of time, the energy at low frequency inside the noise wavefield is not strong enough to excite the structure.
- ii) The existence of significant lateral discontinuities and the potential influence of 2D/3D effects arising from faulting and folding in the city as well as the geological heritage can explain the broad frequency range of amplification and indirectly support the difference observed between SSR and the H/V method.

The main objective in this thesis is the construction of the first experimental 3D velocity model of the Tehran basin and the surface ground motion simulation, in order to enable us to predict more realistic surface ground motion for future earthquakes and resolve the ambiguity raised by the previous study. Despite its importance indeed, all the existing seismic hazard assessments in Tehran have not considered the multi-dimensional effects yet, and there is a lack of studies that have explored the geometry and elastic properties of the basin rocks/sediments.

To do that, in **Chapter 1** I will make an overview of the Tehran area in terms of different aspects related to geology, geophysics, geotechnics, etc. I will introduce the tectonics and geological conditions of the Alborz Mountain range (north of the Tehran basin) as an active region as well as

the geomorphological structure of the basin as a tectonized area, filled by more or less thick alluvial deposits prone to a huge possibility of 2D/3D site effects. Then, the active faulting around and within the Tehran basin will be described as these characteristics can strongly influence the geometry of the basin and then the seismic hazard and risk in Tehran city. Saying active faults, the earthquakes are not far. So current seismicity and historical earthquakes will be discussed to show how dangerous this region is, in terms of potential devastating earthquakes.

Since the impact of an earthquake is strongly linked to the seismic waves' velocity and geometrical properties of the medium, a synthesis will be done about the known geophysical-geotechnical data that can give some indications about the subsurface structure/layers in velocity as well as the derived knowledge about the basin's geometry (bedrock depth). Additionally, I will realize a state of the art about site effect studies in Tehran which reveals again a significant site amplification problematic in the Tehran basin.

Chapter 2 is dedicated to the methods used to construct the Tehran 3D shear wave velocity structure model. First of all, the most reliable experimental method to extract f_0 and its related amplification (A_0), the SSR method (site to reference), will be introduced and then the H/V method as a tool to retrieve f_0 will be described. Following that, the processing of H/V ratio and some examples of retrieving frequency–depth relations with H/V ratio will be discussed. Since the Tehran basin is assumed as a 2D/3D basin, I also introduce the potential and limitation of H/V ratio in complex subsurface structures. After, I will explain how the ellipticity of Rayleigh waves can be extracted from a single-station and used to retrieve shear wave velocity, and I will describe a new approach based on the Random decrement technique (Hobiger et al., 2009) to retrieve Rayleigh wave ellipticities from earthquake data. Then the array methods will be discussed as a tool to retrieve the shear wave velocity at a given site. Finally, the inversion method, processing, parametrization, limitations and the usefulness of using joint inversion to constrain at best the inverted S-wave velocity profiles will be discussed.

Chapter 3 focuses on the construction of the 3D velocity structure of the Tehran basin. Writing as a paper, this chapter presents the collected data that I used, which encompassed the acquisition of near-surface and geotechnical data as well as the five campaigns of single station measurements and the two campaigns of active and passive seismic noise array measurements in Tehran city. The data processing leads to the fundamental resonance frequency map. To retrieve the 1D shear wave velocity profile, the inversion of the dispersion curve is done by combining all available data that

covers almost the entire frequency range to ensure the most valid 1D profiles. Finally, to build the 3D shear-wave velocity model for the Tehran basin, an empirical relationship between bedrock depth and fundamental resonance frequency is defined, allowing to map the seismic bedrock depth, while the interpolation between the 1D velocity profile gives an idea about the velocity structure up to the bedrock. This velocity structure is then converted to a 3D velocity model after establishing a representative V_s layering model for the basin.

Finally, the principal aim of the **Chapter 4** is to perform 3D numerical simulations of seismic ground motion to improve our understanding of the Tehran sedimentary basins effect on long-period earthquake ground motion. In this context, this chapter is structured into four main sections beginning by providing a brief explanation of the necessity of 2D/3D simulation in Tehran. After that, I explain the spectral element method (SEM) and its mathematical foundation. It will help to understand how to use SEM for simulating wave propagations and provides a short but sufficient understanding of the concepts and principles that the SEM relies on. The third section of the chapter is dedicated to the details of the EFISPEC3D code (De Martin, 2011 and De Martin et al., 2013), with a review about the code structures and analysis of its components. The section gave an understanding of how this numerical code works and how it can be effectively utilized for simulations of seismic wave propagation. Furthermore, the section also covers the preparation steps of EFISPEC3D data input, which is an essential step in our modeling process. In the final section, the results obtained from the modeling are presented and analyzed, with an emphasis on the interpretation of the simulation's outcomes, including validation of the robustness of results, comparing the results with observation data and exploring the sensitivity of the results to some incoming data.

CHAPTER 1

Quick overview of Tehran's basin

Geology, seismicity and site effect

1-1 Introduction

Tehran basin is a perfect example of a high potential region to be impacted by seismic risk due to the high density of the population, the high-level hazard from potential far and local earthquake sources, and the high probability of strong site effects. In this regard, although the earthquake risk in Tehran has always been a matter of concern, there is a significant lack of comprehensive studies on the Tehran seismic risk. As a result, it's essential to start learning more about the basin's characteristics to be prepared to study its seismic risk.

So, in this chapter, I provide a quick overview of the geology, seismicity, and site effects within the Tehran basin. This chapter aims to address the potential risk by conducting a thorough analysis of the active tectonics and active faults and reviewing the geology surrounding and within the city of Tehran. By doing so, I will obtain a better understanding of the active tectonic processes and identify seismic activity. Furthermore, I introduce the sedimentary formations within the basin, to explore one of the key factors that contribute to the increased risk, "site effects".

In this regard, the state of the art regarding site effect studies in Tehran will be examined. The goal is to gather relevant information about the bedrock depth, which will equip us with the latest knowledge on the region's geometry and characteristics, which will be utilized in the next chapters.

1-2 Tectonics around Tehran and geology of the basin

When we are studying the Tehran seismic hazard, it is inevitable to study the seismotectonic and geological context of northern Iran, especially the central Alborz. The Alborz mountain range is an east-west trending mountain range with 600 km long and 100 km width divided into western, central, and eastern parts. It is part of the Alpine-Himalayan seismic belt that passes through northern Iran. The Alborz range is considered a region of active deformation within the Arabia-Eurasia collision zone due to the huge tectonic stresses linked to the northward convergence of central Iran toward Eurasia (Allen et al., 2003). Tehran is situated on the southern flank of the central part.

1-2-1 Tectonics and faults

Iran is one of the most seismically active countries in the world, with many major faults that cover most of the country (Hessami et al., 2007; Figure 1-1). Meanwhile, Alborz is regarded as one of

Iran's most active and well-known seismic zones. The active tectonics of central Alborz are relatively well documented and appear to accommodate N-S regional shortening by partitioning onto separate thrust and left-lateral strike-slip faults (e.g., Jackson et al., 2002; Vernant et al., 2004; Ritz et al., 2006; Hollingsworth et al., 2010). The activity of thrust and left lateral faults in Alborz is totally compatible with the internal deformation of central Alborz. Studies on the North Tehran fault and the Mosha fault (close to Tehran) show a reverse-fault mechanism during the Neogene (Tchalenko et al., 1974), which changes to the present strike-slip motion (Allen et al., 2003; Bachmanov et al., 2004; Guest et al., 2006). Between longitudes 50°E to 54°E, where Tehran is located roughly at longitude 51°30'E, a wide V-shaped structure characterizes the central Alborz form, with folds and faults trending NW-SE in the western part and NE-SW in the eastern part. A cross-section through the Alborz mountain range at the exact longitude of Tehran city also shows the active tectonic of this region (Stoecklin, 1974; Allen et al., 2003; Figure 1-2). Currently, the geodynamics of the Alborz are divided between thrust and strike-slip mechanisms. The major thrust faults are the Khazar fault, the North-Alborz reverse fault, the North Tehran Fault, the Garmsar fault, and the Parchin fault, while the Taleqan, Mosha, and Firuzkuh faults are left-lateral strike-slip faults. All these active faults are located at a distance of less than 150 km from the metropolitan city of Tehran (Figure 1-1).

Central Alborz is divided into three different units: 'High Alborz', 'Alborz Border Fold, and 'Anti-Alborz'. The High Alborz is composed of Paleozoic, Mesozoic, and Tertiary rocks, which have been piled up due to many folds and massive thrusts and are bounded to the south by the Mosha fault. The Alborz border fold was formed almost entirely by rocks of the Tertiary Karaj Formation, with a moderately folded volcanic and pyroclastic complex that is finally overturned on the alluvial beds in the northern part of the Tehran basin (Tchalenko et al., 1974; Figure 1-1). Anti-Alborz, the city's eastern mountains, have a totally different structure from the northern mountains. The altitude of this mountain range varies between 1200 and 2000 meters, which is much lower than the numerous 4000-meter summits in the High Alborz. Anti-Alborz consists of Cretaceous limestone outcrops forming the Sepayeh anticlinorium in the North (the biggest peak in Anti-Alborz) and Cenozoic formation in a synclinal position, with granodiorites masses and volcanic lavas in the South. In the southwest, the Bibishahrbanu cape is located as a NW-SE anticlinal structure with a Paleozoic core (Tchalenko et al., 1974; Hourcade, 1982).

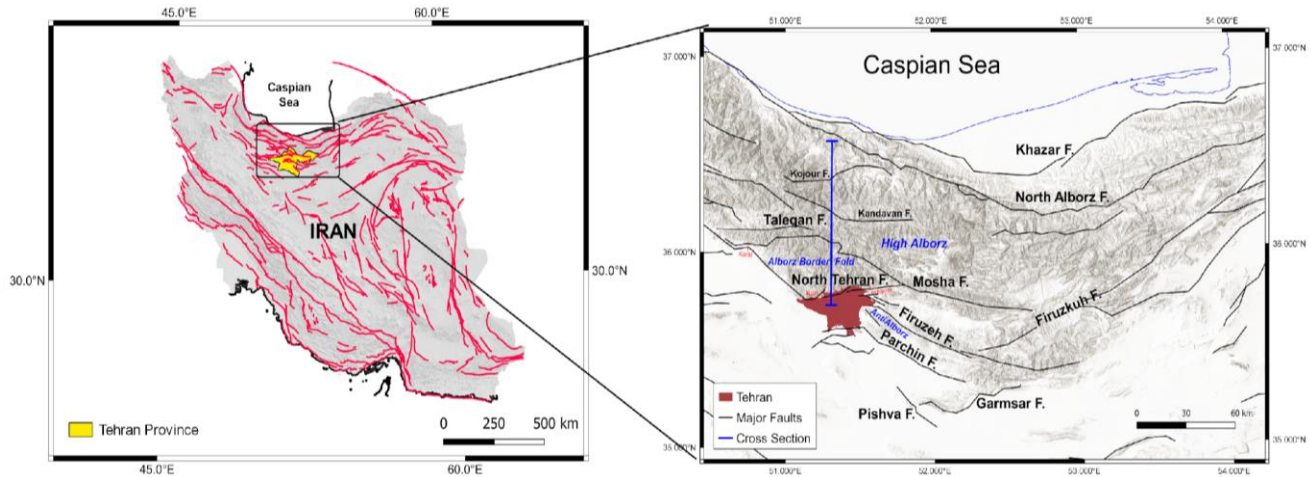


Figure 1-1: Left: Active fault map of Iran (from Hessami et al., 2007). Right: Tectonic structure of central Alborz with main faults (black lines) and location of central Alborz's unit (blue text).

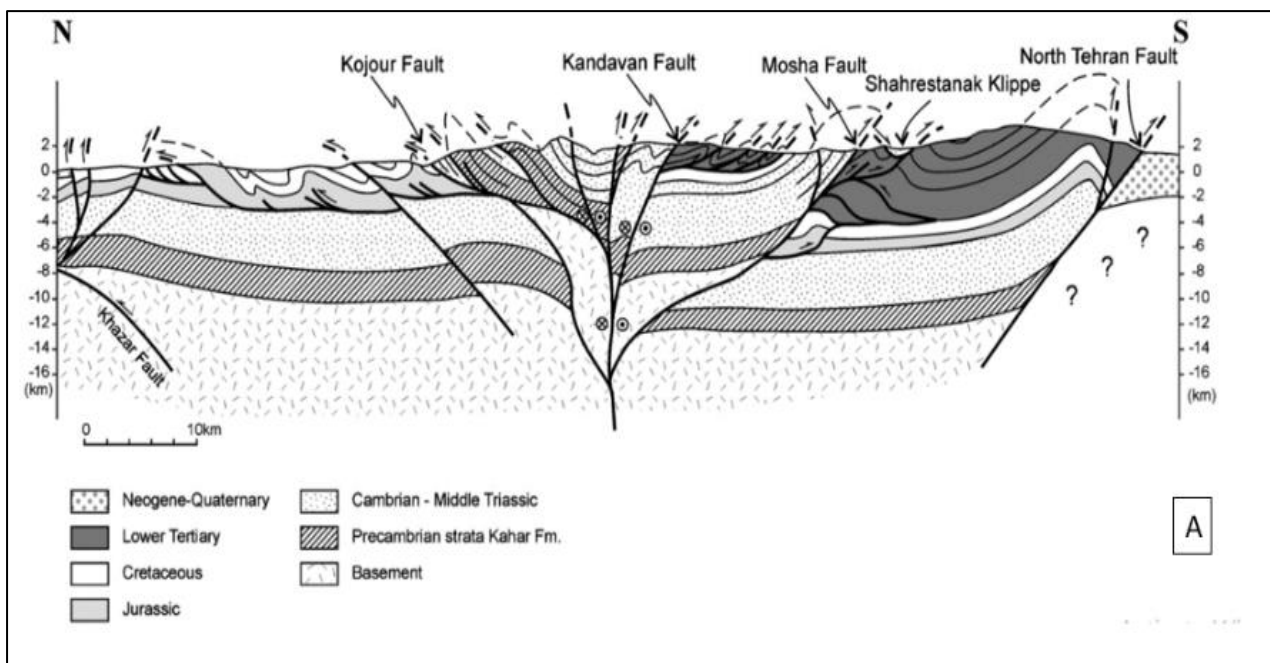


Figure 1-2: Cross section of Alborz range at the longitude of Tehran (Allen et al., 2003). This cross section is located on figure 1-1-right with a blue line.

To conclude this section, based on historical and recent seismicity, I will also briefly describe four important faults with documented seismicity close to Tehran city that may have a significant impact all over the Tehran region in case of an earthquake:

- **The Mosha fault (see location on Figure 1-1):** This fault is one of the most hazardous faults located only 30 km North of Tehran. The hazard is strongly supported by current seismicity and historical activity evidence. The fault can be followed for around 170–220 km from the Firuzkuh area to the East to the Taleqan area to the West. The trace of the Mosha fault reproduces the motion partitioning between reverse faults and left-lateral strike-slip faults (Jackson et al., 2002). To the West, the Mosha fault consists of an approximately E-W western 70 km segment (south of the Taleqan fault), while to the east, the Mosha fault appears as a WNW-ESE striking 130 km long segment. Several historical earthquakes were identified in the Mosha fault system. At least I know about three famous events in 958, 1665, and 1830 with a magnitude larger than 6.5 that could be attributed to the Mosha fault.
- **The Taleqan fault (see location on Figure 1-1):** The Taleqan fault is a sinistral-reverse fault that extends along the northern edge of the Taleqan village. The fault is located around 50 kilometers northwest of Tehran. The western segment of Mosha fault is parallel to the sinistral reverse Taleqan fault. The exact relations between the Mosha and the Taleqan faults are not clear. However, that could be part of a local partitioning, suggesting a recent kinematical change in the Alborz (Guest et al., 2006). Originally, the Taleqan fault was mapped as a north-dipping normal fault but in a review of Iranian geological maps, Annells et al. (1975) remapped it as a south-dipping high-angle reverse fault, bringing Upper Proterozoic–Lower Cambrian rocks onto the Eocene Karaj Formation. There also has been several paleo–rock avalanches and landslides in the area that could be related to the seismological activity of the Taleqan fault. Nazari et al. (2009) suggest that the source of the 958 Ruyan earthquake and the poorly known 1428 earthquake should be linked to the Taleqan fault. For recent seismicity, the 8 November 1966 earthquake with Mb 5.0 occurred on the Taleqan fault.
- **The Pishva fault (see location on Figure 1-1):** The Pishva fault is a northeast-dipping reverse fault with a lateral component, in a NW-SE orientation and 35~55 km long. This fault is located at southeast of Tehran. This fault has clearly cut quaternary sediments, and near the fault, the conglomerate layers represent the lower parts of the more ancient formation of Tehran’s alluvium. Along the Pishva fault, no historical seismic data has been documented. However, Ritz et al. (2012) suggested that the

Pishva fault is the source of the 855 “Ray” earthquake. Also, this fault recently has high activity where for example the earthquakes of 13 August and 14 September 2015 (three events, Mb 3.6, 4.1, and 4.4) occurred along this fault.

- **The Parchin fault (see location on Figure 1-1):** The Parchin faults is a n northeast-dipping normal with the length of 70 km extends from the southern Evankey (Semnan Province, East of Tehran) to the southeastern edge of the city to the West. The Pliocene and quaternary sediments are cut clearly by a NW-SE trending structure (Berberian et al., 1985). It's possible that the historical earthquake of 280 BCE and 743 were caused by the rupture of this fault. Microseismicity studies also show a relatively high seismic activity along this fault (Ashtari et al., 2005; Tatar et al., 2012). In recent years, several earthquakes have occurred in close proximity to the fault, including the 12 May 1993 earthquake with a magnitude of 4.3, the 17 October 2009 earthquake with a magnitude of 4.0, and the 20 February 2011 earthquake with a magnitude of 4.0. Additionally, the 22 August 1988 earthquake with a magnitude of 5.3 and the 23 August 1988 earthquake with a magnitude of 5.1 were located near the southeastern end of the Parchin fault.

1-2-2 Morphological and structural geology

Tehran basin is not a morphologically integrated basin and divided into the piedmont zone at North and plain zone at South. While the piedmont features numerous faults and folds, the plain area is almost flat.

The generic term of “piedmont” is defined as the gently sloped area at the base of a mountain or the mountain ranges (Parsons and Abrahams, 2009; Figure 1-3). In Tehran, although the general definition is the same, it refers to the alluvial zone of the mountain front that have been rises by tectonic movements (Abbassi and Farbod, 2009).

Engalenc (1968) suggested a close dependence between the brittle tectonics of the piedmont bedrock (with fragile behavior, i.e., piano key tectonics) and the folding system which is formed during the late or post-Pliocene contraction phase, thinking that anticlines and synclines were formed on raised or collapsed bedrock compartments. This shows that the importance of detailed knowledge, about the structural geology of piedmont area, is a possible guide to explain subsurface topography.

Tehran Piedmont is limited to the North by the North Tehran Fault (Figure 1-4A). This fault clearly divided the rock formations from the alluvial deposits. To the South, there is no clear line separating the piedmont and plain areas. According to Engalenc (1968), the southern boundary starts from the area that is entirely covered by recent silty deposits. Abbassi and Farbod (2009) suggested that the Tarasht Fault is a boundary between these two zones. According to their studies, the boundary is marked by the recent activity of the north-dipping E–W Tarasht thrust fault, which is partly recognizable on aerial photographs. Although, other studies (e.g., Berberian et al., 1985) do not consider the fault zone between the heights related to the piedmont and the flat parts related to the plain zone.

Generally, the most southern hills and ridges in central Tehran (including from East to West: Abbas Abad, Andisheh, Bagh-e Feyz, and Chitgar hills) with higher altitudes than the southern parts are accepted by many researchers as the southern boundary of the piedmont and so the limit with the plain. All these hills (some of them has no names) are located north of Enghelab Street, at the beginning of the flat part of the basin (Figure 1-4A).

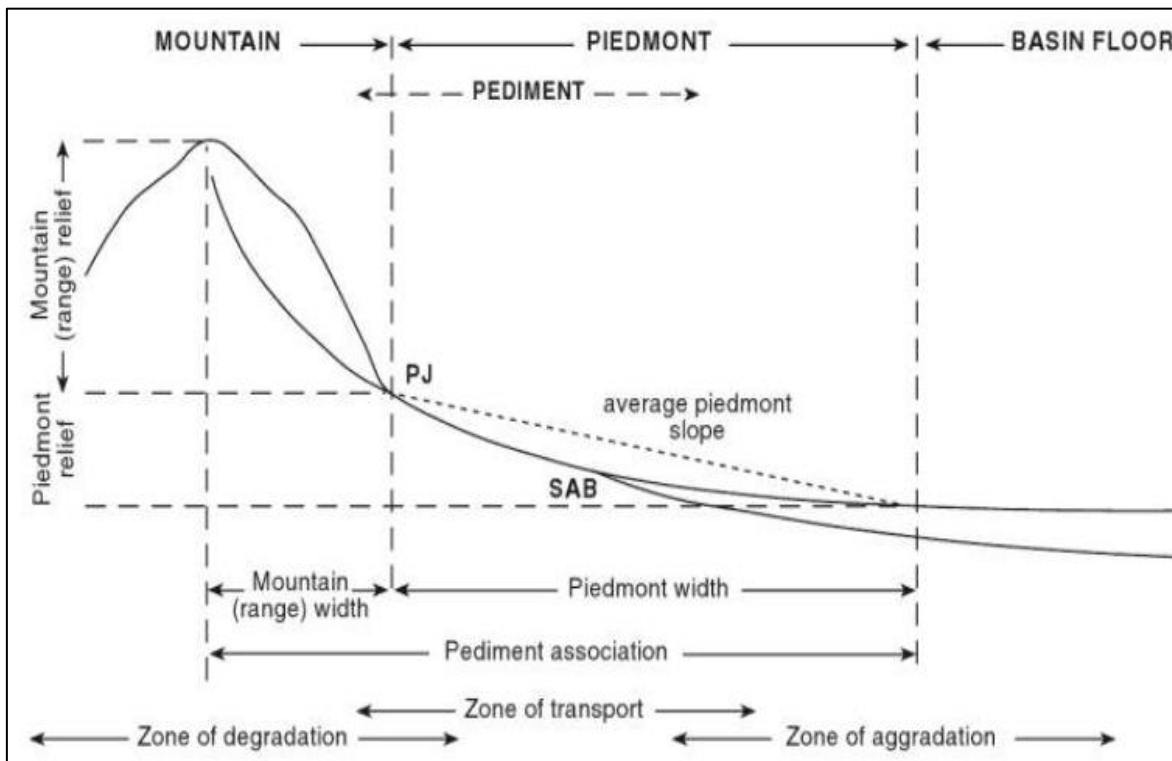


Figure 1-3: Schematic diagram displaying the exact definition of piedmont between the mountain and the plain (Parsons & Abrahams, 2009). Piedmont in Tehran is defined from subaerial alluvial boundary (SAB) near the mountain front.

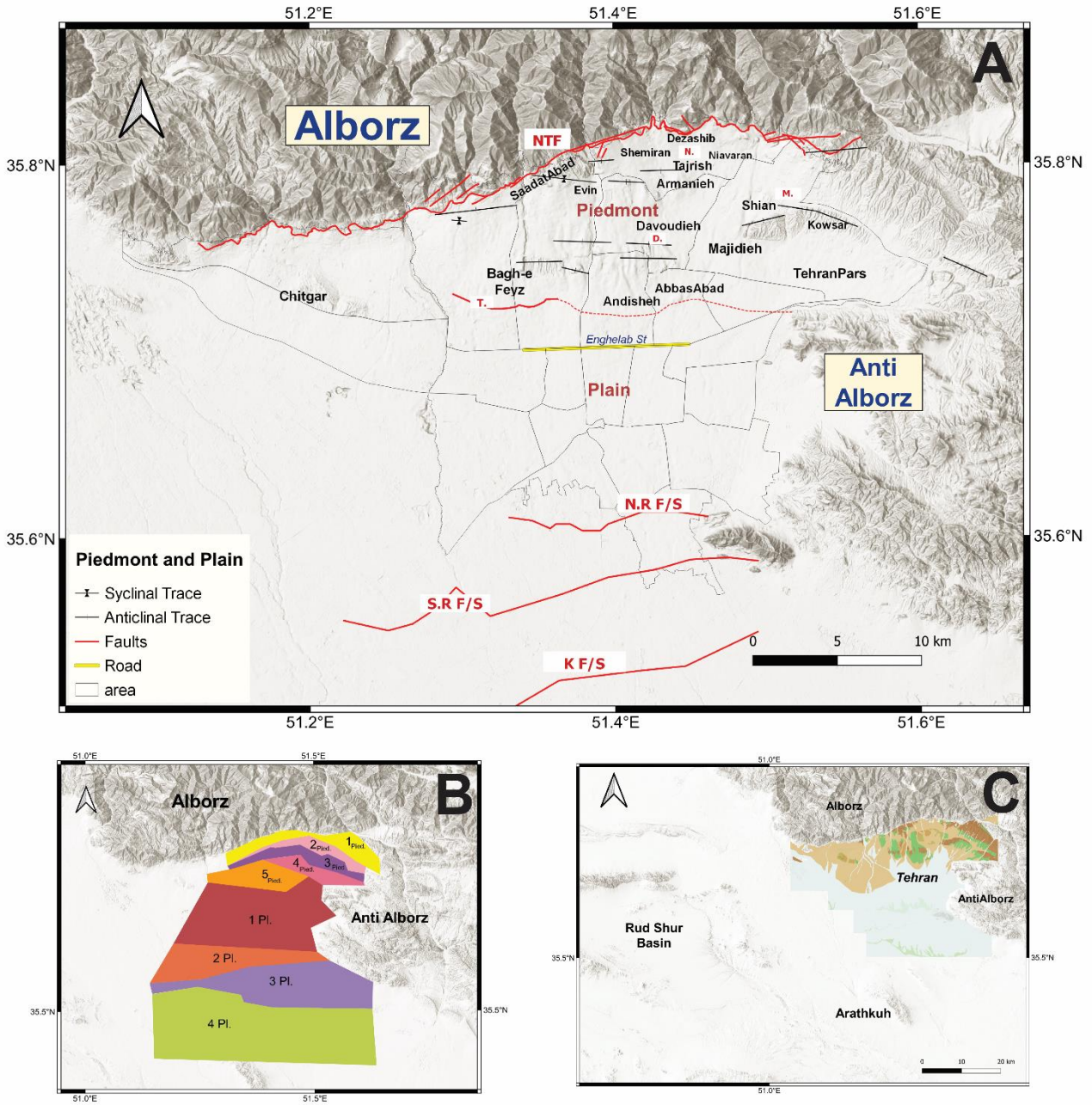


Figure 1-4: Terminology for the Tehran basin definition. A: geological, geomorphological and tectonic map of the piedmont and plain areas. NTF: North Tehran Fault; N.: Niavaran Fault; M.: Mashmodieh or Lavizan Fault; D.: Davoudieh Fault; T.: Tarasht Fault; N.R. F/S: North Ray Fault or escarpment; S.R. F/S: South Ray Fault or escarpment; K F/S: Kahrizak Fault or escarpment. 9 Anticlinal and 2 synclinal traces are also show in this figure (after Knill & Jones, 1968). B: map showing the different zones of Piedmont and plain introduced by Berberian et al. (1985). C: Location of Arathkuh (southern limit of basin) and RudShur Basin, small local depression separated from the Tehran Basin.

Regarding structural geology, Rieben (1955) introduced a relatively large number of folds for this area. It is confirmed by the folding observed especially in “A” formation. In fact, one of the key features that shaped the piedmont morphology is related to these folding structures and Rieben (1955) introduced seven anticlinal axes in the “A” formation. Knill and Jones (1968), continuing this study, proposed 11 axes (9 anticlinal and two synclinal axes) defining a series of E-W trending folds had contorted the 'A' Beds structure (Figure 1-4A). Thus, the piedmont can be subdivided into a series of 5 highs and depressions (Berberian et al., 1985) mainly formed by folding and inner-city faults (Figure 1-4B).

Tehran plain is much less known than the piedmont zone because the plain is covered mainly by urban areas with no discernible geological indication since the city became the capital of Iran. Tehran plain is part of the giant Iranian central basin, connected to Dasht-e-Kavir in central Iran (Engalenc, 1968). So, southern limits are not recognizable. However, a series of NW-SE ridges of Neogene volcanic outcrops, located approximately 30 km south of plain near the Arathkuh, could be consider as the southern basin boundary. Tehran plain is also separated from the Rud Shur Basin, a small local depression partly separated from the Central Basin, located southwest of Tehran (Figure 1-4C).

The geology of the plain zone is rather simple than piedmont. This area is covered mainly by sub-recent alluvial deposits and divided into four sub-zones. The sub-zones present as follows: Tehran main plain (North of N.R. F/S), Ray Depression (between N.R. F/S and S.R. F/S), South Ray Depression (between S.R. F/S and K F/S) and Kahrizak Depression (South of K F/S) as defined by Berberian and Yates (2018). These depression zones were formerly presumed to be a sequence of thrust faults, but the mechanism of these faults is still unclear. Nazari et al. (2010) believed that the three topographic escarpments (the North Ray, South Ray, and Kahrizak) match with a preserve shoreline southwest of the Parchin fault. He suggested that these three escarpments were most likely to be lake terraces. However, De Martini et al. (1998) proposed a trust mechanism based on geomorphic and trench observations at least along the Kahrizak fault/system. This debate is still continuing and will be addressed in the following sections when I talk about active faulting in Tehran.

1-2-3 Tehran's sedimentary formations

Tehran's alluvial deposits are the legacy of long periods of rising and erosion of the southern slopes of the Alborz mountain range and divided into four main series by different geologists with different naming systems (Rieben, 1955; Engalenc, 1968; Knill and Jones, 1968; Vita-Finzi, 1969; Berberian et al., 1985; Pedrami, 1987).

In 1955, Rieben named the Tehran basin sediments A, B, C, and D deposits (Figure 1-5). Following the Rieben (1955) studies, other scientists classified the Tehran alluviums using minor adjustments and a different naming system. Among these studies, the more used stratigraphy logs are coming from Engalenc (1968) and Pedrami (1978) as shown on Figure 1-5 confirming the separation of the whole stratigraphic column in four different blocks as defined by Rieben (1955, 1966). Nonetheless, due to variability and complexity of each formation, even if the different classifications give the property of the sediment material (Table 1-1), they do not offer useful information regarding the geotechnical features of the sediments. For example, based on geotechnical and in-situ testing, the B formation is divided into five sub-branches with distinct features (Table 1-1). Furthermore, the B and D formations exhibit differing behavior in the North and in the South, suggesting that even if alluvium have formed at the same time and situated in the same strata, geotechnical properties might differ strongly from a place to another place for the same stratigraphic level. Table 1-1 displays the most recent classification of alluvium in Tehran from a geotechnical and soil mechanics point of view (Fakher et al., 2007; Cheshomi et al., 2018).

A geological cross-section, in Tehran basin alluvium, is commonly used as a benchmark for many studies (Figure 1-6) and drawn from the Rieben (1955) classification and the number of shallows to medium depth boreholes done by JICA & CEST (2000). This cross-section shows that there is no estimate of the Tehran's bedrock depth. Also, there is no difference between A and B sediments which have completely different features from geological or geotechnical point of view.

Finally, the most updated Tehran alluvial deposits map is shown in Figure 1-7 (Abbassi and Shabanian, 2023). Based on these new observations, the limits of A formation are much extended in the northern parts when for B formation, the limits are slightly extended towards south. Abbassi and Shabanian (2023) did not find new features for C and D formations and just changed the naming/chronological system based on some geomorphological interpretation. (For more detail

see: Abbassi and Farbod (2009)). Detailed features of each formation will be reviewed in chapter 3.

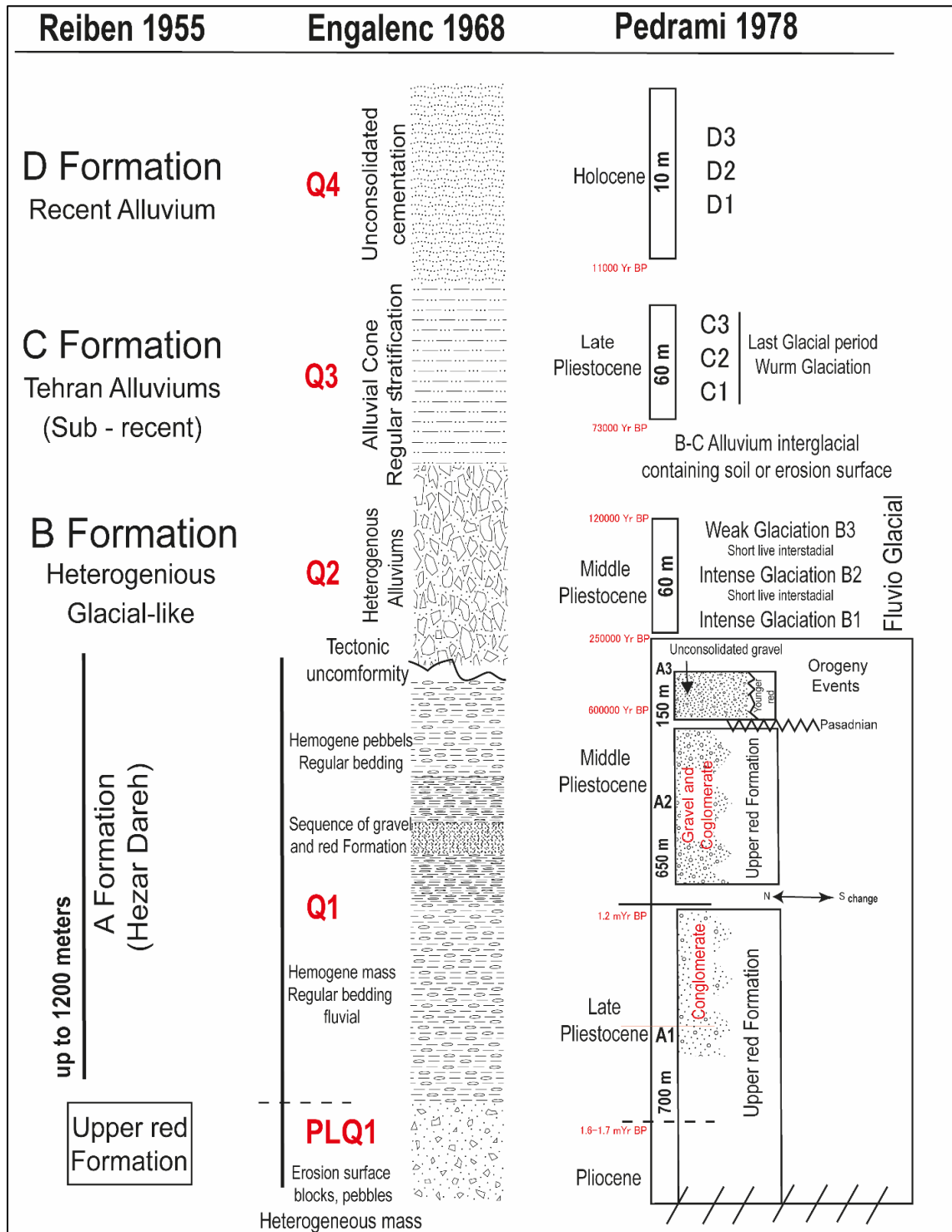


Figure 1-5: Synthesis of the stratigraphic sequences of the Tehran basin following Reiben (1955, 1966), Engalenc (1968) and Pedrami (1978).

Table 1-1 Determination of geotechnical properties based on geological features (inspired from Fakher et al., 2007).

Rieben Classification		elevation	Structural geology	Grain Size	Age	Thickness	cementation	Grain shape	Contact shape	C	phi	E
A		Almost 1500 m	Folded and dip 0–90 deg	From clay to boulders up to 45 cm	5 MA	Up to 1200 m	Strongly cemented	Angular	Interlocking	1.4 -1.5	45- 50	2000- 2500
									Floating	0.6- 0.7	35- 40	1000- 1500
								Semi Round	Interlocking	0.7- 0.8	40- 45	1500- 2000
									Floating	0.3- 0.4	30- 35	400 - 500
B	Bn	1200- 1500 m	Unconformability over A series, dip lower than 10 deg	From clay to boulders more than 200 cm diameter	700 KA	Up to 60 m	Uncemented	Angular and Semi round	Floating	0.1- 0.2	36- 42	1200- 2000
				From clay to boulders up to 100 cm								
				From clay to boulders up to 50 cm				Angular and Semi round	Floating and interlocking	0.3- 0.6	33- 40	500- 1200
				From clay to boulders up to 10 cm								
	Bs	1000 m		Silt and clay		up to 10 m		Rounded	Pointed	More than Bn		
	C		1100 – 1500 m	Horizontal	From clay to boulders up to 20 cm	50 KA	Up to 60 m	Weakly to moderately cemented	Angular	Interlocking	0.1- 0.15	35- 40
Floating										0.2- 0.3	30- 35	300- 400
Rounded									Interlocking	0.4- 0.5	30- 35	400- 500
									Floating	0.1 – 0.1	20- 25	200- 300
D	D1	1200 – 1400 m	Horizontal	From clay to boulders up to several meters	10 KA	Less than 10 m	Uncemented	Semi round and Rounded	Floating	Less than Bn		
	D2	1100 – 1000 m								Rounded	Pointed	0.1- 1

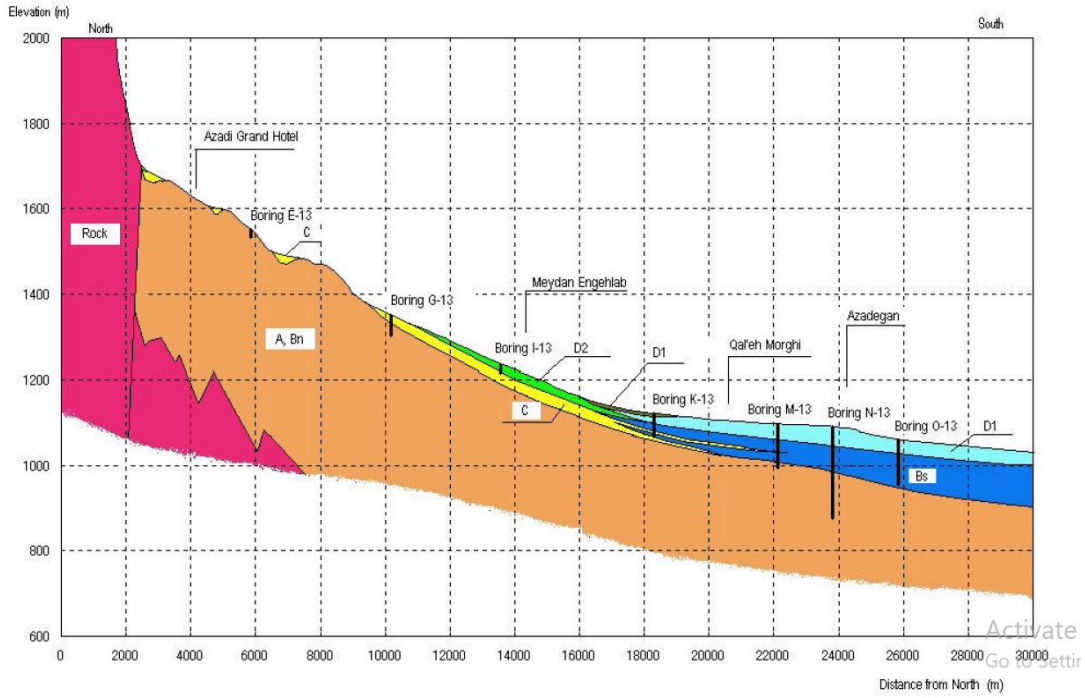


Figure 1-6: Geological cross-section of Tehran alluviums based on Rieben classification and borehole data (JICA & CEST, 2000).

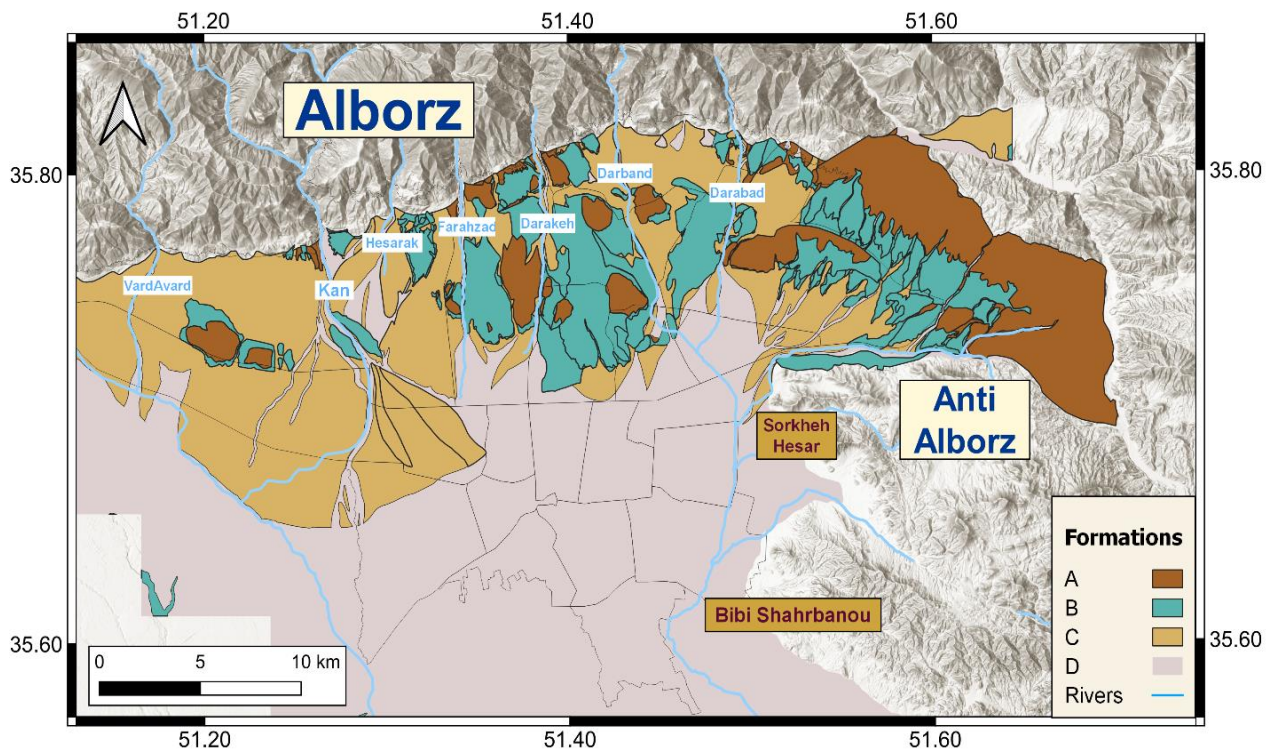


Figure 1-7: The latest release of geological map of Tehran basin sediments (after Abbasi and Shabanian, 2023).

1-3 Active Faults in Tehran basin

Besides the Central Alborz main faults, some quaternary faults within the basin have been identified and described (Berberian et al., 1985), and these local faults can trigger sizable earthquakes. The Berberian et al. (1985) report is the first attempt to categorize and study the Tehran basin faults. In the mentioned report, faults are divided into three categories: main faults with a length of more than 10 km, moderate faults (between 2-10 km), and inferior faults. Over the years, the report has remained mostly intact, and small changes have been done, based on new observations and fieldworks. The new efforts from TDMMO (Tehran Disaster Mitigation and Management Organization) and IIEES to characterize the Tehran basin faults began few years ago in order to determine the boundaries of Tehran basin faults as a new standard for urban construction (Abbasi and Mokhtari, 2020).

1-3-1 Large scale Fault

The North Tehran Fault is the biggest and probably the most debated fault in Tehran. Sometimes it is described as Tehran's largest threat and sometimes as an inactive fault (Berberian and Yeats, 2018). In fact, a 1999-2000 microearthquake survey close to the North Tehran Fault (described later) found no seismicity along this fault, except for few dispersed microearthquakes that were eliminated after a relocalization (Ashtari et al., 2005). Similar studies with 2004–2010 microearthquakes showed just very few events located along the North Tehran Fault (Vasheghani Farahani et al., 2014). This lack of seismicity over a short measuring period cannot be assumed as an absence of seismic hazard linked to this fault. However, based on field observations, some researchers think that the NTF is inactive (Abbassi and Farbod, 2009). Some authors also believed that the activity of the North Tehran Fault is transferred to the left-lateral strike-slip Niavaran fault which is considered as one of the main active faults inside the city with more than 15 km length (Figure 1-8, Table 1-2). For Niavaran fault, there are clear evidences of quaternary activity such shift of the quaternary deposits (Abbassi and Farbod, 2009). There are also additional indications that the length of this fault exceeds 15 kilometers and extends northeast of Tehran up to the Masha fault (personal communication with Abbassi).

The Lavizan fault is another very important faults in Tehran basin (Figure 1-8, Table 1-2). It is an east-west trending south dipping thrust fault that extends in the north and northeast of Tehran city

with a longitude of about 25 km. The topographical changes along this active fault can be identified in the northeast of Tehran where the Lavizan Hill is about 9 km long and located 4 km south of the mountain front. Contrary to the North of the Tehran basin, major faults in South of Tehran are a controversial debate. In the first report of Tehran faults (Berberian et al., 1985), North Ray fault was introduced as E-W–trending faults with 16.5 km long located 9 km south of central Tehran while the continuation of the North Rey fault disappears under the young river sediments of Karaj. Also, based on groundwater table measurements (Knill and Jones, 1968), groundwater cascades were reported along the North Ray Fault, which was hypothesized to be a reverse fault, displacing recent alluvial deposits and groundwater level (Fegghi, 1999). Eastward, this fault seems to be connected to the Major Parchin Fault. With roughly the same characteristic, the South Ray fault is located 13 km south of central Tehran city with a E-W trend and 18.5 km length. As mentioned before, Nazari et al. (2010) reported that the North Ray, South Ray, and also Kahrizak fault (far South) match with ancient shorelines at an elevation of 1055 m. They believed that these features correspond to erosional rather than tectonic processes. So, for Nazari et al. (2010) i) the flatness of the upper and the lower surfaces, ii) the long and regular streams that incised the upslope upper surfaces, and iii) the fact that the deposits are horizontal and without deformations are the main reasons to consider the Kahrizak, North Rey, and South Rey as scarps corresponding to shorelines and not to real faults. This debate is still one of the most controversial assumption about Tehran basin faults but very important because if these traces are considered as faults, due to the length and close distance to the city, they can be very dangerous for Tehran region, increasing strongly the hazard.

Table 1-2: Tehran’s active faults identified in the Tehran basin from reports done by TDMMO and IIEES.

Name	Comment	Length	Name	Comment	Length	Name	Comment	Length
Sohanak	P. NTF	3.5	Kaj	P. NTF	3.5	Davoudieh		6.4
Beheshti	P. NTF	1.5	Niavaran		>15	TakhtTavous		1.5
BouAli	P. NTF	1.5	Chitgar	Fault zone	?	Narmak		2.6
Velenjak	P. NTF	1	Tarasht		6.5	Lavizan		25
Farahzad	P. NTF	2	BagheFeyz		4	Tanbakoe		2
IranPars	P. NTF	1.5	Abas Abad		3.5	Ray north	Fault?	?
Enghelab	P. NTF	1.5	Vanak Park		4.5	Ray South	Fault?	?
Evin	P. NTF	1.6	TV		3.3			

1-3-2 Minor faults

According to Abbasi and Mokhtari (2020) works, Tehran has 23 fault segments in its urban area including the north Tehran fault system. In fact, 8 out of 23 fault segments can be considered the segments of the north Tehran fault zone (Figure 1-8; Table 1-2). Based on field observations, local horst-and-graben structure, constructed by parallel minor faults mostly in north-central part of Tehran. For example, N and NW trending TV, Bagh-e Feyz, and Vanak-Park faults clearly affect the quaternary deposits as reverse and normal faults.

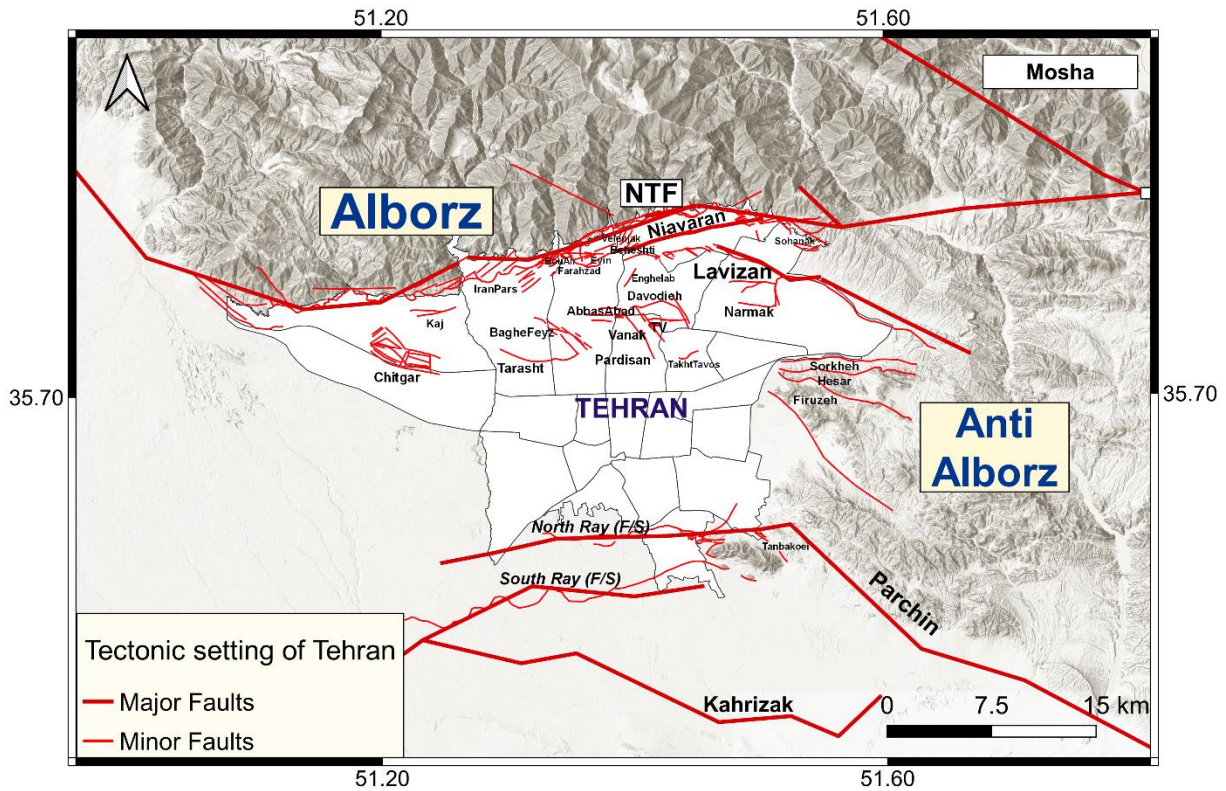


Figure 1-8: Synthesis of the active faults within the Tehran basin. Parchin, Moshah, SorkhehHesar and Firuzeh are out-basin faults but also shown in this figure (from Berberian et al., 1985; Nazari et al., 2010).

1-4 Seismicity around Tehran

According to Berberian and Yeats (2018), Tehran seems to be in a seismic gap. With numerous active faults inside or very close to the Tehran city, there is a huge potential for generating devastating earthquakes at any time. There have been no earthquakes with a magnitude greater than 5.5 in the instrumental era since 1930 (until 2023/01/01) around Tehran. Between 1900 and 2015, just small magnitude events were reported near the Tehran basin, most of them assigned to the

Mosha, Parchin, Pishva or Garmsar faults. During this period, The North Tehran Fault and other inner-city reverse faults have not shown clear evidence of earthquake higher than magnitude 2.5 to 3.5. This fact is important because historical earthquake (Ambraseys and Melville, 1982; Berberian and Yeats, 1999) and paleo-seismic trench studies (Nazari et al., 2009, 2010, 2011) determined many strong paleo-earthquakes in this area.

1-4-1 Historical earthquakes

No matter how low is the current seismicity existing in Central Alborz, the region seems to have been hit by some devastating earthquakes in the past. The first report on the historical catalog of earthquakes in Iran goes back to the famous studies by Ambraseys and Melville (1982) on the historical seismicity of North-Central Iran and All-Persian Earthquakes. Despite various limitations and doubts regarding their estimated magnitudes and meizoseismal areas, it has been the primary source for studying past earthquakes for many years.

Recently Berberian and Yeats (2018) reviewed the historical (pre-1900) earthquakes that affected the Greater Tehran-Ray region by more details (Table 1-3).

The largest reported historical earthquake in the Alborz Mountains was the 856 CE Komesh (modern Damghan) earthquake in the eastern Alborz with an estimated magnitude of Ms 7.9 (Ambraseys and Melville, 1982). This earthquake did not affect the Tehran or surrounding area. The second biggest event is the 958 CE Ruyan earthquake (North of Tehran?) to which it has been assigned a magnitude of Ms 7.7. On the contrary to the 856 CE Komesh earthquake, the 958 earthquakes hit strongly the city and ruined Tehran (Ray) based on many historical reports. However, Berberian and Yeats (2018) using archaeological information and paleo seismologic trench studies stated that both estimated magnitudes (856 and 958 eq.) are too large.

At least five historical earthquakes of magnitude 7.0 (four in a radius of 50 kilometers around central Tehran) and two earthquakes of magnitude in-between 7.0 and 6.5 (two in a radius of 50 kilometers) have been reported. Most of these earthquakes destroyed or damaged the city of Ray for many times in history (now Ray is one of the southern districts of Tehran). The five major events with the magnitude over seven are characterized it in more detail below. It seems that if I exclude destructive earthquakes in the Ray-Tehran region with unknown sources, the 958 Ruyan and the 1830 Lavasanat earthquakes, both located along the central segment of the Mosha fault, were the closest large-magnitude earthquakes that had a massive effect in the Tehran area.

The 230 BCE Ray Earthquake

Gorshkov et al. (2009) attributed a magnitude of Ms 7.6 for this event, with the epicenter at 35.50°N 51.50°E. The basis for attributing this enormous magnitude for this event is an unclear paleo seismic trench analysis which cannot totally justify the given magnitude. It would make necessary to reject the reported magnitude and suggested sources. About the source, De Martini et al. (1998) and Tatar et al. (2015) considered that the earthquake took place along the Garmsar or Parchin fault. Of course, this earthquake is a pre-historical one.

The 855 May 22 Ray Earthquake

Ambraseys and Melville (1982) estimated a magnitude of Ms 7.1 for this earthquake, with an epicenter at 35.6°N – 51.5°E. However, according to Djamour et al. (2012), the 855 earthquake may occur along the North Tehran Fault. In contrast, the Pishva fault in southern Tehran has been suggested by Ritz et al. (2012) as a source of this event.

The 958 “Ruyan” Earthquake

Ambraseys and Melville (1982) assumed an NW-SE trending meizoseismal area of 150 × 60 km for this earthquake, giving it a magnitude of Ms 7.7 and named it the “Ray-Taleqan earthquake”. If the Ms 7.7 magnitude for this earthquake is correct which is also reported by many authors, the event might be regarded as an earthquake from the Central Alborz, that could affect the Ray and Tehran region. Due to the huge affected area, some studies proposed the simultaneous rupturing of several major active faults in the Alborz during a single mega-earthquake (De Martini et al. 1998; Nazari et al. 2009; Djamour et al. 2012). About the source, Berberian and Yeats (1999) assumed the western Mosha as a probable responsible for this event, Nazari et al. (2009) believed that the source might be the Taleqan fault. Furthermore, Ghassemi et al. (2014) stated that this event is probably involving a more complex fault system that included the Taleqan, North Tehran and Mosha faults.

The 1177 “Ray/Qazvin” Earthquake

According to Ambraseys and Melville (1982), the source of the 1177 Ms 7.2 earthquake was the same as the 1962 BuinZahra (Mw 7.2) earthquake southwest of Tehran on the Ipak fault, which is about 150 kilometers West of Ray/Tehran. It does not seem to be thrustable because the 1962 earthquake with the same characterization on Ipak fault causes only slight damages in the city of Rey or Tehran. Ritz et al. (2012) proposed that the most recent earthquake recorded in North Tehran Faults trench should be related to 1177 events and consider the magnitude between 6.2 to 6.8 for

this event. However, it is impossible that the Qazvin, located 140 kilometers northwest of Tehran, could have been destroyed by an earthquake with such low magnitude.

The 1830 “Lavasanat” Earthquake

The most recent earthquake to strike the current Tehran metropolitan region was the Lavasanat earthquake on the central segment of the Mosha fault on March 27, 1830, with an epicenter 30 kilometers northeast of the city and an estimated magnitude of Mw 7.0–7.4. Fortunately, enough data and reports are available for this event to limit the meizoseismal region (Ambraseys and Melville, 1982; Berberian, 1994). Based on damage reports, the 1830 earthquake along the Mosha fault may have generated a VII+ intensity near Tehran. Besides historical reports, there is some evidence that the Mosha fault cuts young colluvial sediments (Ab-Ali ski resort, 40 km north east of Tehran) that might be related to the both 1665 Damavand earthquake or 1830 Lavasanat earthquake (Solaymani Azad et al., 2011). Although the reported magnitude of Ms 7.1 (Ambraseys and Melville, 1982) is acceptable, it may be slightly underestimated. Because with an estimated 80 km surface rupture and destruction, it was possibly comparable to the June 20, 1990 Mw 7.3 Rudbar earthquake (NW of Tehran) one of the most destructive in last passed years.

Table 1-3: Pre-historical, historical and instrumental earthquakes in Tehran region with the magnitude greater than 4.0.

Date	Time (UTC)	Lat.	Lon.	Mag.	Date	Time (UTC)	Lat.	Lon.	Mag.
230BCE Ray		35.48	51.82	>7	1988/08/23	05:30:51.0	35.37	52.24	Mw 5.2
855 Ray				7	1988/08/23	10:58:12.0	35.28	52.32	Mb 4.6
864 Ray				>6	1988/08/23	14:56:08.0	35.64	52.40	Mb 4.0
958 NE Tehran		35.81	51.76	>7	1988/10/24	17:01:57.0	35.17	52.26	Mb 4.9
1177 Ray- Qazvin		36.1	50.43	>7	1988/10/26	14:49:20.0	35.119	52.228	Mb 4.7
1665 Damavand		35.75	52.08	6.5	1988/12/03	18:40:59.0	35.15	52.205	Mb 4.4
1830 Lavasanat		35.81	51.76	7.1	1991/01/22	12:04:25.0	35.44	52.323	Mb 4.5
1930/10/02	15:32:00.0	35.76	51.99	Ms 5.2	1994/11/21	18:55:18.0	36.051	51.913	Mb 4.5
1930/10/07	20:53:06.0	35.8	52.1	mb 5.0	1998/12/03	13:13:34.0	36.064	50.972	Mb 4.3
1945/05/11	20:17:28.0	35.18	52.4	mb 4.7	2002/10/10	12:13:43.0	35.89	52.33	Mb 4.7
1954/09/02	22:47:00.0	35.3	52	M 4.5	2002/10/15	16:56:08.0	35.82	52.232	Mb 4.0

1955/11/24	00:00:00.0	35.76	52.05	Mb 4.0	2003/03/09	22:50:12.0	35.69	51.68	ML4.0
1957/07/02	00:42:00.0	36.07	52.47	Mb 7.0	2003/12/24	03:50:00.0	35.174	50.503	mb4.7
1957/07/02	01:16:51.0	36.08	52.37	Ms 4.6	2006/12/20	04:39:20.4	35.74	51.89	ML4.1
1957/07/04	22:43:47.0	35.9	52.2	M 4.5	2011/02/20	11:22:16.3	35.47	51.78	ML4.2
1960/06/01	05:07:00.0	35.8	51.8	M 4.0	2012/02/10	08:59:40.0	35.59	52.42	ML4.6
1966/11/08	03:14:11.0	36.09	50.74	mb 4.8	2014/05/10	22:04:53.8	36.1	52.06	ML4.0
1967/02/16	11:55:32.0	35.4	51.9	mb 4.5	2014/08/16	23:55:56.9	36.02	52.3	ML4.2
1970/06/27	07:57:56.0	35.13	50.76	mb 4.8	2015/08/13	18:42:11.7	35.185	51.919	ML4.1
1970/10/03	06:57:03.0	36.01	51.31	mb 4.1	2017/12/20	19:57:37.3	35.686	50.932	ML5.1
1974/01/10	16:36:19.0	35.81	51.97	M 4.6	2017/12/26	21:24:34.2	35.684	50.93	ML4.2
1979/02/22	05:07:17.0	35.20	52.1	mb 4.6	2018/04/01	18:26:23.0	35.528	52.369	ML4.1
1980/12/19	16:54:18.0	35.24	52.37	mb 4.5	2019/05/20	02:45:23.0	35.4	52.45	Mb4.2
1982/10/25	16:54:50.0	35.10	52.30	MS5.4	2020/05/07	20:18:21.9	35.75	52.04	ML5.1
1983/03/25	11:57:49.0	36.03	52.29	Mw5.5	2020/05/27	09:11:37.8	35.75	52.01	ML4.0
1983/03/26	04:07:19.0	35.99	52.24	mb5.4	2020/12/18	23:35:15.3	35.76	51.99	ML4.0
1983/05/29	17:15:38.0	35.19	52.12	mb4.4	2021/08/15	12:41:50.5	35.79	51.851	ML4.1
1988/08/22	21:23:38.0	35.31	52.34	Mw5.3					

1-4-2 Microseismicity

Ashtari et al. (2005) is the first instrumental study that recorded and analyzed small earthquakes around Tehran. Using the permanent seismological network (Institute of Geophysics of the University of Tehran, Figure 1-9A), from January 1996 to July 2000, it has been recorded 4900 events, reduced to 1066 events after considering the event recorded by at least five stations and removing the explosions from quarries. Also, with two temporary dense networks installed in 1999-2000, it has been gathered 319 events during the 1999 experiment and 114 events during the 2000 experiment. From both permanent and temporary networks, the results indicate that the highest level of activity in the southern flank of Central Alborz is located around the Mosha and the Garmsar faults, eastern part of Tehran. The results also show an apparent northward dip associated with the Mosha and the Garmsar faults and a clear strike-slip left-lateral motion, oriented WNW–ESE for eastern Mosha that confirm a geodynamic oblique-slip mechanism regime.

Another campaign of micro seismic study was operated for five months in 2006 with 44 portable seismological stations around the Moshfa fault (Tatar et al., 2012; Figure 1-9). During this shot period, it has been recorded 538 earthquakes at more than four stations. Among these, 148 events have an RMS less than 0.3 s. The stations were located in the east and helping to investigate the seismicity of central and eastern segments of the Moshfa as long as the North Tehran and part of the Parchin and Firuzkuh faults. During this experiment, the North Tehran and Parchin faults did not show important activity which is consistent with the results of Ashtari et al. (2005), most of the activity belongs to the eastern part of the Moshfa fault.

Unfortunately, the duration of temporary seismicity studies in Tehran was not enough to consider significant events. Moreover, the level of seismic micro activity during these periods was surprisingly low.

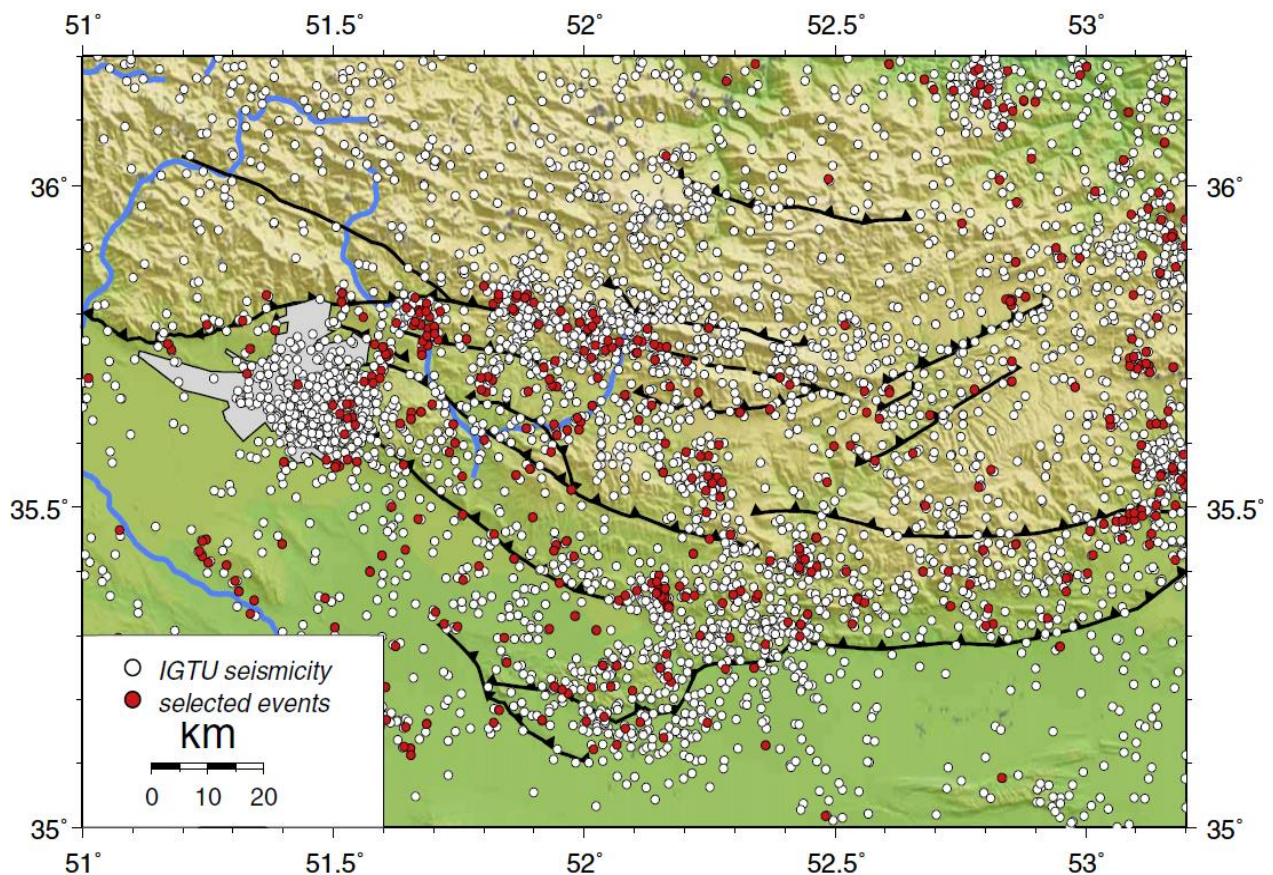


Figure 1-9: C: Micro seismicity located by the Tehran (IGUT) network between 1996 and 2008 (From Tatar et al., 2012)

1-5 State of knowledge about Tehran basin properties

Up to now, our understanding about Tehran basin sediments physical properties has been confined to a few ancient geological studies and a few attempts using geophysical and seismological studies. Besides ancient geological studies (Engalenc, 1968; Tchalenko et al., 1974), three types of efforts have been done in Tehran to determine these physical properties:

- the first one is the determination of Vs using geotechnical data mainly from studies on seismic microzonation of Tehran (Jafari et al, 2001a, 2001b, 2004; JICA and CEST, 2000);
- the second effort is related to some limited ambient noise vibration studies (Shabani, 2010; Fazlavi, 2015) to study site effects in Tehran city and;
- the third one consists in studies to identify the shallow crustal structure of the Tehran basin, which can give some qualitative ideas about the near surface depths (e.g. Shirzad and Shomali, 2013, 2014).

1-5-1 Geotechnical data

The geotechnical studies of Tehran were done by combining a good amounts of boreholes data, seismic refraction profiles, and a few downhole measurements to extract the shear wave velocity at different places. In the northern Tehran, the shear wave velocity reaches the engineering bedrock at a shallow depth of 2-5 meters on average, with a velocity of 600 m/s. However, in southern parts, the value started from 250m/s and gradually increased to 600m/s at the deepest depth reached usually 30~45 meters. Also, there are few local parts in the central south where the shear wave velocity remains under 450 m/s down to 30 meters. In chapter three, the geotechnical studies in Tehran will present in more detail.

1-5-2 Site effect in Tehran

The first and most successful study on Tehran site effect studies was done by Haghshenas in 2005. In this study, 14 seismological stations (station PAR was not working) were installed from February to June 2005 on different sites in the city in a more or less N-S line shape. The location of the stations was determined by potential changes in the geotechnical situation. Most of the stations was located in southern parts of the city where site effects were expected to be more significant. Two stations were considered as references on hard rock in the north and southeast

(JAM and CHA stations) in order to compute site to reference spectral ratio (SSR) from earthquake recordings (Figure 1-10). Beside SSR, H/V on the same earthquake recordings and H/V on ambient noises have been also computed to estimate the site amplification level in Tehran basin.

The SSR revealed a significant ground motion amplification in a wide frequency range, from very low frequencies around 0.4 Hz up to 1-2 Hz. Meanwhile, two stations installed in the city's southwest part of Tehran (MOF and SHL, Figure 1-10) displayed the highest amplification (up to 8). In the northern and central part of the basin (stations FAR, ABM, TAP DAR, Figure 1-10) the observed amplifications (3 to 5) were lower than in the South.

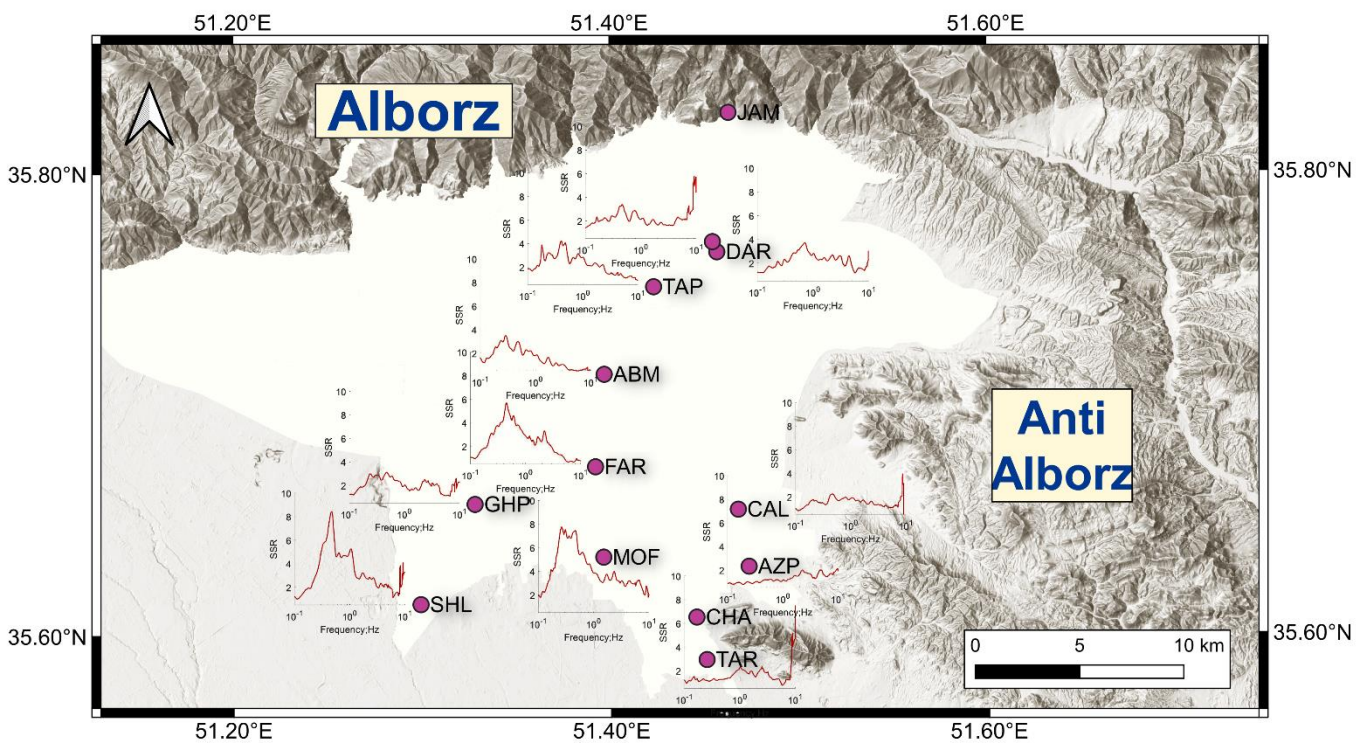


Figure 1-10: SSR results for temporary network station in Tehran considering JAM as reference station (re-drawn from Haghshenas (2005)).

The other approach (H/V on earthquake) provides consistent results with the SSR method, the resonance frequencies had coherent frequency range with SSR results. However, the calculated amplifications from HV-earthquake were lower than the SSR amplifications at the resonance frequencies and also at higher frequencies. This difference is to be expected and interpreted as converted S-P waves that enrich the vertical components in the sedimentary basins.

For H/V on noise, the results are very different: for most of the stations the H/V curves, obtained from one hour of ambient noise (extracted at 1 a.m.), are almost flat at the resonance frequencies indicated by SSR (Haghshenas, 2005). A comprehensive study in 2008 (Haghshenas et al., 2008) shows that Tehran is one of the very few basins in the world where H/V ratio fails to predict the correct site frequency when SSR method identify a low frequency peak.

Two hypotheses have been presented to explain the observed differences in resonance frequencies and amplifications. The first one is the existence of a low velocity contrast at depth corresponding to a deep bedrock with very thick alluvial deposits. This can explain (1) the H/V noise failure to provide coherent results with SSR method and (2) the low frequency amplification in Tehran (from SSR). Because it is possible that at some periods of time, the energy at low frequency inside the wavefield is not strong enough to excite the structure. The second hypothesis is the presence of strong lateral discontinuities, and the possibility of 2/3D effects coming from faulting and folding in the city. This hypothesis is also indirectly supported by the significant difference observed between SSR and the H/V method. In his regard, Bard (1999) proposed that the difference between H/V and SSR amplification amplitudes may be related to 2/3D effects, in such a way that this difference gets larger as 2D and 3D effects get more pronounced in SSR method. The idea is that 1D soil columns should provide simple transfer functions with one fundamental peak and several harmonics with lesser amplitude, while 2D or 3D sites are characterized by broader band transfer functions, because of additional lateral interferences.

The lengthening site effects can be quantified by two methods proposed by Beauval et al. (2003) and Parolai and Bard (2003). The first is based on comparing the group delay of the Fourier spectrum between the study site and the reference site (Sawada, 1998), and the second relies on sonograms of the seismic events recorded at the site and at the reference. The sonogram is a simple time-frequency technique, giving access to the variation of the spectral energy of a seismic signal as a function of time. The two methods give consistent results: significant lengthening effects happened at low frequency, and the strongest lengthening occurred at two most amplified stations of the city (SHL and MOF, Figure 1-10, Haghshenas, 2005).

The first ambient noise array measurements in Tehran in order to extract shear wave velocity were done during the Shabani Ph.D. thesis (2010). She used MSPAC method (Bettig et al., 2001) on circular arrays (150-200 m radius) deployed in the southern part of Tehran where it was expected

the greatest depth of alluvium. Joint inversion of the surface wave dispersion curves derived from the arrays and the ellipticity of Rayleigh waves, allowed to estimate the bedrock depth to more than 700 meters.

However, the bigger campaign of array measurements in Tehran was done by Fazlavi (2015), deploying 11 noise arrays in two cross-sections from North to South and East to West (Figure 1-11). The results proposed a 2D velocity model that with an increase of velocities from North to South and a gentle deepening of the bedrock to the most southern part of the city.

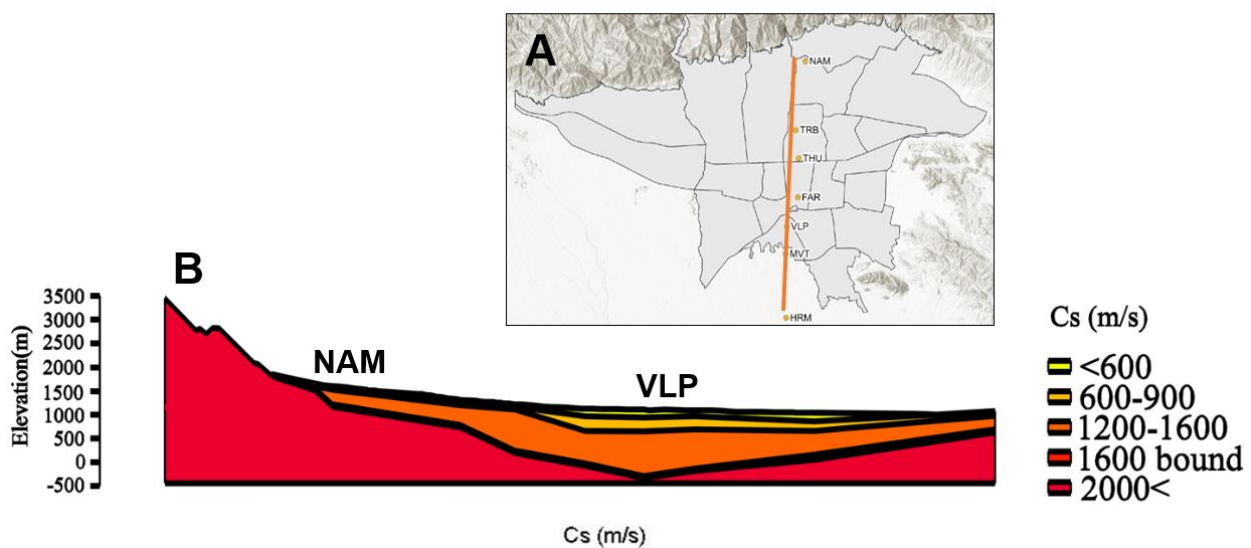


Figure 1-11: Fazlavi (2015) studies. A) Location of arrays for North-South cross section. B) 2D velocity profiles for Tehran basin (redrawn from Fazlavi 2015)

1-5-3 Bedrock depth

As mentioned before, Engalenc (1968) was the first to report some qualitative ideas about the geological bedrock in Tehran. He suggested that Tehran piedmont have a fragile behavior originated from the late or post-Pliocene contraction phase and the hinges of the pediment gravel anticlines superimposed on these fractures. To the South, he considers a series of breaks in the NW-SE direction crossing the plain similar to what he had seen at the borders in the South. However, the bedrock depth is totally inaccessible from direct observations in the Tehran plain.

Following Engalenc (1968), the bedrock of Tehran should be formed mainly by Green Tuffs of Karaj formation, with pre-Oligocene age observed through very few outcrops in eastern parts of the basin, as well as volcanic rocks, limestone, and dolomites of anti-Alborz.

Due to the presence of alluvial deposits and the absence of deep boreholes, it is impossible to determine the precise depth of the bedrock. Moreover, there is no chance to collect direct observations because of the massive urbanization covering all geological markers. The main hypothesis, based on a limited gravity survey carried out in 1957 (S.A.G.P., 1957), suggests that the Anti-Alborz continues under the Tehran city, bounded to the North by an E-W extension of the Sorkkeh-Hesar fault and a NE_SW extension of BibiShahrbanou mountain (Tchalenko et al., 1974). Unfortunately, the original data and the context of the mentioned reports are not available. In the S.A.G.P (1957) reports, the methodology to computed the bedrock depth is also unclear. However, the gravity survey results are mentioned in some studies as the first and only geophysical observations about Tehran bedrock. Based on this survey, the deepest parts of the basin are located South-West of the basin with a bedrock depth up to 1000 m.

Besides these gravimetrical measurements, the geophysical studies carried out by C.G.G. (1965) suggested the extension of anti-Alborz, by electric resistivity measurements. It indicates that the thickness of the "B" formation is rising in a region west of the buried Anti-Alborz block.

As a synthesis, a working hypothesis for the structure of the bedrock in the Tehran basin may be formulated as follows: the bedrock depth increases from the North Tehran Fault in the North to the central parts marked by western extension of the Sorkkeh Hesar. South of this, there is a bowl shape plain located between extension of the Sorkkeh-Hesar fault and NE_SW extension of BibiShahrbanou.

Finally, according to the existing seismic stations around Tehran to monitor the seismicity of the Alborz, it is feasible to perform seismic tomography in this area to study shallow crustal structures. These stations are close enough to identify shallow parts to a depth of two kilometers (Shirzad et al., 2018).

Shirzad and Shomali (2013) extract the group velocities from the ambient noise tomography in this area, using ten accelerometers, 12 short-period seismometers (corner frequency ≥ 1 Hz), and two broadband seismometers (0.01–100 s). The shortest and longest interstation distances were 5 and 30 km, respectively. The results gave the Rayleigh wave group-velocity tomography for a 1 to 7 s period (Figure 1-12). Based on the depth sensitivity kernels as a period function (Zhou et al., 2004),

the group-velocity 1s and 2s period could resolve the depth corresponding to possible alluvium deposits. The results (Figure 1-12) show the relatively lower velocity in the south and west of the city for 1s and a narrow band low-velocity zone for 2s.

Shirzad et al. (2018) did also some surface wave dispersion measurements from micro-seismic signals using the multiple-filter analysis technique (Herrmann, 1973) down to 3 s. period to well-constrained the regional crustal structure up to 6 km. Dispersion curves were inverted using the nonlinear iterative damped least Squared and finally represented in 2D cross-sections. Shear wave velocity profiles in this study show that the alluvial thickness varies between 300 (minimum sensitivity) and ~ 1500 m in the Tehran basin. However, the resolution of this study is not enough precise to develop some detailed map lower than 1 km.

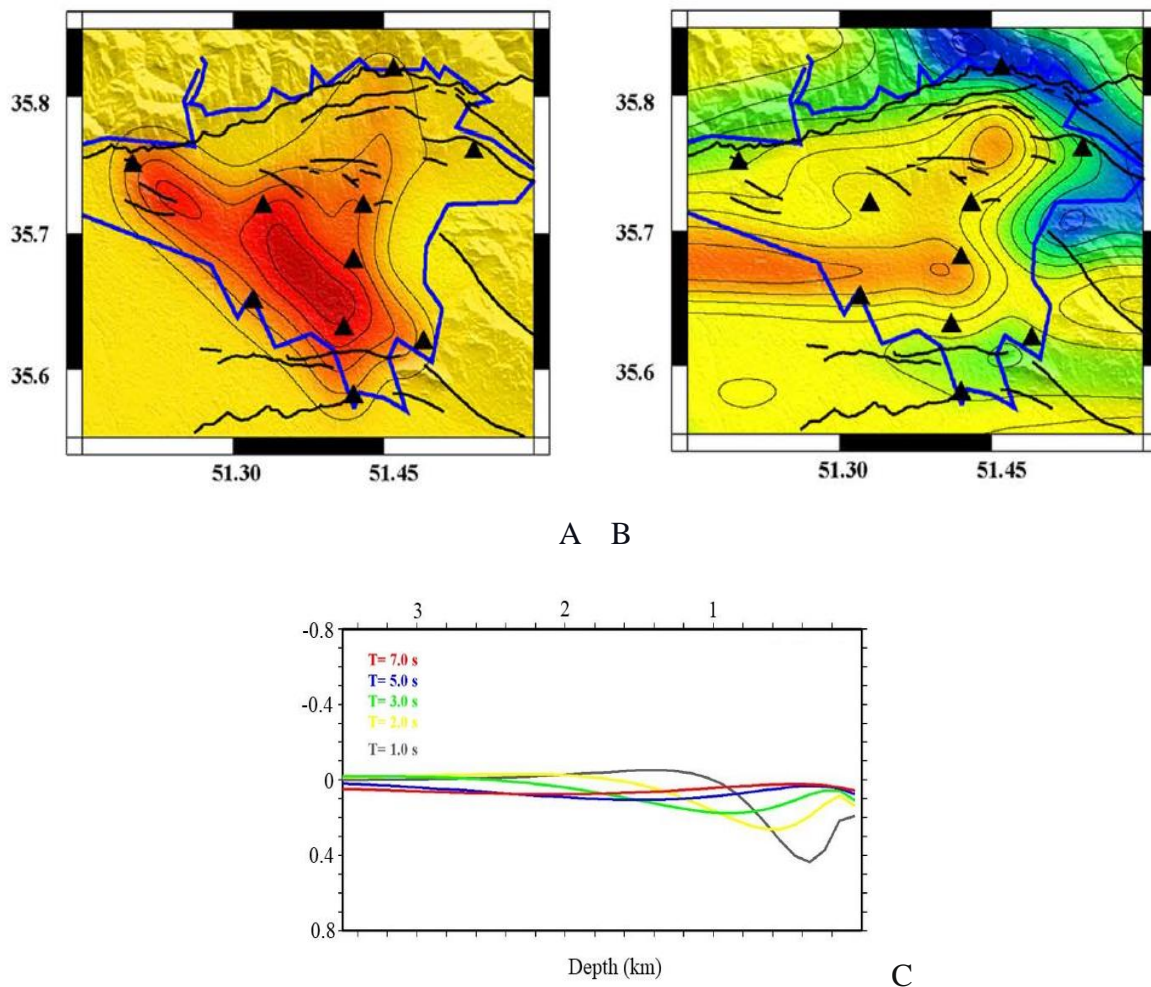


Figure 1-12: Shirzad and Shomali (2013) tomographic results from seismic noise data. A: Rayleigh wave group-velocity tomography map for 1s. period. B: Rayleigh wave group-velocity tomography map for 2 s. period. C: the sensitivity kernel in depth for 1 s. and 2 s. period

1-6 Conclusion

This chapter provides an overview of the current understanding about the characteristics of the Tehran Basin, including its tectonic and geological settings. The tectonic part covers the central Alborz tectonics and the faults surrounding Tehran. after this review, I introduce the structural geology and sedimentary formation of the Tehran Basin and then represent all active faults in Tehran, along with a review of the city's historical and current seismicity.

Furthermore, I briefly review the available geotechnical data and then introduce the first site effect study in Tehran. The chapter also covers the limited research conducted on extracting physical properties (shear wave velocity) of the basin and bedrock depth. However, due to the scarcity of available data on this topic, further studies are required to achieve a satisfactory level of understanding. The next chapter will introduce methods for extracting these parameters to supplement the existing research.

CHAPTER 2

Methods to construct the 3D shear wave velocity

structure of Tehran's basin

2-1 Introduction

In order to explain the reason for the significant site effects observed in Tehran, it is inevitable to answer the following inseparable questions: “What is the real geometry of the Tehran basin? and What are the geophysical/geotechnical properties in the basin?”

Non-invasive methods are one of the most efficient methods to answer this question in urban and large-scale environments. It is due to the fact that typical invasive methods (mainly boreholes) have some limitations in order to map 2/3D site geometry, such as the large number of boreholes to drill, the limited penetration depth (typically few tens of meters for classical down-holes or cross-holes methods) and the difficulties of drilling in urban areas. This chapter presents the various non-invasive methods used to derive the 3D shear-wave velocity model of Tehran's basin.

2-2 Single-station methods

In the following sections, I present the single-station methods based on earthquakes or seismic ambient noise recordings, these methods aiming at providing the fundamental resonance frequency of the soil and, for some methods, the amplification of the ground motion at the fundamental resonance frequency.

2-2-1 Site-to-Reference method (SSR)

2-2-1-1 Principles and retrieved indicators

Borcherdt (1970) was the first to propose the site-to-reference (SSR) method, which consists in comparing earthquakes recorded simultaneously at a sedimentary site with recordings from a nearby station assumed to be on outcropping bedrock. It is assumed that records from the reference station have no site effect and contain the same source and propagation effects as records from the sedimentary site. The SSR curve is then obtained by dividing the Fourier amplitude spectra of the records (horizontal components) at the site by the Fourier amplitude spectra at the reference site to extract the empirical frequency-dependent site amplification, from which the fundamental resonance frequency and the related amplification can be extracted.

The SSR can be calculated using various seismic phases: P, S, early and late coda waves. However, most often the S wave phase in horizontal components is selected, considering the fact that these

waves carry the most energetic part of the seismic signals (Field and Jacob, 1995; Kato et al., 1995; Su et al., 1996).

In Tehran, Haghshenas (2005) selected the P, S and early coda phases of the events based on the successful results from Field (1996) in the Coachella Valley (southern California) and his own sensitivity analysis.

Typically, the Fourier spectra are calculated in a frequency band where the signal-to-noise ratio is greater than a threshold fixed from 3 to 5 as recommended (Haghshenas, 2005). The obtained Fourier amplitude spectrum for each event is smoothed using the Konno–Ohmachi function (1998) and the average SSR is obtained using geometric mean of individual SSRs obtained for all the earthquake events. The final results give the frequency-dependent amplification of the site (Figure 2-1A) where the highest amplification (A_0) at low frequency corresponds to the fundamental resonance frequency (f_0).

2-2-1-2 Application

The SSR method has been applied in a very large number of studies to evaluate site amplification (LeBrun et al., 2001; Pilz et al., 2009). This method can also be used even in case of strong 2/3D site effects (Cornou and Bard, 2003; Bindi et al., 2009). In such a case, the SSR curve most often exhibits a plateau of amplification beyond the resonance frequency as illustrated in Figure 2-1B and observed at many sites.

2-2-1-3 Limitation

In practice, most of the time the reference station is just located on a rocky site near the sedimentary basin/valley under study. Ideally, the reference site should be an unweathered rock site without topography to avoid as much as possible the reference site to also face any site amplifications. For instance, Steidl et al. (1996) examined some rock sites at San Jacinto mountains (southern California) and showed that the reference stations can suffer site amplification between 2 and 5 Hz caused by the near-surface weathering and cracking of the rocks. Moreover, the reference station should be also located close enough to the site and the hypo central distance of the earthquakes should be much greater (at least ten times) than the distance between the site and the reference station (Field and Jacob, 1995).

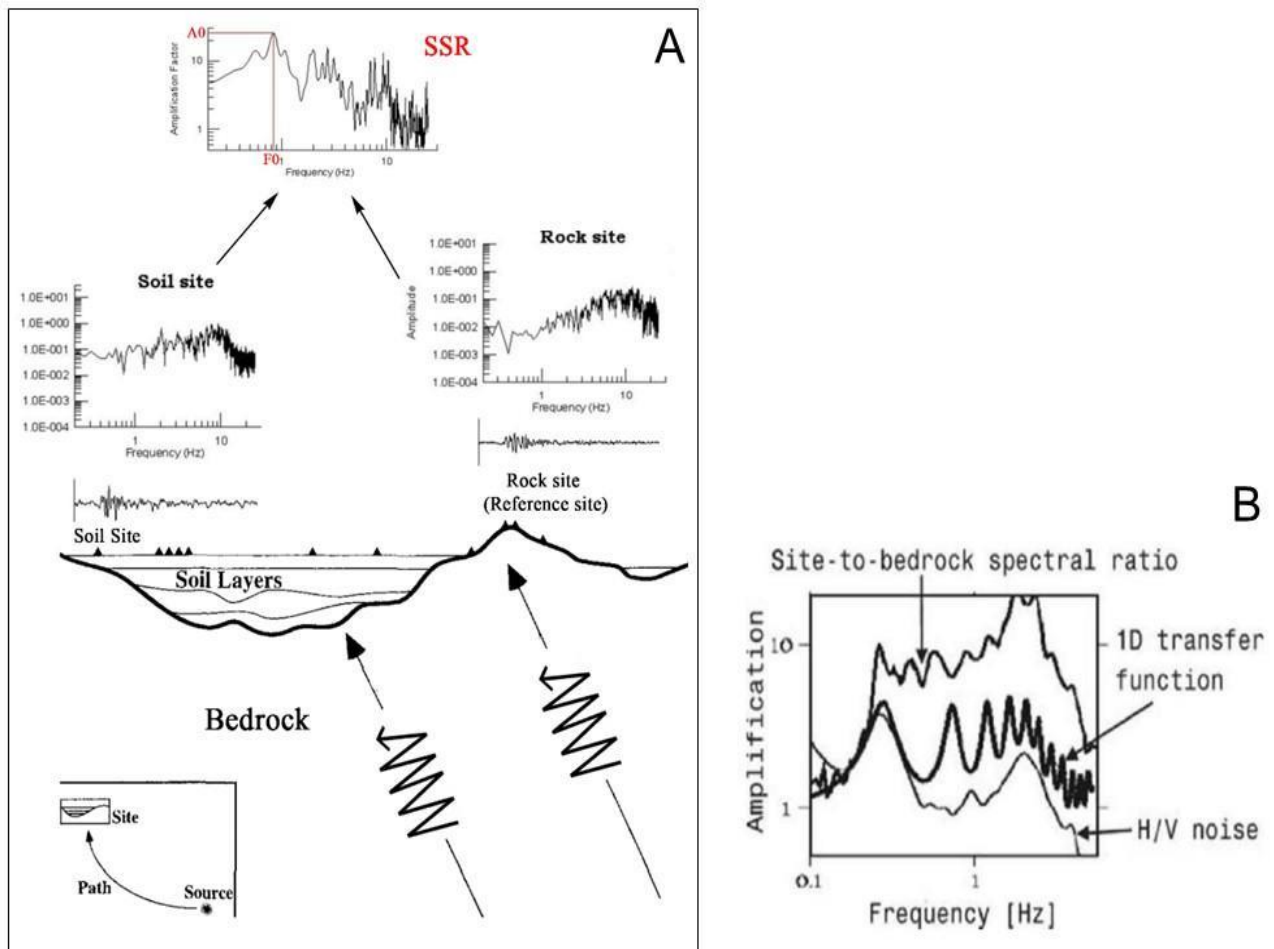


Figure 2-1: A) The principle of SSR computation, modified after Steidl et al. (1996). B) SSR obtained in the Grenoble valley for a 2.5 Ml seismic event occurred 15 km far from the basin compared to 1D transfer function and H/V noise curve (adapted from Cornou & Bard, 2003).

2-2-2 H/V method (noise and earthquake)

H/V method is an alternative simple method widely used for estimating the fundamental resonance frequency of the site. H/V is defined as the ratio of the Fourier amplitude spectra of the horizontal and the vertical components of seismic ambient vibrations recorded at a single station. Lermo and Chávez-García (1993) also applied the H/V ratio technique for earthquake motions using the ratio of the S-wave Fourier amplitude spectra of horizontal over vertical components.

2-2-2-1 Principles and retrieved indicators

The original idea of Nakamura (1989)¹ expressed that the single station H/V was able to determine the resonance frequency and amplification with simpler equipment and conditions rather than SSR. By his assumption, for the 1D horizontally layered structures with no or smooth lateral variations, the H/V peak always provides a reasonable estimate of the resonance frequency and amplification of the basin in terms of multiple reflections of SH waves. Although based on his assumption on SH waves, he believed that the method could estimate both resonance frequency and amplification factor, Empirical evaluation of the H/V method for a large number of sites located in various sedimentary valleys worldwide showed that the fundamental resonance frequency (f_0) extracted from the H/V curves just correlated very well with the site's resonance frequency (Haghshenas et al., 2008). While the H/V amplitude at f_0 was always smaller or equal to the actual amplification of the sites (Haghshenas et al., 2008; Figure 2-2). In this regard, Cultrera et al. (2014) conducted a study to evaluate the correlation between H/V computed from seismic ambient noise and weak earthquake motions to quantify the relationship. However, they found a weighted average for their study, they concluded that the reliability of the process explained only by specific geological settings.

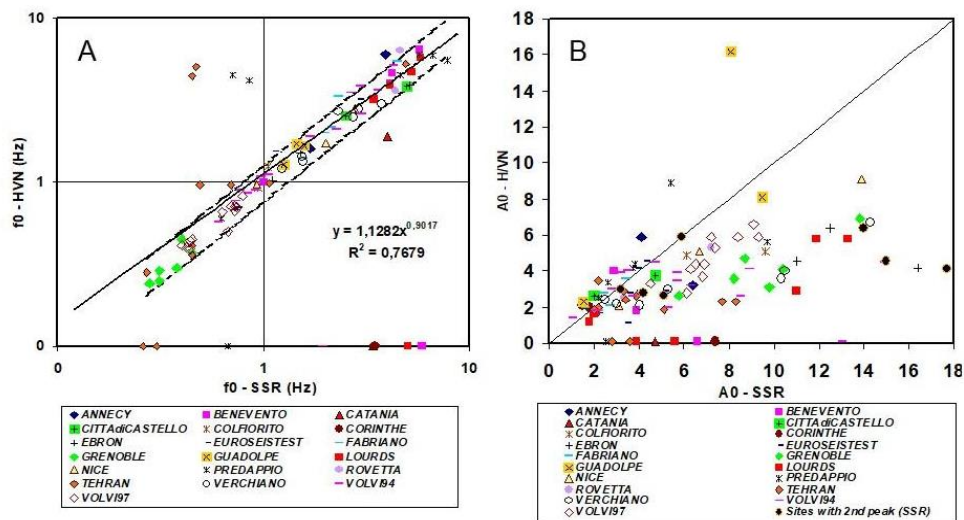


Figure 2-2: A: Correlation between H/V peak frequency (f_0 -H/V) and SSR fundamental frequency (f_0 -SSR) and B: H/V amplitude (A_0 -H/V) and SSR amplitude (A_0 -SSR) for SESAME (2004) sites (adapted from Haghshenas et al., 2008)

¹ which is first called Quasi Transfer Spectrum to avoid the ambiguity comes from the using of term "H/V" between S-wave H/V resonance or H/V on Rayleigh waves

From a numerical point of view, H/V modeling was done for the first time by Lachet and Bard (1994). They randomly distributed various sources at a depth of 2 meters in a circular pattern around a central receiver and demonstrated the similarity between the fundamental resonance frequency derived from noise synthetics and the theoretical resonance frequency of the site. They also show that the simulated H/V peak resembled the ellipticity of the fundamental mode of Rayleigh waves. They concluded that the shape of the curve is controlled by the polarization curve of fundamental Rayleigh waves and the level of amplification depended on various factors, such as the Poisson ratio and the distance between the source and receiver. This modeling confirms the method's capacity to discover f_0 . While at f_0 , the H/V amplitude was always less than or equal to the real amplification.

The processing of H/V curves is very straightforward. A standard processing method for analyzing H/V curves was proposed during the EU-SESAME (2001-2004) project (Bard, 2008). The processing is done by selecting the three components of ambient noise vibration and searching for stationary windows on the three components, by using an LTA/STA anti-trigger criterion to avoid the windows consisting of energetic transients' signals.

The next step is conducted by calculating each window's Fourier amplitude spectrum on the three components and smoothing the individual spectrum using the Konno and Ohmachi (1998) function. Then the mean of the smoothed horizontal spectrum is computed for each window. Several merging procedures, arithmetic (Chavez-Garcia et al., 2007), geometric (Piccozi et al., 2005) or quadratic (Bonnetoy-Claudet et al., 2008), are possible to define the horizontal average spectra (H).

Following that the spectral ratio (H/V) for each individual window is calculated. The last step is the computation of the geometric mean of the H/V spectral ratio across all windows. Figure 2-3 shows the schematic view of the different steps.

Beyond noise studies, Lermo and Chávez-García (1993) applied the H/V for earthquake motions. The H/V on Earthquake is also defined as the ratio of the S-wave Fourier spectra of horizontal over vertical component and used for site amplification studies (Reipl et al., 1996; Horike et al., 2001). This definition is similar to the receiver function technique proposed by Langston (1979) to investigate crustal structures.

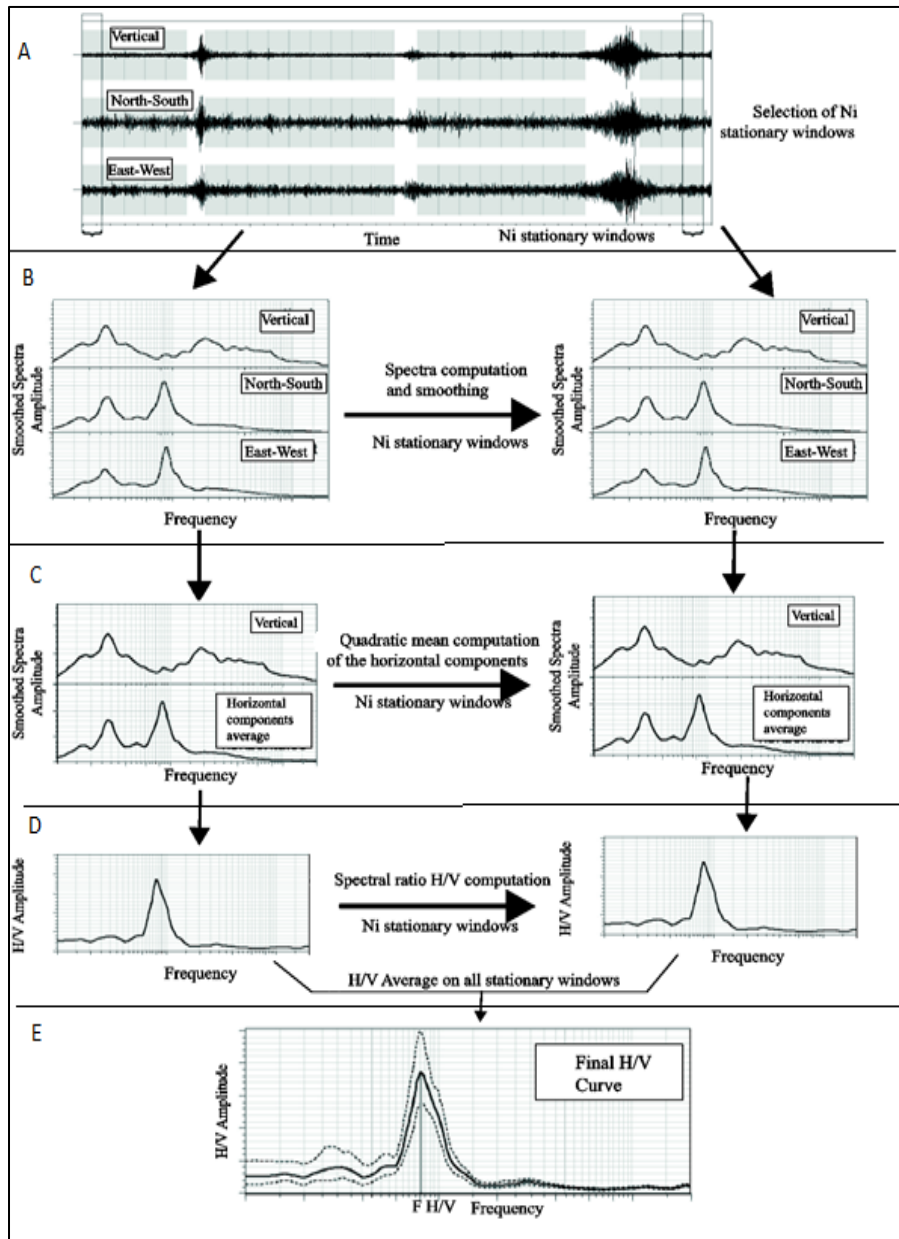


Figure 2-3: The various steps to retrieve H/V curves from seismic ambient noise recordings (adapted from Bonnefoy-Claudet, 2004).

2-2-2-2 Application

During the 30 years of developing and applying the H/V method (Molnar et al., 2022), the H/V method has been proved to be a very efficient non-invasive technique to measure the fundamental resonance frequency of soil. The H/V method has been widely used to map the fundamental resonance frequency variation, especially for microzonation studies (e.g. Lebrun et al., 2001;

Lunedei and Albarello, 2009). The method has shown its effectiveness in utilizing both noise and earthquake recordings (Haghshenas et al., 2008) and additionally the series of sensitivity analysis on the H/V method regarding its temporal stability (Guillier et al., 2007), the measurement conditions (Chatelain et al., 2008) and the effect of the duration and processing parameters (SESAME, 2001–2004) demonstrated the method's reliability in different conditions.

H/V is also used as a simple and efficient tool to evaluate bedrock depth (h) through the inverse power empirical relationships between f_0 and h

$$(h = af_0^{-b}) \text{ (eq. 2-1)}$$

where a and b are curve-fitting parameters (e.g., Ibs-von Seht and Wohlenberg, 1999; Fairchild et al., 2013 and Thabet, 2019). Table 2-1 provides some examples of this relationship with correlation parameters for different parts of the world.

Table 2-1: Parameters (a and b) of the inverse power frequency– thickness relationship $h = af_0^{-b}$ for some sedimentary basins around the world. f_0 is the fundamental resonance frequency and h is the seismic bedrock depth.

Location	Study	a	b	Rs	N. of sites	f0 (Hz)	h-range (m)
Lower rhine (Germany)	Ibs-von Seht &Wohlenberg, 1999	96	1.388	0.98	102	0.1-5	15-1600
		146	1.375	0.75			
Cologne (Germany)	Parolai et al., 2002	108	1.551		337	0.25-20	2-500
Bam (Iran)	Motamed et al., 2007	135.2	1.979				
Izmit bay (Turkey)	Ozalaybay et al., 2011	141	1.270	0.91	239	0.25-3.8	20-1100
Sydney (Australia)	Harutonian et al., 2013	73	1.170	0.94	15	4.2-27	1.2-13.3
CapeCod (USA)	Fairchild et al., 2013	90.53	1.000	1.00	164	0.73-2.43	118-460
Japan	Thabet, 2019	117.13	1.197	0.94	224	0.095-22.5	2-1500
		105.14	0.899	0.62	64	0.198-17.13	4-625
		132.67	1.084	0.90	36	0.304-12.55	6-550
		116.62	1.169	0.98	55	0.095-22.5	3.5-1500

Since the shape of the H/V curve depends on the characteristics of the earth's layer (references), H/V curve can be used to invert the shear wave velocity profile (Fäh et al., 2001, 2003; Arai and Tokimatsu, 2004; Picozzi et al., 2005) assuming that the seismic ambient noise wavefield is mainly composed of Rayleigh waves. Sánchez Sesma et al. (2011) proposed a new method by introducing the H/V as a property of the medium, containing all types of body and surface waves. In this method, the source and receiver are assumed to be at the same location and correlating a component of the displacement wavefield with itself enables estimating the parameter called Directional Energy Density (DED). DED is the energy density of the displacement in each of the orthogonal directions, corresponded to the imaginary part of the Green's function as follows (Sánchez-Sesma et al., 2011):

$$\frac{H}{V}(X, f) = \sqrt{\frac{Im[G_{11}] + Im[G_{22}]}{Im[G_{33}]}} \text{ (eq. 2-2)}$$

This formulation allows the calculation of the contributions of all wave types to lead to full H/V inversion. Lonsi et al. (2015) explored this formulation to retrieve the velocity structure. However, He demonstrated that inverting the H/V in any case still requires a priori information about the structure to converge to a valid soil profile.

2-2-2-3 Limitation

The interpretation of the H/V curve is challenging in 2D/3D geological structures. First of all, the peculiar shape of the curves usually indicates lateral heterogeneities in the subsoil. Experimental studies show H/V curves of low amplitude (typically around 2 to 3), sometimes flat or plateau-shaped, near the valley edges or strong lateral heterogeneities of the medium (Uebayashi et al., 2012; Salloum et al., 2014).

Matsushima et al., (2014) is also reported a significant directional dependency of the H/V in the Kyoto and Fukushima basins in Japan. The H/V curve exhibiting differences between longitudinal and transversal component of H/V: the longitudinal component almost parallel to the strike of the Obaku fault exhibited a larger peak H/V amplitude and a lower peak frequency compared to the transverse component perpendicular to the fault trace. Such directional dependency of the H/V was also reported in the Bolzano basin in northern Italy by Sgattoni and Castellaro (2020).

By simulating seismic ambient noise in various 2D valleys, Guillier et al. (2006) showed that H/V curves most often exhibit a broad or plateau-like shape close to the valley edges having a significant

sediment-to-bedrock sloping interface. Such findings were confirmed on seismic ambient noise synthetics of real seismic noise recordings by Uebayashi (2003) and Uebayashi et al., (2012) for sites in Japan and by Leroux et al., (2012) in an Alpine valley. In such cases, the H/V peak frequencies are found to significantly overestimate the 1D resonance frequency (from 20% in Uebayashi et al., (2012) up to 80% in Guillier et al., (2006)). Interestingly also, the H/V curve can exhibit a flat curve at some sites with large lateral variation of the sediment-to-bedrock interface as reported by numerical modeling (Uebayashi, 2003; Leroux et al., 2012) or observations (Di Giulio et al., 2012). To summarize, H/V curves peculiar shapes, such as broad or plateau-like shapes, most of the times indicate strongly laterally variable bedrock interface and should be interpreted with caution.

2-2-3 Ellipticity of Rayleigh waves

Ellipticity of Rayleigh waves is defined as the ratio between the horizontal and the vertical Rayleigh wave particle motions. The ellipticity is related to the local soil structure, because, for a layered structure, the Rayleigh waves are dispersive and the ellipticity varies with frequency, the particle motions being prograde or retrograde (Malischewsky & Scherbaum, 2004).

2-2-3-1 Principles and retrieved indicators

The seismic noise wavefield comprises different modes of Rayleigh and Love surface waves and body waves and the relative contribution of these waves in the noise wavefield varies from site to site (Endrun, 2011). Accordingly, the classical H/V is always overestimating the ellipticity of Rayleigh waves due to the presence of other wave types (Poggi et al., 2012). It means that if the wavefield was composed exclusively of single-mode Rayleigh waves, the H/V and ellipticity curves would be the same. This fact raises another question: even if ambient noise vibration mostly consists of surface waves, what should I do with the effects of Love waves and S body waves?

Two methods (HVTFA and RayDec) were introduced to reduce the effects of possible body and Love waves in the seismic noise wavefield. HVTFA has been introduced by Fäh et al., (2003) and developed during the SESAME (2001-2004) and NERIES (2008) projects. HVTFA is based on the time-frequency analysis of the continuous wavelet transforms of the seismic ambient noise. The maximum values of the vertical signal in the time-frequency decomposition are extracted in each frequency and, the spectral ratio is calculated by phase-shifting the horizontal component by $\pi/2$

which is the phase shift between horizontal and vertical Rayleigh wave components. The averaging of the calculated spectral ratios allows then to extract the ellipticity of the Rayleigh waves in frequency domain (Figure 2-4).

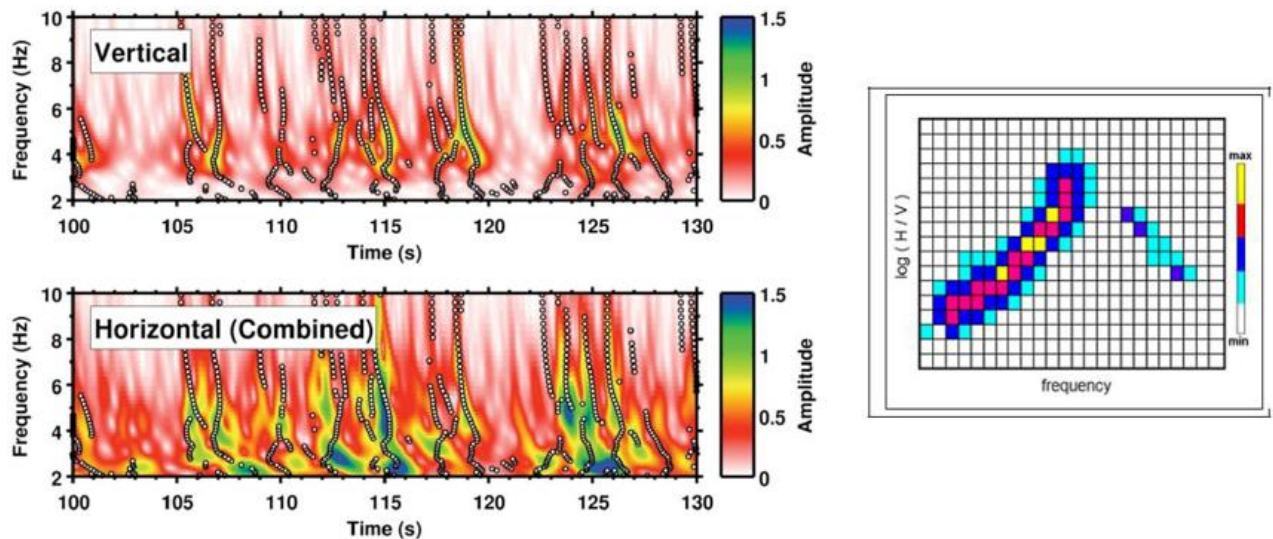


Figure 2-4: (left panel) Amplitude spectra are shown in terms of time and frequency while the maximum value in time on the vertical axis and the corresponding value on the horizontal axes (white points) are extracted. (right panel) For each frequency, the saved ratios are analyzed statistically in a 2D histogram representation (adapted from Poggi et al., 2012).

Besides HVTFA, the RayDec method is based on the random decrement technique (Asmussen, 1997) which is considered an efficient way to estimate the Rayleigh waves ellipticity (Hobiger et al., 2009).

The RayDec (**R**ayleigh Wave Ellipticity by Using the Random **D**ecrement Technique) method basically sums and stacks buffered signal time windows for the three-components for various frequencies, time window length being frequency dependent, typically 10 periods the frequency target (Hobiger, 2011). More precisely, for a given frequency, the method searches all time windows for which the first sample of the time window corresponding to the vertical component of the filtered signal changes its sign from negative to positive values. The two NS and EW components are phase-shifted by $\pm\pi/2$. The horizontal component is formed by projecting the NS and EW components to the azimuth such as this azimuth maximizes the correlation between the vertical and the horizontal component. The buffered time windows of the vertical and horizontal

components are then stacked, using the correlations as weighting factors, to get one signal for each vertical and horizontal component. The ratio is defined as the square root of the energies in the buffered signals (Figure 2-5). This procedure is repeated for different frequencies in order to get the ellipticity of Rayleigh waves as a function of frequency and the stacking process eliminating at best the body and Love waves.

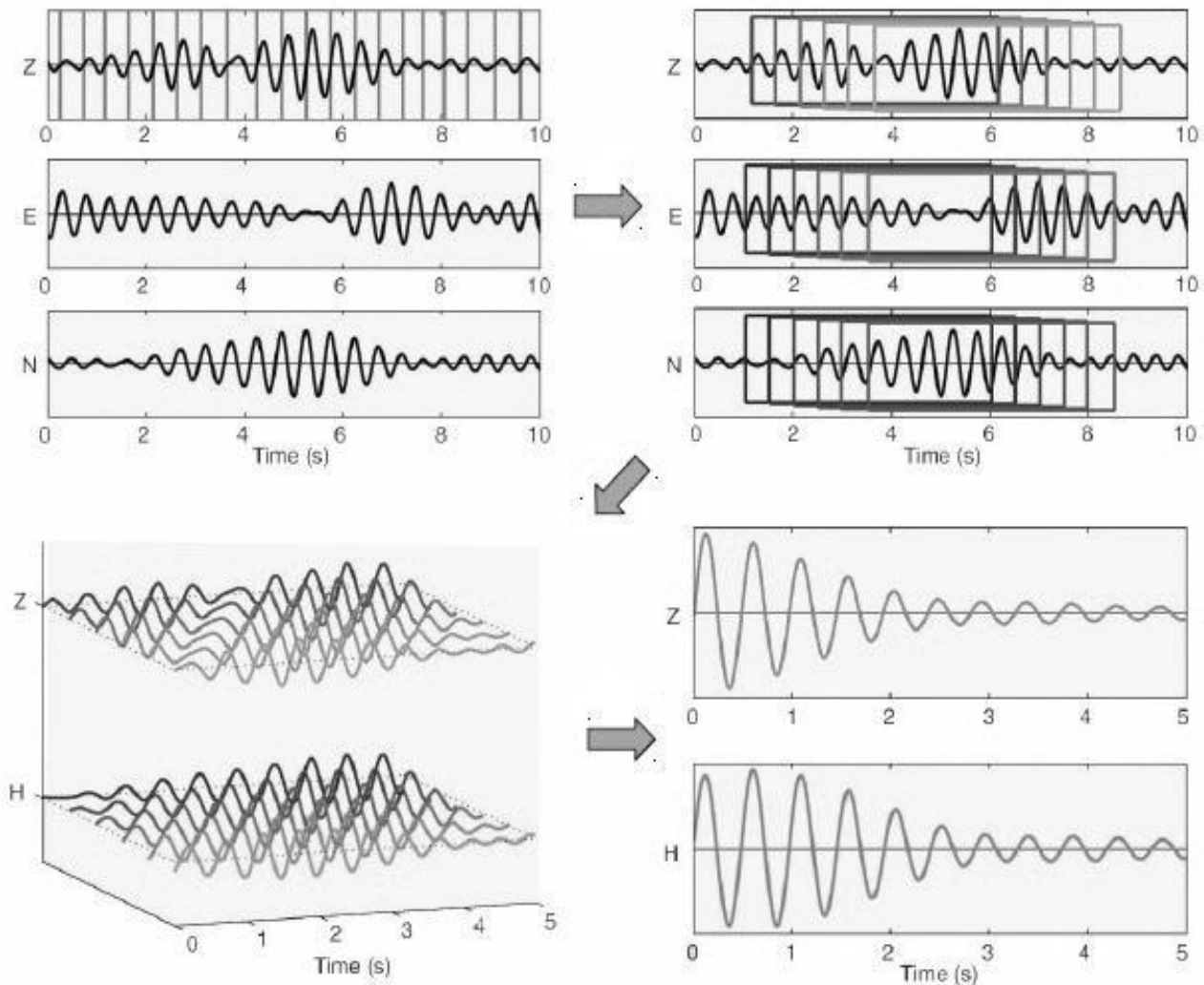


Figure 2-5: (top panel) At a given frequency narrow band f , signal blocks extracted on all three components for each detected zero crossing from negative to positive on the vertical component, the N and E components being phase-shifted by $\pi/2$. (bottom panel) The N and E signals are projected in the azimuth that maximizes the correlation with the vertical component to form the horizontal time blocks. All the vertical and horizontal signals are then summed, which yields a single vertical and horizontal signal. Next, the ellipticity at frequency f is measured from the energy of these summed signals (adapted from Hobiger, 2011).

Like the H/V method, RayDec method can also be applied on earthquake motions using the surface waves part of the recordings. Generally, surface waves can be extracted from coda parts of the earthquake, defined as the backscattering waves generated from heterogeneities in the earth that occur after the arrival of the main seismic waves (P and S). Zeng (2006) showed that even though the body waves are scattered at earlier arrival times, scattered surface waves become dominant when the source's distance increases. Also, the scattered surface waves will dominate even in earlier coda as the surface wave conversion mechanism appears in the shallow layers. Using RayDec method on coda waves (RayDecC) could thus be a new efficient tool to extract reliable Rayleigh waves ellipticity from the earthquakes.

For RayDecC method, I choose the Perron et al. (2018) formulation (originally by Aki 1969) to define the start time of the coda:

$$T_c = 4.6(T_S - T_p) + T_0 \text{ (eq. 2-3)}$$

where the T_p and T_S determine the P-wave and S-wave first arrivals and T_0 is the earthquake occurrence time. The end time of the coda, T_{end} , is defined as the time corresponding to 95% of the accumulated energy evaluated on the three components between T_p and the end of the record. To extract the Rayleigh waves ellipticity from seismic noise measurements, Hobiger (2011) suggested that a signal length of at least 300 seconds is necessary. However, he mentioned that even with only 120 seconds of recording, reliable ellipticity estimates can still be obtained.

For the application on earthquakes, the coda waves can be very limited depending on the type of seismicity. In such a case, I suggest keeping earthquake recordings for which at least one minute of coda is available to get at least one estimate of ellipticity with a minimum reliable frequency of 0.2 Hz, and then to average the estimated ellipticities over a large number of earthquakes.

2-2-3-2 Application

The FTAN and RayDec methods have been applied in several studies (e.g. Fah et al., 2003; Hobiger et al., 2013). From seismic noise data recorded on 14 European sites within the EU-NERIES project, Hobiger et al. (2013) performed joint inversion of Rayleigh wave ellipticity estimated at low frequency from RayDec and high-frequency dispersion curves and showed the ability of the ellipticity inversion in retrieving the V_s profile provided, however some other information/data about the soil properties. Nowadays, these methods are widely used in order to characterize and extract shear wave velocity in various sedimentary basins (e.g., Gouveia et al., 2016), at strong

motion stations (Hobiger et al., 2021a) and even on Mars planet seismic recordings (Knapmeyer-Endrun et al., 2017; Hobiger et al., 2021b)

2-2-3-3 Limitation

Ellipticity is considered as an efficient tool to estimate velocity profiles, but with some limitations. First of all, different velocity profiles can have the same ellipticity curve. Scaling the velocity profiles (depth, shear and pressure waves by the same factor) does not change the ellipticity function. It means that Rayleigh waves ellipticity curves should never be inverted without additional constraints as detailed in Hobiger et al., (2013).

The HVTFA and RayDec methods most of the time performs well in extracting the right flank of the fundamental mode of the Rayleigh wave ellipticity (Fäh et al., 2009; Poggi and Fäh, 2010; Hobiger et al., 2013; Gouveia et al., 2016; Knapmeyer-Endrun et al., 2017) since at higher frequency the noise wavefield is also composed of higher modes of Rayleigh waves which can be difficult for the HVTFA method and even impossible for RayDec method to properly identify and extract. The right flank of the ellipticity does however carry most of the information about the deepest soil layers structure (Fäh et al., 2001).

2-3 Array (multi-station) methods

In contrast to the single station methods, array methods are able to provide the direction of propagation and phase velocity of a seismic wave propagating across an array of sensors.

Array methods allow measurement of the dispersion curves of surface waves over a wider frequency range compared to the single-station RayDec or HVTFA methods that enables extraction of ellipticity estimates in a limited frequency range only beyond the fundamental resonance frequency of the soil. In the following sections, I detail the various methods used in this PhD, to extract dispersion curves of Rayleigh and Love surface waves from passive and active surface wave measurements.

2-3-1 Principles of the methods

2-3-1-2 The FK and RTBF passive array methods

When a seismic plane wave propagates across an array of sensors at a given frequency, the array output can basically be calculated by summing time shifted signals according to the time delays for the plane wave to reach each sensor. The location of the output's maximum (called beam power) in the wavenumber domain (kx, ky) provides an estimate of the phase velocity and the azimuth of the traveling waves across the array for the given frequency (Lacoss et al., 1969; Woods & Lintz 1973; Capon, 1969; Asten and Henstridge, 1984). This procedure is called F-K analysis. F-K analysis can be used both on active and passive array measurements. In active surface waves methods, the direction of the plane wave propagation is known (as the source location is known) and the beam output can be done by simple 2D transformation (from time-space to frequency-wavenumber, Park et al., 1999). Since the direction of the plane wave propagation is unknown in the seismic noise wavefield, the estimation of the phase velocity and azimuth can be done by doing a grid search in the wavenumber domain to search for the wavenumber vector that maximizes the array output.

To understand better the F-K method, let's consider a single harmonic plane wave signal propagating at station i:

$$x_i(t) = s(t - \vec{r}_i \vec{u}_o) \text{ (eq. 2-4)}$$

where x_i is the stations, s is the waveform which has the relative time shift depends on \vec{r}_i (stations position) and \vec{u}_o (slowness or velocity vector)

The signal propagates with the true slowness vector \vec{u}_o . Delaying the signal by a slowness vector \vec{u} gives:

$$\tilde{x}_i(t, \vec{u}) = s(t + \vec{r}_i(\vec{u} - \vec{u}_o)) \text{ (eq. 2-5)}$$

Summing up the delayed signals at different sensors according to the slowness vector \vec{u} , the beampower function $b(t, \vec{u})$ is then:

$$b(t, \vec{u}) = \frac{1}{N} \sum_{n=1}^N s(t + \vec{r}_i(\vec{u} - \vec{u}_o)) \text{ (eq. 2-6)}$$

where N is the number of sensors

Eq 2-6 can be written in the frequency domain:

$$P(\omega, \vec{u}) = \int_{-\infty}^{\infty} |B(\omega)|^2 d\omega = \int_{-\infty}^{\infty} \left| \frac{1}{N} \sum_{n=1}^N S(\omega) e^{j\omega \vec{r}_i \cdot (\vec{u} - \vec{u}_0)} \right|^2 d\omega = \int_{-\infty}^{\infty} |S(\omega)|^2 |B(\vec{k} - \vec{k}_0)|^2 d\omega \quad (\text{eq. 2-7})$$

In equation (2-7) $|B(\vec{k} - \vec{k}_0)|^2$ is called the beamforming array response. If $\vec{k} = \vec{k}_0$, then the beampower is maximized and the azimuth and propagation velocity of the plane wave can be estimated (equation 2-8 and 2-9; Figure 2-6):

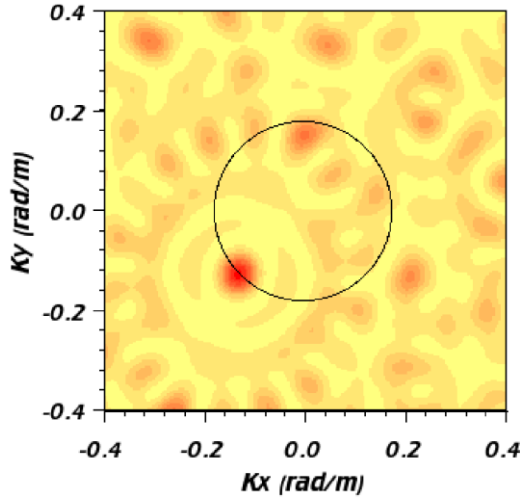


Figure 2-6: Example of array response from single time window f-k analysis result. The maximum beam power found at $\vec{k} = \vec{k}_0$ is shifted from the center

$$\theta = \left(\frac{k_y}{k_x} \right) \quad (\text{eq. 2-8})$$

$$v = \frac{\omega}{|\vec{k}|} \quad (\text{eq. 2-9})$$

Using the vertical component, the FK method (Lacoss et al., 1969; Woods & Lintz 1973) and also high-resolution FK methods (Capon, 1969) are widely used to extract the Rayleigh waves dispersion curves (see: Garofalo et al., 2016a). In order to exploit the full potential of three-component seismic noise recordings, Wathelet et al. (2018) proposed a high-resolution beamforming method (RTBF) allowing to extract both the Rayleigh wave dispersion curve and signed ellipticity. Following Poggi & Fäh (2010), the RTBF method also includes the estimation of Love waves dispersion curves by basically projecting the north and east components on the direction of propagation.

2-3-2 Array geometry and response

To design an optimized array configuration, Asten & Henstridge (1984) suggested the simple following criteria:

- the number of stations must be greater than the number of plane waves at any moment,
- the array diameter should be at least as large as the longest wavelength of interest and,
- the station spacing should be less than half the shortest wavelength for each direction.

Tokimatsu (1997) offered another formulation which became more popular based on the recommendations proposed by Sheu et al. (1988):

$$D_{\max} > \lambda_{\max}/3 \text{ (eq. 2-10)}$$

$$D_{\min} < \lambda_{\min}/2 \text{ (eq. 2-11)}$$

where the D_{\max} is the aperture of the array, D_{\min} is the interstation distance and λ_{\min} and λ_{\max} is the minimum and maximum wavelength.

In 2D array geometry, these limits (D_{\min} and D_{\max}) also depend on the azimuth of propagation of the waves crossing the array, which can be different from the maximum and minimum distance between receivers (Wathelet et al., 2008).

In order to better define the array resolution limits, the 2D array response function can be used.

$$R(k_x, k_y) = \frac{1}{n^2} \left| \sum_{i=1}^n e^{-j(k_x x_i + k_y y_i)} \right|^2 \text{ (eq. 2-12)}$$

where R is the 2D array response for the wavenumber K_x and K_y in 2D plane along the x and y directions.

From this equation, the theoretical resolution and aliasing limits are directly derived from the array response illustrated in Figure 2-7: k_{\min} is used to quantify the array resolution and is defined as the capability of the array to separate two close wavenumbers. The resolution limit is defined as the radius of the central peak measured at the mid-height (0.5) of the theoretical array response (Figure 2-7). The wavenumber related to the occurrence of aliasing, k_{\max} , is identified from the most prominent side lobes in the array response. k_{\max} is classically defined as the lowest wavenumber for which a sidelobe reaches at least an amplitude of 0.5 (Figure 2-7).

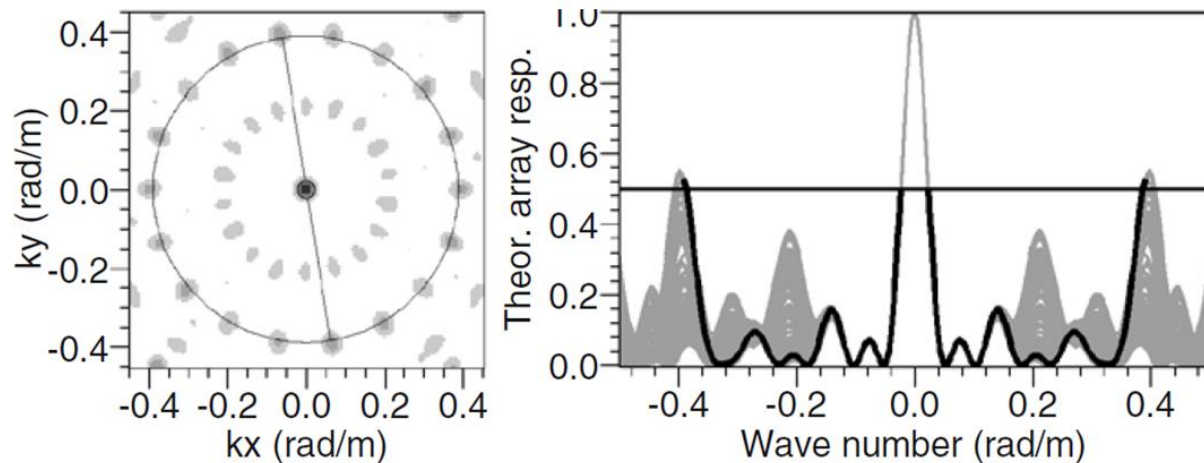


Figure 2-7: (left) Theoretical frequency–wavenumber array responses and (left) the 2D section across an azimuth of the theoretical frequency–wavenumber determining k_{min} (here at 0.04 rad/m) and k_{max} (here at ± 0.4 rad/m) (adapted from Foti et al., 2018).

2-3-3 Processing and retrieved results (dispersion curve – signed ellipticity)

2-3-3-1 Dispersion Curve

As briefly mentioned, Wathelet et al. (2018) presented a new method for obtaining dispersion curves and signed ellipticity using Rayleigh wave three-component beamforming (RTBF), which is the method used in this PhD implemented in the Geopsy software (Wathelet et al., 2020). To retrieve dispersion curves using RTBF algorithm, ambient noise must be simultaneously recorded by 3 component sensors at multiple sites and like any array studies, the array response can be calculated based on the array geometry to get the array resolution limits (Figure 2-8).

The RTBF algorithm is then applied at each frequency narrow band splitting the time series in windows whose length is inversely proportional to the center frequency. The output of the RTBF array processing provides many parameters including for each frequency: the absolute start time of the window, the center frequency, the polarization (Love or Rayleigh), the slowness, the azimuth of the wave propagation and the ellipticity (for Rayleigh wave). Finally, the final dispersion curve can be picked (manually or automatically) from the probability density function (PDF) of the samples in the frequency-phase velocity domain (Figure 2-9).

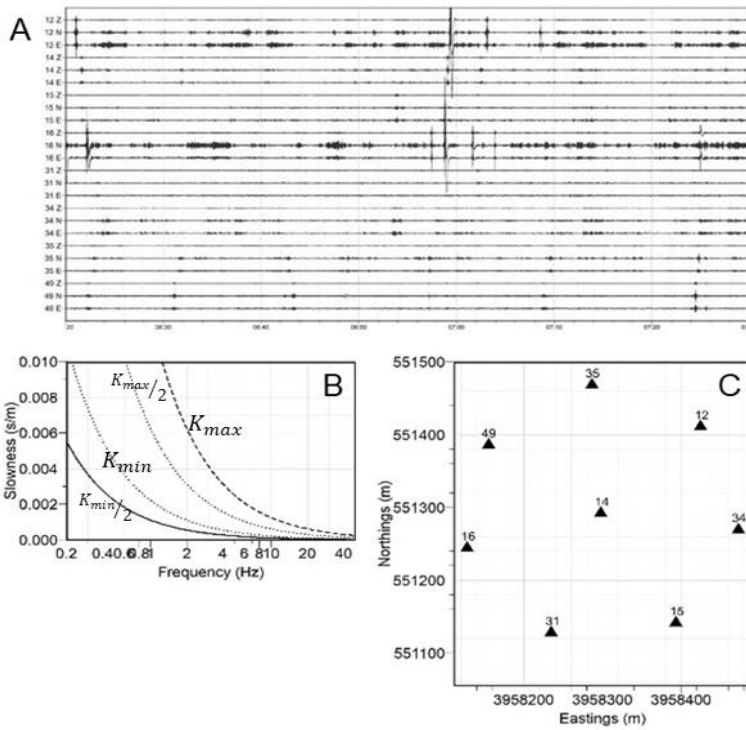


Figure 2-8: A) ambient noise signals recorded at 8 station simultaneously. B) the array limits (k_{max} , k_{min} , $k_{max}/2$ and $k_{min}/2$) and C) the array geometry.

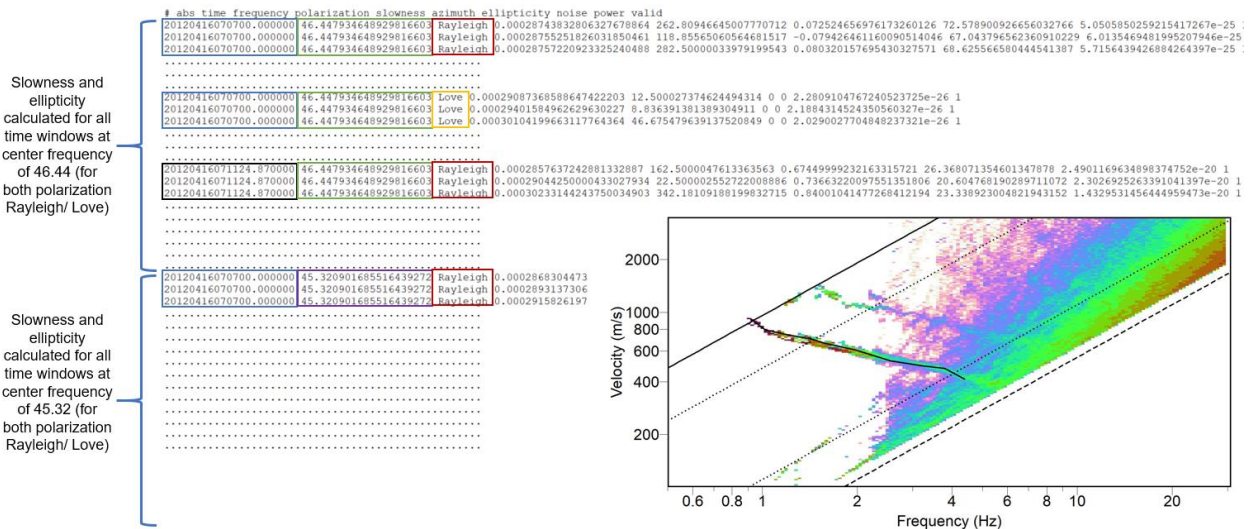


Figure 2-9: A) Schematic view of an array analysis output file. For each time windows, slowness (1/phase velocity) can be extracted for Rayleigh and Love waves. For Rayleigh waves, the corresponding ellipticity values can also be determined. B) The manual picking of a dispersion curve (black curve) from the PDF frequency-Rayleigh velocity.

2-3-3-2 Signed ellipticity

The basic concept of signed ellipticity relies on radial decomposition of the propagating Rayleigh waves. In this situation, the ellipticity can be identified as the amplitude ratio between the horizontal-radial and the vertical F-K power-spectra of the three component F-K analysis.

There are some benefits using three-component array methods to obtain ellipticities rather than single station methods. First, array methods enable the estimation of Rayleigh wave ellipticity over a wider frequency range for each identified Rayleigh wave mode. Second, the sense of rotation of the Rayleigh waves can be extracted (Figure 2-10). The particle motion can retrograde (indicated by negative angle values) or prograde (indicated by positive angle values). This additional information can be very useful in the inversion of Rayleigh wave ellipticity to better constrain the impedance contrast between soil layers that produce change of sense of rotation and singularities.

Similar to dispersion curves, the ellipticity can be easily extracted from the PDF of ellipticity estimates.

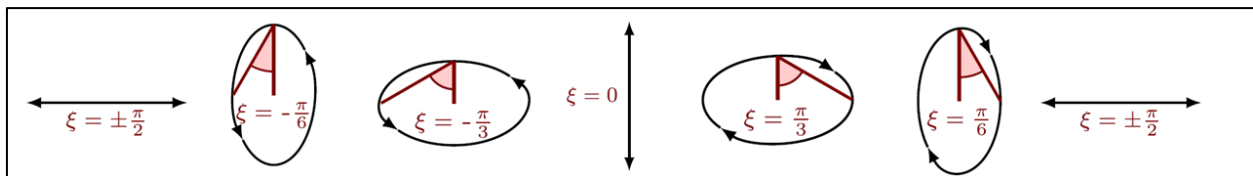


Figure 2-10: Representation of ellipticity angle (ξ) for different prograde/retrograde values. Ellipticity angle can be varies between $\pm \frac{\pi}{2}$ (adapted from Marano et al., 2012).

2-3-4 Active array method: MASW

Besides passive array methods, Multichannel Analysis of Surface Wave (MASW) popularized by Park et al., (1999) is generally used for retrieving the high-frequency part of the dispersion curves. In this method, the waves are generated by hitting the ground using vibroseis, sledgehammer or other impulsive source which are recorded by multiple geophones evenly spaced along a survey line. With this approach, surface waves can be extracted to determine the very near-surface shear wave velocity profile, typically up to ten to twenty meters (Renalier, 2010).

2-3-4-1 Processing and retrieved results

The MASW method can be divided into three steps.

As a first step, for the source, it is important that the energy provided by the seismic source penetrates over the required frequency range covering the targeted investigation depth. Since the wavelength is determined by both the frequency and the phase velocity, it should be preliminary

guessed before choosing the source to ensure that the seismic survey provides useful data. One of the most commonly used seismic sources is a sledgehammer striking on a metal plate. For best results, the weight of the sledgehammer should be at least 5 kg, with an 8 kg sledgehammer being the most commonly used choice (Foti et al., 2018).

For receivers, vertical geophones with cut-off frequency of 4.5 Hz is the most common receiver used for shallow targets. The receivers are linearly placed on the surface and the impulsive source generates a seismic wave that propagates through the line of receivers.

It is recommended to perform multiple shots to increase the signal-to-noise ratio and hence to improve the phase velocity estimation. Typically, at least three different shot offsets are also recommended, with two shot offsets at both extremities of the profile and one in the profile center. Figure 2-11 shows the schematic view of data acquisition of MASW method. The other parameters such as receiver spacing (dx), receiver spread (L) and source offset (X_1) also impact the investigation depths (Park et al., 2002; Foti et al., 2018). Suggested values of receiver spacing (dx) for near-surface characterization range from 0.5 to 4 m. Also, since the surface wave becomes planar only after traveling a certain distance from the source, X_1 should be large enough (depends on the longest wavelength) to avoid near-field effect (O’Neil, 2004).

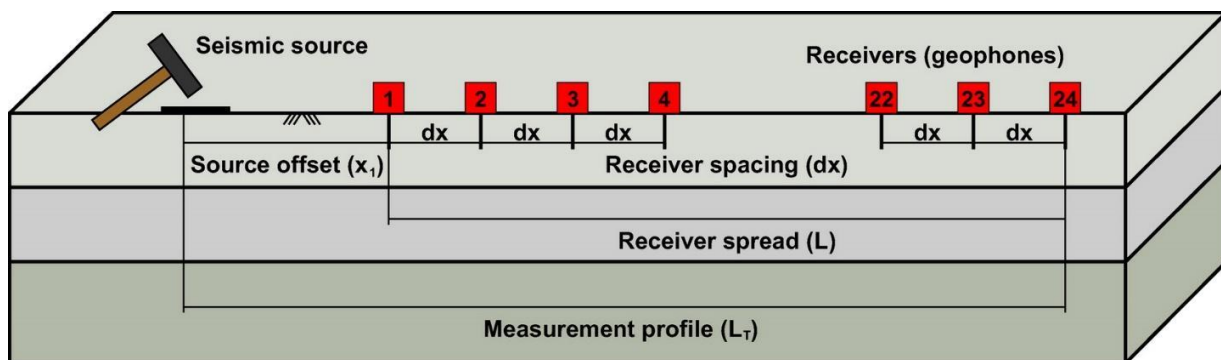


Figure 2-11: Schematic view of data acquisition for MASW method (adapted from Olafsdottir et al., 2019).

For processing, a 2D wavefield transformation is used to convert the raw field data from the time-offset (T-X) domain to the frequency-wavenumber (F-K) domain. This involved applying a 2D Fourier transform over time and distance, resulting in the wavefield represented in the frequency-wavenumber (F-K) domain (Figure 2-12). The F-K spectrum can be expressed as a sum of modal contributions as follows (Tselentis and Delis, 1998):

$$F(f, k) = \sum_m S_m(f) \cdot [\sum_{n=1}^N e^{-\alpha_m(f) \cdot x_n} \cdot e^{-i(k - k_m(f)) \cdot x_n}] \text{ (eq 2-13)}$$

where S_m is the source function, N is the number of geophones, x_n the distance from the source of the n th receiver, α_m and k_m are respectively attenuation and wavenumber for the m^{th} mode.

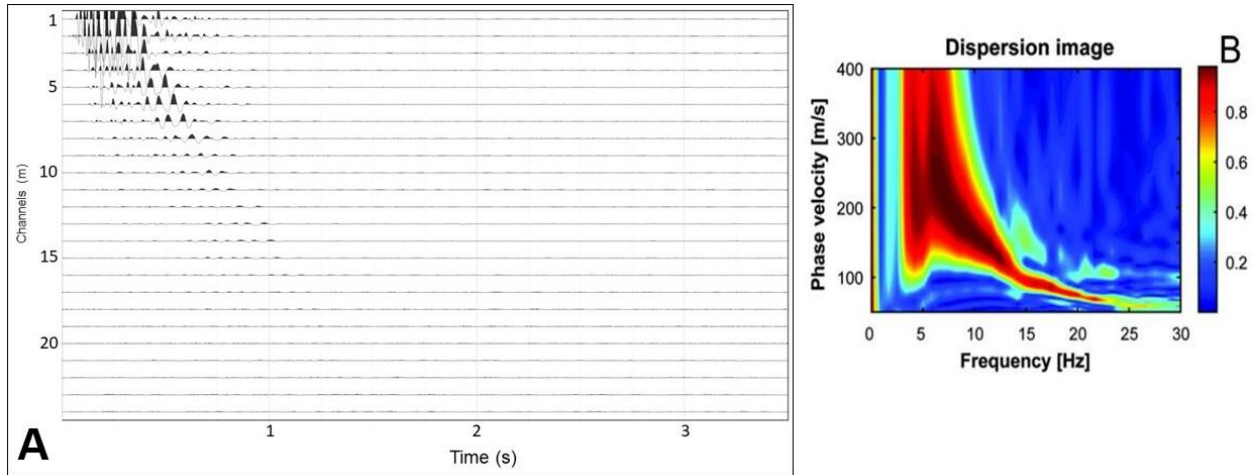


Figure 2-12: Schematic view of 2D wavefield transformation of A) time-offset (T-X) domain to B) frequency-wavenumber (F-K) domain.

2-3-4-2 Application and limitation

MASW can be used for both Rayleigh and Love wave phase velocity estimates, depending on the type of excitation. MASW is typically used for two main applications. The first involves extracting V_{s30} directly from the inversion of the high frequency dispersion curve (if the maximum measured wavelength is large enough to enable reaching such a depth), while the second involves the refinement of the high frequency part of the dispersion curve in addition to passive array methods when the estimation of dispersion curves over a broad-band frequency band is targeted. In this study, I focused on the second application of MASW and tried to extract high frequency dispersion curves of the Rayleigh waves in Tehran's basin.

2-4 Inversion

Extracting one-dimensional shear wave velocity profiles from surface wave dispersion curves is a classic inversion problem in geophysics (Herrmann, 1973). The inversion of surface waves relies on finding the best-layered earth models whose theoretical dispersion curves have the lowest misfit/error compared with the experimental data (Wathelet et al., 2004). However, the ill-posed

nature of the problem and its non-linearity make that there is no unique answer to these problems (e.g., Cox and Teague, 2016, Foti et al., 2018).

2-4-1 Principles and main inversion methods

Initially, local search algorithms were proposed to solve inversion problems, which requires an initial earth model. Although such methods are highly efficient in terms of computation time, they may converge to a local minimum instead of the global minimum of the misfit function. This occurs because the search for the optimal solution is restricted to a small region around the initial model (Socco et al., 2010).

Another approach is to use global search algorithms such as Monte Carlo method (Socco and Boiero, 2008), Genetic Algorithm (Yamakana and Ishiada, 1996), Simulated annealing (Beatty et al., 2002), Neighborhood algorithm (Sambridge et al., 1999; Wathelet, 2004) and etc. In such algorithms, a large number of initial models are used and the search is performed over the entire parameter space to find theoretical models of the earth's structure that reproduce the observed dispersion data with the least error quantified through the misfit function (Wathelet et al., 2004).

2-4-2 Neighborhood algorithm and ground model parameterization

In this study, the conditional neighborhood algorithm, which is implemented in the *dinver* module of Geopsy software, is used for inversion processing (www.geopsy.org; last access: 01/01/2023; Sambridge et al., 1999a, b; Wathelet, 2004).

The basic idea of this algorithm is to generate a set of earth's model samples at each iteration, with the sampling density function derived from all previous models using the neighborhood approximation (NA). In NA the parameter space is thus divided into Voronoi cells using previous best models in terms of lowest misfits in such a way that the prior samples' knowledge drives the search for new models.

The Voronoi cells are defined by the following parameters (Figure 2-13):

- n_{s0} is the number of models chosen randomly inside the parameter space at the beginning of the inversion;
- n_r is the number of best cells (with the lowest misfit) where the n_s models are generated;
- n_s is the number of models to generate at each iteration.

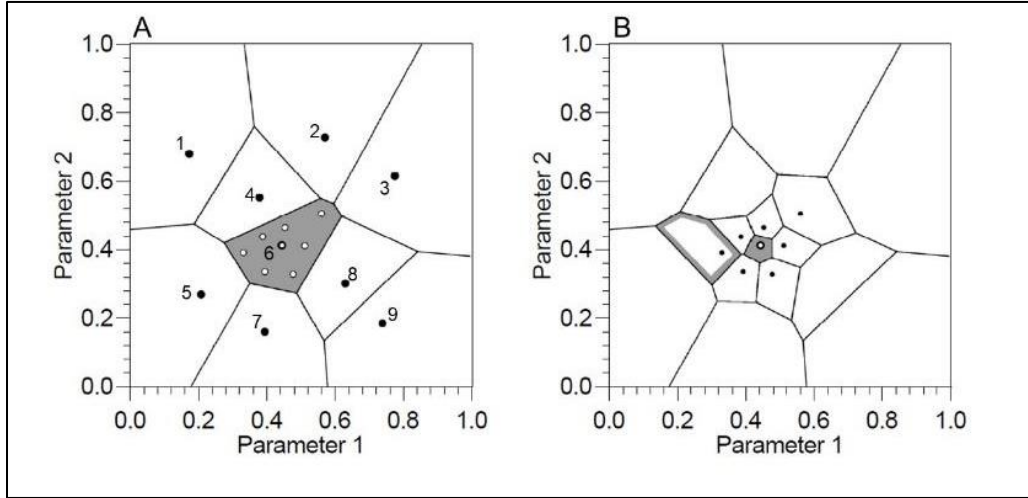


Figure 2-13: Example of Voronoi cells for a two-dimensional parameter space. A) The first iteration with $n_{s0} = 9$ leads to find the cell with the lowest misfit (cell number 6). B) the cell number 6 is divided to $n_s=7$ new cells to search for minimum misfit for the second iteration.

In the conditional neighborhood algorithm (Wathelet et al., 2004), the misfit function is defined as:

$$misfit_{dc} = \sqrt{\sum_{i=1}^{n_F} \frac{(x_{di} - x_{ci})^2}{\sigma_i^2 n_F}} \quad (\text{eq 2-14})$$

where x_{di} is the measured phase velocity at frequency f_i , x_{ci} is the forward-modeled phase velocity at frequency f_i , σ_i^2 is the uncertainty of the phase velocity and n_F is the number of frequency samples.

Note also that as in any inversion global algorithms, there is no single solution for S-wave profiles. This is the reason why it is useful to represent the set of inverted S-wave profiles instead of the best misfit one in order to better picture the S-wave velocity structure and identify the depth ranges that are the best constrained according to a given misfit value (Figure 2-14).

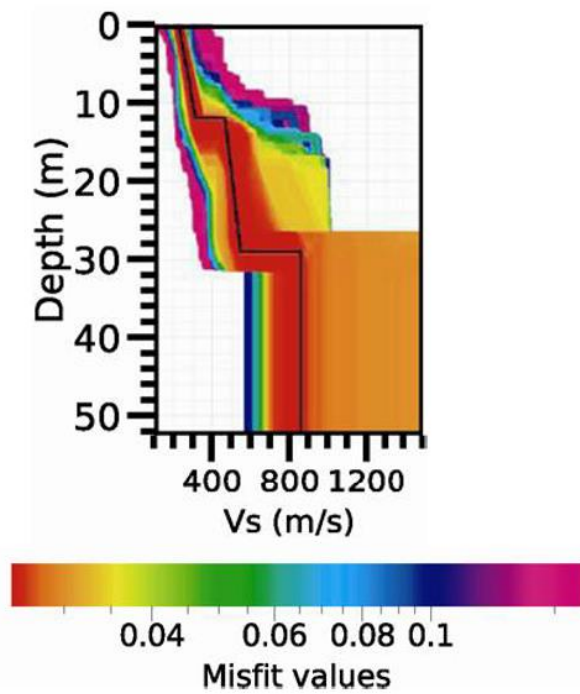


Figure 2-14: Example of inversion with parameterization involving two layers with linear increase of V_s with depth over half space. The black V_s profile indicates the theoretical V_s profile while the inverted V_s profiles are indicated in color. The color scale depends on the misfit values (adapted from Renalier, 2010).

In Geopsy, the inversion requires an initial ground model parameterization consisting of homogeneous linear elastic layers over a half-space, namely: number of layers and possible range of thickness, density, S-wave and P-wave velocity in each layer. Since dispersion curves are very slightly sensitive to density, density is most often fixed to a representative value depending on the geology of the site under study. The ratio between P-wave and S-wave velocities are constrained by the Poisson ratio whose range can be defined in the inversion (generally from 0.2 to 0.5, unless some specific information on the site is known).

Despite the fact that the parametrization is a user task, several studies have been done to make the process more systematic or rule-based (Renalier, 2010; Di Giulio et al., 2012; Cox and Tague, 2016). These studies indicate that a limited number of layers (from 3 to 5) is usually sufficient to get a good agreement between the measured and forward models dispersion data.

Additionally, to estimate the ground model parameterization, the correlation between the phase velocity of Rayleigh waves and the S-wave velocity can also be utilized. This correlation can provide an initial approximation of the S-wave velocity parametrization. Xia et al. (1999) estimated

the difference between Rayleigh wave phase velocity and the S-wave velocity to be about 10 to 15%, defining the following relationship for this ratio, where ν is defined as Poisson ratio.

$$V_S = \frac{(1+\nu)}{(0.874+1.117\nu)} V_R \text{ (eq. 2-15)}$$

The minimum and maximum measured wavelength can also be used to constrain the ground model parameterization. Typically, the maximum resolvable depth is indeed about one-third to half of the maximum wavelength and the minimum layer thickness is related to about half of the minimum measured wavelength (Cox and Tague, 2016; Foti et al., 2018)

In addition to the information provided by the mentioned approaches, a priori information on the geological conditions of the studied area can be crucial to have robust parameterization. The thickness, density and properties of the subsurface layers can be estimated based on known geological data, such as geological maps, borehole logs or even previous seismic surveys. Incorporating this prior knowledge into the parameterization constrains the range of acceptable models and reduce the uncertainty in the inversion process.

2-4-3 Combined inversion and penetration depth

The schematic figure presented in Figure 2-15 is intended to sketch the importance of utilizing joint inversion. In fact, each individual processing methods only covers a part of the frequency or wavelength range. The uncertainties in the inversion process will be reduced when dispersion estimates are available for the whole frequency/wavelength range target covered. However, it is often impossible to obtain dispersion data over the entire frequency band with a single method, particularly at low frequency for deep sedimentary basins corresponding to geological layers close to the interface between sediments and seismic bedrock. Therefore, joint inversion is essential to combine the data from different methods and cover a broad frequency/wavelength range, which can help reduce uncertainties and improve the accuracy of the inversion results (Figure 2-15).

In this regard, MASW provides information of the shallowest geological layers with measured wavelength typically ranging between a couple of meters and 100 m (Renalier, 2010; Foti et al., 2018). Passive arrays can provide dispersion estimates up to wavelength of 1000 m depending on the array geometry and the noise wavefield content (Renalier, 2010; Foti et al., 2018).

In deep sedimentary basins, the ellipticity curves and H/V fundamental resonance frequency below 1 Hz can also provide additional constraints up to seismological bedrock.

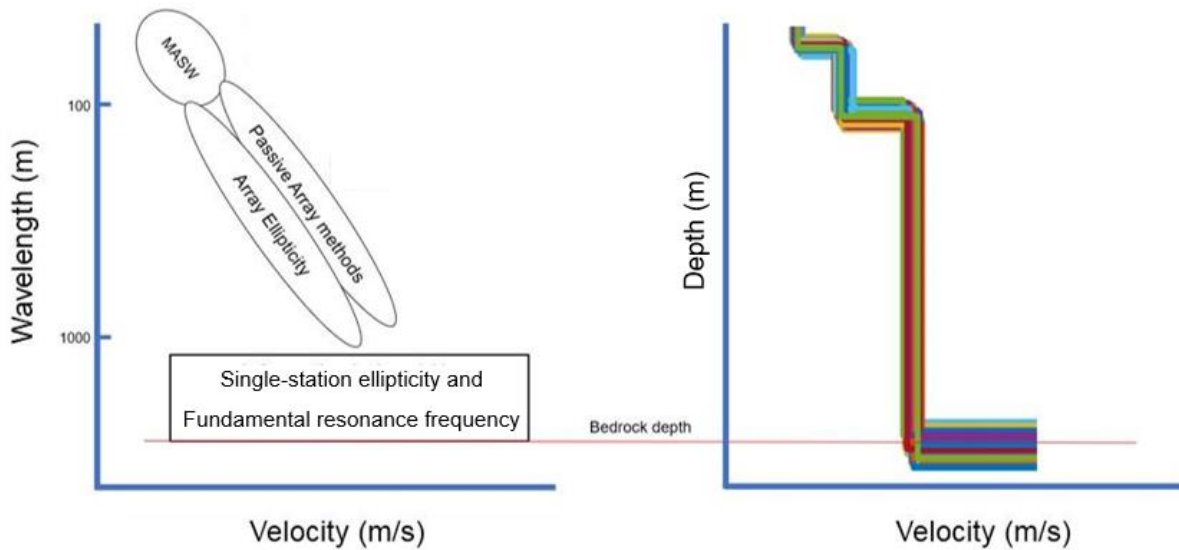


Figure 2-15: Schematic view of the contribution of each method in the frequency/wavelength domain.

2-5 Conclusion

This chapter has provided the necessary methods and data required to construct the 3D velocity structure model of Tehran's basin. The RTBF method can be used to extract both Rayleigh and Love waves dispersion curves together with the signed ellipticity of Rayleigh waves in the intermediate frequency range, typically from 1 Hz to 20 Hz. The MASW method can also be used to extract the high-frequency dispersion curves sensitive to the stiffness of the most superficial layers, while the RayDec and RayDecC methods can be used to extract the most reliable ellipticity curves at low frequency. All these data can then be jointly inverted to get shear wave velocity profiles. Using H/V, I can find the fundamental resonance frequency of the soil (f_0) and use empirical relationships between the f_0 and the depth to the seismic bedrock (h). In the upcoming chapter, I will soon see how all these methods work in practice. for the Tehran's basin.

CHAPTER 3

3D velocity structure of Tehran's basin

General Introduction

The construction of the three-dimensional velocity structure is the essential ingredient for conducting seismic response analysis. However, In Tehran, this task remains unaccomplished due to several challenges. Primarily, the lack of enough resources to conduct big campaigns of experimental studies is a significant challenge in constructing the velocity structure. Additionally, the deep structure of Tehran basin poses difficulties in using traditional geotechnical. According to this issue, even the deepest borehole in Tehran, (see: JICA and CEST, (2000) for more detail), was not able to reach the bedrock depth.

Therefore, it seems that non-invasive methods become the only feasible option for constructing a three-dimensional velocity structure in Tehran. Non-invasive methods, as discussed in the preceding chapter, are the sets of methods mainly involve seismic ambient noise recordings at one or multiple stations. Developed during the last 30 years (SESAME, 2001-2004; Bard et al., 2006; NERIES, 2006-2010; Garofalo et al., 2016a, b) these methods have shown their capabilities to retrieve main site parameters used to characterize the site response.

So, this chapter aim to construct the first ever velocity structure by integrating extensive geophysical surveys, geotechnical and geological data. Written mostly as a paper, this chapter devoted to construct the model and introduce representative V_s and V_p for sediments and seismic bedrock to be further used for seismic ground motion prediction in Tehran's basin.

3D shear-wave velocity model of Tehran's (Iran) sedimentary basin by means of geotechnical, geological and geophysical data

Authors

Saeed Soltani^{a,b,*}, Ebrahim Haghshenas^c, Bertrand Guillier^d, Cécile Cornou^d

Affiliation

a- Ph.D. Student, International Institute of Earthquake engineering and Seismology (IIEES), Tehran, Iran

b- Ph.D. Student, Univ. Grenoble Alpes/CNRS/IRD/IFSTTAR, ISTerre, Grenoble, France

c- Ph.D. International Institute of Earthquake engineering and Seismology (IIEES), Tehran, Iran

d- Ph.D. Univ. Grenoble Alpes/CNRS/IRD/IFSTTAR, ISTerre, Grenoble, France

* Corresponding author:

E-mail address: saeed.soltani@univ-grenoble-alpes.fr

Abstract

Tehran's basin (Iran) is located in the central Alborz seismic zone, a region with very high seismicity due to the existence of numerous large active faults. According to the model proposed by Engalenc (1968) the Plio-Quaternary alluviums of Tehran consist in homogenous cemented conglomerates estimated up to 1000 m thick. In the city of Tehran, analysis of earthquakes recorded by a temporary seismological experiment (Haghshenas, 2005) has outlined a significant amplification of ground motion (up to 7-8) over a wide frequency range from about 0.4 Hz to 3 Hz. Haghshenas (2005) suggested that such amplification is due to the existence of thick alluvial deposits and the presence of strong lateral discontinuities leading to multidimensional site effects. In order to better understand and predict the effects of the geometry and mechanical properties of the surface ground motion in Tehran, we developed a 3D shear-wave velocity model of the Teheran's basin by integrating all available geophysical, seismological and geological data. Geological data include 197 available geotechnical or geological logs within Tehran city. Geophysical data comprise 33 seismic ambient noise arrays and 13 active surface waves profiles

in order to derive shear-wave velocity profiles. Finally, 575 single-station seismic ambient noise recordings have been also integrated. Shear-wave velocity down to the deep seismic bedrock was derived by joint inversion of Rayleigh and Love wave dispersion curves, ellipticity of Rayleigh waves and fundamental resonance frequency. The final three-dimensional structure of the basin is then achieved by integrating the geological and geophysical information. This model outlines a large variation in the seismic bedrock depth (from about 90 m to about 900 m) with strong lateral variation from the northeast to southwest of the basin.

Keywords

3D geological model

Ambient seismic noise

Surface waves inversion

Tehran sedimentary basin

Resonance frequency

Introduction

Tehran region is located in one of the most tectonically active regions in Iran, due to dynamic deformations inside the Arabia–Eurasia collision zone (Allen et al., 2003). According to the latest Earthquake Model of the Middle East (Giardini et al., 2018) the peak ground acceleration (PGA) with 10% probability of being exceeded in 50 years at outcropping rock is estimated around 0.5 g in the Tehran region, which positions Tehran as one of the most earthquake-prone large metropolises in the Middle East. Filled in by alluvial deposits coming from the erosion of the southern slopes of the Alborz Mountain range, Tehran basin also faces large surface ground motion amplification (site effects). The first site effect study in Tehran (JICA and CEST, 2000) was done by the Japan International Cooperation Agency (JICA) and the Centre for Earthquake and Environmental Studies of Tehran Municipality (CEST). In this study, soil profiles, based on N-SPT values, down to the engineering bedrock indicated the deepest soil profile to be 150 meters depth in south of Tehran with low-to-moderate 1D site amplification throughout the city. However, Haghshenas (2005) installed seismological stations from February to June 2002 at different sites in Tehran city, including two stations on outcropping rock in the north and southeast of the Tehran's basin. Empirical site amplification computed from earthquake recordings using the site-to-reference method (Borcherdt, 1970) revealed a significant ground motion amplification over a broad frequency range, from very low frequencies around 0.4 Hz to about 3 Hz, suggesting significant 2D/3D site effects due to basin-edge diffracted surface waves at lateral discontinuities as observed in other basins (e.g., Field, 1996; Cornou and Bard, 2003; Smerzini et al., 2011; Theodulidis et al., 2018) and a rather deep sedimentary basin. The observed amplifications were larger for the sites located in the southern part of the city compared to the northern area (Figure 3-1).

Despite the importance of site effects in Tehran, most of the current knowledge on the geometry and geology of the Tehran basin comes from ancient geological studies (Rieben, 1955; Engalenc, 1968; Tchalenko et al., 1974). Relying on structural geology, these studies determined the stratigraphy and formations of Quaternary alluviums in Tehran. More recently, some studies focused on the morphotectonic of the Tehran region and the detailed mapping of the faults and folds in quaternary deposits by combining aerial photos and new field investigations (Abbassi and Farbod, 2009; Soleymani Azad et al., 2011). The use of earthquake recordings (Shirzad et al., 2019;

SoltaniMoghadam et al., 2019) or seismic ambient noise (Shirzad and Shomali., 2014; Asadi et al., 2017) have allowed to derive P- or S-wave velocity structure for the region of Tehran. These velocity structures outlined the presence of stiff sedimentary materials and a deepening of the seismic bedrock up to 1.4 km depth in the southwest part of the basin, with however a too limited resolution to enable deriving a robust 3D velocity model of the alluvial deposits within the Tehran's basin. Also, the lack of detailed velocity model prevents any ground motion prediction to properly account for local site effects (Zafarani et al., 2013; Hamzehloo et al., 2007; Jalalhoseini et al., 2018).

The objective of this paper is thus to develop a 3D shear-wave velocity model of the Tehran basin to be further used for seismic ground motion prediction in Tehran's basin. The use of seismic ambient noise with single-station methods such as H/V (see Molnar et al., 2022 for a recent review) or array methods (e.g., Foti et al., 2018; Socco and Strobbia., 2004) has been proved to be very efficient for retrieving the fundamental resonance frequencies and shear-wave velocity profiles in sedimentary areas (e.g., Zor et al., 2010; Manakou et al., 2010; Cushing et al., 2020; Panzera et al., 2022). However, Haghshenas et al., (2008) shows that Tehran is one of the very few deep sedimentary basins for which the H/V method sometimes fails to predict the fundamental resonance frequency around 0.3-0.4 Hz, H/V curves being flat at low frequency, contrary to H/V curves or empirical site amplification derived from earthquake recordings. Difficulties in interpreting H/V at low frequency could be attributed to strong 3D site effects (e.g., Maresca et al., 2006; Haghshenas et al., 2008; Uebayashi et al., 2012; Le Roux et al., 2012) or a lack of energy of the seismic noise at low frequency (Haghshenas et al., 2008).

In this paper, we used a large set of geotechnical, geophysical and seismological data already available through past studies or that we collected, namely 575 single-station seismic ambient noise measurements, 33 seismic noise array measurements, 13 active seismic surface waves (MASW) profiles, 197 geotechnical boreholes and 13 sites with earthquake/noise recordings. These data were combined to derive a seismic bedrock depth map and the shear-wave velocity layering for the Tehran's basin, while carefully taking care of the capability of the seismic noise properties to extract robust surface waves dispersion estimates (Rayleigh and Love wave dispersion curves, Rayleigh wave ellipticities), especially at low frequency (< 1 Hz). These geophysical results are then compared and combined to develop a geological model in terms of quaternary geological units and faulting systems, to finally derive a 3D velocity model for the sedimentary basin of Tehran.

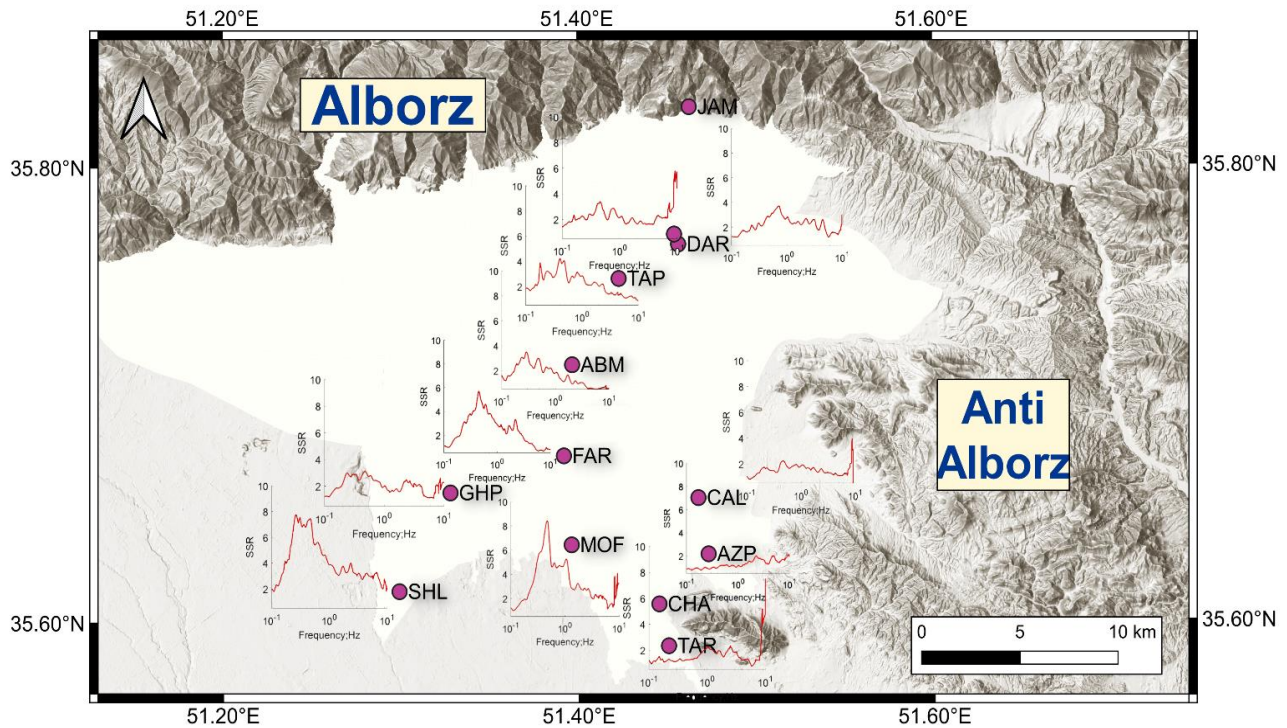


Figure 3-1: Site amplification (site-to-reference spectral ratio) results of temporary seismological network in Tehran, with JAM as the reference station. The highest amplification values, reaching up to 8, are observed at MOF and SHL stations in south and southwest areas (re-drawn after Haghshenas 2005).

3-1 Tectonic, geological and geophysical settings

3-1-1 Tectonic settings

In northern Iran, the Alborz Mountain range has been formed by compressional deformation under large tectonic stresses due to the northward convergence of central Iran toward Eurasia (Allen et al., 2003). Tehran is situated in the southern flank of the central Alborz Mountains (Figure 3-2A) which, according to Vernant et al. (2004), absorbs 8 mm/year of the overall 14 mm/year shortening rate between the central Iranian block and Eurasia. On the eastern margin of the basin stand the Anti-Alborz Mountains (Figure 3-2B) which have a different structure from the Alborz Mountains, the former formed as an anticlinal structure with a Paleozoic core and the latter formed during Alpine orogeny in Cretaceous (Dellenbach, 1964).

In this area, the activity of both thrust and left lateral faults is fully compatible with the internal deformation of central Alborz (Allen et al., 2003). The faults that are located within a 150 km

radius from the metropolitan city of Tehran (Figure 3-2A) appear to be the result of the geodynamic regime in this area (Jackson et al., 2002; Ritz et al., 2006). Even though the current seismicity in central Alborz is low (Ashtari et al., 2005; Tatar et al., 2012), many historical and recent destructive earthquakes occurred in this region (Ambraseys and Melville, 1982), while paleoseismological studies (Nazari et al., 2009; Ritz et al., 2012) revealed ancient earthquakes for this region (Figure 3-2A) as synthesized by Berberian and Yeats (2018).

Beside central Alborz, numerous faults also pass through the Tehran basin. Table 3-1 summarizes the recent efforts from TDMMO (Tehran Disaster Mitigation and Management Organization) and IIEES (International Institute of Earthquake Engineering and Seismology) to characterize the Tehran basin active faults (Abbassi and Mokhtari, 2020; Figure 3-2B).

The North Tehran Fault (NTF) has been probably the most controversial fault structure in the Tehran basin in terms of structuring geometry and actual seismogenic activity. Engalenc (1968) and Tchalenko (1975) believe that NTF is not a single fault trace and consists on left-stepping en-echelon faults. In contrast, some authors assumed the NTF as a single, low-angle north dipping fault (Berberian and Yeats, 1999; Allen et al., 2003). Generally, NTF is defined from the junction of the Mosha fault eastward to Kazem Abad neighborhood (Karaj) westward. In the studied area (north Tehran), NTF makes the boundary between rock formation and alluvium and seems to be not active (Abbassi and Farbod, 2009) because of the local high Mountain sinuosity index (Silva et al., 2003) and the lack of formation of very recent alluvial fans in this region (Abbassi and Farbod, 2009). However, some authors believed that the activity of the central NTF is actually transferred to the left-lateral strike-slip Niavaran fault, inside the Tehran basin (Figure 3-2B), since the Niavaran fault is cutting the quaternary alluvial deposits on the western parts of the fault (Abbassi and Farbod, 2009).

Ritz et al. (2012) proposed that some active faults in the central parts of the basin are secondary structures of NTF, interpreted as folds or elongated low ridges controlled by shortening component of the fault zone (Bayasgalan et al., 1999). For Pardisan Fault (Figure 3-2B), Talebian et al. (2016) estimated the slip-rates of at least 1 mm/year using optically stimulated luminescence, but they could not give any direct information about the seismogenic potential of this thrust fault. Close to the Pardisan Fault, there is evidence of a north-dipping east-west trending fault called Tarasht Fault (Figure 3-2B) which is recognized on some outcrops cutting young alluvial fans. However, the eastern parts of this fault are not well recognizable due to the city's expansion (Abbassi and

Shabanian, 1999). These north-dipping central faults, like Pardisan, Tarasht and the south-dipping Lavizan thrust fault, have played an important role in uplifting the central parts of the piedmont because these faults cut through the Late Pleistocene alluvial sediments in some outcrops (Abbassi and Farbod, 2009). There is also some evidence for local horst-and-graben structure at center of basin, constructed by parallel minor faults. Finally, some north and northwest trending faults clearly affect the deposits as reverse and normal faults (e.g., TV-Fault, Bagh-e Feyz Fault and Vanak Faults; Abbassi and Farbod, 2009; Figure 3-2B).

In the south of Tehran, Nazari et al. (2010) observed that the North Ray, South Ray, and Kahrizak Faults align with ancient shorelines, indicating that they may have resulted from erosional processes rather than tectonic activity. However, the nature and origin of the faults in the south of Tehran are still under discussion and further research is needed to fully understand their characteristics.

Table 3-1: Tehran's active faults with their lengths from [46]. NTF: North Tehran Fault.

Name	Length (km)	Name	Length (km)	Name	Length (km)	Name	Length (km)	Name	Length (km)
Abas Abad	3.5	Davoudieh	1.5	Kahrizak ³	35	North Ray ³	18.5	Tanbakoee	2
BagheFeyz	4	Enghelab ¹	35	Kaj ¹	3.5	NTF	75	Tarasht	6.5
Beheshti ¹	1.5	Evin ¹	3.5	Lavizan	25	South Ray ³	16.5	TV	3.3
BouAli ¹	1.5	Farahzad ¹	25	Narmak	2.65	Sohanak ¹	3.5	VanakPark	4.5
Chitgar ²	?	IranPars ¹	1.5	Nivaran	14	TakhtTavous	1.5	Velenjak*	1

¹ NTF Segments

² Fault Zone

³ Fault or escarpment

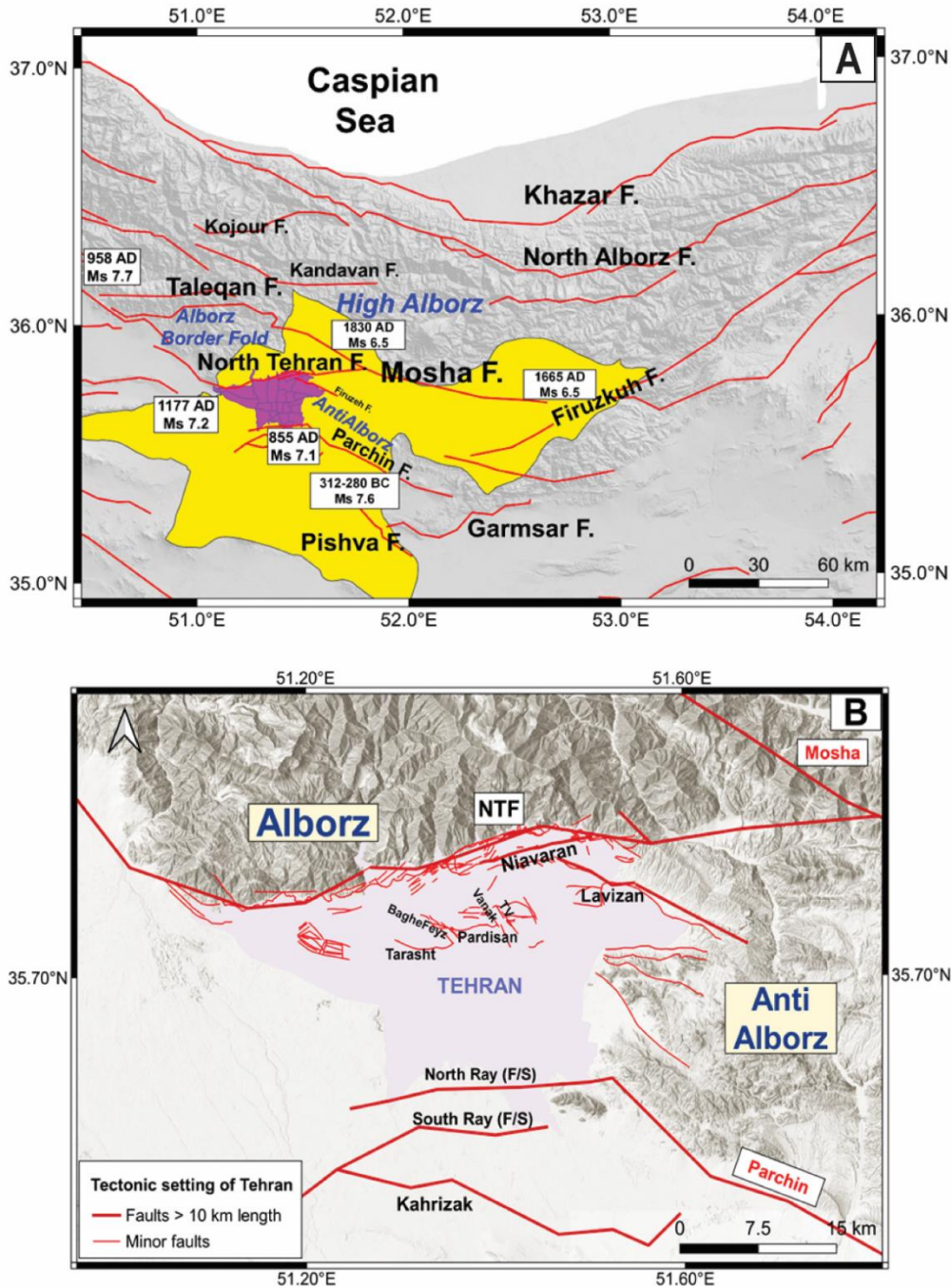


Figure 3-2: Tectonic setting of Central Alborz (A) and Tehran region (B). A: Central Alborz with main faults (red lines) and units (in blue), the historical earthquakes with $M_s \geq 6.5$ are displayed in white rectangles (for details, see Berberian and Yeats, 2018). The Tehran city location is displayed in red filled area. B: Faults close and inside the Tehran's basin: faults over 10 km length (thick red lines) and other important quaternary faults (thin red lines, see Table 3-1 for detail). The three main faults (North Tehran Fault, NTF, Moshā and Parchin) close to Tehran are labelled in red

3-1-2 Geology of the Tehran's basin

The Tehran alluvial basin is bordered to the north by the southern flank of the central Alborz Mountain range where the NTF separates remarkably the Eocene rock formations (central Alborz) from the Quaternary alluvial deposits (Tehran Basin). To the east, the Quaternary alluviums are bordered by the Anti-Alborz Mountains range made of different geological formations from Devonian to Tertiary sedimentary rocks. West of Tehran, the basin limits are not clearly recognizable and the Rud Shur Basin, 80 km west of the Anti-Alborz, is the closest geological features (Figure 3-3A). Finally, the south of the basin is connected to the silty plains of the central Iran (Engalenc, 1968) and the southern limits of Tehran basin are also not identifiable. However, we considered a northwest-southeast Neogene volcanic hills, Arath Kuh at approximately 30 km south of Tehran city, as the southern boundary of the basin (Figure 3-3A).

Tehran basin has different morphological features and is divided into a piedmont zone in the north and a plain zone in the south (Figure 3-3B). Abbassi and Farbod (2009) stated that the limits between piedmont and plain are marked by the Tarasht Fault (Figure 3-2B). The alluvial deposits which constitute the Tehran basin are divided into four main series introduced by different authors with different naming systems (Rieben, 1955; Engalenc, 1968; Knill and Jones, 1968; Vita-Finzi, 1969; Pedrami, 1987). In this work, we follow the Rieben (1955) Tehran's basin deposit definition which classified these series from the oldest to the newest deposits as A, B (Bn, Bs), C and D (Figure 3-3B):

- (i) The oldest deposits in Tehran consist in a folded conglomerate formation named 'A' or HezarDareh due to badland geomorphology of this formation in northeastern hills of Tehran. The 'A' formation is deposited on brittle bedrock of the piedmont and the southern limits are probably located at the far end of piedmont zone at south (Engalenc, 1968). Rieben (1955) proposed the age of Pliocene-Early Pleistocene for this formation, while Engalenc (1968) divided it into Plio Quaternary and Quaternary parts. The origin of the 'A' Formation can no longer be recognized, but one hypothesis is that these alluviums were mainly coming from the northeast, possibly having an alluvial and fluvial origin from Jajroud river in the far northeast and spread over the Tehran plain defining a gigantic alluvial cone (Engalenc, 1968; Pedrami, 1987; Figure 3-3B, yellow dashed lines).

Regarding lithology, this formation consists in homogeneous conglomerates with 85 percent of the pebbles coming from Eocene Karaj Formation Green Tuffs. The regularity of the bedding (10 to 25 cm thick) is another recognizable feature of the 'A' formation and its layers dips are almost vertical (50-70 degrees). According to Rieben (1955), the thickness of 'A' deposits can range between 10 meters (close to the basin borders) to 1000 meters.

- (ii) The subsequent formation, which unconformably overlays the 'A' formation, is called 'B' formation. The age of 'B' formation is estimated to middle Pleistocene (Rieben, 1955). The 'B' formation has a fluvio-glacial origin coming from the north and has been deposited mostly on eroded surfaces of unit 'A' and looks like Alpine moraines (Bn). Rieben (1955) mentioned the same age's formation in south Tehran called Bs formation. Regarding lithology, to the north the 'Bn' formation is composed by very heterogeneous material from big boulders to gravelly grains distributed in a silty matrix while it consists in clay and sand materials in the south of Tehran (Bs). The bedding is generally horizontal with a maximum dip of 15 degrees. The average thickness of 'B' is estimated to 60 meters but it varies strongly from place to place (Pedrami, 1987).
- (iii) The 'C' formation is an alluvial conglomerate that covered most parts of Tehran piedmont. The age of the 'C' formation is estimated from middle to late Pleistocene. Vita-Finzi (1969) estimated the age of 50000 years BP and Pedrami (1987) proposed the age of Wurm glaciation (73000 years BP) for this formation. This formation consists in alluvial fans from north to south, with a moderate grain size where the proportion of coarser pebbles decreases from north to south. The lithology is characterized by a red conglomerate made of laterite crusts with better cementation than 'B' formation deposits. The 'C' formation is characterized by thin beds of gravel and alignments of small pebbles with almost horizontal bedding. The average thickness for the 'C' formation is also estimated to be 60 m (Rieben, 1955).
- (iv) The 'D' formation is the youngest stratigraphic unit of the Tehran's basin. The age of the 'D' formation is estimated to be less than 10000 years BP (i.e., Holocene; Vita-Finzi, 1969).

With alluvial and fluvial origin, the ‘D’ formation comes from north Mountain valleys and has deposited on current or ancient riverbeds and spread all over the Tehran plain to the south. According to Engalenc (1968), the ‘D’ deposits are mixed with older deposits close to the piedmont. Regarding lithology, the grain size is very fine and made of silt and clay with poorly consolidated to unconsolidated cementation. The thickness based on the observation in construction excavations is estimated to be about 10-15 meters, consistently with the 1.4m/1000Yr sedimentation rate that produced at least 14 m thick deposits (Pedrami, 1987).

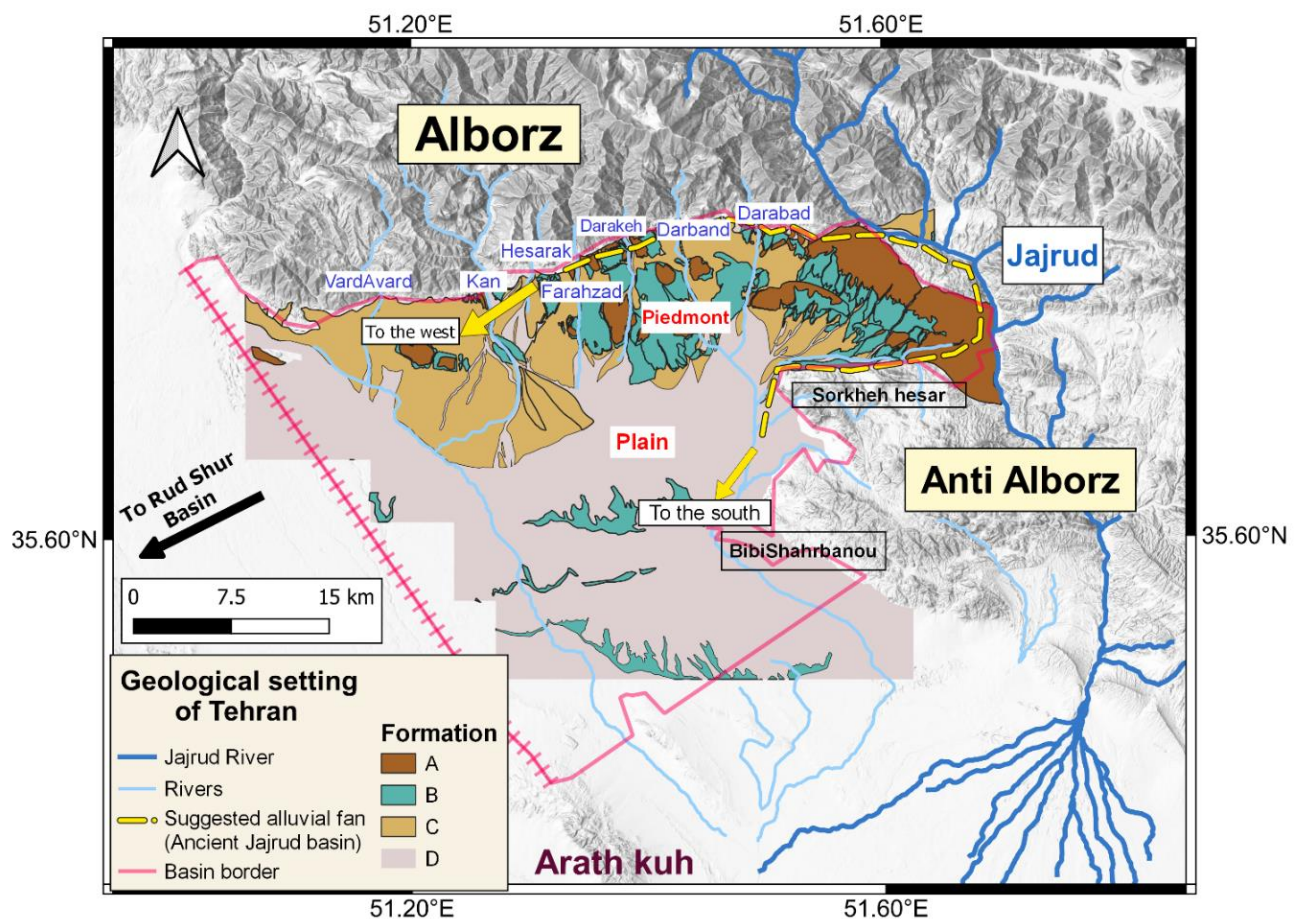


Figure 3-3: A) The studied area of the basin for the 3D velocity model (red line) where the southwestern unrecognizable basin limits are shown by a dash red line. B) Tehran’s quaternary sediments in the piedmont and the plain of the Tehran’s basin. Map modified from Abbassi and Shabanian 2023

3-1-3 State of knowledge on Tehran's basin geometry, bedrock depth and near-surface deposits

Our knowledge about Tehran's basin geometry and bedrock depth is very limited. According to Engalenc (1968), the bedrock of the Tehran piedmont is probably formed by rocks with fragile behavior structured by "en touches de piano" tectonics developed during the late Pliocene contraction phase. The bedrock is mainly made up of Green Tuffs of Karaj formation with very few outcrops in eastern parts, as well as volcanic rocks, limestones and dolomites from Anti-Alborz. There is no surface evidence of the bedrock characteristics in the plain of Tehran.

A gravity survey, carried out in 1957 (S.A.G.P., 1958), suggested that the Anti-Alborz continues under the city in a northwest-southeast direction and is limited (Tchalenko et al., 1974) to the north by an east-west extension of the Sorkheh-Hesar zone and a northeast-southwest extension of BibiShahrbanou Mountain (see Figure 3-3B). Considered then as a deep depression filled by strong accumulations of old alluvium, the maximum alluvium thickness of the basin was estimated about 1100 m in the southwest of the city (Fookes and Knill, 1969).

Using the existing seismological stations around Tehran to monitor the seismicity of the Alborz region, Shirzad and Shomali (2014) performed a seismic ambient noise tomography that indicated a bedrock depth ranging from 400 m to 1400 m, with thicker sediments in the southwest part of the basin. Such sediments thickening was also observed by Asadi et al. (2017) using Love and Rayleigh surface waves ambient noise tomography. Shirzad et al. (2019) and SoltaniMoghadam et al. (2019) proposed a 1D crustal P-wave velocity model for the Tehran and Central Alborz regions, respectively. However, the resolution of these studies is not fine enough to develop a detailed basin geometry or a velocity model for alluvial deposits within the Tehran's basin. The few studies of sediment thickness and shear-wave velocity (V_S) profiles in Tehran's basin using seismic ambient noise (Shabani et al., 2011; Fazlavi, 2015) indicate that the bedrock depth in the southern parts of the Tehran basin is about 700 meters depth.

For the near surface soil condition, the most noticeable study about the shallow structure of the Tehran basin has been performed for seismic microzonation purposes (JICA and CEST, 2000). This survey was conducted by gathering the information of more than 400 boreholes over 187 sites. In most cases, the JICA borehole depths are not exceeding 50 meters and the deepest borehole reaches 200 meters southwest of Tehran city. This study (JICA and CEST, 2000) allowed to define

41 representative soil profiles (SP) based on the standard penetration test (N-SPT) values up to the engineering bedrock's depth (defined as $V_s > 580$ m/s; Figure 3-4). The deepest SP is 150 m in the southwest of Tehran (SP#1) while the shallowest SP is 0 m (rock site, SP #41, see Appendix A for more detail).

3-2 Surface wave base methods

In order to derive a 3D V_s model of the Tehran's basin, we collected and analyzed seismological, active seismic and seismic ambient noise datasets. This section details the methods used in this paper to extract the dispersion properties of surface waves (dispersion curves, Rayleigh wave ellipticities) and the soil resonance frequencies, as well as the inversion method used to retrieve the V_s profile.

3-2-1 Single station methods

SSR (Site-to-reference Spectral Ratio) is the most validated and reliable experimental method to extract the fundamental frequency and amplification of a sedimentary site. This method is based on dividing the Fourier amplitude spectrum of an earthquake recorded at a sediment station by the Fourier amplitude spectrum of the same earthquake recorded at an outcropping rock station (Borchert, 1970).

The H/V method is defined as the Fourier amplitude spectra ratio of the horizontal to vertical components of ambient vibrations recorded at a single three-components seismological station according to the original idea of Nakamura (1989). The H/V method is widely used to extract the fundamental resonance frequency of sedimentary covers (see Molnar et al., 2022, for a recent review) from seismic noise measurements but it can also be used on earthquakes (e.g. Satoh et al., 2001). The H/V method is also often used to establish the empirical relationship between the bedrock depth (h) and the fundamental resonance frequency (f_0 ; among others, Ibs-von Seht and Wohlenberg, 1999; Guéguen et al., 2007; Gosar and Lenart, 2010; Fairchild et al., 2013; Thabet, 2019).

The RayDec method is based on the Random Decrement Technique (Asmussen, 1997). This method suppresses the contribution of Love and body S-waves in the noise wavefield in order to

extract the ellipticity of the fundamental mode of the Rayleigh wave (Hobiger et al., 2009), which can be further inverted to extract shear-wave velocity profiles (Hobiger et al., 2013).

3-2-2 Multi-station active and passive surface wave methods

The Multi-Channel Analysis of Surface Waves (MASW) method, popularized by Park et al. (1999), is an active source method used for retrieving surface wave dispersion curves using Frequency-Wavenumber (F-K) method (Lacoss et al., 1969; Capon, 1969). Most often, MASW measurements are used to constrain the high frequency part of the dispersion curve (> 5 Hz).

Seismic ambient noise measured synchronously by an array of seismometers can also be used to extract the dispersion curves of surface waves (Foti et al., 2018). For such passive surface wave measurements, the two main processing approaches are the spatial autocorrelation methods (e.g., SPAC: Aki, 1957; MSPAC: Bettig et al., 2001; ESAC: Ling and Okada, 1993; MMSPAC: Asten, 2006) and the F-K methods (e.g., Lacoss et al., 1969; Capon, 1969). Methods based on seismic ambient noise are generally used to constrain the low frequency part of the dispersion curve (Foti et al., 2018) depending on the array geometry. Even though almost all seismic noise array measurements are performed with three components sensors, the vertical component is most often used to extract the Rayleigh dispersion curves. FK-based processing methods exploiting the three components, to derive both the Rayleigh and Love waves dispersion curves and the signed ellipticities of Rayleigh waves, have been developed in recent years by Poggi and Fäh (2010) and Wathelet et al. (2018). In this paper, we use the RTBF method proposed by Wathelet et al. (2018). Extraction of dispersion curves over a broad frequency range depends on the equipment properties as the seismometer instrumental response, the number of seismometers and the array layout properties (geometry and size) that limit the resolution capabilities of any linear or 2D arrays (Wathelet et al., 2008; Foti et al., 2018).

3-2-3 Inversion

In a general definition, the inversion of surface waves dispersion curves is the process of finding the best-layered earth models whose theoretical dispersion curves best explain the experimental data (Wathelet et al., 2004) and the best fit between the theoretical and experimental data is usually used to quantify a misfit function. The inversion methods split into two categories: (i) the local

search algorithms that perturbate an initial velocity model to find the best solution and (ii) the global search algorithms that use an initial set of models to find the best set of velocity profiles. The neighborhood algorithm (Sambridge, 1999a, b; Wathelet, 2008), used in this study, is one of the most used global search algorithms for surface waves inversion.

Dispersion estimates (Rayleigh and/or Love wave dispersion curves, Rayleigh wave ellipticities) obtained from active and passive surface wave methods are often jointly inverted in order to better constrain shear-wave velocity models (e.g., Hobiger et al., 2013; Foti et al., 2018). Besides, since the surface wave inverse problem is inherently ill-posed (non-uniqueness of the solutions), a priori information may have an essential role in constraining the final inversions. The a priori information can include a set of geological constraints like geologic logs, geotechnical data or specific P or S wave values (Socco et al., 2010)

3-3 Geotechnical and geophysical data

The methods described in the previous section were implemented on several sets of data gathered in Tehran's basin. In this paper, we used 575 single-station seismic noise measurements, 33 seismic noise array measurements, 13 MASW profiles, 197 geotechnical boreholes and 13 sites with seismological recordings.

3-3-1 Near surface geophysical and geotechnical data

In addition to geotechnical data collected by JICA and CEST (2000), other studies in Tehran have been conducted by IIEES (Jafari et al., 2001a, b; Jafari et al., 2004) with new downholes and surface seismic refraction surveys (Figure 3-4). From the data collected by IIEES, we used 63 surface refraction or downhole surveys and completed the dataset by 134 more recent data from verified downholes derived from new local constructions projects collected by IIEES between 2010 and 2020 (Figure 3-4).

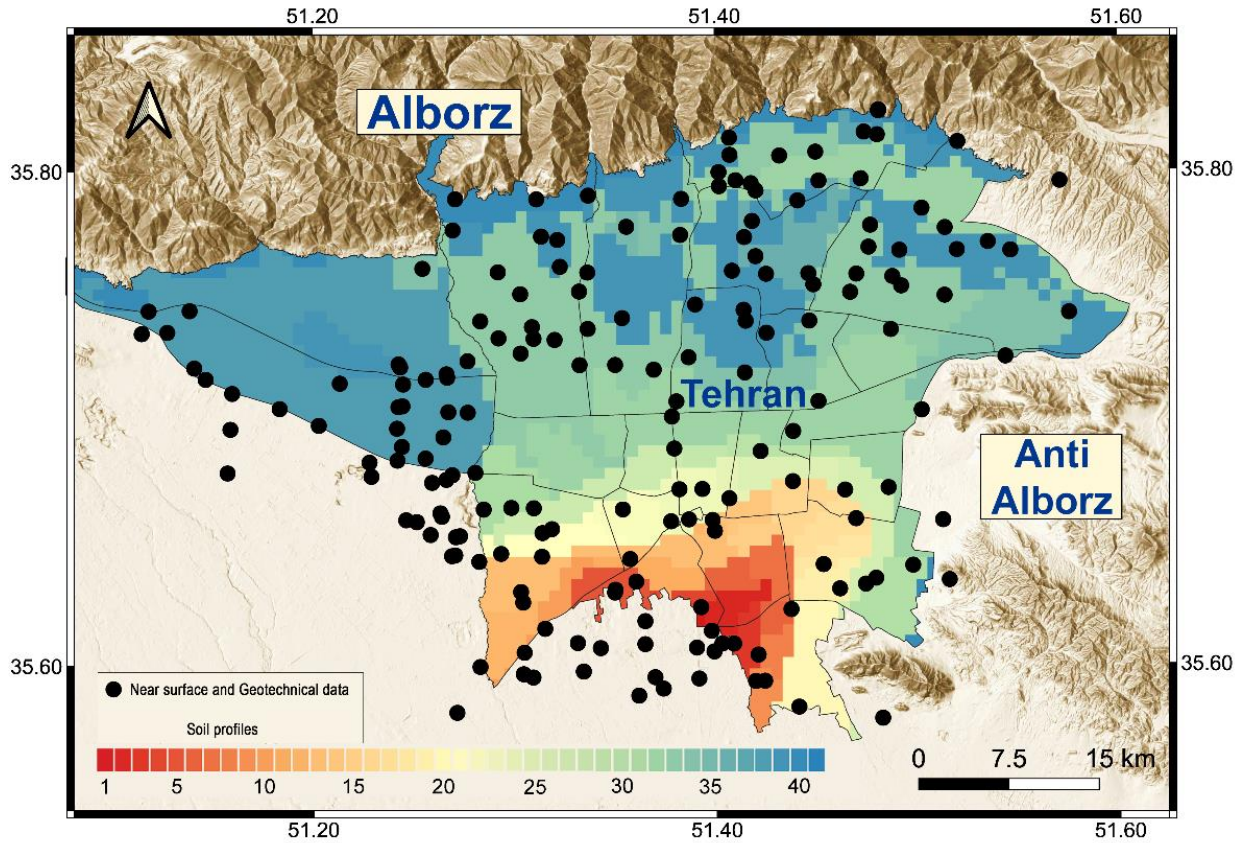


Figure 3-4: Distribution of the 197 near surface (seismic refraction profiles) and geotechnical data used in this study (black dots). In background, the representation of the 41 JICA and CEST (2000) soil profiles (see soil profiles description in appendix A, from the softest profile labeled as #1 to the stiffest one labeled as #41).

3-3-2 Single station data

In order to estimate the fundamental resonance frequency (f_0) over the whole Tehran city, we collected seismic ambient noise data at 884 sites coming from different measurement campaigns as described on Figure 3-5:

- The first campaign consisted in five-month continuous recordings (February to June 2002) by 13 temporary seismological stations where 11 stations were located on alluvial deposits and 2 at outcropping rock (Haghshenas, 2005; Figure 3-1). This campaign allowed to record from 42 to 146 earthquakes that were used to estimate site amplification, including site resonance frequency (Haghshenas, 2005). During this experiment, 62 single station ambient

noise measurements distributed all over the Tehran city (Figure 3-5, orange dots) have been also done. In both cases, the sensors used were Güralp CMG40T velocimeters with cut-off frequency of 10 s connected to Reftek digitizers;

- The second campaign was conducted in 2016 with 124 single station measurements in a 2 by 2 km grid all over the city (Figure 3-5, blue dots). The velocimeters used were Lennartz LE3D-20s (cut-off frequency of 20 s) connected to Kelunji EchoPro or Parsian digitizers (www.geoparsian.com, last accessed 01/01/2023);
- The third campaign has been carried out in early 2017 with 60 measurements focusing on the northeast Tehran basin between Alborz and Anti-Alborz Mountain ranges (Figure 3-5, brown dots). Deployed instruments were the same as for the 2016 campaign;
- The fourth campaign has been done in 2017 and 2018 leading to 195 measurements (Figure 3-5, yellow dots). This study has been performed using CitySharkII digitizer (Chatelain et al., 2012) and a Lennartz LE3D-5s velocimeter (cut-off frequency of 0.5 Hz);
- The fifth campaign has been done during various IIEES projects in 2020, especially in the west and southwest of the city leading to 94 measurements (Figure 3-5, green dots). The sensors used were Lennartz LE3D-20s connected to Parsian digitizers.

In addition to these 30 minutes duration single station seismic noise recording, 7 seismological stations recorded seismic noise from 1 day to 1 week (Figure 3-5, red dots). Deployed instruments were the same as for the 2020 campaign.

Finally, 329 single station recordings were collected from the 33 seismic ambient noise arrays deployed from 2015 to 2021 (Figure 3-5, black squares). The seismic noise array experiments included Güralp CMG6TD or Lennartz LE3D-20s seismometer connected to Parsian digitizers.

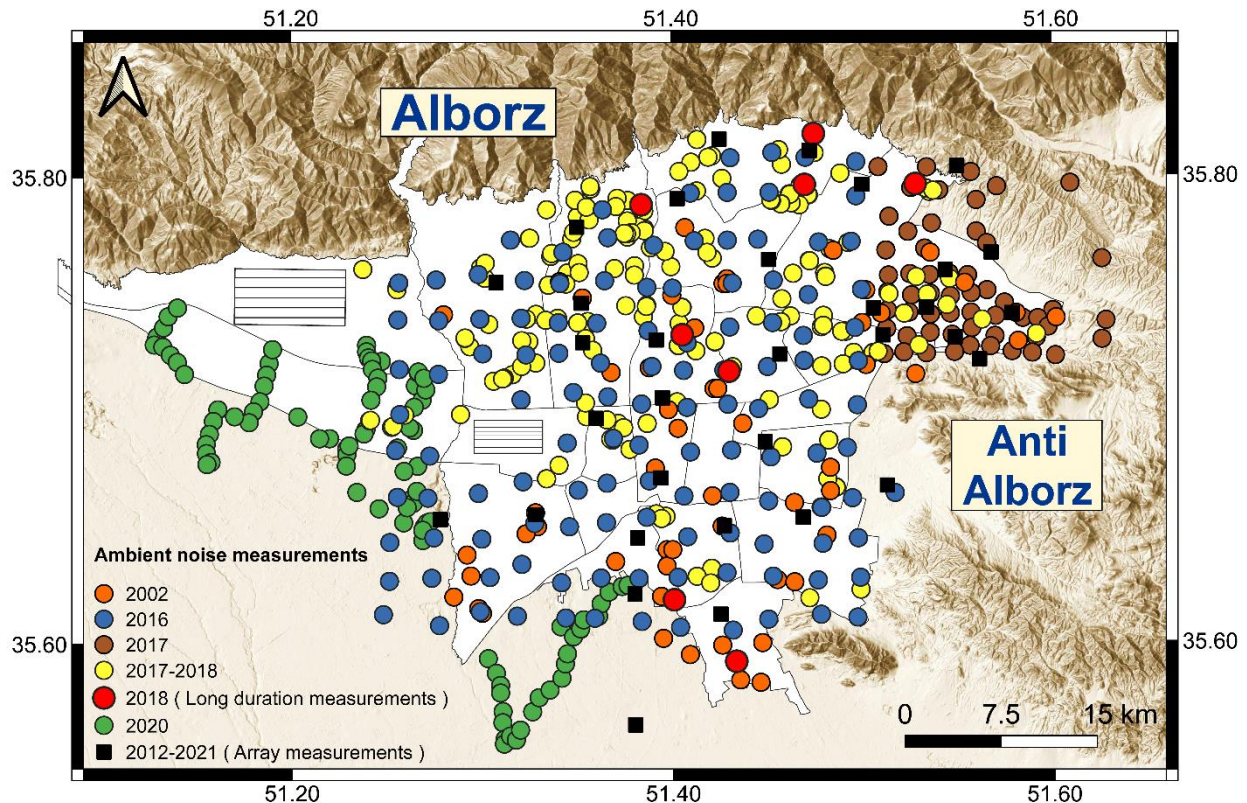


Figure 3-5: Spatial distribution of single station seismic noise measurements used in this study. Dashed rectangles: areas with restricted access.

3-3-3 Active and passive surface wave measurements

Data from the 33 seismic ambient noise arrays and 13 MASW profiles (Figure 3-6) were acquired during two field campaigns. The campaign held in 2012-2015 consisted in 11 seismic ambient noise array measurements along NS and EW cross-sections (Figure 3-6, black squares), while the second campaign (2017-2021) consisted in 22 arrays in order to cover other parts of the basin (Figure 3-6, white squares). For both campaigns, seismometers were located on nested circles with radius of 30-50 meters and 100-200 meters or along a circle of 150-200 m radius with one sensor in the center and seven to nine others angularly equal spaced. All measurements involved at least 90 minutes of seismic noise recording.

MASW measurements (Figure 3-6, black and white crosses) were performed between 2017 and 2021 at 13 array sites using an ABM digitizer with 24 vertical 4.5 Hz geophones and geophone spacing of 3 to 4 meters. The sledgehammer source offset was ranging from 5, 10 and 15 meters from each profile extremity and one shot was also performed at the profile center.

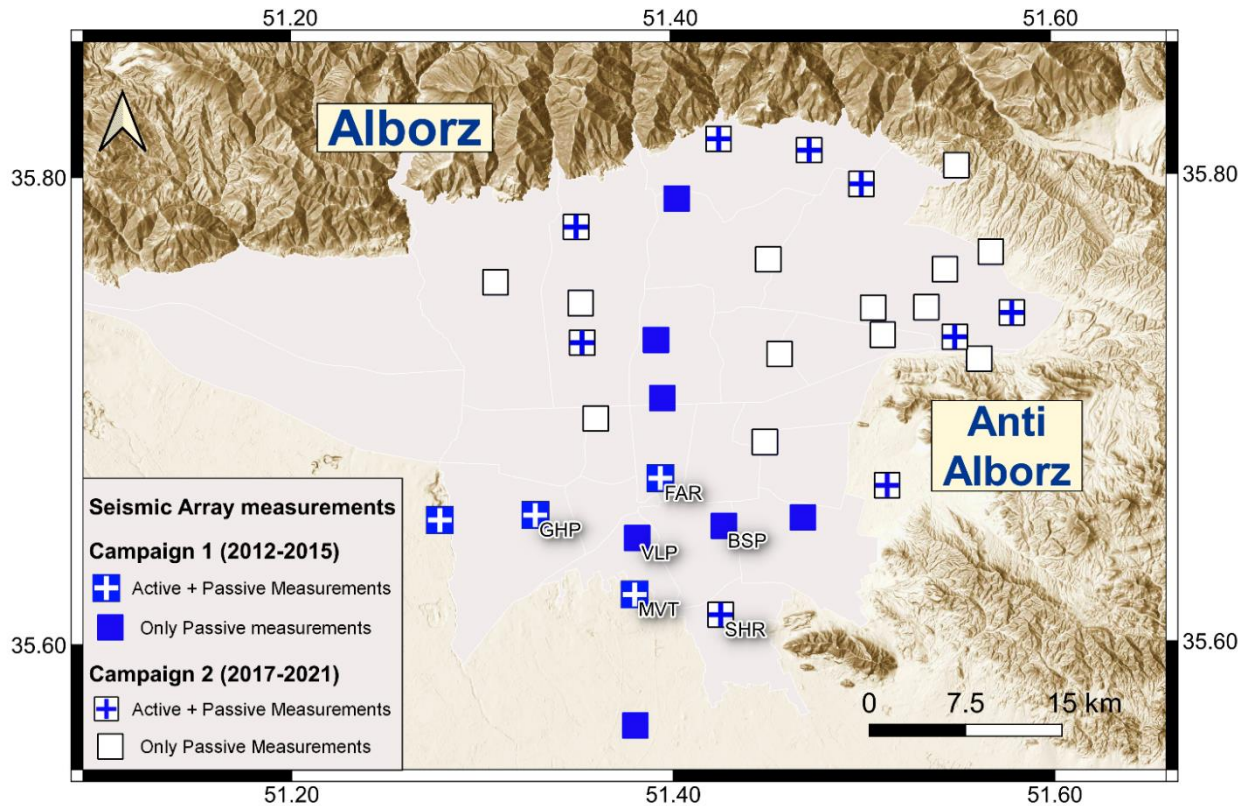


Figure 3-6: Location of the 33 seismic noise arrays in Tehran as well as the 13 MASW profiles

3-4 Data processing and results

3-4-1 Near surface stiffness

As geotechnical data are limited to near surface, the time-averaged shear-wave velocity over the first 30 m, V_{S30} , was inferred following the N-SPT– V_{S30} correlation proposed by JICA and CEST (2000): $V_s = 161 N^{0.277}$. Figure 3-7 shows the spatial distribution of V_{S30} over Tehran for the 197 sites. Most of the V_{S30} values are higher in the northern part of Tehran with an average over 600 m/s, while in the southern part of Tehran, V_{S30} are lower with an average close to 400 m/s, consistently with the soil profile lithology (Figure 3-4) and the decrease of the grain size of the quaternary sediments from the North towards the South. These V_{S30} values distribution are also consistent with the findings of Shafiee and Azadi (2007) that related each geological unit to a range of V_{S30} values inferred from seismic refraction profiles and downhole measurements.

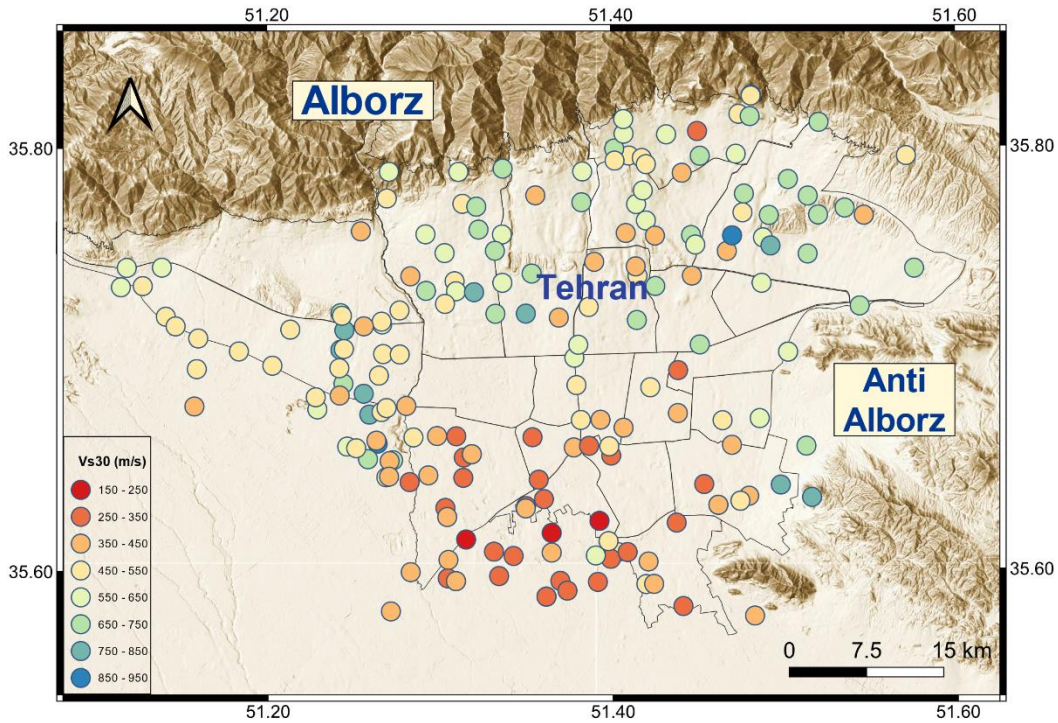


Figure 3-7: Spatial variation of V_{s30} in Tehran inferred from the 197 near surface and geotechnical data (Figure 3-4).

3-4-2 Fundamental resonance frequency

Single station ambient noise recordings were performed in order to map the fundamental resonance frequency (f_0) throughout the Tehran's basin from H/V method. Seismic noise data were processed using the Geopsy software (Wathelet et al., 2020; www.geopsy.org, last accessed July 2023). As the expected resonance fundamental frequency can be as low as 0.3 Hz (Haghshenas, 2005; Haghshenas et al., 2008), noise time series have been splitted into time window duration of 50 seconds leading to a minimum of 35 windows for the shorter duration recordings (30 minutes). The Konno and Ohmachi smoothing parameter (Konno and Ohmachi, 1998) was fixed to 40 and the H/V curves computed between 0.2 to 20 Hz. For the 33 seismic noise arrays, we consider only the fundamental resonance frequency given by the H/V curve from the averaging of all individual H/V curves of each station of the array. This means that the initial set of 884 H/V curves has been

reduced to 575 HV curves (542 single station measurements and 33 averaged H/V curves from seismic noise array measurements, Figure 3-8A).

Although the number of H/V curves is large, it has been possible to extract the fundamental resonance frequency (f_0) and related amplitude (A_0) from only 159 H/V curves (Figure 3-8B; see Appendix B for more detail on H/V curves). Indeed, four different types of H/V curves had to be defined to help identifying f_0 and A_0 :

- H/V curves displaying a very clear peak that fulfills the SESAME (2004) requirements (Figure 3-8C) are considered as acceptable peaks allowing the extraction of f_0 and A_0 ;
- H/V curves exhibiting a wide peak or a plateau-like shape that fulfills the SESAME (2004) requirements except that H/V peak width is too large (Figure 3-8D). In such a case, f_0 and A_0 have been picked at the highest frequency of the H/V wide peak following Guillier et al. (2006) indications for these types of large H/V peak;
- H/V curves with low amplitude peak fulfilling the SESAME (2004) requirements except that the amplitude of the H/V peak is close or lower than 2 (Figure 3-8E). We consider such curves as acceptable to determine f_0 and A_0 according to the findings of Guillier et al. (2007) in Tehran. Using one week of seismic noise recordings by the DAR station during the 2002 experiment (Figure 3-1), Guillier et al. (2007) indeed observed that the H/V peak amplitude at 0.9 Hz varied from 1.3 to 2.3 and was over or equal to 2.0 only 20% of the time;
- the other H/V curves that display unclear peaks, following none of the SESAME (2004) criteria, are assumed as not acceptable for f_0 and A_0 determination (see Figure 3-8F).

Besides, for 7 of the 33 seismic noise arrays, f_0 and A_0 could not be extracted due to inconsistent H/V curves from one station to another.

Figure 3-8B indicates that most of the f_0 values are lower than 1 Hz (85% of the peaks), which suggests a deep sedimentary basin. The spatial distribution of f_0 over the whole Tehran basin clearly separates the basin into two areas (Figure 3-9): in the south and southwest parts of the basin, the fundamental resonance frequencies are always lower than 0.5 Hz, except for few peaks close to the Anti-Alborz Mountains; while resonance frequencies are higher than 0.5 Hz in the center, north and northeast parts of the city. This suggests a relative deepening of the seismic bedrock from northeast to southwest.

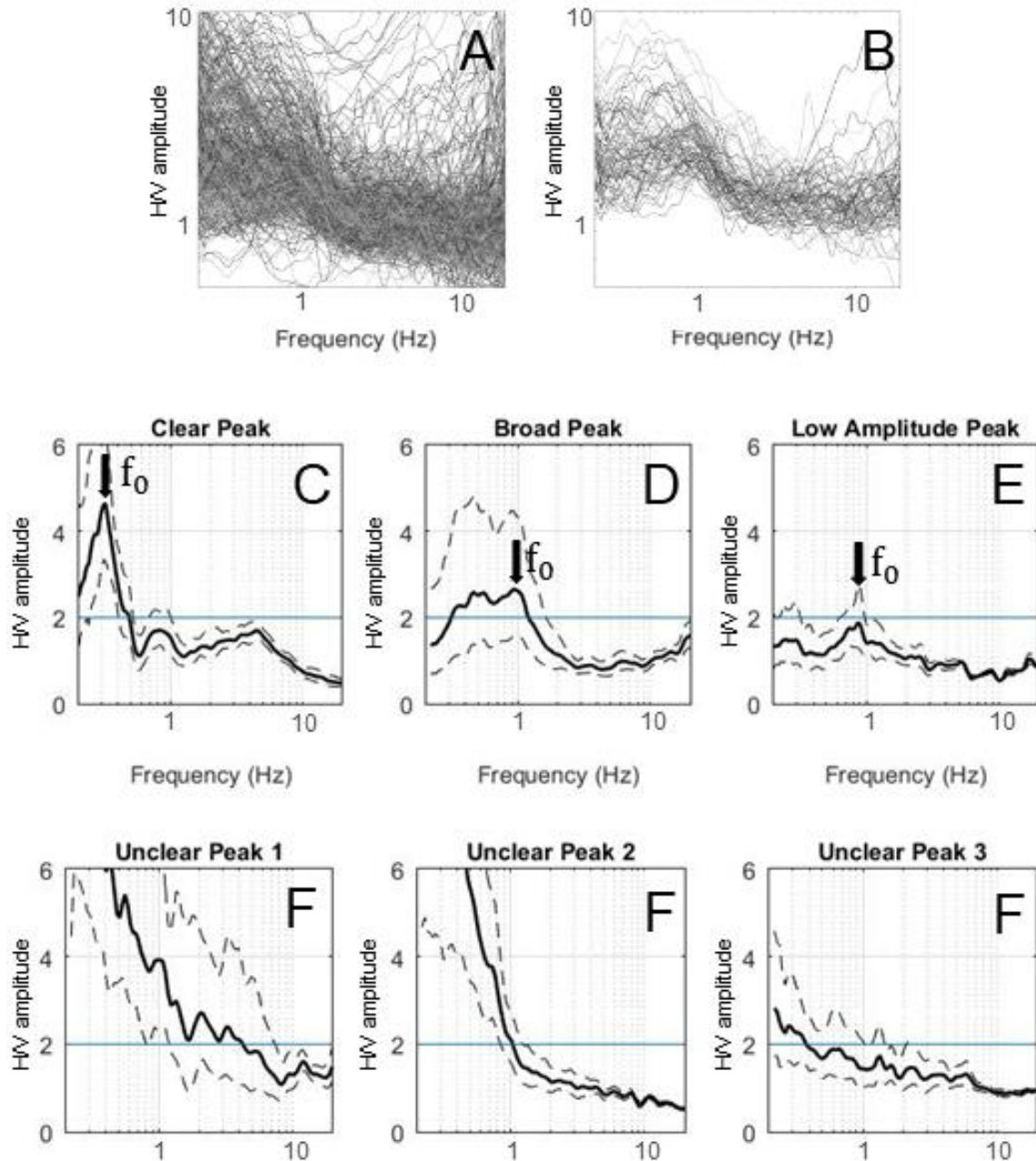


Figure 3-8: H/V curves in Tehran's basin and their 4 typologies following the SESAME (2004) criteria. A: all the 575 average H/V curves. B: the 159 interpretable average HV curves from which HV peak frequencies have been extracted. C: typical H/V curve with a clear peak allowing the f_0 and A_0 determination. D: example of H/V curve with a broad peak type. E: H/V curve with a low amplitude peak. F: various examples of H/V curves that could not be interpreted. In C, D, E and F, the thick and thin dashed lines indicate the average H/V curve with its uncertainty, respectively. The peak frequency (f_0) is indicated by the arrow.

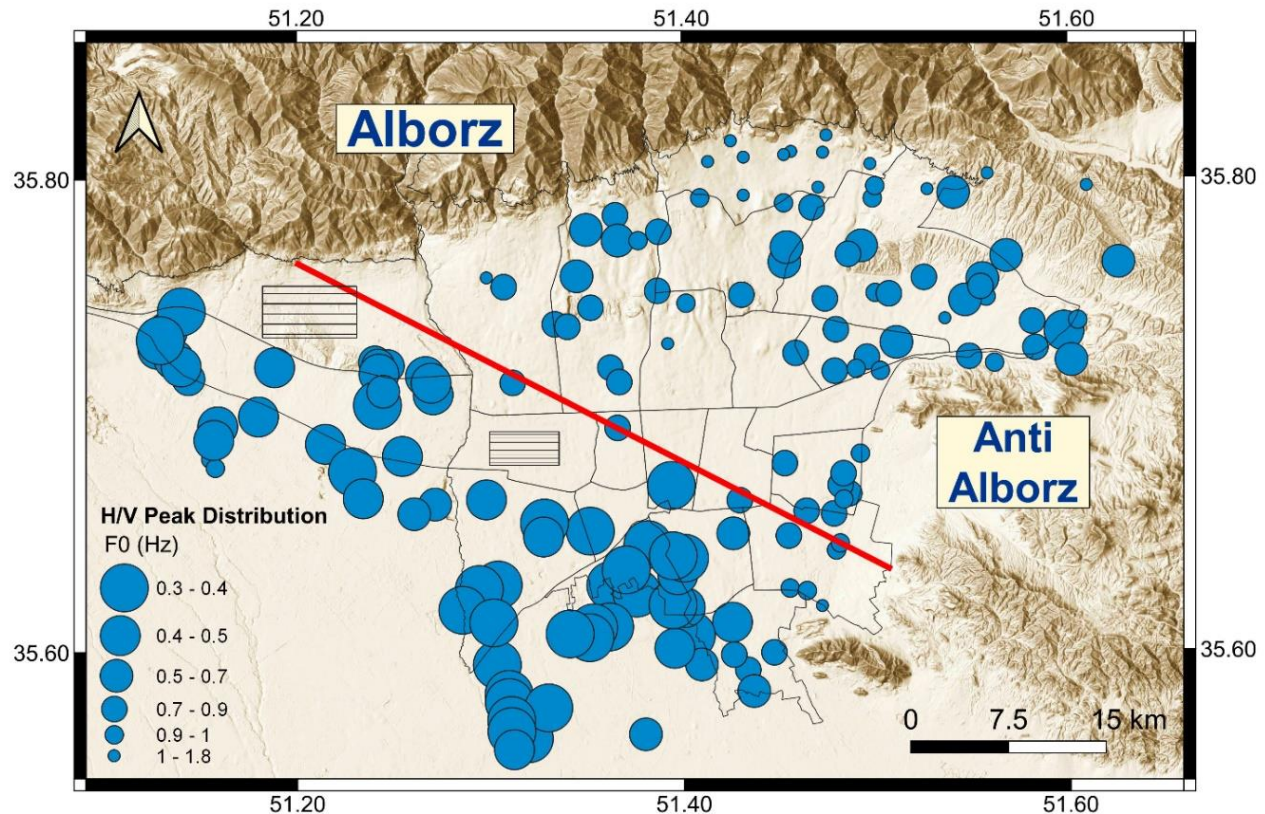


Figure 3-9: Spatial distribution of H/V peak frequencies in Tehran's basin with a hypothetical line (in red) that separates the northeast part of the basin with frequencies higher than 0.5 Hz and the southwest part of the basin with frequencies lower than 0.5 Hz. Dashed rectangle: area with restricted access.

3-4-3 Surface waves dispersion estimates

From the MASW measurements at 13 sites (Figure 3-6), the dispersion curves of the fundamental Rayleigh wave mode (R0) have been extracted between 12 and 70 Hz, consistently with the maximum interpretable wavelength defined as 0.4 times the length of the profile (O'Neill, 2004). We analyzed the 33 seismic ambient noise arrays using the RTBF method (Wathelet et al., 2018) with a frequency-dependent time window length of 50 times the center period. After computing the probability density function (PDF) of phase velocities in the frequency – phase velocity domain for both Rayleigh and Love waves (Figure 3-10A-B), the corresponding dispersion curves with their uncertainty (Figure 3-10D-E) are extracted within the array resolution (Wathelet et al., 2008). The PDF for the signed ellipticities of Rayleigh waves is also computed (Figure 3-10C) and the

signed ellipticity angle is extracted for each identified Rayleigh wave mode (Figure 3-10F). This procedure has been applied to all arrays leading to obtain 33 dispersion curves for the fundamental mode of the Rayleigh waves (R0), 4 dispersion curves for the first higher mode of the Rayleigh waves (R1) and 12 dispersion curves for the fundamental mode of Love waves (L0). The detail for each array is summarized in Table 3-2 (see also Appendix D for more detail on the dispersion curves and ellipticities).

Table 3-2: Data used for the inversion of V_s profile (the - sign means no data): V_{s30} , fundamental resonance frequency (f_0) derived from H/V curve and related maximum amplitude (A_{0j}), maximum ($\lambda_{max}/\lambda_{min}$) and minimum (λ_{min}) extracted wavelength for MASW and ambient seismic noise array measurements (Array); dispersion curve modes (DC mode) obtained from array processing; R0: fundamental mode of Rayleigh wave, R1: first higher mode of Rayleigh wave, L0: fundamental mode of Love wave; ellipticity of Rayleigh wave from array processing (RTBF method) or RayDec method; N indicates negative angle, P positive angle; seismic bedrock depth.

Parameter	V_{s30} (m/s)	f_0 (Hz)	A_0	MASW $\lambda_{max}/\lambda_{min}$ (m)	DC mode	Array $\lambda_{max}/\lambda_{min}$ (m)	Ellipticity from RTBF	Ellipticity from RayDec	seismic bedrock depth (m)
Arrays									
ABS	550	-	-	15/4	R0+L0	935/288	R0N	R0N	356
BBA	450	0.6±0.05	6.1±1.9	-/-	R0	763/138	R0N	R0P	447
BSP	350	0.65±0.1	2.4±0.6	-/-	R0	657/124	R0N	R0N	350
DAR	500	0.9±0.05	2.2±0.5	-/-	R0	775/98	R0N	R0N	344
ELM	650	0.7±0.1	2.5±0.5	-/-	R0	1107/174	R0N	R0N	427
ESII	700	-	-	13/7	R0	494/77	R0N	-	NR
FAR	300	0.38±0.05	2±0.3	34/9	R0+R1+L0	797/165	R0N+R1P	R0N	780
GIIP	400	0.35±0.05	3.0±0.5	14/10	R0+R1	644/155	R0N+R1P	R0N	910
HRM	300	0.65±0.15	2.5±0.2	-/-	R0+R1+L0	252/81	R0N+R1P	R0N	400
INT	600	0.9±0.15	1.7±0.3	-/-	R0	798/122	R0N	R0N	293
KIJJ	300	0.6±0.05	3.4±1	11/6	R0+R1	1201/650	R1P	R0N	537
KIIV	400	0.6±0.1	2.6±0.8	-/-	R0	318/76	R0N	-	410
MET	600	0.6±0.1	4.6±1.5	-/-	R0+L0	749/164	R0N	R0P	560
MRZ	750	-	-	24/12	R0	753/186	R0N	-	NR
MVT	200	0.35±0.05	2.6±0.5	11/6	R0	758/118	R0N	R0N	672
NAM	500	0.9±0.2	1.6±0.4	-/-	R0+L0	623/46	R0N	-	380
NVR	550	-	-	13/5	R0+L0	637/82	R0N	-	147
NZM	550	0.9±0.15	1.3±0.2	-/-	R0	914/139	R0N	R0N	296
OZG	700	0.9±0.1	2±0.5	24/11	R0	772/13	R0N	R0P	343
PLC	400	0.75±0.1	7±1	-/-	R0	649/130	R0N	R0P	346
PRD	700	0.85±0.1	3.7±0.2	-/-	R0	916/166	R0N	R0P	440
PRZ	450	0.8±0.1	1.7±0.5	-/-	R0	941/122	R0N	R0N	356
SAD	600	1.1±0.1	1.6±0.1	10/6	R0+L0	719/193	R0N	R0N	257
SDI	400	0.6±0.1	6±0.5	16/7	R0	712/169	R0N	R0P	503
SIIR	300	0.55±0.1	7±2	5/3	R0	394/67	R0N	R0P	270
SKII	600	0.9±0.15	2.5±0.5	-/-	R0+L0	613/69	R0N	R0N	426
SOII	600	-	-	-/-	R0	613/294	-	-	NR
TIIR	650	0.9±0.15	1.5±0.5	-/-	R0+L0	690/148	R0N	R0N	393
TIUU	550	-	-	-/-	R0+L0	723/162	R0N	-	340
TKII	700	-	-	23/8	R0+L0	870/158	R0N	-	89
TOS	550	0.85±0.1	1.6±0.3	-/-	R0	786/118	R0N	R0N	266
TRB	550	1.08±0.1	2±0.5	-/-	R0	638/60	R0N	-	254
VLP	300	0.32±0.05	3±0.1	-/-	R0+L0	1116/110	R0N	R0N	816

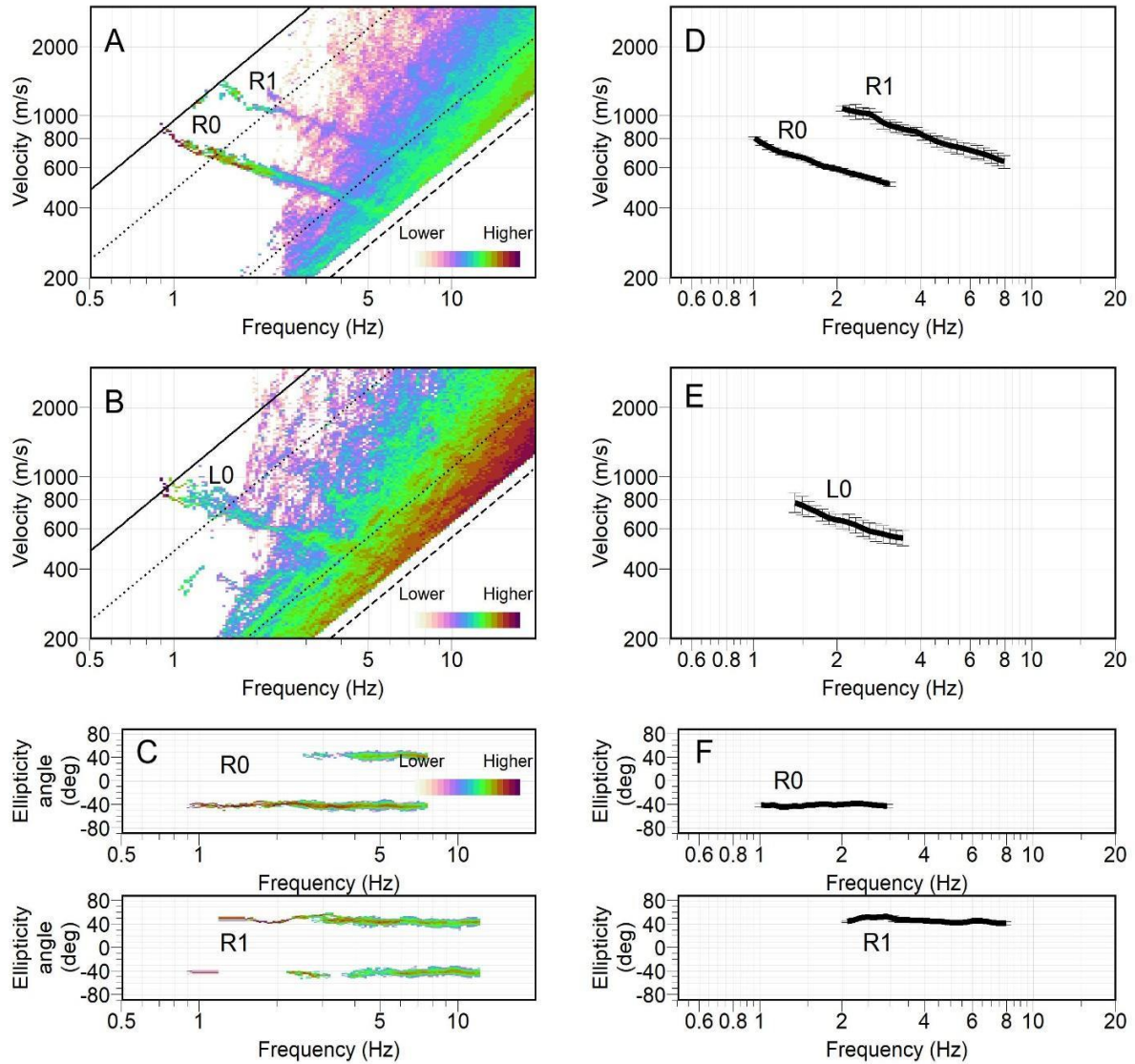


Figure 3-10: Array processing results at FAR site (A-C) and the extracted dispersion curves and ellipticities of Rayleigh waves with their uncertainty (D-F). A: Probability density function (PDF) of Rayleigh wave phase velocities as a function of frequency for modes R0 and R1. B: PDF of Love waves phase velocities as a function of frequency for the fundamental mode L0. C: PDF of the Rayleigh wave ellipticity angles as a function of frequency for R0 (upper panel) and R1 (lower panel). D: extracted dispersion curves for the fundamental (R0) and first higher mode (R1) of Rayleigh waves. E: extracted dispersion curve for the fundamental mode (L0) of Love waves. F: extracted ellipticity angle curve for the fundamental R0 (upper panel) and first higher mode R1 (lower panel) of the Rayleigh waves. In A and B, the theoretical array resolution limits (black lines), as defined in Wathelet et al. (2008), are indicated: $k_{min}/2$ (dashed line), k_{min} (continuous line), $k_{max}/2$ (dashed line), k_{max} (plain line).

The fundamental mode (R0) of Rayleigh phase velocities as a function of wavelength (Figure 3-11A) clearly allows to distinguish faster phase velocities in the northeast part of the basin at a given wavelength (Figure 3-11B, black lines) and softer ones in the south part of the basin (Figure 3-11B, red lines) that may indicate softer material and/or deeper seismic bedrock in the south. Finally, fundamental mode dispersion curves for Love waves could be extracted only for 12 of the 33 arrays (Table 3-2, L0), which could witness some strong deficiency of Love waves in the Tehran seismic noise wavefield.

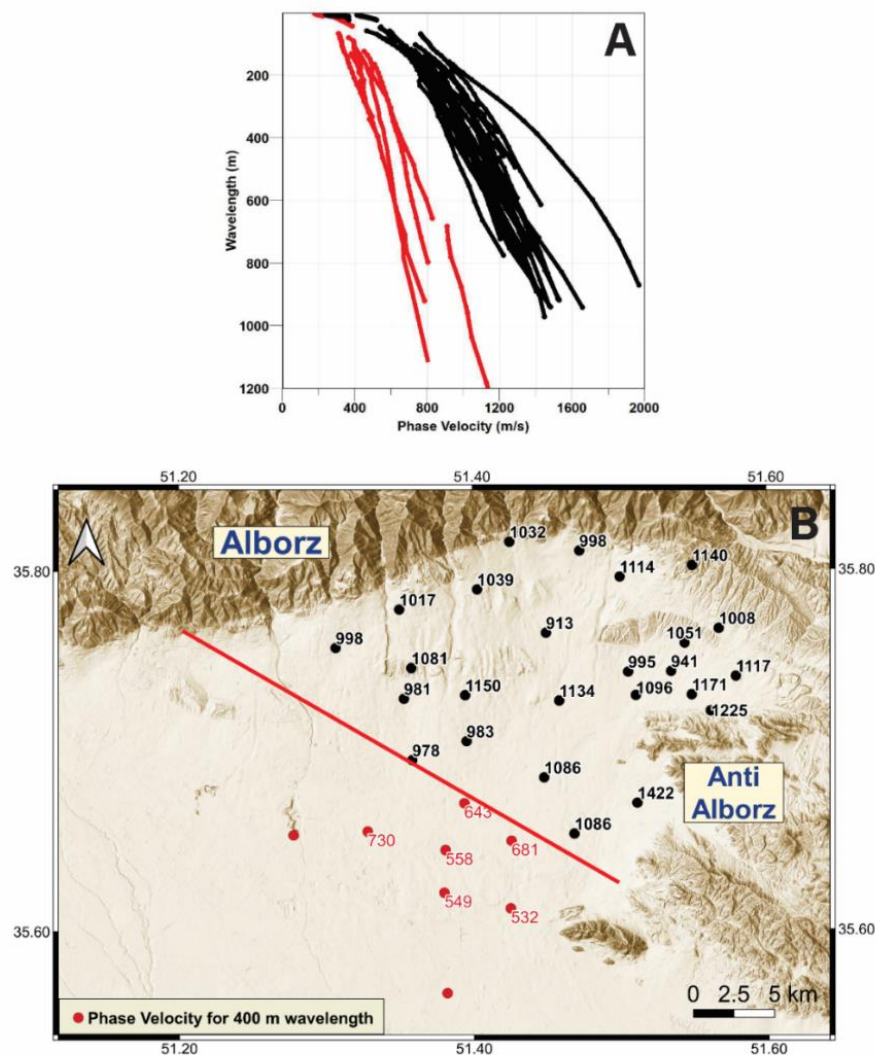


Figure 3-11: A: Rayleigh wave phase velocity as a function of wavelength for the different arrays. B: spatial distribution of the phase velocities at 400 m wavelength with a red hypothetical line separating the northeast and the south part of the basin.

For the ellipticity, the Rayleigh wave absolute ellipticity was also extracted using the RayDec method (Hobiger et al., 2009) in order to extend the estimation of the ellipticity close to the fundamental resonance frequency, i.e., in the low frequency range not covered by ellipticities from RTBF processing due to the limited array resolution (Figure 3-10). In most of the sites, the RayDec method has allowed to extend the dispersion estimates at low frequency (below 1Hz) as indicated in Figure 3-12, when the high frequency is mostly controlled by the MASW data. In the 1-10 Hz frequency band, the data are mainly coming from the RTBF processing, i.e. the Rayleigh (R0-R1) dispersion curves and the Love ones (L0).

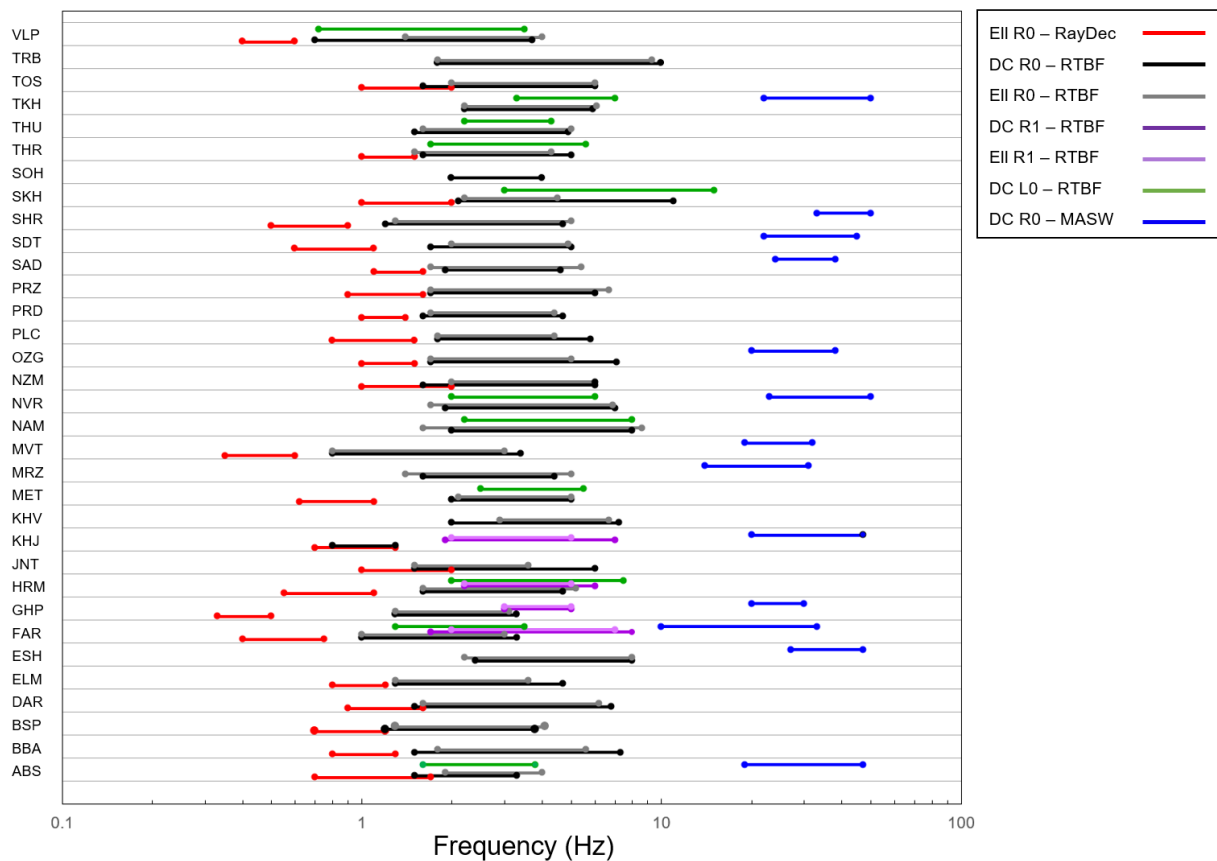


Figure 3-12: The frequency range of dispersion curves and Rayleigh wave ellipticities.

As the seismic noise level in Tehran is low at low frequencies (Guillier et al., 2007) and the majority of H/V measurements were unable to provide an estimate of the resonance frequency, we compared the ellipticities extracted from the seismic ambient noise using array data with those extracted from

the coda of regional earthquakes, which have a larger low-frequency energy content. The method used to extract the ellipticity of Rayleigh wave from the coda part of the earthquakes (RayDecC) is indicated in Appendix C. Ellipticities derived from seismic ambient noise and earthquake coda at 5 temporary seismological stations (AZP, MOF, SHL, FAR and DAR) from the 2002 seismological experiment (Haghshenas, 2005) are indicated in Figure 3-13. The ellipticities extracted with both methods are very consistent with each other, suggesting that (i) the Rayleigh waves ellipticity is not linked at all to the amount energy of the waves (low energy for RayDec on seismic noise and high energy for RayDecC applied to coda earthquakes) and (ii) the ellipticity derived applying the RayDec method to seismic ambient noise recordings is fully thrustable and can be used while inverting the dispersion estimates to get the V_s ground profile.

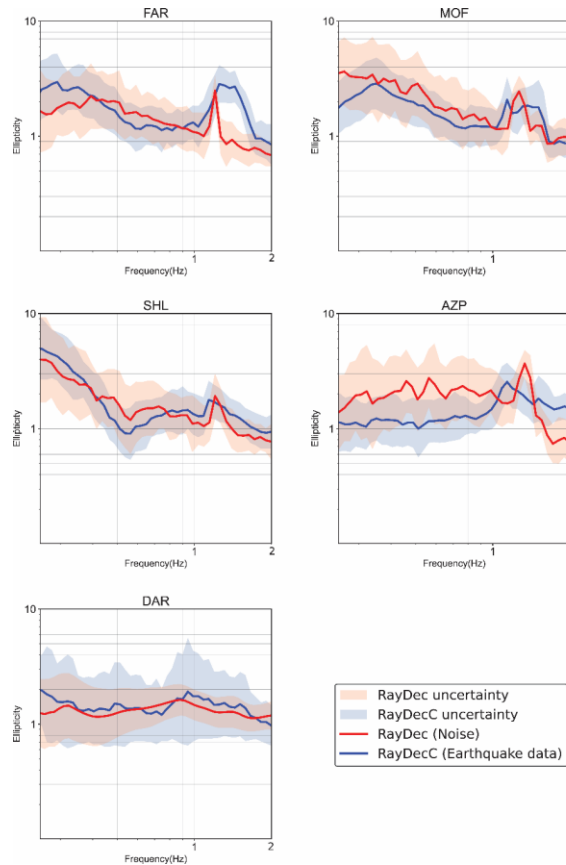


Figure 3-13: Comparison of ellipticity curves extracted from seismic noise recordings (RayDec method, in blue; Hobiger et al., 2009) with the ellipticity extracted from earthquakes coda recordings (RayDecC method, in red; Aki, 1969; Zeng 2006). The number of earthquakes used is 47, 99, 64, 37 and 42 for AZP, MOF, SHL, FAR and DAR seismological stations (Figure 1), respectively.

3-4-4 Shear-wave velocity inversion

Global search methods like the neighborhood algorithm (Wathelet, 2008) requires defining a ground model parameterization to be used in the inversion. The influence of ground model parameterization is widely discussed in literature by means of experimental (Renalier et al., 2010; Di Giulio et al., 2012) or systemically approaches (Cox and Teague, 2016). All these studies agreed that ground model parameterization with a limited number of layers (from 3 to 5) is generally sufficient to enable reliable shear-wave velocity inversion. Considering the known geological layering in Tehran, three layers over a half-space model was chosen for the ground model parameterization. The most surficial layer corresponds to Tehran's most recent D alluvial formations while the second and third layers corresponds to the B/C and A formations, respectively. The minimum resolvable depth and maximum investigation depth were defined as the half of the minimum (λ_{\min}) and maximum (λ_{\max}) measured wavelength extracted from R0 combining the dispersion curves from MASW (when exists) and seismic noise arrays, according to current practice (Foti et al., 2018).

The data used in the inversion are (Table 3-2):

- V_{S30} inferred from geotechnical studies in order to define the V_s range in the topmost 30 m in the ground model parameterization;
- Fundamental resonance frequency (f_0);
- Rayleigh and Love waves dispersion curves for the fundamental and higher modes;
- Rayleigh wave ellipticity angles for the fundamental and higher modes whatever the origin (RTBF, RayDec and RayDecC). Since RayDec method does not provide the ellipticity sign, we fix at first trial the sign of the RayDec ellipticity to be consistent with the sign of the ellipticity coming from RTBF processing.

The first V_s inversions lead to satisfactory results for most of the arrays, such as at ABS and FAR sites (Figure 3-14A-B), except for 6 sites (BBA, MET, PLC, PRD, SDT and SHR) for which the RayDec ellipticity could not be correctly inverted even if the inverted ground models were able to explain (i) the fundamental resonance frequency, (ii) the measured dispersion curves and (iii) the ellipticity angle derived from RTBF processing. As illustrated in Figure 3-14C for PLC site (as an example), it can be observed that the R0 ellipticity angle at this site, assumed to be negative (red curve in Figure 3-14C for PLC) should be positive (green curve in Figure 3-14C for PLC) to allow

satisfactory inverted ellipticities and this is the case for the 5 other sites (BBA, MET, PRD, SDT and SHR). All inversion results are provided in Appendix D.

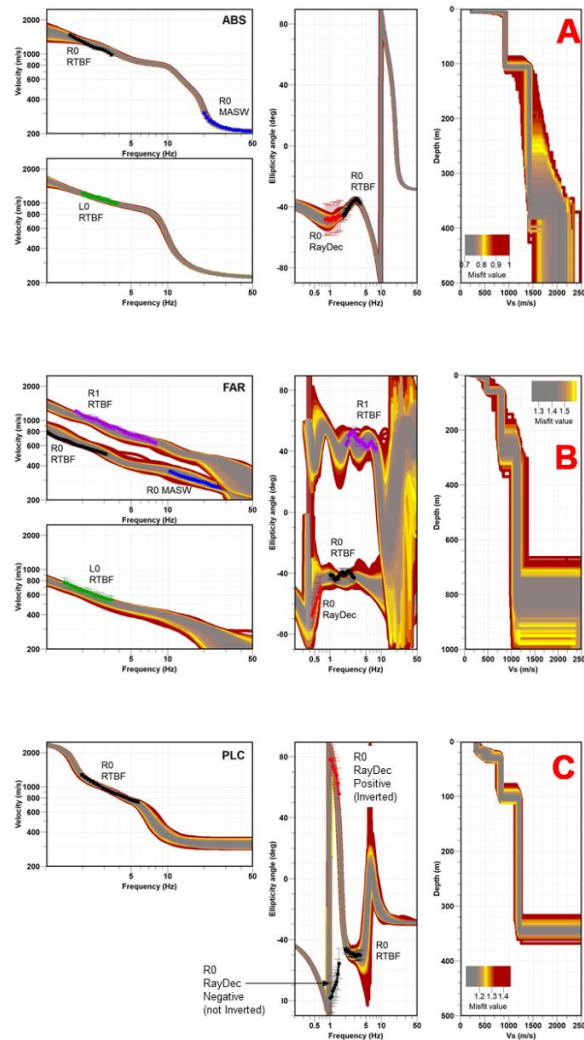


Figure 3-14: Inversion results for ABS (A), FAR (B) and PLC (C) sites. Black curves: Fundamental Rayleigh wave mode (R0) dispersion curve from RTBF processing and related ellipticity curve (including uncertainty). Purple curves: First higher Rayleigh wave mode (R1) dispersion curve from RTBF processing and related ellipticity curve (including uncertainty). Green curves: Fundamental Love wave mode (L0) dispersion curve from RTBF processing (including uncertainty). Blue curves: dispersion curves for R0 mode from MASW processing. Red curves: Rayleigh wave ellipticity angle inferred from RayDec - method (including uncertainty). Notice that for PLC array, the ellipticity angle indicated in black corresponds to the ellipticity angle inferred from RayDec assuming a negative sign. In each panel, the forward modeled dispersion and ellipticity curves as well as the shear-wave velocity profiles are indicated in color, gray colors indicating models with the lowest misfit.

The H/V peak amplitude at these 6 sites exhibit high value, greater than 3.5. These high H/V peak amplitudes for Tehran’s basin suggest that these sites could present a prograde particle motion (positive ellipticity angle) beyond the fundamental resonance frequency in relation with a large bedrock-sediment velocity contrast (Malischewsky et al., 2008). For these 6 sites, the impedance contrast leading to a positive ellipticity angle has been searched manually. For example, at PLC site (Figure 3-14C), V_s in bedrock should be at least 2650m/s to observe a positive ellipticity (Figure 3-15) when lower V_s in bedrock implies negative ellipticity. At these 6 sites, the minimum shear-wave velocity contrast between rock and sediments necessary to get a positive ellipticity angle at low frequency ranges from 2.06 to 2.36 (Table 3-3). Note that KHJ site also exhibits a high H/V amplitude ($\approx 3.4 \pm 1.0$) at the fundamental resonance frequency ($f_0 \approx 0.6 \pm 0.05$ Hz).

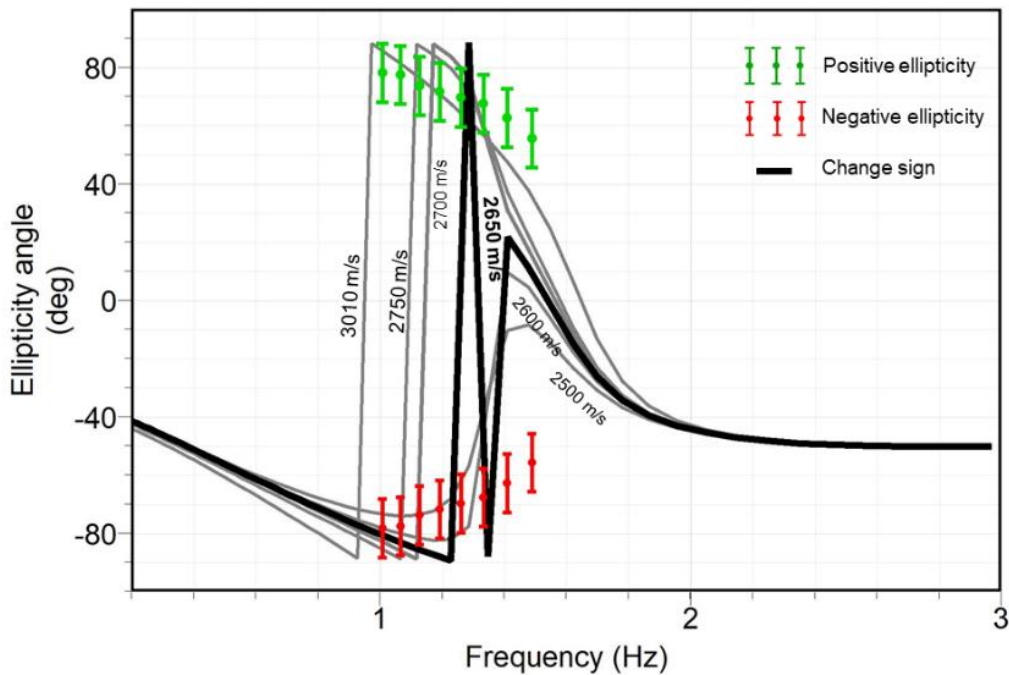


Figure 3-15: Variation of the fundamental Rayleigh wave ellipticity angle as a function of the frequency for various shear-wave velocity contrasts between sediments and seismic bedrock (gray and black curves) at PLC site. The black curve stands for the velocity contrast (values indicated in the figure) leading to a change of the ellipticity angle from negative to positive values for frequencies below 1.4 Hz. The red and green dots, with related uncertainty, correspond to the ellipticity angle inferred from the RayDec method assuming negative or positive angle.

Table 3-3: For the 6 array sites that provide a high H/V amplitude (> 3.5), Minimum shear-wave velocity (V_s) in bedrock that leads to a change of the ellipticity from negative to positive angle. V_s in the deepest sediment layer is extracted from the V_s profiles coming from the inversions.

Array	BBA	MET	PLC	PRD	SDT	SHR
Deepest layer V_s (m/s)	1226	1401	1226	1421	1288	642
Minimum bedrock V_s (m/s)	2850	3300	2650	3150	2850	1325

The inversions allow to derive the V_s profiles down to the seismic bedrock whose depth varies from 89 m to 910 m (Table 3-2) for the best misfit V_s profiles, except at 3 sites (ESH, MZR and SOH) due to a lack of dispersion estimates at low frequency.

Without any deep downhole in the Tehran's basin that reached the seismic bedrock, it is not possible to validate inverted V_s profile. However, the deepest downhole in JICA and CEST (2000) reveals a clayey soil profile with shear wave velocity less than 800 m/s up to 140 m. This downhole was located close to the MVT site, that provides inverted V_s profile in agreement with V_s values from the downhole.

3-5 Building a 3D shear-wave velocity model for Tehran's basin

The main objective of this paper is to construct a reliable V_s model down to the seismic bedrock depth for the Tehran basin. Ibs von Seht and Wohlenberg, (1999) developed an empirical relationship correlating the seismic bedrock depth and the fundamental resonance frequency to interpolate the bedrock depth over a sedimentary basin from the knowledge of the fundamental resonance frequencies only. Figure 3-16A displays the seismic bedrock depth (H) derived from inversion (Table 3-2) with an uncertainty fixed to ± 50 meters as a function of the fundamental frequency (f_0) for the 26 array sites with uncertainty on f_0 varying between 0.05 and 0.2 Hz. Regression between f_0 and H values indicates an inverse power relationship as follows:

$$H = 301.1 f_0^{-0.925} \text{ with } R^2 = 0.88 \quad (\text{e.q. 3-1})$$

Figure 3-16B displays the fundamental resonance frequency-sediment thickness relationship obtained for Tehran basin together with relationships from 8 other sites worldwide (adapted from Thabet, 2019). It indicates that the Tehran's basin is relatively deep and also stiffer compared to other well-known basins, consistently with geological and geotechnical studies that indicate Tehran deposits as stiff soils (Engalenc, 1968; JICA and CEST, 2000; Shafiee and Azadi, 2007).

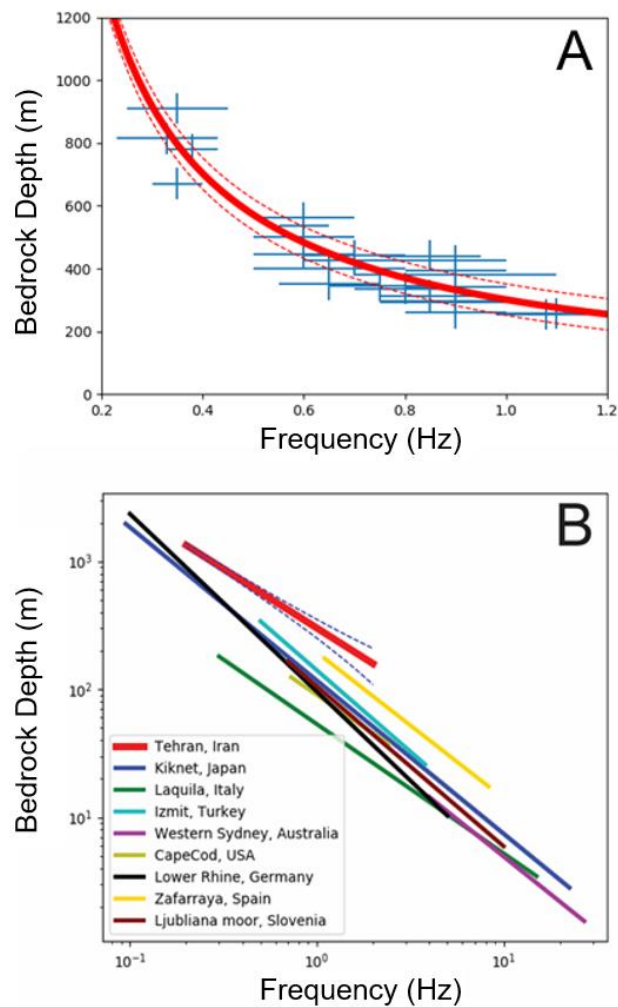


Figure 3-16: A. Relationship between the fundamental resonance frequency and the seismic bedrock depth in Tehran's basin. The red line represented the inverse power fitted curve and red dashed lines are the $\pm 50\%$ confidence intervals. B. Comparison of the relationship obtained in Tehran's basin with other sedimentary basins over the world (adapted from Thabet, 2019).

Applying the resonance frequency – bedrock depth relationship (Eq. (3-1)) to the 159 sites exhibiting a clear resonance frequency allows to map the seismic bedrock depth throughout the Tehran’s basin (Figure 3-17). While seismic bedrock depth is found to vary between 200 and 400 m in the northeast of the Teheran’s basin, the bedrock depth is increasing in the southwest with maximum bedrock depth reaching 900 m.

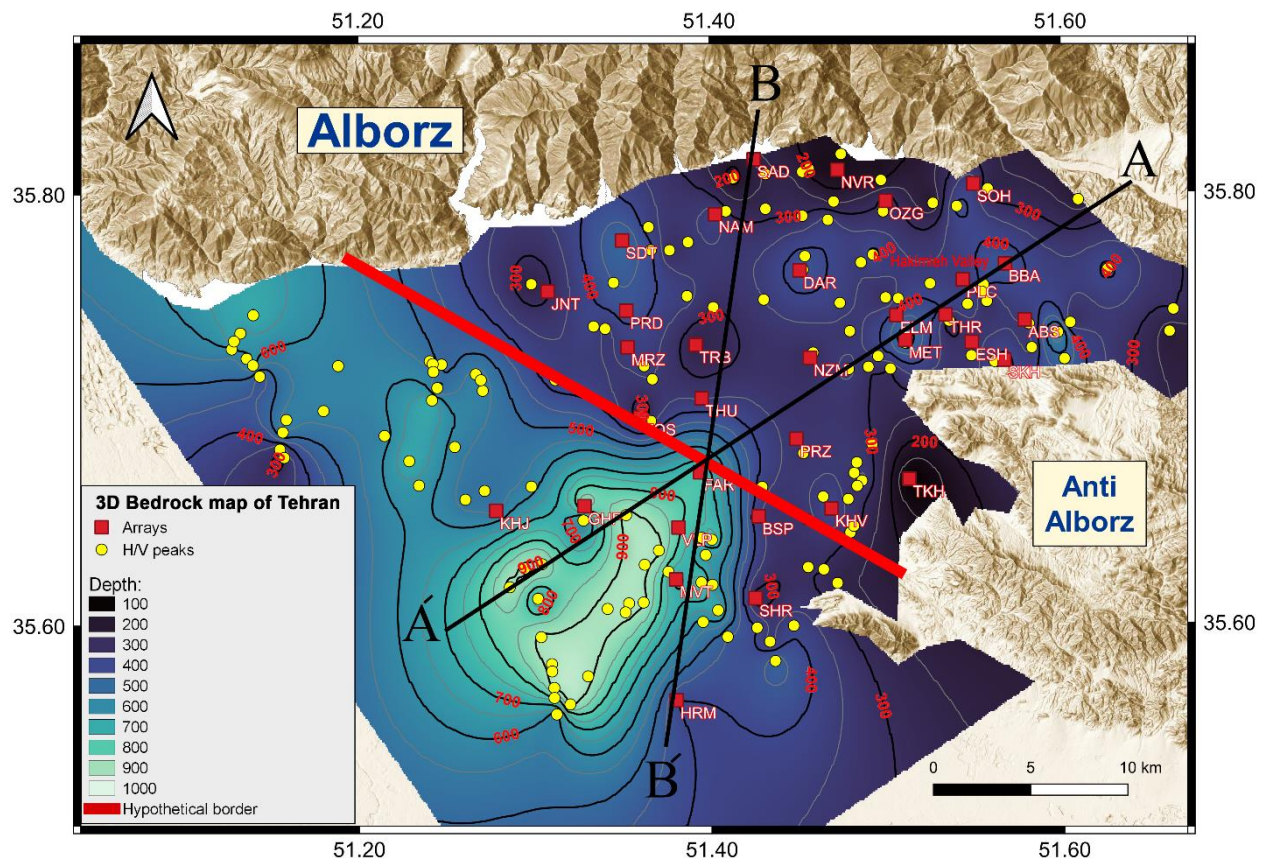


Figure 3-17: Seismic bedrock depth of Tehran obtained from the relationship between the fundamental resonance frequency and the seismic bedrock depth. The red squares indicate the seismic array location.

The yellow dots represent the location of used H/V to estimate bedrock. The red line shows the hypothetical border separating the NE and the SW of the basin. The black line indicates the cross sections.

Combining all the inverted V_s profiles coming from each array, the seismic bedrock depths inferred from the resonance frequency-sediment thickness relationship and V_{s30} inferred from geotechnical data allows to extract two cross-sections (Figures 3-18 to 3-19). For each of these 2 cross-sections two panels are shown:

- the first one (upper panel, Figures 3-18A and 3-19A) is a geophysical interpretation based on the V_s profiles extracted from inversion and the seismic bedrock depth extracted from the 3D seismic bedrock depth map (Figure 3-17). These geophysical cross-sections are created by interpolating between one-dimensional V_s profiles using linear interpolation scheme.

- the second panel (lower panel, Figures 3-18B and 3-19B) shows a geological interpretation of the corresponding geophysical interpretation sections. We assumed that, for the most superficial layer, V_s between 500 to 1000 m/s represents the more recent alluvium which are 'B', 'C' and 'D' formations, distinction between the formation being deduced from the geological and geotechnical data. The deep layer with velocities ranking between 1000 to 1500 m/s represents the oldest and more consolidated Quaternary sediment, corresponding to the 'A' formation.

These cross sections outline a shallower depth of bedrock in the northern part of the basin with an abrupt depression in central part of the basin (close to FAR-GHP and VLP sites). In the southwestern part of the basin, it can be observed a gentle uplifting of bedrock toward the southern hills of the basin. In the northeastern area, the cross-sections suggest an uplift of the bedrock depth, which may be the signature of folding structures.

From about 50 m thick in the northeastern part of the basin, thickness of the superficial layer (B-C-D formations) increases up to about 300 m in the center of the basin (close to FAR-GHP and VLP sites) while reaching about 150-200 meters in the southwest.

Beneath this superficial layer, the stiffer layer (corresponding to A formation) is thicker in the southwest (about 800-850 m thick) compared to the northeast (about 200-300 m thick) part of the basin, with a decreasing thickness close to the NTF (about 40-60 m thick at SAD, Figure 3-19B).

Figure 3-20 displays the shear wave velocity distribution of the superficial (Figure 3-20A) and deep layers (Figure 3-20B) in the Tehran basin. For the superficial layer, the shallowest velocities are observed in the southern part of the basin, indicating the recent sedimentation regime from north to south (formations 'C' and 'D'). The lower velocities observed in stations NVR and SAD in north can be attributed to the presence of local valleys. However, the highest shear wave velocity is found in the north-central stations and between the Alborz and Anti-Alborz.

For the deeper layer, a similar pattern is observed, with the highest shear wave velocity located in the eastern region between the Alborz and Anti-Alborz Mountain ranges. This can be attributed to the accumulation of the ancient 'A' formation sediments in this part. It also appears that the characteristics of the deep layer gently change below the PRD and NZM stations.

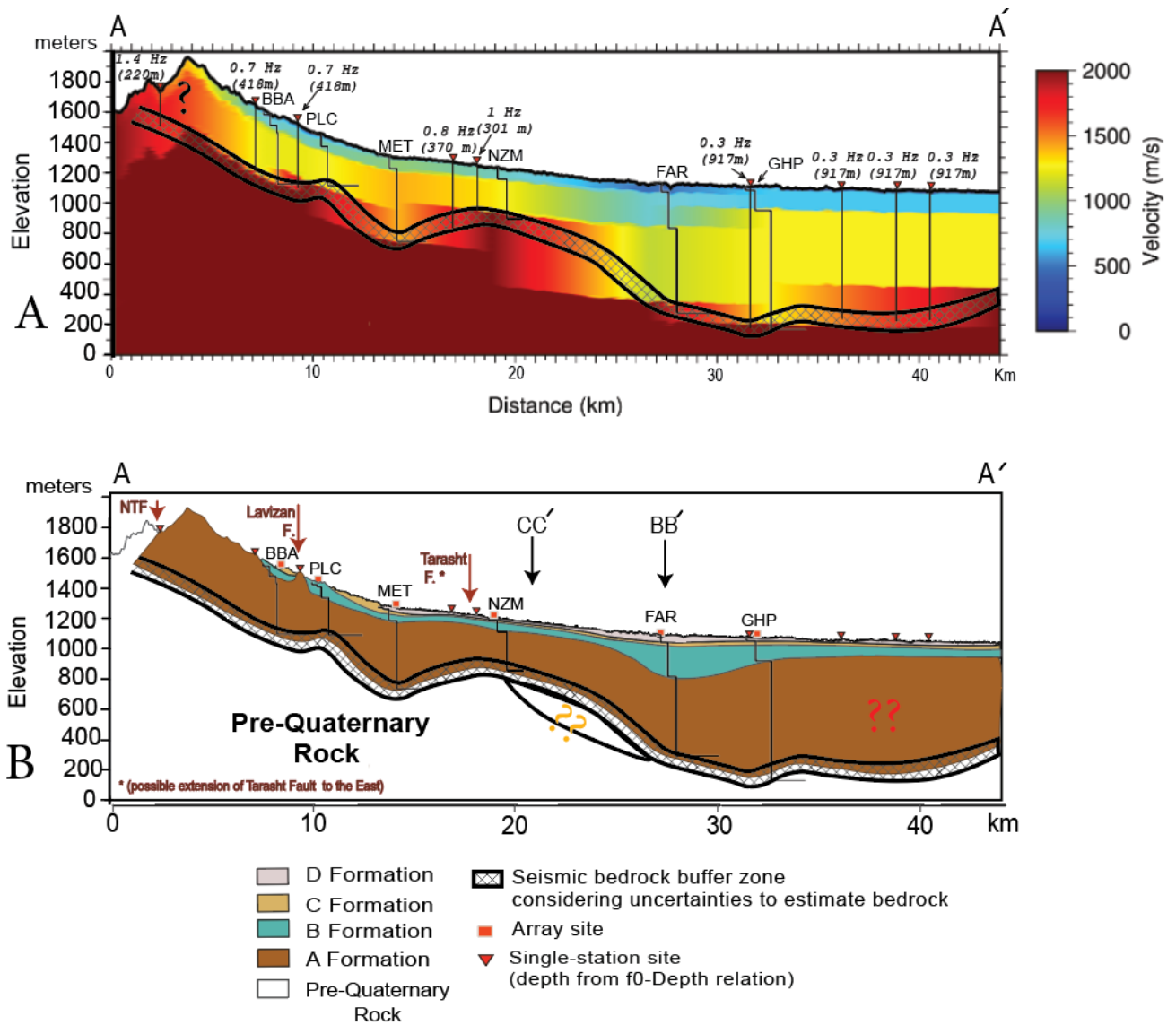


Figure 3-18: Interpretation of the geophysical (A) and geological (B) AA' cross section. A: geophysical representation with the inverted Vs profiles (names of the arrays are indicated on the cross-section) and the bedrock depth inferred at single-station sites using the resonance frequency-sediment thickness relationship. The dashed area represents the uncertainty on the seismic bedrock depth fixed to +/- 50 m. B: geological interpretation inferred from geophysical data and surface geology. The red question marks correspond to limited knowledge about the extension of A formation under the southern part of the city. . The yellow question marks correspond to the doubt about the bedrock depth shape between NZM and FAR due to the absence of data.

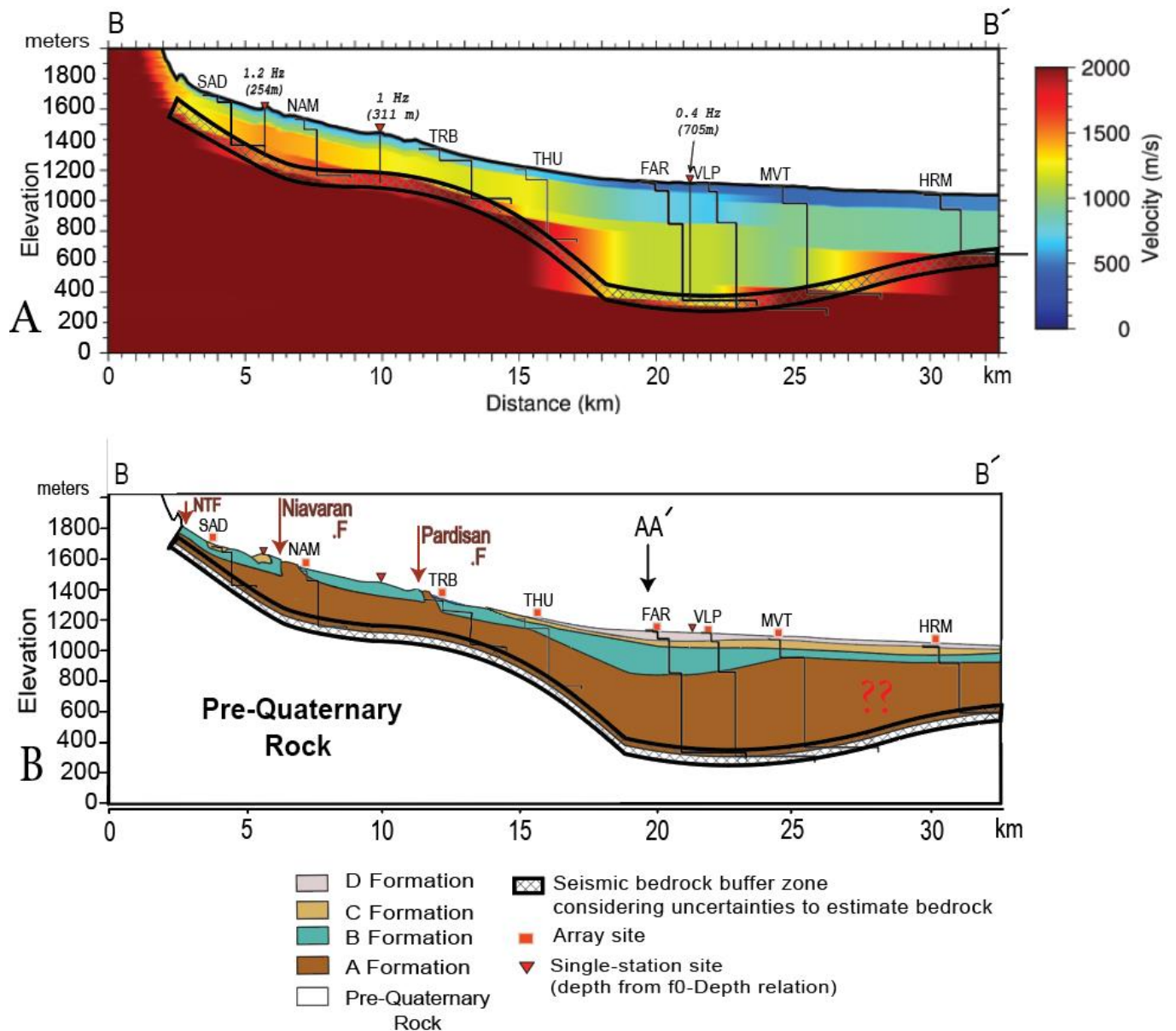


Figure 3-19: Interpretation of the geophysical (A) and geological (B) BB' cross section. A: geophysical representation with the inverted V_s profiles (names of the arrays are indicated on the cross-section) and the bedrock depth inferred at single-station sites using the resonance frequency-sediment thickness relationship. The dashed area represents the uncertainty on the seismic bedrock depth fixed to ± 50 m. B: geological interpretation inferred from geophysical data and surface geology. The red question marks correspond to limited knowledge about the extension of A formation under the southern part of the city.

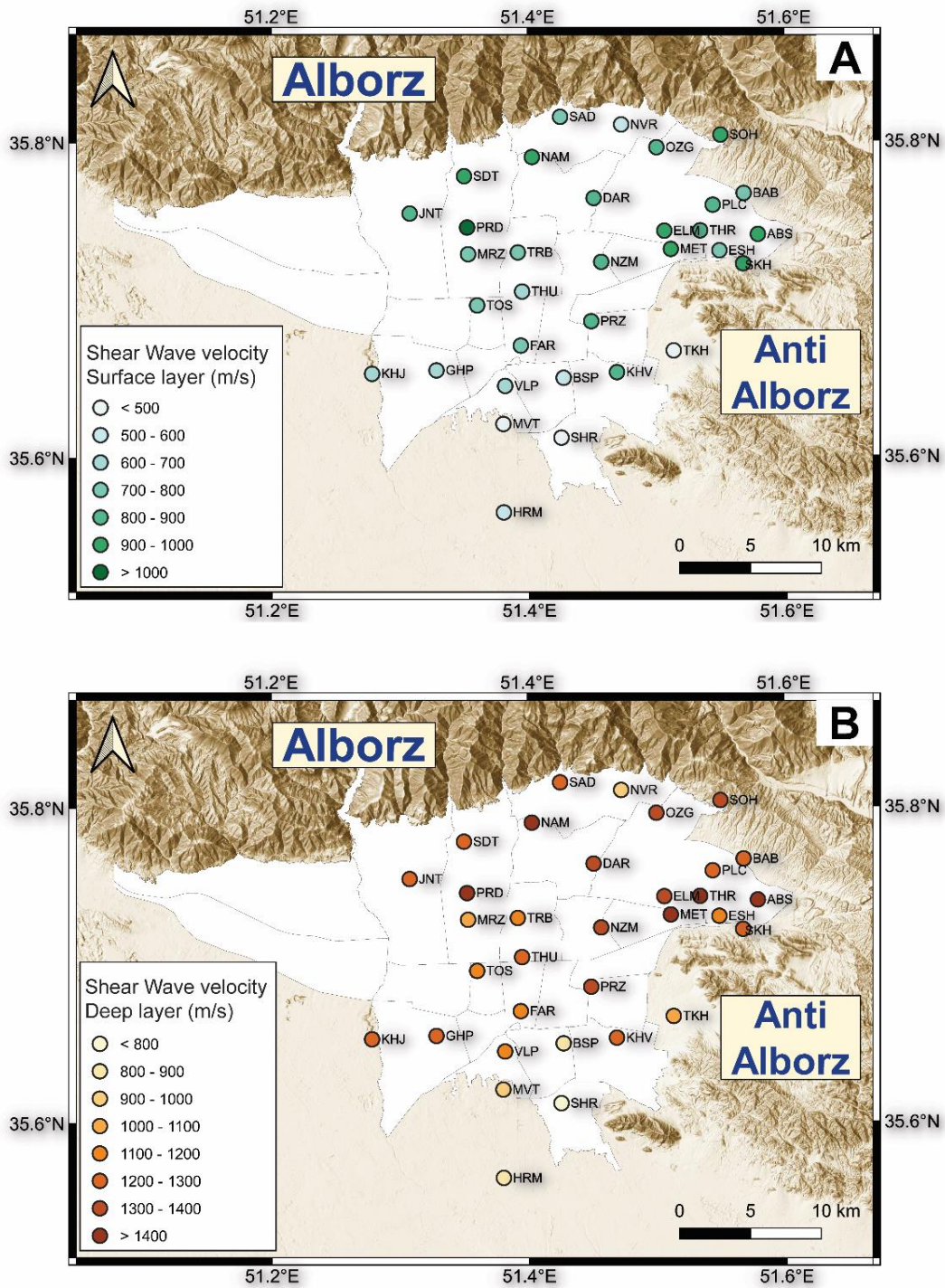


Figure 3-20: Distribution of shear-wave velocities for A) the surface layer corresponding to B, C or D formation and B) the deep sediment layer corresponding to A formation.

3-6 Discussion and conclusion

This paper is a first attempt to construct a 3D velocity model of the Tehran's basin from a large set of various geological, geophysical (active and passive surface wave methods, single-station methods) and geotechnical data. The V_s structure of the basin from the surface to the seismic bedrock depth has been inferred at 26 sites in Tehran from joint inversion of Rayleigh and Love waves dispersion curves, ellipticity of Rayleigh waves, resonance frequency, constrained by available geological and geotechnical information. The determination of the relationship between fundamental resonance frequency and seismic bedrock depth at these 26 sites and its application to 159 sites exhibiting a clear resonance frequency has allowed to map the seismic bedrock interface. Interestingly, the H/V method applied on seismic ambient noise was in most cases failing to provide the fundamental resonance frequency of the site, consistently with previous studies (Haghshenas, 2005; Guillier et al., 2007). Indeed, only 25% of the large set of single-station measurements could be used to extract the fundamental resonance frequency of the soil, the majority of these measurements being located in the southern part of the basin. One of the reasons could be the lack of energy in the lower frequency part of the seismic noise wavefield (< 1 Hz). However, the comparison of the ellipticity of Rayleigh wave coming from seismic noise recording (low energy at low frequency) with earthquake codas (larger energy at low frequency) at 5 sites outlines that both ellipticities are very similar, which suggests that the lack of energy in the seismic noise wavefield at low frequency might not be the only reason for the H/V method failure to provide the fundamental resonance frequency. A deeper understanding of the seismic noise wavefield characteristics would require long duration dense array measurements of both seismic noise and earthquake recordings.

The 3D map of the seismic bedrock interface indicates that Tehran's basin is relatively shallow in the northeast (about 400 m depth) and deep in the southwest (up to 900 m) of the city with a rather abrupt transition from northeast to southwest. The V_s profiles outline the presence of a superficial layer of thickness varying from 50 m to 150 m with V_s from 500 m/s to 1000 m/s overlaying a stiffer layer with V_s ranging from 1000 m/s to 1500 m/s and thickness varying from 200 m in the northeast to 800 m in the southwest. Both seismic bedrock depth and V_s spatial variation throughout the Tehran basin are consistent with the seismic tomography performed in the region (Shirzad and Shomali, 2014) and known geology, the deepest part of the basin forming a local bowl shape,

consistently with the deep depression proposed by geological studies (Engalenc, 1968; Tchalenko et al., 1974). Interestingly, inversion of V_s profile including the ellipticity angle of Rayleigh at low frequency at some site has allowed to provide a first estimate of the minimum V_s in seismic bedrock that is most probably larger than 2600 m/s.

Previous studies have indicated that site effect in Tehran may be linked to the north-south sedimentation regime from the northern highlands and the east-west geological structures such as faults, resulting in a north-south increase in amplification and a decrease in resonance frequencies (Haghshenas, 2005). According to our findings, there is a northeast-southwest trend in the observed variations of sediment thickness, which could be attributed to the presence of northwest-southeast structures. The existence of these discontinuities was previously unknown and were only recently mentioned by some researchers (Abbassi and Ghods, 2020) based on geological field observations. This northeast-southwest discontinuity with a rather laterally abrupt sediment deepening in the center of the basin most probably control the observed site amplification (Figure 3-1), with larger amplification in the southwest part of the city at low frequency.

Since the Tehran's basin comprises a larger area than the region studied in this study, further measurements will be necessary to extend the 3D velocity model, especially towards the south and the west. However, this first 3D velocity model can be used to perform the first 3D numerical simulations of ground motion in Tehran in order to understand and quantify the multi-dimensional site effects on the site amplification/ground motion.

../

Now we are ready to adopt our 3D velocity model to be used in the numerical simulation. However, in order to make the model compatible with simulation community codes, we need to make certain definitions and simplifications which will be discussed in following section.

3-7 Representative V_s and V_p models for sediments and seismic bedrock

In order to be able to simulate ground motion in the Tehran basin up to 2 Hz, i.e. that encompasses most the expected site effects at low frequency (Figure 3-9), it needs to derive from the different V_s profiles presented in the previous sections a V_s (and V_p) model representative of the sedimentary layers in the basin, as well as the P- and S-wave velocity in the bedrock.

3-7-1 Seismic bedrock velocity and uncertainty in bedrock depth map

The S-wave velocity in the seismic bedrock cannot be determined solely by inversion results, although our inversion at some sites indicate that the V_s in bedrock is at least 2.6 km/s (Table 3-3). Beside this, previous studies on crustal structures in Tehran have also proposed certain values for bedrock velocity. For example, Abbassi et al., (2010) created a simplified model for the crustal velocity structure in the southern edge of the central Alborz (the exact location of Tehran) from the results of local earthquake travel time inversion and joint inversion of receiver functions and Rayleigh waves. Their model resulted in $v_p = 5.4$ km/s up to a depth of three kilometers and a $\frac{v_p}{v_s}$ ratio of 1.77. Based on their model, the v_s for bedrock velocity can be estimated to 3.05 km/s. Shirzad et al., (2018) also introduced the shallow/upper crustal shear wave velocity structure from the inversion of Rayleigh wave dispersion measurements and found a quick transition in v_s at depth below 2 km corresponding to the possible bedrock, with a v_s which ranges between 3 km/s and 3.4 km/s at this depth. As regards V_p , Rezaei Far and Kissling (2018) suggested value of 5.9 km/s based on a dataset of more than 25,000 first P-arrivals for all northern part of Iran including central Alborz. Recently, SoltaniMoghadam et al., (2019) proposed 5.35 km/s for V_p using fuzzy self-tuning particle swarm optimization method (Nobile et al., 2018) at a very shallow crustal structure below 5 kilometers. All mentioned values found in literature are shown in Table 3-4.

Given these proposed values for bedrock velocity, I selected for V_s the value of 3 km/s presented by Abbassi et al. (2010) for the southern edge of the central Alborz close to the Tehran, also observed by Shirzad et al. (2018) beneath Tehran and confirmed by our current study. For V_p , we consider the value of 5.2 km/s assuming a Poisson coefficient of 0.25.

Table 3-4: P- and S- wave velocity for the Alborz region for depth shallower than 5 km

Reference	Vs (km/s)	Vp (km/s)	Reference	Vs (km/s)	Vp (km/s)
Priestley et al., 1994	-	5.6	Shirzad et al., 2018	3~3.2	-
Tatar et al., 2007	3.2	5.6	Rezaei Far et al., 2019	-	5.9
Abbassi et al., 2010	3.05	5.4	Maheri Peyrov et al., 2020	-	5.3
Nemati et al., 2013	-	6.0	SoltaniMoghadam et al., 2020	-	5.35
Shomali and Shirzad, 2015	2.9	-			

Due to the fact that the 3D bedrock depth model is generated by interpolation (Figure 3-17), the interpolated bedrock depth value at a specific array site location is not strictly identical to the inverted 1D velocity profile value (Table 3-2). This error comes from the Kriging method for interpolation which involves fitting a mathematical model to the spatial correlation structure of the data, which is used to predict values at locations where data is not available. The accuracy of the kriging method depends on the spatial correlation structure of the data and the variogram model used which defines as the covariance exhibited between each pair of points in the sampled data. In this interpolation, I used a linear variogram to interpolate the data implemented in Surfer Golden software and the smoothing process was done in QGIS using a smoothing distance of 50 meters in order to avoid abrupt changes in bedrock depth especially at the basin's edges. Figure 3-21 shows the differences in bedrock depth before and after interpolation and smoothing.

3-7-2 Representative velocity layering model for sediments

3-7-2-1 Comparison between 1D resonance frequencies and observed H/V peak frequencies

Using the best velocity models from the inversion at the 33 array sites and considering the rock P- and S- velocities defined in the previous section, I calculated the 1D SH-wave transfer function using the Thompson-Haskell propagator matrix approach (Kennet, 1983). For these simulations, I assumed a sediment density of 2000 kg/m³ and a rock density of 2700 kg/m³.

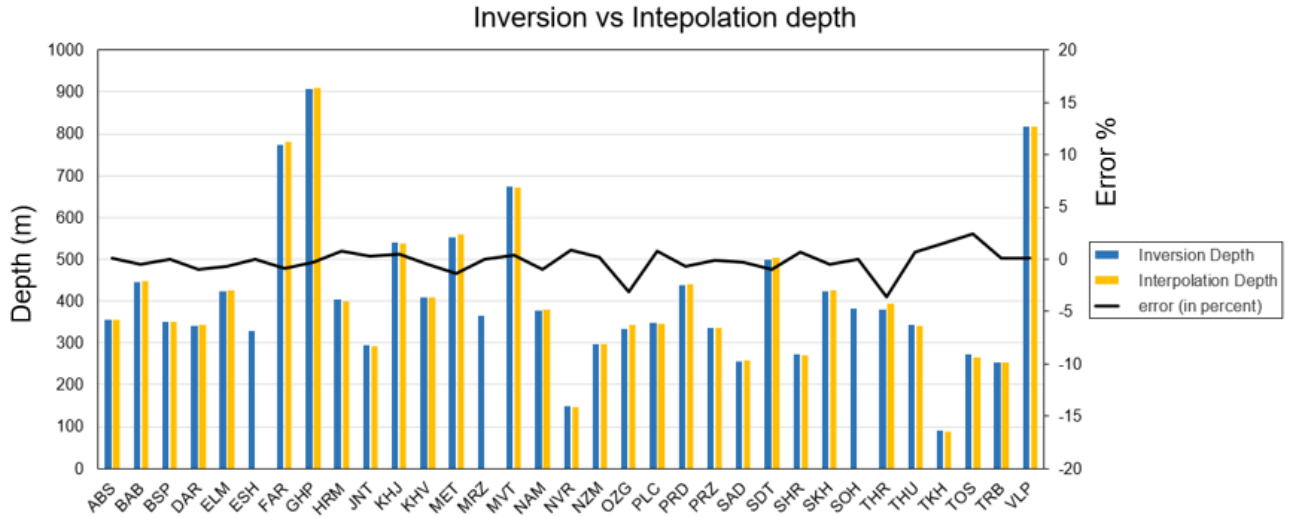


Figure 3-21: The differences between inverted (blue bars) and interpolated (yellow bars) bedrock depth. Left axis indicates the depth and the right axis indicates relative error that does not exceed about 5%.

As examples, the SH transfer function for two selected stations (DAR in the north and FAR in the south) are illustrated in Figure 3-22. The theoretical 1D resonance frequencies are then compared with observed H/V peak frequencies (f_0) values in Tehran (see Table 1; Appendix B).

Figure 3-23 shows the H/V peak frequencies with related uncertainty and the theoretical f_0 . For the seven stations where H/V curve did not exhibit any peak, the only displayed values are the theoretical ones. Table 3-5 provides the relative error between the two resonance frequency estimates which also displayed in Figure 3-24.

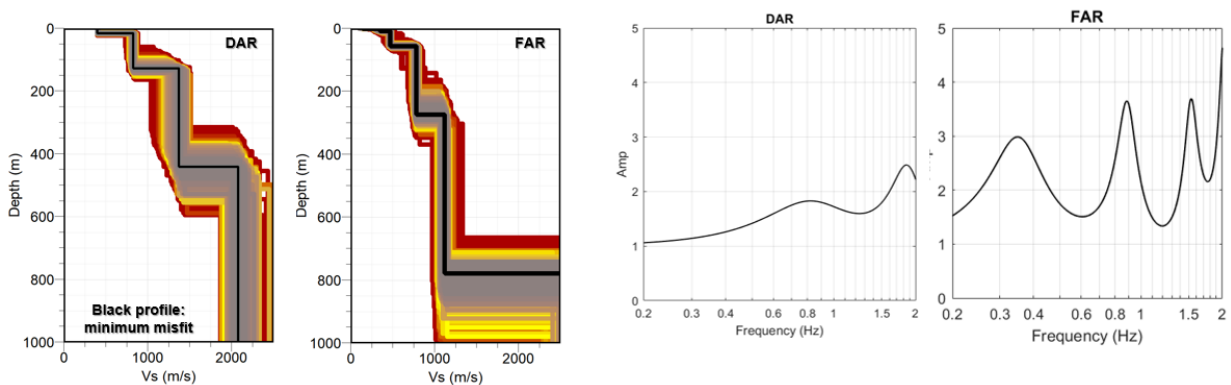


Figure 3-22: Example of SH transfer functions for two sites in north (DAR) and south (FAR) of Tehran. The best misfit profiles are indicated in black on the inversion results (left panel) and the corresponding theoretical SH transfer function are indicated in the right panel.

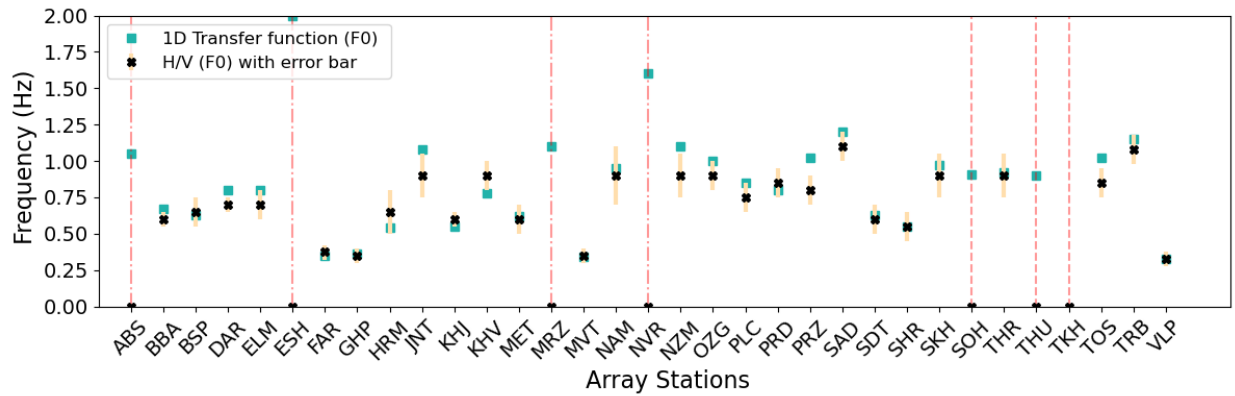


Figure 3-23: Fundamental resonance frequencies (f_0) extracted at array sites (black squares) with estimated error (orange lines) and the theoretical f_0 (green square) from 1D transfer function. The red dashed lines represent the array sites at which no f_0 could be extracted from H/V curves.

The relative errors between the theoretical and the measured resonance frequencies for four stations (JNT, TOS, PRZ, and NZM) exceed 20%, while for other stations, the errors are acceptable because they fall within the range of the uncertainty of the actual H/V peak frequencies. This good agreement between theoretical and observed frequencies was expected, given that resonance frequencies were used in the inversion of velocity profiles (Table 3-2). For the four stations JNT, TOS, PRZ and NZM that are located close to the transition between the shallowest and deepest sediments in Tehran, the larger difference reflects the difficulty the inversion had in finding the best 1D velocity model in a context of seismic wave propagation more complex than 1D.

Table 3-5: Relative error between the measured and the theoretical f_0 .

Station	Relative error %						
BBA	-11.7	JNT	-20	OZG	-11.1	SKH	-7.8
BSP	3.1	KHJ	8.3	PLC	-13.3	THR	-2.2
DAR	-14.3	KHV	13.3	PRD	5.9	TOS	-20
ELM	-14.3	MET	-3.3	PRZ	-27.5	TRB	-6.4
FAR	7.9	MVT	2.9	SAD	-10	VLP	3.1
GHP	-2.9	NAM	-5.6	SDT	-5		
HRM	16.9	NZM	-22.2	SHR	-1.8		

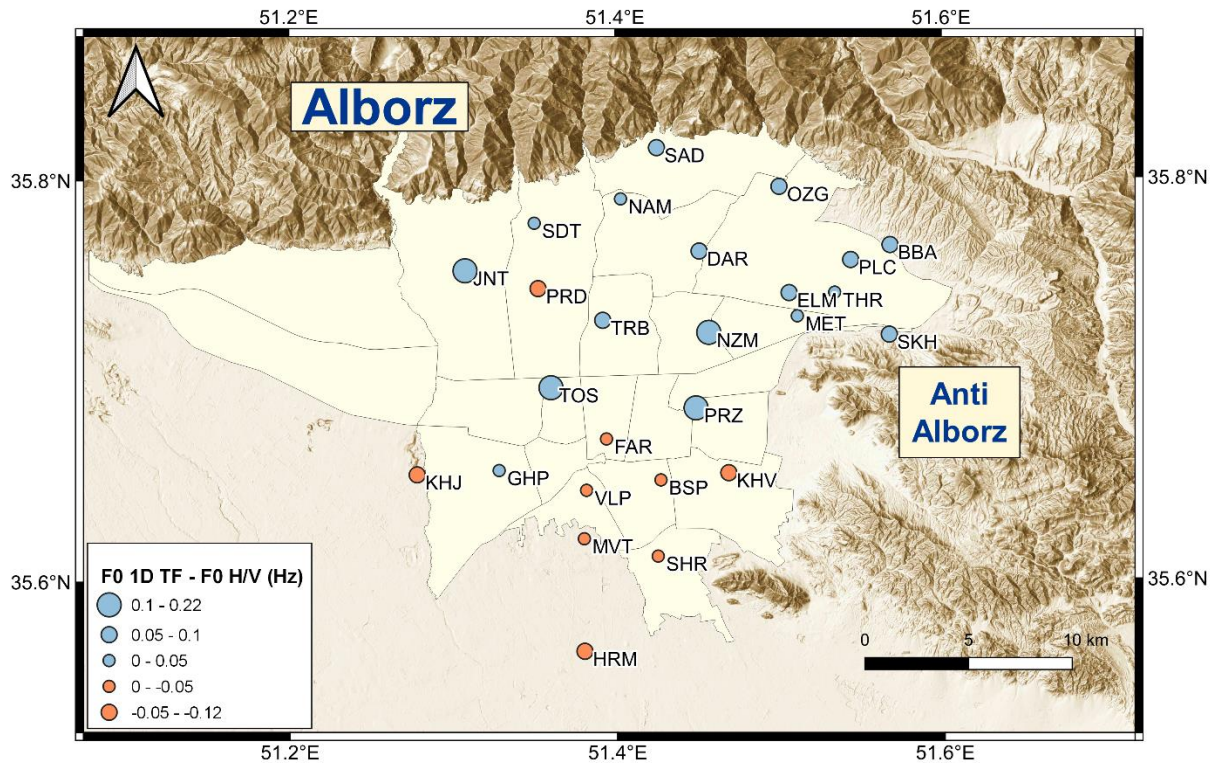


Figure 3-24: Tehran Basin map showing the absolute difference between f_0 from the transfer functions and the f_0 extracted from the H/V curves.

3-7-2-2 Simplification of the Vs layering in sediments

According to the inversion results and based on Tehran geology, the majority of V_s profiles consisted in three to four sedimentary layers overlying the seismic bedrock. In most cases, the most superficial layers correspond to the superficial formation D of Tehran sediments and remain relatively thin i.e., less than ten to twenty meters thick. It could thus be possible to exclude these shallow layers when deriving a representative V_s profile without significantly impacting the ground motion simulation results in the low-frequency band (< 2 Hz) i.e. for the largest wavelengths.

Example of such simplification of the V_s profiles is illustrated in Figure 3-25 for two sites, showing that the theoretical 1D site transfer functions are not significantly modified at the fundamental resonance frequencies. Comparison between theoretical fundamental resonance frequencies including or not the most superficial layers provides very similar frequencies as indicated in Figure 3-26, which confirms that the best misfit V_s profiles can be simplified to two sedimentary layers overlying the bedrock by removing the most superficial sedimentary layers.

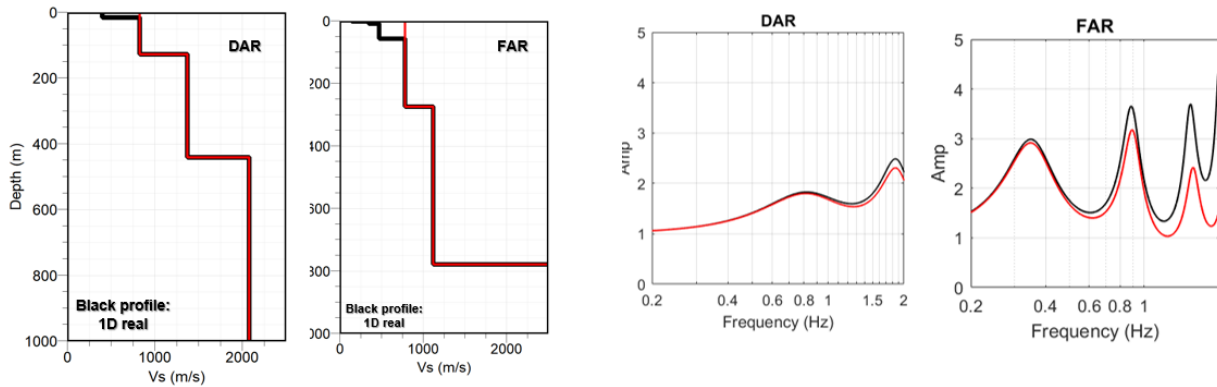


Figure 3-25: Best misfit Vs profile (in black) for two sites in north (DAR) and south (FAR) of Tehran (left panel) and the simplified Vs profile (in red) (left panel), and the corresponding theoretical SH transfer functions for the best misfit Vs profile (in black) and the simplified one (in red, right panel).

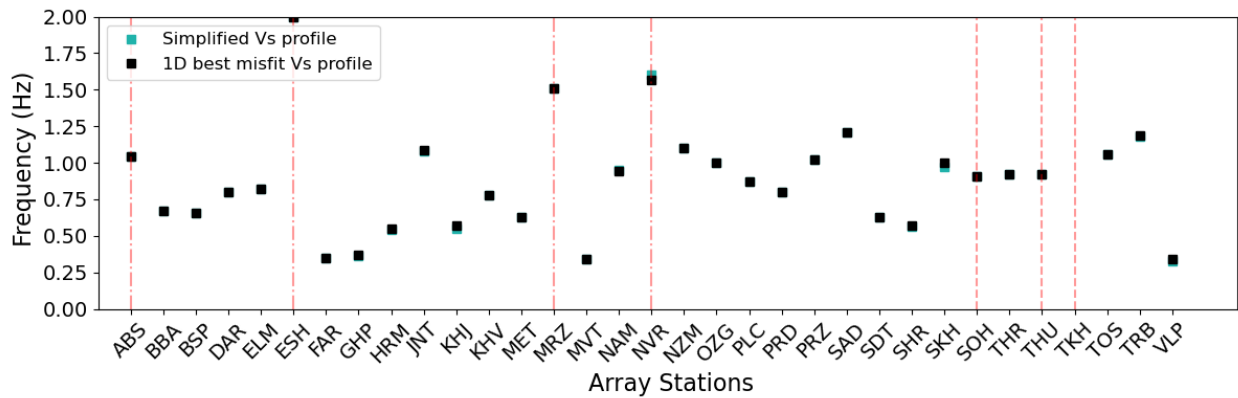
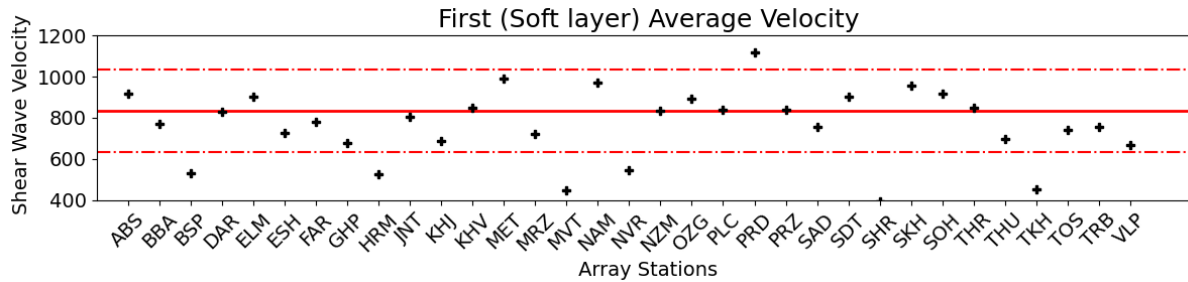


Figure 3-26: Theoretical f_0 from best misfit Vs profiles (3 or more sedimentary layers, in green) and the simplified one (2 sedimentary layers, in black). The maximum difference between frequencies is less than 0.03 Hz.

Next, I observed that the subsurface structure is characterized by layers of sediments with slightly varying lateral Vs (Figure 3-20). For the sake of simplicity in the implementation in the wave propagation simulation code (De Martin, 2011; EFISPEC3D) and given that I do not have the enough spatial resolution of Vs allowing to provide a Vs model with laterally varying Vs, I computed an average Vs for the first (soft layer corresponding to formation B) and second (hard layer corresponding to formation A) sedimentary layers from the simplified Vs profiles derived at the 33 array sites (Figure 3-27). In Figure 3-27, I fixed an error at ± 200 m/s for the first layer (red dashed lines) and at ± 250 m/s for the second layer (blue dashed lines). The Vs averages were estimated excluded 27 stations with outlier values (i.e. exhibiting values not inside the fixed error). The average Vs for the soft layer is 835 m/s, while for the hard layer, it is 1272 m/s. For Vp, we

consider a value of 1670 m/s and 2544 m/s for the soft and hard layers, respectively, assuming a Poisson ratio of 0.33 in lack of any other information of V_p in sediments.

A



B

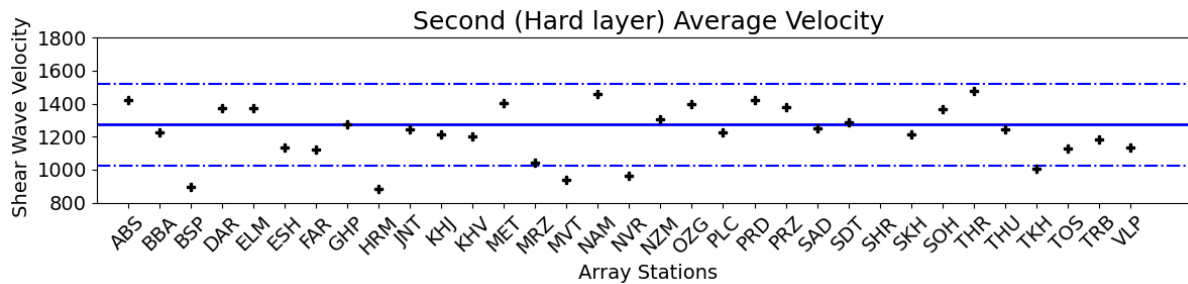


Figure 3-27: Distribution of V_s (black crosses) for the soft layer (A) and the hard layer (B) for the 27 array sites. The red or blue plain lines represent the average velocity from the 27 sites. For the soft layer (A) the dashed lines represent ± 200 m/s and for the hard layer (B) the dashed lines represent ± 250 m/s.

The thicknesses of the soft layer are determined at any location in the basin by 3D interpolation of the interface between the soft and the hard layer from the 33 array sites, while the thickness of the hard layer is simply given by the difference between the bedrock depth map and the thickness map of the soft layer.

These simplified V_s structure thus allow us to compute the 1D transfer function not only at the array station, but also in all other areas of the basin.

Then, the theoretical SH transfer functions are computed at all array sites using this simplified V_s layering model. Comparison between theoretical fundamental resonance frequency derived from this simplified V_s model and H/V peak frequencies at the 33 array sites (Figure 3-28) indicates that the sites identified as outliers in the averaging process lead to the greatest error (out of NVR and TKH sites which have no H/V f_0). Among these stations, BSP, MVT and SHR have relative errors of 30%, 30%, and 78% respectively. The difference in frequencies for other sites is less than 20% with the mean value of 5.2% (Figure 3-29).

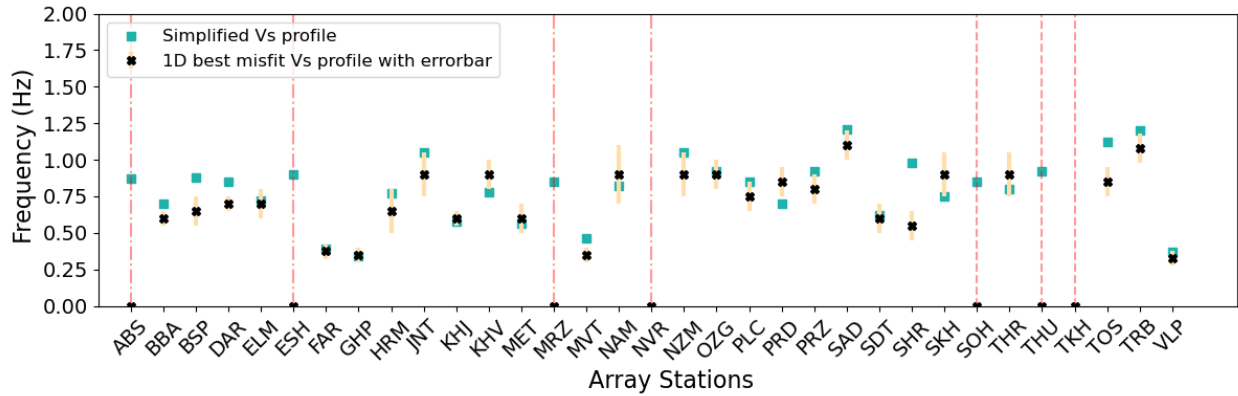


Figure 3-28: Fundamental frequencies (f_0) extracted from array stations (black x) with estimated error (orange bars) and the calculated f_0 (green square) from 1D transfer function for double simplification 1D models. The red dashed lines represent the arrays without f_0 coming from H/V curves.

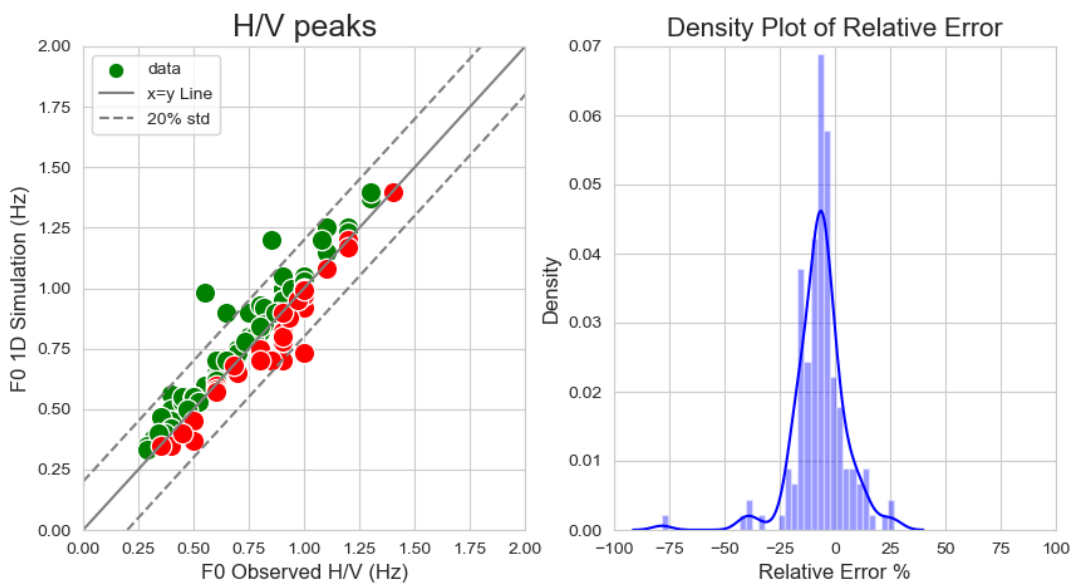


Figure 3-29: Evaluation of the errors linked to the simplified Vs model comparing the fundamental frequencies derived from H/V curves and from the 1D simplified Vs layering model. Left panel: scatter plot of f_{0HV} peaks and f_{0TF} extracted from 1D SH transfer functions. The dash line represents the 20% standard deviation. Right panel: the density plot of the relative error between the observed H/V peak frequencies and the theoretical ones.

3-8 General Conclusion

In this chapter, I derive the velocity structure of Tehran basin using an extensive geophysical, geotechnical and geological surveys. It shows that the basin has a large variation in the seismic bedrock depth (from about 90 m to about 900 m) with strong lateral variation from the northeast to southwest and possible multi-dimensional effects of basin deepening in those areas. The retrieved model is compatible with known geological knowledge of the basin and gives an idea about the geometry and physical properties of the basin. Then I simplify the velocity structure to make it usable in our 3D numerical scheme. While the simplifications may have led to an overestimation of the shear wave velocity in some parts of the basin, the obtained error values can help us to interpret the results of the final 3D model more accurately.

In the next chapter, I will discuss how to incorporate this velocity model into EFISPEC3D code and analyze the simulation modeling results, considering the findings of this chapter.

Chapter 4

*3D numerical simulation of the seismic response of the Tehran
sedimentary basin*

4-1 Introduction

In chapter one I introduced the first site effect study in the Tehran basin done by Haghshenas (2005). Although in a first glance, the geometry of the vast urban area of Tehran does not resemble a typical narrow 3D types of valley's, the probable large thickness of quaternary alluviums with lateral discontinuities make multidimensional effect possible in this basin (Haghshenas, 2005). According to that study, the existence of multidimensional effects is directly observed from SSR and indirectly supported by the significant difference between observed SSR and the H/V results (see also: chapter 1; section 1-5-2) although the lack of sufficient energy at low frequencies within the seismic noise wavefield could also be responsible for this notable discrepancy.

To find out what caused these observations, I designed passive and active seismic campaigns to understand the geometry and physical properties of the sedimentary basin. In Chapter three, I successfully created the first ever 3D velocity structure for the Tehran basin that revealed a clear lateral discontinuity in the sediment-to-bedrock interface situated in the center of the basin and very thick and stiff sediments.

Once the 3D velocity structure model is constructed, it is essential to validate its accuracy and reliability. The primary method for assessing the model's reliability is by subjecting it to physics-based numerical simulations and evaluating how well observations can be reproduced through numerical simulation. In present chapter, I will verify the accuracy and reliability of the acquired model by performing 3D numerical simulations of surface ground motion. These simulations will employ the velocity structure model that allowed for the set-up of a 3D computational model.

During the validation process, I will compare the results from the simulations with the site-to-reference (SSR) results from Haghshenas (2005). The objective of this comparison is to determine whether the 3D structure model can accurately reproduce the local site amplification characteristics. Then I will use these ground motion simulations to study site amplification characteristics throughout Tehran's basin.

4-2 Numerical methods in seismology

4-2-1 Introduction

We live in a three-dimensional world and the waves that travel from an earthquake source; reach the surface layers and amplify; all pass through a three-dimensional medium. It means that 1D response analysis cannot fully describe the physics of the wave propagation and predict the real ground motion on the surface. Therefore, without 3D analysis, it is hard to understand how the whole 3D medium affects the seismic wave propagation.

As mentioned in previous chapters, the main advantage of the experimental methods is the direct measurement of site effect indicators. However, the experimental methods have some disadvantages. First, in most cases, it might be not enough recording stations available to achieve the necessary resolution to calculate amplification all over the basin. For example, in Tehran, despite the moderate seismicity, it is not always feasible to construct new temporary seismic stations or permanent networks due to a lack of financial resources and the high level of seismic noise. Additionally, the number of recorded events in limited time might be not enough, which could make it difficult to study uncertainties and to identify all of the dependencies to input motion (Bard, 2021).

In this situation, numerical methods, derived from applied mathematics to solve 3D partial differential equations, could be an alternative to study the seismic response all over the basin for different earthquake scenarios.

Nowadays, numerical methods are the main tools for extracting quantitative information from complex seismic wave propagation. In this study I use them to evaluate 3D site effects in Tehran's basin caused by 3D medium properties such as surface and subsurface topography, lateral discontinuities, and local velocity changes (Chaljub et al., 2015).

Some of the more widely used numerical modelling methods in seismology are: the finite-difference method (FDM) (Boore 1970; Virieux, 1986; Moczo et al., 2014), Fourier pseudo-spectral method (FPS) (Furumura and Kennett, 2005), Finite element method (FEM) (Bielak and Xu, 1999; Zienkiewicz et al., 2013), and Spectral element method (SEM) (Komatitsch and Vilotte, 1998; Chaljub, 2000). Each method has its advantages and disadvantages depending on the

application while, the FDM is the simplest and, historically, was the first numerical method used in seismological research.

However, in recent years, SEM became the most popular and powerful tool in seismology. In fact, SEM combines the best parts of all the other methods into one efficient numerical approach using i) the FDM benefits for time interpolation, ii) the accuracy and fast convergence of FPS, and iii) the geometric flexibility of the FEM methods (Komatitsch et al., 2004; Igel, 2017). Due to SEM's popularity, flexibility, and efficiency, many SEM codes have been developed to solve the seismic wave propagation in the last 20 year (e.g. Specfem3D, Peter et al., 2011; SES3D, Gokhberg and Fichtner, 2015; AxiSEM, Nissen-Meyer et al., 2014; RegSEM, Cupillard et al., 2012; and others). In this chapter, I will introduce and implement open source EFISPEC3D code (Element-FInis SPECtraux3D) (De Martin, 2011; De Martin et al., 2013) in Tehran's basin using the new sedimentary basin model.

At the end, it should be mentioned that the goal in this section is not to study all mathematical aspects of the numerical methods. Even so, I must introduce a series of basic concepts borrowed by the SEM from the other methods. First, the basic concepts of FDM help to understand the basics of numerical methods and then it helps to solve time-derivative parts of the elastic wave equation in SEM. Then, using pure mathematical analysis based on implementation of plane waves within the FDM (von Neumann analysis), I can generate some fundamental stability relationship (Courant–Friedrichs–Lewy; CFL criterion) for numerical analysis. Finally, reviewing the concepts of basic functions from PSM and assembly from FEM methods I can develop the spectral element algorithm.

4-2-2 Finite difference method

In applied mathematics and physics, differential equations are used to explain various physical phenomena. These equations can be solved using both analytical or numerical approaches. Because analytical approaches only apply to simple models, numerical methods must be used to solve complex problems like the 3D simulation of seismic waves in sedimentary basins. In fact, inside each limited area where there is abrupt changes in material properties (e.g. an interface in a sedimentary basin) analytical methods could not be applicable but it always possible to define a

suitable numerical relation for solving wave equations (Kramer, 1996). For all methods, the final purpose is to replace wave equation derivatives with some mathematical relations that can be easily calculated (Igel, 2017).

Among all methods, the finite difference method (FDM) is considered the most basic grid-based method. In this method, the partial derivatives of elastic wave equation ($\rho \partial_t^2 u = \partial_x (\mu \partial_x u) + s$) (eq. 4-1) are replaced by the FDM approximation of the derivative. Here the ρ stand for density, u is displacement, μ is Lamé parameter and s is the external force.

FDM approximation for the function $f(x)$ defines the limit of the distance between two grid points as below:

$$d_x f(x) \approx \frac{f(x+dx) - f(x)}{dx} \text{ (forward finite difference) (eq. 4-2)}$$

FDM approximation can be also defined by two other “central” and “backward” finite difference approximations based on the definition of grid points location.

$$d_x f(x) = \frac{f(x+dx) - f(x-dx)}{2dx} \approx \frac{f(x+dx) - f(x-dx)}{2dx} \text{ (central finite difference) (eq. 4-3)}$$

$$d_x f(x) = \frac{f(x) - f(x-dx)}{dx} \approx \frac{f(x) - f(x-dx)}{dx} \text{ (backward finite difference) (eq. 4-4)}$$

By introduction of these definition and with the same procedure, the second derivatives of function $f(x)$ can also easily write down by mixing a forward and a backward formula:

$$d_x^2 f(x) \approx \frac{\frac{f(x+dx) - f(x)}{dx} - \frac{f(x) - f(x-dx)}{dx}}{dx} = \frac{f(x+dx) - 2f(x) + f(x-dx)}{dx^2} \text{ (eq. 4-5)}$$

Reaching the numerical approximation of the second derivative, the Taylor series mathematical concept allows to express the accuracy of the approximation. It used to derive the FDM approximations of derivatives by expressing the exact solution of the differential equation. So, by rejecting high order parts of Taylor series, I can derive FDM approximations that are accurate up to a certain order of the truncation error. So, in practice, the accuracy of FDM can be improved by definition of higher order operators of Taylor series. In this regard, for forward and backward FDM, the Taylor series can be written as:

$$f(x + dx) = f(x) + f'(x)dx + \frac{1}{2}f''(x)dx^2 + \dots(\text{eq. 4-6})$$

Which yields to:

$$\frac{f(x+dx)-f(x)}{dx} = f'(x) + \text{err}(dx)(\text{eq. 4-7})$$

While for central FDM it can be defined as

$$\frac{f(x+dx)-f(x-dx)}{2dx} = f'(x) + \text{err}(dx^2)(\text{eq. 4-8})$$

These formulas indicate that centered FDM converges more rapidly to the correct derivative on a regular grid.

It is obvious that for numerical simulation using computers, the continuous form of FDM is not practical. To use FDM in real simulation, the second derivative of the elastic wave equation should be written in discrete space and time notation as follows (Figure 4-1).

$$[\rho \partial_t^2 u = \partial_x(\mu \partial_x u) + s] \leftrightarrow [\rho \frac{u_j^{n+1} - 2u_j^n + u_j^{n-1}}{dt^2} = \mu(\frac{u_j^{n+1} - 2u_j^n + u_j^{n-1}}{dx^2}) + s_j^n] (\text{eq. 4-9})$$

Where the increment du and dt is defined as $u_j = jdu$ and $t_n = ndt$ and j and n are equal to 0 to the end (Figure 4-1).

The main problem related to discrete notation goes back to the solution of the time extrapolation for time in $(n+1)$ (u_j^{n+1}). It can be solved using the information from the previous grid points (n , $n-1$) by matrix inversion at each time step as below.

$$u_j^{n+1} = c_j^2 \frac{dt^2}{dx^2} [u_j^{n+1} - 2u_j^n + u_j^{n-1}] + 2u_j^n - u_j^{n-1} + dt^2 s_j^n (\text{eq. 4-10})$$

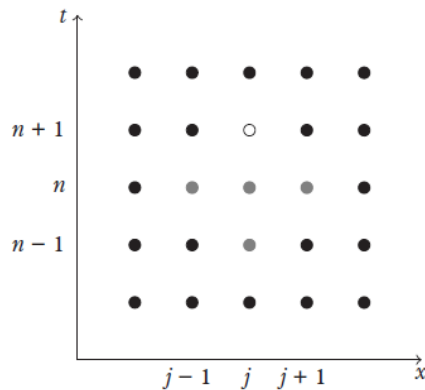


Figure 4-1: Illustration of the space-time discretization scheme and elastic wave equation of the FD algorithm (adopted from Igel, 2017).

Here, it is necessary to note very important concept related to working with discrete schemes. In a discrete scheme, the velocity of the wavefield becomes frequency dependent as a function of the discretization which is caused by the famous concept called numerical dispersion. Von Neumann stability analysis (Charney et al., 1950) is an important step used to check the stability of all numerical solutions and will be described in detail in the following section.

4-2-3 Stability analysis

To understand the von Neumann analysis, I should use the complex harmonic plane wave and insert it into the FDM numerical method. First of all, It can be written easily in continuous form that the acoustic wave equation relation converges to the famous known dispersion relation as below:

$$\partial_t^2 p = c^2 \partial_x^2 p$$

$$p(x, t) = e^{i(kx - \omega t)} \rightarrow \begin{cases} d_x^2 p = -\omega^2 e^{i(kx - \omega t)} \\ d_t^2 p = -k^2 e^{i(kx - \omega t)} \end{cases} \rightarrow -\omega^2 e^{i(kx - \omega t)} = -c^2 - k^2 e^{i(kx - \omega t)} \rightarrow$$

$$c = \frac{\omega}{k} \text{ (eq. 4-11)}$$

Here ω is the angular frequency and K is the wavenumber.

The complex harmonic plane wave is then written in discrete form as :

$$p_j^n = e^{i(k_j dx - \omega_n dt)} \text{ (eq. 4-12)}$$

Similarly, the other space and time steps can be written as:

$$p_{j+1}^n = e^{i(k_{j+1} dx - \omega_n dt)} = e^{ik dx} e^{i(k_j dx - \omega_n dt)} = e^{ik dx} p_j^n \text{ (eq. 4-13)}$$

$$p_{j-1}^n = e^{-ik dx} p_j^n \text{ (eq. 4-14)}$$

$$p_j^{n+1} = e^{-i\omega dt} p_j^n \text{ (eq. 4-15)}$$

$$p = e^{i\omega dt} p_j^n \text{ (eq. 4-16)}$$

By these definitions, the wave equation can be represented in form below:

$$\begin{aligned}
 \frac{p_j^{n+1} - 2p_j^n + p_j^{n-1}}{dt^2} &= c^2 \left(\frac{p_j^{n+1} - 2p_j^n + p_j^{n-1}}{dx^2} \right) \text{ (eq. 4-17)} \\
 &= \\
 e^{i(k_j dx - \omega_n dt)} \left[\frac{e^{i\omega dt} - 2 + e^{-i\omega dt}}{dt^2} \right] &= c^2 \left[\frac{e^{ikdx} - 2 + e^{-ikdx}}{dx^2} \right] e^{i(k_j dx - \omega_n dt)} \\
 &= \\
 e^{i\omega dt} + e^{-i\omega dt} - 2 &= c^2 \frac{dt^2}{dx^2} [e^{ikdx} + e^{-ikdx} - 2] \text{ (eq. 4-18)}
 \end{aligned}$$

By implementing Euler relation ($\cos(x) = \frac{1}{2}(e^{ix} + e^{-ix})$) to the (eq. 4-18) I have:

$$\cos(\omega dt) - 1 = c^2 \frac{dt^2}{dx^2} \cos(kdx) - 1 \text{ (eq. 4-19)}$$

$$[1 - \cos(x) = 2\sin^2\left(\frac{x}{2}\right)] \rightarrow \sin^2\left(\omega \frac{dt}{2}\right) = c^2 \frac{dt^2}{dx^2} \sin^2\left(k \frac{dx}{2}\right) \text{ (eq. 4-20)}$$

$$\sin\left(\omega \frac{dt}{2}\right) = c \frac{dt}{dx} \sin\left(k \frac{dx}{2}\right) \text{ (eq. 4-21)}$$

In equation 4-21, the values of the sine terms on either side should fit inside the range [-1, 1]. If not, the solution will explode and become unstable. So, to have the stable solution the relationship always must be, $c \frac{dt}{dx} \leq 1$.

This condition is called the Courant–Friedrichs–Lewy (CFL) criterion. In this relation, there are two kinds of velocities; the physical velocity in the medium (c) and the grid velocity ($\frac{dt}{dx}$). Simply if I use non-optimal values for dx and dt , the numerical approach will display numerical dispersion. In fact, the criteria indicate that if I have a spatial grid and the seismic wave propagating at velocity c , there is a limitation that should be indicated in time steps simulation depending on CFL criterion. In this regard, for each numerical study, the dt values should be derived from CFL criterion before the simulation starts.

Finally, to understand the effect of grid number on numerical dispersion I recall the phase velocity $c(k)$ from CFL criterion:

$$\sin\left(\omega \frac{dt}{2}\right) = c \frac{dt}{dx} \sin\left(k \frac{dx}{2}\right) \rightarrow$$

$$\omega = \frac{2}{dt} \left[c \frac{dt}{dx} \sin\left(k \frac{dx}{2}\right) \right] \rightarrow c(k) = \frac{\omega}{k} = \frac{2}{k dt} \left[c \frac{dt}{dx} \sin\left(k \frac{dx}{2}\right) \right] \text{ (eq. 4-22)}$$

In this formula the phase velocity depends on the wave number and as it seen below only in the unreal case of $c \frac{dt}{dx} = 1$ the formula exactly recovers the analytical solution as below.

$$c(k) = \frac{2}{k dt} \left[1 \sin\left(k \frac{dx}{2}\right) \right] = \frac{2}{k dt} k \frac{dx}{2} = \frac{dt}{dx} \text{ (eq. 4-23)}$$

However, this is not possible in real simulation since the CFL limit ($c \frac{dt}{dx} = 1$) varies in space in heterogeneous material and it's not always equal to one. In real simulation and based on sampling theorem I can define the minimum (Nyquist) wavelength ($2dx$) and Nyquist wavenumber ($\frac{\pi}{dx}$) and then the phase velocity $c(k)$ which depends on the number of grid points per wavelength.

The Figure 4-2 shows that whenever the grid sampling is not enough to have enough minimum number of grid points per wavelength, the numerical phase velocity is systematically lower than the real velocity and it leads to disintegrated waveform. In fact, the tail shape of disintegrating waveforms is the result of energy propagating with a delay at lower velocities.

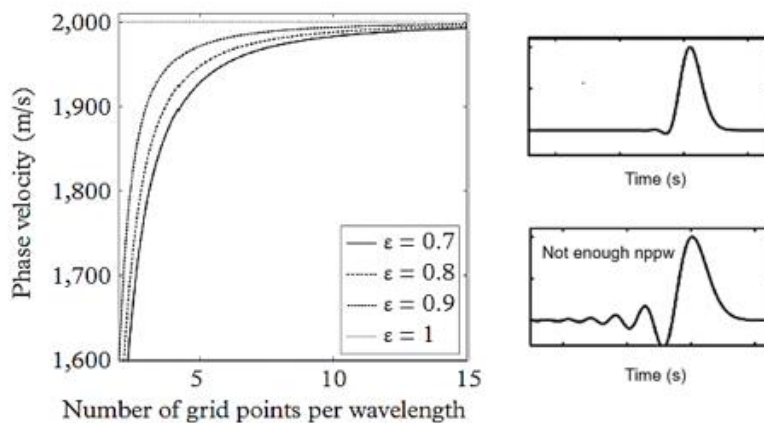


Figure 4-2: left: The numerical phase velocity as a function of the number of grid points for various CFL criteria. As the number of grid points per wavelength increases the correct velocity is recovered (adapted from Igel 2017) Right: an example of left tail shape distorted waveform propagated in space as a result of numerical dispersion caused by deficient number of (grid) points per wavelength (nppw).

4-3 Spectral element method

4-3-1 Introduction

In order to understand the “superiority” of SEM in seismic wave modeling in sedimentary basins, it is important to first explore why the other three main methods are not as effective as SEM.

In general, when dealing with heterogeneous models like sedimentary basins, the FDM method poses several challenges. The first challenge is the inaccuracy in implementing free-surface boundary conditions. For SEM this problem is easily solved as a product of weak representation of the wave equation which leads to natural implementation of free-surface condition (Komatitsch et al., 2005). Also, The SEM has a higher convergence rate which means that the method can achieve a given level of accuracy with fewer grid points or time steps. This is because SEM uses a high-degree polynomial basis (Lagrange polynomials), which allows for greater flexibility in approximating the true solution by fewer points (Komatitsch et al., 2005).

The second method, PSM, is a method which has the same core as SEM that means it uses the spectral convergence of function interpolation (for specific choices of basis functions). However, in SEM, the discretization and integration based on the Gauss-Lobatto-Legendre (GLL) points results in a diagonal mass matrix that greatly simplifies the final algorithm to calculate numerical simulation (Komatitsch and Vilotte, 1998). Additionally, since the PSM is not working on elements, it inherently requires significant global communication which limits its ability to scale on parallel hardware. It makes the method less powerful for solving huge 3D problems and adapting to models with complex geometry.

Finally, while FEM is an efficient method for fixing the free boundary condition, it still requires the solution of a huge linear system of equations because of the non-diagonality of the mass matrix (Igel, 2017).

4-3-2 Mathematical overview of SEM

The Spectral Element Method has been extensively reviewed in numerous technical publications, with detailed specifications of its ingredients and formulation (e.g. Schubert, 2003; Komatitsch et al., 2005). In this section, I will only provide a brief overview of the method and then talk about the points that help to better understand the practical section.

First, by limiting the discussion to one-dimensional systems, I simplify the mathematical complexity, as the transformation from one to three dimensions can be achieved easily through tensorization. This will help to better understand the aspects of the method, which rely heavily on its matrix properties.

First of all, as mentioned in eq. 4-1, the general wave equation of a one-dimensional medium can be written as follows:

$$\rho(x)\partial_t^2 u(x, t) = \partial_x(\mu(x)\partial_x u(x, t)) + s(x, t) \text{ (eq. 4-24)}$$

In 1D, the spatial domain is 0 to H and time is 0 to t. To obtain the weak or Integral formulation, first the equation should be multiplied by a time-independent test function $v(x)$. It can be any continuous and well-behaved function whose functions and first derivative are square integrable over the spatial domain. Then, the resulting equation should be integrated over the whole spatial domain. Obviously, both steps do not alter the final solution of the equation.

$$\int_D v(x)\rho(x)\partial_t^2 u(x, t)dx - \int_D v(x)\partial_x\mu(x)\partial_x u(x, t)dx = \int_D v(x)s(x, t)dx \text{ (eq. 4-25)}$$

To solve the equation, the second term can be solved using integral by parts method which results in one integral over boundary, l , and the other over domain, D .

$$-\int_D \mu(x)\partial_x v(x)\partial_x u(x, t)dx = -\int_l v(x)\mu(x)\partial_x u(x, t) dl + \int_D \partial_x v(x)\mu(x)\partial_x u(x, t)dx \text{ (eq. 4-26)}$$

Since $\mu(x)\partial_x u(x, t) = \sigma_l = 0$, the integral over boundary vanishes and the formula leads to the final form of the weak formulation as below.

$$\int_D v(x)\rho(x)\partial_t^2 u(x, t)dx + \int_D \partial_x v(x)\mu(x)\partial_x u(x, t)dx = \int_D v(x)s(x, t)dx \text{ (eq. 4-27)}$$

This is the first benefit of using SEM, where the physical free-surface boundary condition is simply fulfilled by the new form of equation.

The next step is to use the Galerkin method. By using the Galerkin principle, I can approximate the solution by a linear combination of basis functions. By substituting the approximation, I will obtain a system of algebraic equations, which can be solved using matrix methods.

$$u(x, t) \approx \underline{u}(x, t) = \sum_{i=0}^{Np} u_i(t) \varphi_i(x) \text{ (eq. 4-28)}$$

I also replace test function $v(x)$ with the same basis function $\varphi_j(x)$ and leads to the following equation for the unknown coefficients $u_i(t)$:

$$\sum_{i=1}^{Np} \partial_t^2 u_i(t) \int_D \rho(x) \varphi_i(x) \varphi_j(x) dx + \sum_{i=1}^{Np} [u_i(t) \int_D \mu(x) \partial_x \varphi_i(x) \partial_x \varphi_j(x) dx] = \int_D \varphi_i(x) s(t) dx \text{ (eq. 4-29)}$$

Here the Np is the number of points for polynomial order which will be described after choosing the proper function as test functions. Here I can also represent this formula at its famous matrix form:

$$M \partial_t^2 u(t) + K u(t) = s(t) \text{ (eq. 4-30)}$$

In this step, after obtaining the general matrix formula, I should map all of the processes in the element domain since by knowing the solution in one element, I can generalize the equation to other elements as well. For each element, it is necessary to go to the local coordinate system via the coordinate transformation, where each element is mapped onto the standard interval of $[-1, 1]$ (Figure 4-3).

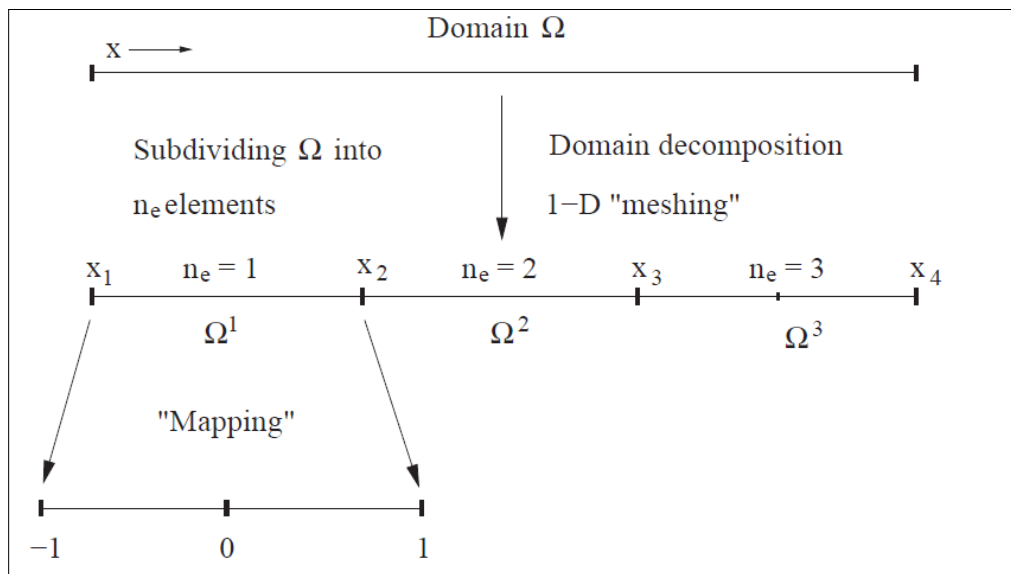


Figure 4-3: Domain decomposition from the whole domain to “ n_e ” elements, mapping each element to the interval of -1 to 1 (adapted from Schubert, 2003).

By decomposition in one element, I have the new form of formula (eq 4.29) as follows:

$$\begin{aligned} & \sum_{i=1}^{Np} \partial_t^2 u_i^e \int_{-1}^1 \rho[x(\xi)] \varphi_i^e[x(\xi)] \varphi_j^e[x(\xi)] J d\xi + \\ & \sum_{i=1}^{Np} u_i^e \int_{-1}^1 \mu[x(\xi)] \partial_\xi \varphi_i^e[x(\xi)] \partial_\xi \varphi_j^e[x(\xi)] (J^{-1})^2 J d\xi = \\ & \int_{-1}^1 \varphi_j^e[x(\xi)] s[x(\xi), t] J d\xi \text{ (eq. 4-31)} \end{aligned}$$

In this equation or in better words, the matrix system of Np equations, the $x(\xi)$ is the forward mapping to elements defined as:

$$x(\xi) = F_e(\xi) = x_e + h_e \frac{(\xi+1)}{2} \text{ (eq. 4-32) it is for } \begin{cases} \xi = -1 \xrightarrow{\text{yields}} x(\xi) = x_e \\ \xi = 1 \xrightarrow{\text{yields}} x(\xi) = x_e + h_e \end{cases}$$

Here h_e is the length of an element that can vary for each element.

Similarly, $\xi(x)$ is the inverse mapping defined as:

$$\xi(x) = F_e^{-1}(\xi) = 2 \frac{(x-x_e)}{h_e} - 1 \text{ (eq. 4-33) it is for } \begin{cases} x = x_e \xrightarrow{\text{yields}} \xi(x) = -1 \\ x = x_e + h_e \xrightarrow{\text{yields}} \xi(x) = 1 \end{cases}$$

Also, the J stands for The Jacobian. The Jacobian $\frac{dx}{d\xi}$ is used to transform integrals from one coordinate system to another defined as follows:

$$\int_{D_e} f(x) dx = \int_{-1}^1 f(\xi) \frac{dx}{d\xi} d\xi \text{ (eq. 4-34)}$$

$$\text{While for our 1D case, } J = \frac{h_e}{2} \text{ and } J^{-1} = \frac{2}{h_e}.$$

The only remaining unknown parameter at equation (4-31) is to determine a proper function for φ_j^e function. For the basis function of φ_j^e I choose the Lagrange polynomial as follows:

$$\varphi_i = l_i^N(\xi) = \prod_{j \neq i}^{N+1} \frac{\xi - \xi_j}{\xi_i - \xi_j} \quad (\text{eq. 4-35}) \quad \text{it is for}$$

$$l_{i \neq j}^N(\xi_j) = 0 \quad l_i^N(\xi_i) = 1$$

$$l_i^N(\xi_j) = \delta_{i,j} \quad (\text{eq. 4-36})$$

Now, the only question is about the choice of the points (i) where the polynomial is calculated. It should be chosen by the so-called Gauss-Lobatto-Legendre (GLL) points. GLL points are defined and represented as follows (Figure 4-4). The importance of selecting these values will become clear when I introduce the numerical integration scheme at the end.

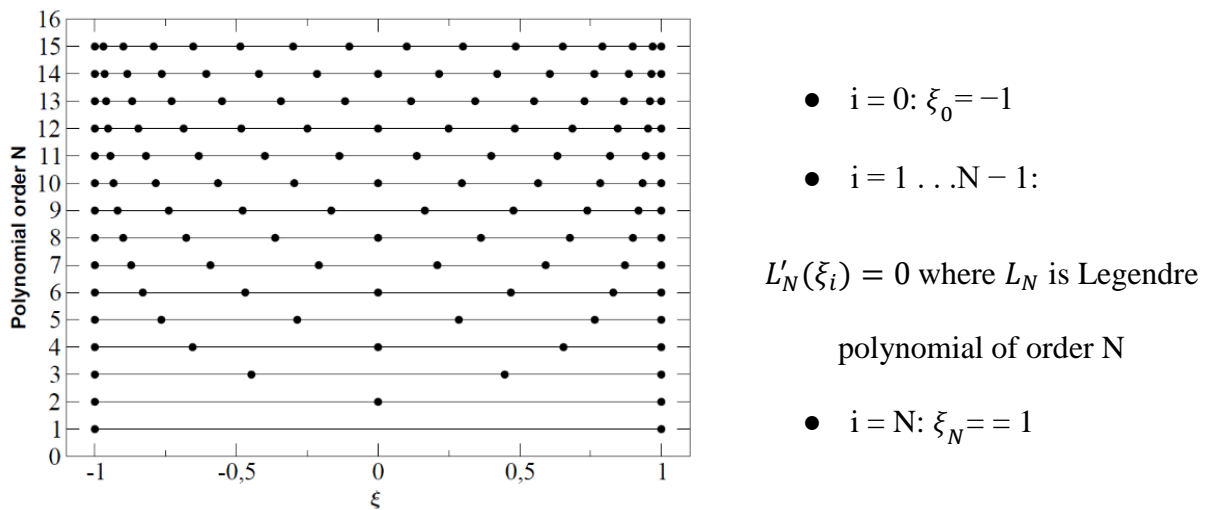


Figure 4-4: GLL points between -1 and 1 as a function of the polynomial order N (adapted from Chaljub, 2000)

Now I can rewrite the formula (eq 4-29) with the Lagrange polynomial instead of basis (test) functions:

$$\begin{aligned} & \sum_{i=1}^{N+1} \partial_t^2 u_i^e \int_{-1}^1 \rho(\xi) l_j(\xi) l_i(\xi) J d\xi + \\ & \sum_{i=1}^{Np} u_i^e \int_{-1}^1 \mu(\xi) \partial_\xi l_j(\xi) \partial_\xi l_i(\xi) (J^{-1})^2 J d\xi = \\ & \int_{-1}^1 l_j(\xi) s[\xi, t] J d\xi \quad (\text{eq. 4-37}) \end{aligned}$$

The problem here is to solve the integral while the analytical solution again is not possible due to the spatial dependence of μ and ρ . In fact, spatial dependence is necessary to maintain flexibility in heterogeneous models. Here, numerical integration techniques (such as Gauss quadrature) must be employed to obtain the solution. Here I need to use this kind of Integration scheme to replace the function with polynomial approximation that can be integrated.

Mathematically, the integration scheme for an arbitrary function defined in the interval -1 and 1 can be written as:

$$\int_{-1}^1 f(x)dx \approx \int_{-1}^1 P_N(x)dx = \sum_{i=1}^{N+1} w_i f(x) \text{ (eq. 4-38)}$$

Or specifically for the GLL point ξ_i :

$$\int_{-1}^1 f(\xi)d\xi \approx \int_{-1}^1 P_N(\xi)d\xi = \sum_{i=1}^{N+1} w_i f(\xi_i) \text{ (eq. 4-39)}$$

By this definition, I can rewrite the whole formula, (eq. 4-29), for the last time replacing the integral by the sum retrieved from the Integration scheme. Here, w_k or the weight of polynomials can be obtained from the any mathematical handbook tables.

$$\begin{aligned} & \sum_{i=1}^{N+1} \partial_t^2 u_i^e \quad w_k \rho_{\xi} l_j(\xi) l_i(\xi) J \, d\xi + \\ & \sum_{i=1}^{Np} u_i^e \quad w_k \mu_{\xi} \partial_{\xi} l_j(\xi) \partial_{\xi} l_i(\xi) (J^{-1})^2 J \, d\xi \approx \\ & \int_{-1}^1 w_k l_j(\xi) s[\xi, t] J \, d\xi \text{ (eq. 4-40)} \end{aligned}$$

Now, the only unsolved part of the equation 4-40 is the derivative of Lagrange polynomial, $\partial_{\xi} l_j(\xi)$.

To solve it, I use Legendre polynomials defined as:

$$\partial_{\xi} l_k(\xi_i) = \sum_{j=0}^N d_{ij} l_k(\xi_i) \text{ (eq. 4-41)}$$

and rewrite the whole formula and represent it in final matrix form as below:

$$\begin{aligned} & \sum_{i=1}^{N+1} \partial_t^2 u_i^e \quad M_{ji}^e + \\ & \sum_{i=1}^{Np} u_i^e \quad K_{ji}^e = \\ & s_j^e \text{ (eq. 4-42)} \end{aligned}$$

Finally, for matrices M_{ji}^e , K_{ji}^e and s_j^e I introduce each component in follow:

First, M_{ji}^e : Because of using the same polynomials for weak formulation and integration scheme which leads to $l_j(\xi)l_i(\xi) = \delta_{ij}$, the M_{ji}^e matrix became very simple as $M_{ji}^e = w_j \rho_\xi J$. It is evident that utilizing the same GLL point substantially reduces the complexity of the M (mass) matrix and makes the final diagonal mass matrix. So, the final components of M (mass) matrix include only the w_j which can be extracted from table, J which is equals to $\frac{h_e}{2}$ in 1D case and ρ_ξ values.

Second, K_{ji}^e : This matrix is not as easy as M_{ji}^e and written as $\sum_{i=1}^{Np} w_k \mu_\xi \partial \xi l_j(\xi) \partial \xi l_i(\xi) (J^{-1})^2 J d\xi$ that finally leads to the banded matrix and should be solved by computers.

Third, s_j^e : which is equals to $w_k s[\xi, t] J$ and written as a source matrix.

What I calculate up to now, is the results for 1 element. To obtain the final solution I need to assemble the global solution.

So, the example with N=4 GLL points (which has 5 colocation point) for 3 elements is written below:

$$M_{global} = \begin{pmatrix} M_{1,1}^1 \\ M_{2,2}^1 \\ M_{3,3}^1 \\ M_{4,4}^1 \\ M_{5,5}^1 \\ 0 \\ 0 \\ 0 \\ 0 \end{pmatrix} + \begin{pmatrix} 0 \\ 0 \\ 0 \\ 0 \\ M_{1,1}^2 \\ M_{2,2}^2 \\ M_{3,3}^2 \\ M_{4,4}^2 \\ M_{5,5}^2 \end{pmatrix} + \begin{pmatrix} 0 \\ 0 \\ 0 \\ 0 \\ 0 \\ 0 \\ 0 \\ 0 \\ M_{1,1}^3 \end{pmatrix} = \begin{pmatrix} M_{1,1}^1 \\ M_{2,2}^1 \\ M_{3,3}^1 \\ M_{4,4}^1 \\ M_{5,5}^1 + M_{1,1}^2 \\ M_{2,2}^2 \\ M_{3,3}^2 \\ M_{4,4}^2 \\ M_{5,5}^2 + M_{1,1}^3 \end{pmatrix}$$

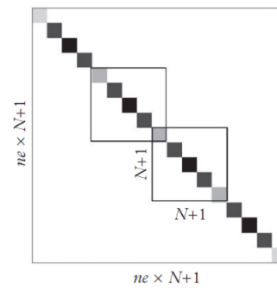


Figure 4-5: representation of Mass Matrix for 3 element each contains 5 colocation point (Adapted from Igel, 2017)

$$K_{global} = \begin{pmatrix} K_{1,1}^1 & K_{1,2}^1 & K_{1,3}^1 & K_{1,4}^1 & K_{1,5}^1 & 0 & 0 & 0 & 0 \\ K_{2,1}^1 & K_{2,2}^1 & K_{2,3}^1 & K_{2,4}^1 & K_{2,5}^1 & 0 & 0 & 0 & 0 \\ K_{3,1}^1 & K_{3,2}^1 & K_{3,3}^1 & K_{3,4}^1 & K_{3,5}^1 & 0 & 0 & 0 & 0 \\ K_{4,1}^1 & K_{4,2}^1 & K_{4,3}^1 & K_{4,4}^1 & K_{4,5}^1 & 0 & 0 & 0 & 0 \\ K_{5,1}^1 & K_{5,2}^1 & K_{5,3}^1 & K_{5,4}^1 & K_{5,5}^1 + K_{1,1}^2 & K_{1,2}^2 & K_{1,3}^2 & K_{1,4}^2 & K_{1,5}^2 \\ 0 & 0 & 0 & 0 & K_{2,1}^2 & K_{2,2}^2 & K_{2,3}^2 & K_{2,4}^2 & K_{2,5}^2 \\ 0 & 0 & 0 & 0 & K_{3,1}^2 & K_{3,2}^2 & K_{3,3}^2 & K_{3,4}^2 & K_{3,5}^2 \\ 0 & 0 & 0 & 0 & K_{4,1}^2 & K_{4,2}^2 & K_{4,3}^2 & K_{4,4}^2 & K_{4,5}^2 \\ 0 & 0 & 0 & 0 & K_{5,1}^2 & K_{5,2}^2 & K_{5,3}^2 & K_{5,4}^2 & K_{5,5}^2 + K_{1,1}^3 \end{pmatrix}$$

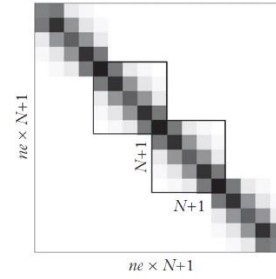


Figure 4-6: representation of Stiffness and source Matrix for 3 element each contains 5 colocation point(Adapted from Igel, 2017)

$$S_{global} = \begin{pmatrix} s_1^1 \\ s_2^1 \\ s_3^1 \\ s_4^1 \\ s_5^1 + s_1^2 \\ s_2^2 \\ s_3^2 \\ s_4^2 \\ s_5^2 + s_1^3 \\ \vdots \end{pmatrix}$$

Finally, to finish this overview it should be noted that to solve the equation in time $u(t + dt)$, it can be used a centered finite-difference approximation formula of the second derivative evaluated at each time step as:

$$u^{new} = dt^2 [M^{-1}(f - K u)] + 2u - u^{old} \text{ (eq. 4-43)}$$

4-4 EFISPEC3D

In this section I focus on practical applications. To accomplish this, I will begin by introducing the specific SEM code (EFISPEC3D) used in our numerical simulations. Following that, I will describe each component of the code in more detail.

4-4-1 Introduction

EFISPEC3D is a free software under CeCILL V2 and GNU GPL V3 licenses that utilizes a SEM method to solve the three-dimensional equations of motion (De Martin, 2011). EFISPEC3D is a Fortran95 code containing one C subroutine that links the code to the external mesh partitioning tool. The code can run on all Unix systems that have Fortran and C compilers and Message Passing Interface library (MPI) (here: Intel parallel studio compiler and Intel MPI library) which allows the program to optimize for multi-core processing and running on separate nodes on a distributed system. The term "distributed" means that the used memory is network-based and to access memory on other processors, specific communication protocols like MPI always must be employed.

EFISPEC3D has three level of MPI communications:

- i) World communication involves exchanging information among all processes and is used for initializing and terminating the program.
- ii) Simulation communication which refers to communication between processes, such as neighboring cells in a wave propagations simulation, and,
- iii) FSurf communication relates to communication between processes involved in computing the boundaries between different regions of a simulation.

To run the code, all of processes should be done on the computational units preferably with the SIMD (Single Instruction Multiple Data) architecture including CPU and GPU clusters (here: DAHU HPCDA UGA; High performance computing and data analysis platform of Université Grenoble Alpes²).

² supported by the Rhône-Alpes region (GRANT CPER07_13 CIRA), the OSUG@2020 labex (reference ANR10 LABX56) and the Equip@Meso project (reference ANR-10-EQPX-29-01) of the Programme Investissements d’Avenir (supervised by the Agence Nationale pour la Recherche).

Since all numerical methods are based on time–space domain solutions, the parallel computation implies that all space dependent fields (e.g. displacements, elastic parameters, etc.) should be mapped on parallel hardware. It can be done using mentioned distributed memory system and new concept called “domain decomposition” (Igel, 2017). For domain decomposition, EFISPEC3D uses METIS library by partitioning finite element meshes. It is done by multi-level recursive bisection algorithm which provides a set of functions for partitioning a graph into multiple subgraphs (Karypis and Kumar, 1998; Figure 4-7). To design the finite element meshes, EFISPEC3D has no internal mesh generator and relies on external mesh tools, with the primary tool being the CUBIT mesh generator developed by Sandia National Laboratories. CUBIT is a software package which is capable of generating meshes for complex geometries, including hexahedral meshes.

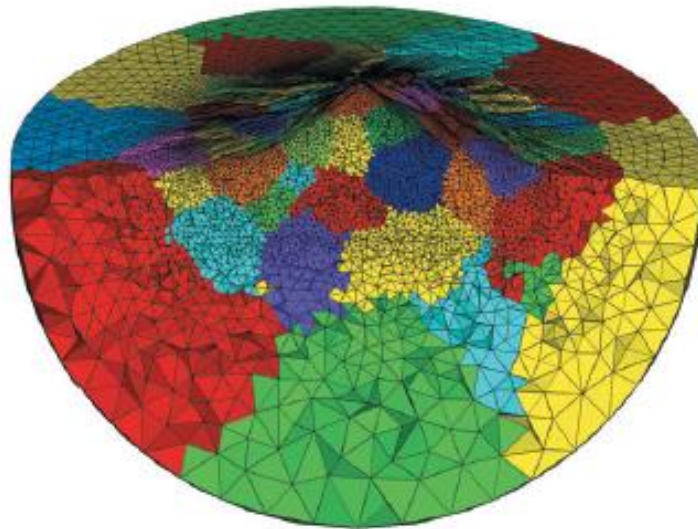


Figure 4-7: Domain decomposition when space-dependent fields are discretized. Here is an example representing the partitioning volumes for unstructured grids in 3D for volcano simulation (adapted from Igel, 2017)

Before going thorough, it should be noted that the validity of EFISPEC3D code has been examined successfully in different projects (e.g.: SCEC (DeMartin, 2011) and E2VP (Chaljub et al., 2015)). For example, Chaljub et al. (2015) verified the efficiency and accuracy of the code for estimating site effects in complex sedimentary basins by designing four canonical models and comparing the results with other numerical solutions including FDM and also another SEM’s code.

Figure 4-8 displays the complete workflow of EFISPEC3D, which begins with the creation of a mesh using mesh generator software, CUBIT, followed by partitioning the mesh using METIS. Each sub-mesh is then assigned to a single calculation center (CPU) and connected through the MPI protocol. Next, for each element, the wave equation is computed after initializing the GLL points, and the final results are obtained.

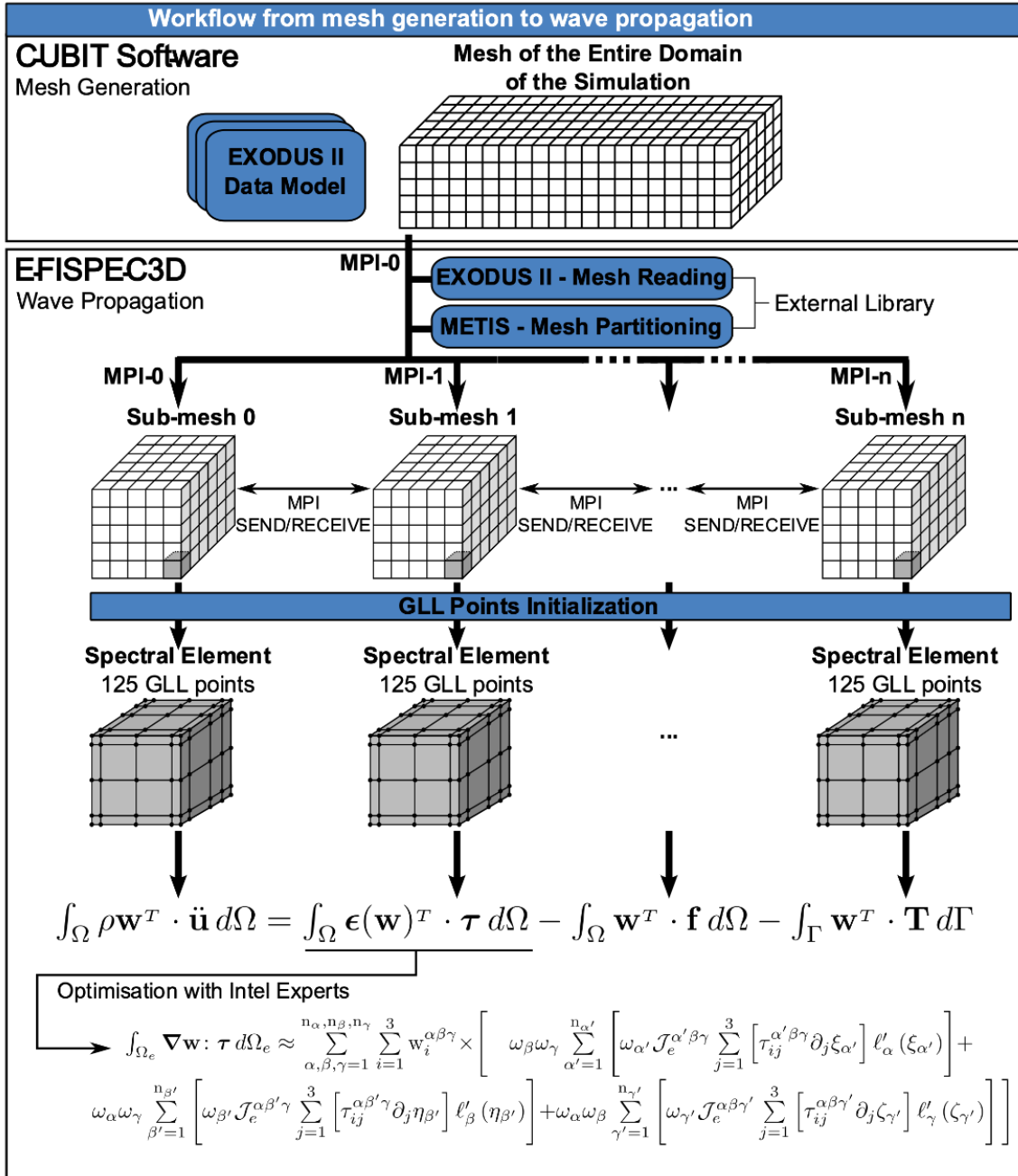


Figure 4-8: EFISPEC3D workflow (adapted from EFISPEC tutorial documents)

4-4-2 Meshing the Tehran's basin domain

4-4-2-1 Introduction

Before talking about mesh generation as an initial stage for each numerical modeling, it is necessary to briefly review the basic definitions of mesh components. For each meshing process, elements or cells are the essential parts defined as the three-dimensional components that divide the model space into smaller pieces. They represent the small region of the object being modeled. The dimensions of the element are always the same as the dimensions of the model space.

In addition, a face is defined as the two-dimensional surface that forms the boundary of the element, a node is a point that marks the corner of the element, and an edge is a line that connects two nodes (Figure 4-9A). Each three-dimensional element is usually defined as 4 different types: the tetrahedron, quadrilateral pyramid, triangular prism, or hexahedron (Figure 4-9B). The hexahedron cell, which I will utilize in our case, is a cube-shaped geometric solid with 8 nodes, 12 edges, and 6 quadrilateral faces.

One other important concept is the type of meshing subdivision is that the meshing can be done using a structured or unstructured mesh. A structured mesh is made up of a regular grid of cells that are all aligned in the same direction. The cells have a fixed shape and size and the grid lines are normally straight and perpendicular to one another. In its most basic form, a 3D structured mesh consists of brick-like objects that the corners of which can be addressed with indices i , j , and k . Structured meshes are easy to generate and ideal for simulating simple geometries or problems with a polyhedron that are not aligned in a particular direction. On the other hand, unstructured meshes are composed of irregular polygons or polyhedral that can adapt to different geometries. Both structured and unstructured meshes can be presented in conformal or non-conformal form. The term "conformal mesh" refers to a mesh where two elements' borders are shared by mesh nodes. Thus, the interaction between two elements and sub-elements is the same. Moreover, the intersection of elements and sub-elements must be of the same type. In the spectral elements and also EFISEC3D code conformal meshes (mostly structured) is utilized (Figure 4-9C).

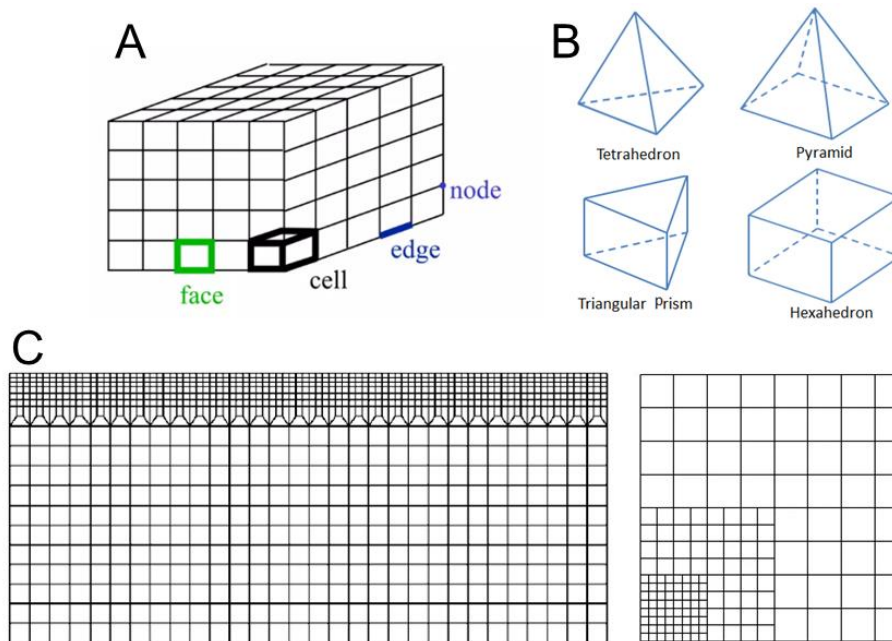


Figure 4-9: A: Basic definition of mesh object, B: Different types of 3D mesh elements, C: The types of meshing subdivision, left: conformal and right: non-conformal structured mesh.

After this simple introduction, it is important to note that the primary challenge in creating a mesh for ground motion simulation is the presence of abrupt changes or discontinuities in geophysical properties. In fact, while the SEM method has the capability to handle physical discontinuities in material properties, the inflexibility regarding the direct use of hexahedra in 3D can result in significant numerical errors. It is because the interfaces cannot be explicitly discretized during the meshing process and the model exhibits a discontinuity that is not aligned exactly with the boundary between spectral elements.

In this regard, Chaljub et al. (2015) by comparing many different numerical solutions, found that the main source of differences between different numerical solutions comes from the issue of the small scales non-coincide boundaries. In such a case, surface waves are much more sensitive when they are not correctly implemented and then the incorrect medium properties cannot fully represent the dispersion properties of the medium.

The solution is to consider the effect of heterogeneities smaller than the minimal wavelength of a wavefield propagating through complex media. But, respecting all discontinuities and developing a mesh that follows exactly layer boundaries is extremely time-intensive and requires a solver

capable of handling many irregular meshes. So, it should be an alternative approach to solve this issue. For that, it is possible to implement the geological layers into the finite element mesh, without the mesh following the geological interfaces, using the concept called “homogenization”. This is done by a simple, isotropic, one-dimensional vertical homogenization method proposed by Capdeville et al., (2010) based on spatial filtering. The most general approach, so-called two-scale homogenization (TSH), leads to fully anisotropic effective media which can be implemented in all SEM’s code (see Capdeville et al., 2020 for a review).

To do homogenization in practice, there is no need to follow all discontinuities in meshes, instead I refine the mesh only when there is shallow velocities and relax the constraint following the interfaces. This allows to design and generate semi-automated mesh of the basin.

The homogenization length (L) is used to implement this concept at EFISPEC3D code. It refers to the characteristic length scale over which the properties of the material being modeled can be considered to be uniform or homogeneous. This length scale should be small enough to capture the local variations in material properties, but large enough to avoid excessively fine meshes and computational costs (Figure 4-10).

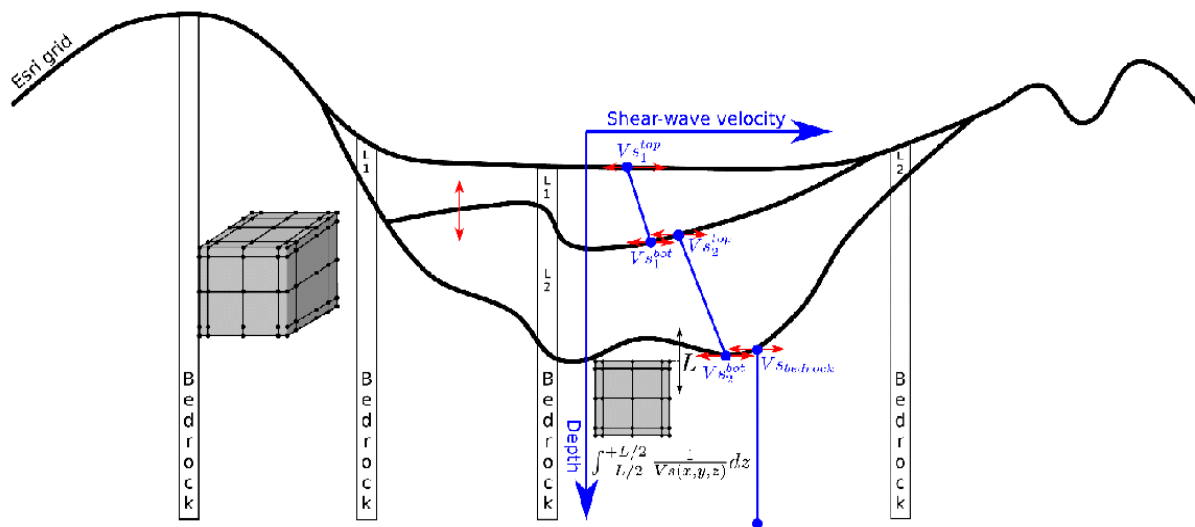


Figure 4-10: Homogenization for velocity profiles: instead of considering the abrupt changes in velocity between two layers the integral of slowness from $L/2$ to $-L/2$ smoothed the velocity profile (adapted from EFISPEC3D tutorial documents).

4-4-2-2 Tehran basin border

The initial stage of each simulation studies involved describing the simulation block and basin borders. For Tehran simulation, the basin border was obtained by extracting information from two 1:100000 geological maps (Tehran and East Tehran) that were published by the Geological Survey of Iran (GSI, 2010). These maps allowed for precise extraction of the boundary between rock and alluvium with a relatively high degree of accuracy.

In the other hand, the simulation block was considered as a tilted square with dimensions of 50 × 50 km, by considering geological constraints described in previous chapters. This tilted square allowed for more efficient use of resources by minimizing absorption boundaries, avoiding any unnecessary enlargement of the model (Figure 4-11A).

Once the simulation block was selected, the digital elevation model topographic map (DEM) was extracted from 30-meter SRTM (Shuttle Radar Topography Mission) elevation data. This map was utilized to define the free surface during the mesh file generation. To use this map, it should be redefined in local coordinates. In order to redefine, two steps were taken. Firstly, the block simulation was rotated counterclockwise by 55.22 degrees with respect to the latitude and longitude values at the left corner. Secondly, these values were translated to the local coordinate 0,0 to create a square simulation block surface with dimensions of 50 km × 50 km (Figure 4-11, B-C)

4-4-2-3 Tehran mesh generation

To make the mesh, CUBIT can provide an efficient way to increase mesh density near the surface of the model in lower velocity sediments since utilizing a coarser mesh in depth can reduce memory requirements. This is achieved by tripling down of the mesh as a function of depth. To achieve a fine mesh resolution as a function of depth, a tool called "Numsplit" can be used. Numsplit refers to the number of times where each edge of an element is splitted into smaller edges in each direction. For instance, when Numsplit has a value of 1, each quadrilateral is divided into nine smaller elements, each tetrahedron is divided into eight smaller elements, and each hexahedron is divided into 27 smaller elements. By increasing the value of Numsplit, the number of smaller elements per element can be increased, resulting in a finer mesh resolution (Figure 4-12).

To define our numerical mesh for Tehran basin simulation, I used a mesh edge size of 900 meters for the coarser (the largest) elements. I then applied a down-tripling twice, once down to the depth of the plane wave source injection and once down to the depth of basin refinement to construct the computation mesh block. Our meshing resulted in a minimum number of points per wavelength of 6.058, which is considered to be adequate for accurately simulating wave propagation since the empirical criterion of “minimum number of grid points per smallest wavelength > 6”, is a criterion that must be satisfied in order to obtain accurate solutions, to avoid numerical dispersion as a rule of thumb.

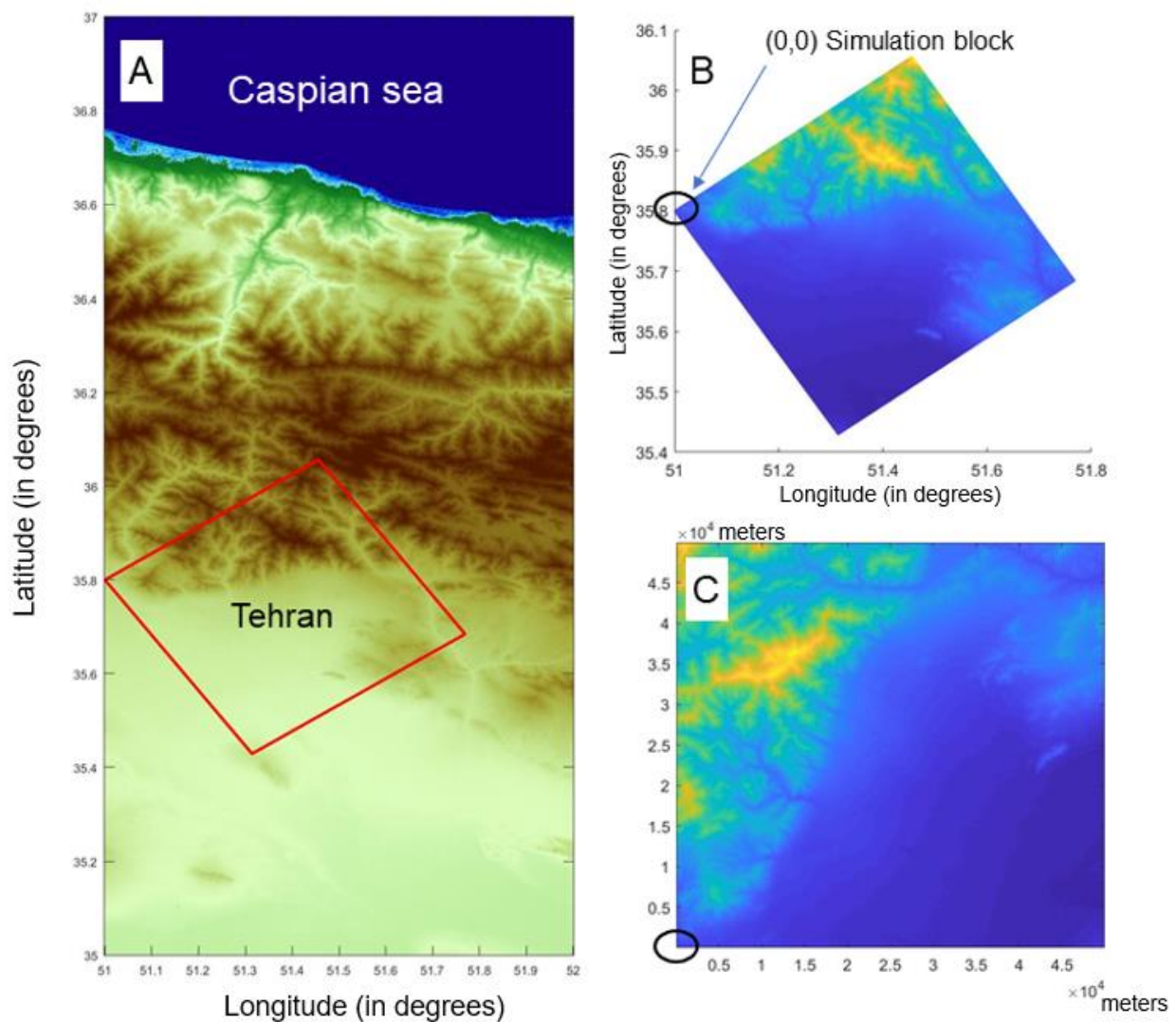


Figure 4-11: A: the simulation block for Tehran study shown in Central Alborz region. B: the extracted region, and C: the rotated and translated block for use on simulation.

In fact, the criterion “ $nppw > N$ ”, is method-dependent. For most finite-difference schemes, N is typically chosen around 10 but for SEM codes such as EFISPEC3D, it is typically selected around 6, that means at least 6 GLL points per wavelength is necessary to obtain accurate results. With even more GLL points per wavelength, the solutions are even more accurate, but the gain is small. Instead, with $N < 6$, the solutions are significantly less accurate.

In this regard N defined as:

$$N = \frac{v_{min}}{(f_{max} * dist_{max})} = \frac{\lambda_{min}}{dist_{max}} \text{ (eq. 4-44)}$$

with $dist_{max}$ is the largest distance between GLL points within an element, and v_{min} is the smallest velocity in this element. f_{max} is the maximum frequency of the simulation, and therefore λ_{min} is the smallest wavelength that propagates through the element. To anticipate this formula in order to design the mesh, it is not obvious to estimate a priori largest distance between GLL points within elements. Instead, I usually consider an approximate distance between GLL points equal to $dist \sim h/4$, with h the element size (edge length). This means that it needs to mesh the regions with v_{min} with elements that have a size smaller or equal to $h \leq \lambda_{min} * \frac{4}{N}$, i.e. $h \sim \leq 0.7 \lambda_{min}$.

After creating the mesh block with satisfactory size, the mesh file is stored in an exodus (ex2) binary format files, where I can apply the topography to the mesh free surface using EFISPEC3D module “EfiSpec3D_cubit_topography”:

```
../EfiSpec3D_cubit_topography <prefix.ex2> zplane <zstart_deforming_dem> dem
```

This command line utilizes three input components:

- i) The stored mesh block file named "teh.ex2" where the "teh" is the hardcoded filename for all other simulation inputs.
- ii) ii) the value called "zstart_deforming_dem" which represents the depth at which the first down tripling was performed. The purpose of these input components is to create a “deformed” mesh that incorporates the new elevation data above the initial depth of "zstart_deforming_dem”.
- iii) iii) the topography file "dem" that was derived from 30-meter SRTM (Shuttle Radar Topography Mission) elevation data.

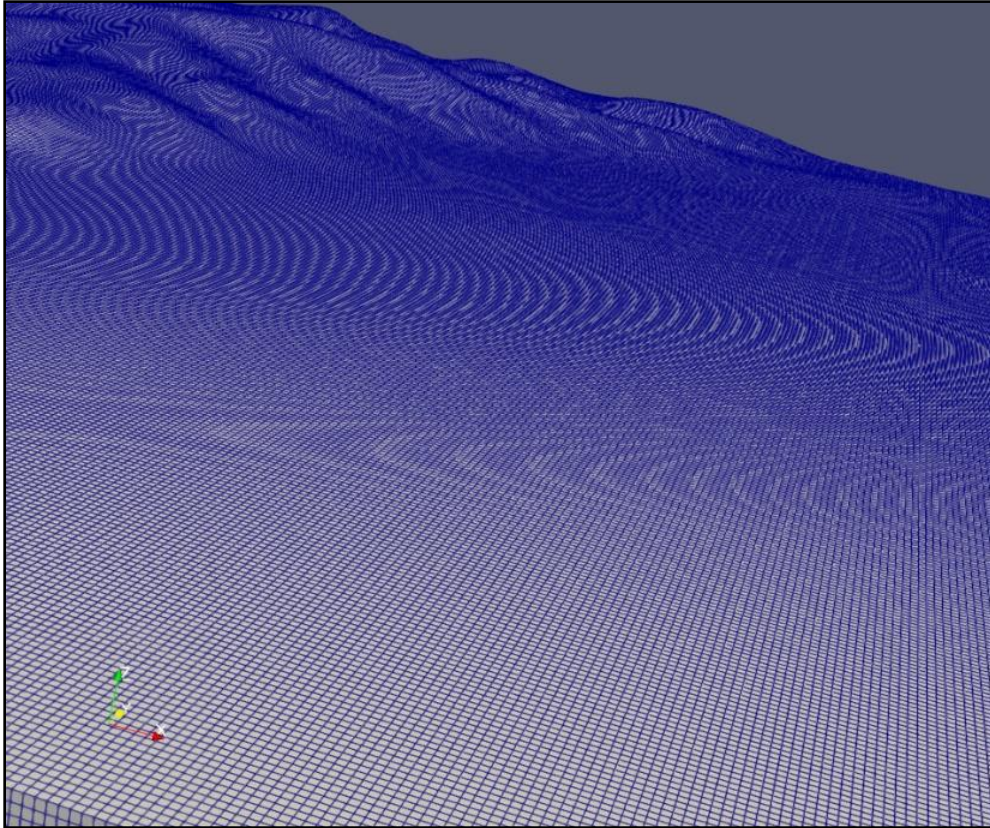


Figure 4-12: snapshot of the mesh utilized in the simulations.

4-4-3 Inputs for Tehran simulation

In addition to "mesh", there are other types of input files that should be used for ground motion simulation in the EFISPEC3D code (Table 4-1). The detailed explanations of each input filetype will be introduced in the following subsections.

Table 4-1: The different input files required for 3D wave propagation simulation using EFISPEC3D code.

Prefix	The prefix of the files needed by a simulation
prefix.cfg	General configuration file
prefix.dcs	Double couple source file
prefix.dcf	Double couple source time function
prefix.sfs	Single force source
prefix.sff	Single force source time function
prefix.fsr	Free surface receiver locations
prefix.vor	Volume receiver locations
prefix.ifi	ESRI ASCII grid file including layer depth
prefix.pwf	Plane wave source time function

4-4-3-1 General configuration (teh.cfg)

There are several parameters that should be tuned before running the simulation. The most important user-defined parameters set should be defined in the “.cfg” file.

There are also some modules within the code (fortran modules) that can also be adjusted by the user to suit the specific simulation requirements. However, after changing each of the internal modules, the code must be recompiled. In this section, the first step is to examine the parameters in the “.cfg” parameters. If any adjustments are necessary, I can then explore the internal module and consider making modifications to them.

- **Time information**

The time information is the heart of simulation, with three important parameters including duration of simulation, time step, and maximum target frequency. The simulation's duration is basically the length of the simulated record in time. For the Tehran simulation, I consider this parameter to be 60 seconds.

The time step, which is perhaps the most important initial parameter in any modeling, is the second parameter included in the time section. Fortunately, EFISPEC3D ensures that this value is appropriate by calculating the CFL criteria. If necessary, the code itself modifies the initial time step.

The maximum desired frequency of simulation should also be noted in the time section. This value in the code is then used to check the number of grid points per smallest wavelength (see Section 4-4-2-3 for detail).

Following that, the receiver saving increment, which by default is 1, can be defined by the user. It indicates that the receiver's time series is preserved after each sample, with the final sampling number equal to the product of timestep and simulation duration.

- **IIR filters**

After time, the next user-defined parameters are the IIR filter design, which only works if the *LG_SNAPSHOT_SURF_GLL_FILTER* parameter at internal "module_global_variables.f90" is equal to true. This module defines all the global variables in EFISPEC3D that can be set as either "true" or "false" to activate or deactivate certain features in the code. For the Tehran simulation, I consider the filter cutoff frequency to be 2 Hz and the filter transition band to be 0.5 Hz.

- **Plane wave definition**

Similar to the previous section, the plane wave parameters are only applicable if the *LG_PLANE_WAVE* parameter in the "module_global_variables.f90" file is set to "true". Once the code has been recompiled, there are three parameters that can be defined for plane wave definition:

- i) the direction of motion. The plane wave motion direction is determined with respect to the x and y directions. A value of 1 (one) indicates that the wave motion direction is parallel to the x-axis,
- ii) the direction of motion and,
- iii) the source time duration. These two last parameters must fulfill a very fundamental relationship related to the fact that the wave must be injected at a depth where no reflected waves can return before the plane wave excitation is complete.

For Tehran, I chose the SH plane wave input depth of -8 km and implemented the z-plane at this depth. The source duration is 4 seconds.

- **Surface and volume snapshots**

In our simulation I decided to only save the surface snapshots (displacement, velocity and acceleration). Surface snapshot saving increment is set to 100 which resulted in 800 snapshots for 60 seconds. The surface snapshot space increment is also assigned to 100 for x and y directions which means the number of receivers for calculating snapshot calculated is equal to:

$$\left(\frac{50000}{100} + 1\right) * \left(\frac{50000}{100} + 1\right) = 251001 \text{ (eq.4-45)}$$

- **Boundary information**

All I need for boundary information is to put the absorption boundary as true in the configuration file. In numerical modeling, absorbing boundaries are defined as the artificial boundaries that are placed around the edges of a computational domain to simulate the effect of an unbounded domain. The purpose of an absorbing boundary is to prevent waves or other types of disturbances from reflecting back into the studied domain, polluting the normal wavefield and interfering with the solution. All absorbing boundaries work by absorbing the energy of incoming waves and converting it into forms of energy that can be dissipated within the boundary. This is usually accomplished by adding a damping term to the equations near the boundary. In EFISPEC3D The P1 paraxial formulation (Stacey, 1988) describes the behavior of waves at the absorbing

boundaries. The P1 paraxial approximation assumes that the wave fronts are nearly planar, and the amplitude and phase of the wave vary slowly with respect to the distance traveled by the wave. The formulation adds complex-valued attenuation coefficients into the wave equation which represents the amount of energy that is absorbed by the boundary proportional to the distance from the boundary (Maufroy et al., 2015).

- **Medium velocity information**

The medium velocity information refers to the mechanical properties of the basin's layers as determined by the experimental velocity structure extracted and simplified in previous chapters. It is defined by the number of materials in "block" mode or the number of layers in "homogenization" mode following the structure type, V_s, V_p, ρ, q_s, q_p and q_f information. Table 4-2 shows the layer medium properties used for Tehran simulations.

Table 4-2: The layer medium properties of the Tehran simulations.

	Layer 1	Layer 2	Layer 3
Type	Sediment	Sediment	Bedrock
Layer (Homogenization mode)	1	2	3
Structure Type	Constant	Constant	Constant
V_s (m/s)	835	1272	3000
V_p (m/s)	1670	2544	5200
ρ (kg/m ³)	2000	2000	2700
q_s	83	127	250
q_p	167	254	500
q_f	50	50	50

The relationship $Q_s = V_s/10$ is a commonly used rule of thumb to estimate the shear-wave attenuation in earth materials, and should not be relied upon as a precise measurement of shear-wave attenuation. It is often used when detailed measurements of Q_s are not available or necessary. However, it is important to note that this relationship is only an approximation and may not hold

true for all materials or in all frequency ranges. The actual value of Q_s may vary depending on different factors such as geological properties, frequency contents, wave type, etc.

4-4-3-2 Medium depth and layer's definition (Teh.ifi)

In EFISPEC3D, the medium depth is described with ESRI Grid ASCII file format. It is a file format widely used to store digital elevation models (DEMs). The file format includes three main parts: header information, cell value information, and optional attribute information.

The header provides the number of rows and columns, the coordinate system, and the size of each cell. For parameters, `ncols` and `nrows` parameters are the number of columns and rows; `xllcorner` and `yllcorner` are the western (left) x-coordinate and southern (bottom) y-coordinate; and `cellsize` is the length of one side of a square cell.

The second part of the file, cell value information, consists of a set of values in "English reading order" (left-to-right and top-to-bottom) that should represent the elevation of each grid cell.

Finally, the optional attribute information, such as minimum and maximum value, nodata values and etc. can be included in the optional attribute information part. (Figure 4-13).

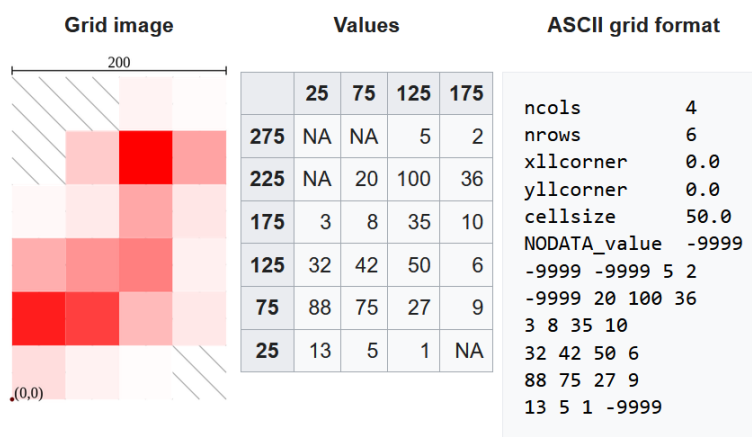


Figure 4-13: An example of grid image with corresponding values and representation with ESRI ASCII grid file format (Esri, Inc., 2023).

To create the medium files to be applied in EFISPEC3D code, I first interpolate our data in Surfer software using the Kriging interpolation technique using the spatial correlation factor (variogram) which describes the degree of similarity between pairs of points at different distances apart. For our model I used a linear variogram (Golden Software, LLC). Then the interpolated raster file is cut by the definition of basin border introduced in section 4-4-2-2. After rotating the clipped data,

except for the values inside the basin, the other values became NaN. For these values, the topography is added to the model using the python mask function to substitute the NaN values with the topography DEM file. Finally, I convert the absolute depth values within the basin to elevation values to acquire the final layer.

The prepared layers must be fulfilling the following conditions in order to be correctly implemented in EFISPEC3D code:

- (i) First, it should be no interface higher than topography interface (introduced as if_0). Meaning that the medium layer should have the value equal or lower than the topography layer at the whole part of the model.
- (ii) Second, the interface if_i cannot be lower than interface if_{i+1} (Figure 4-14).

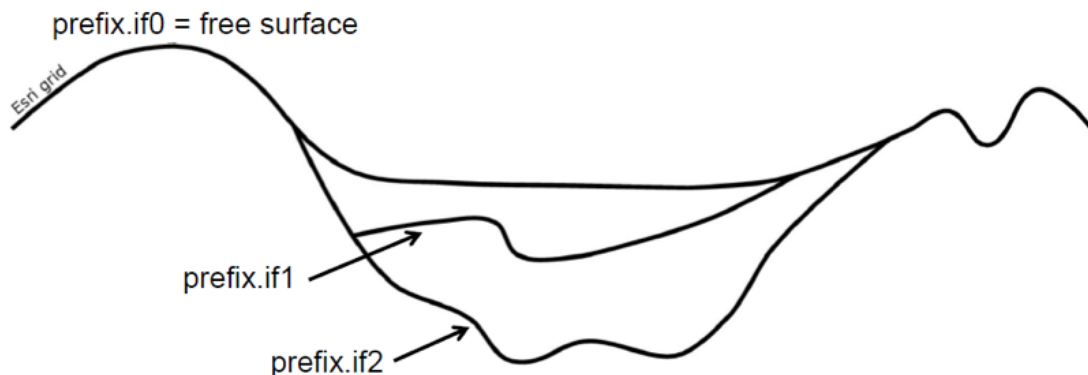


Figure 4-14: 2-layer medium represented in a 2D cross section fulfilling the mentioned criteria (adapted from EFISPEC3D tutorial documents).

4-4-3-3 Source time function (teh.pwf)

The source time function represents the initial energy release of a seismic event, and in our case, it has been created using the unit impulse method from the SciPy library in Python (Figure 4-15). This method generates a Dirac impulse, which has been subjected to a lowpass filter, resulting in a waveform with a maximum frequency of 2 Hz. In this regard, using a combination of repeated zero-phase and non-zero-phase Butterworth filters could get a source impulse that satisfies the causality and the sharp frequency cut-off at maximum target frequency. Using this combination, it is possible to design a filter with some causal components, allowing to satisfy the causality criteria required for seismic analysis.

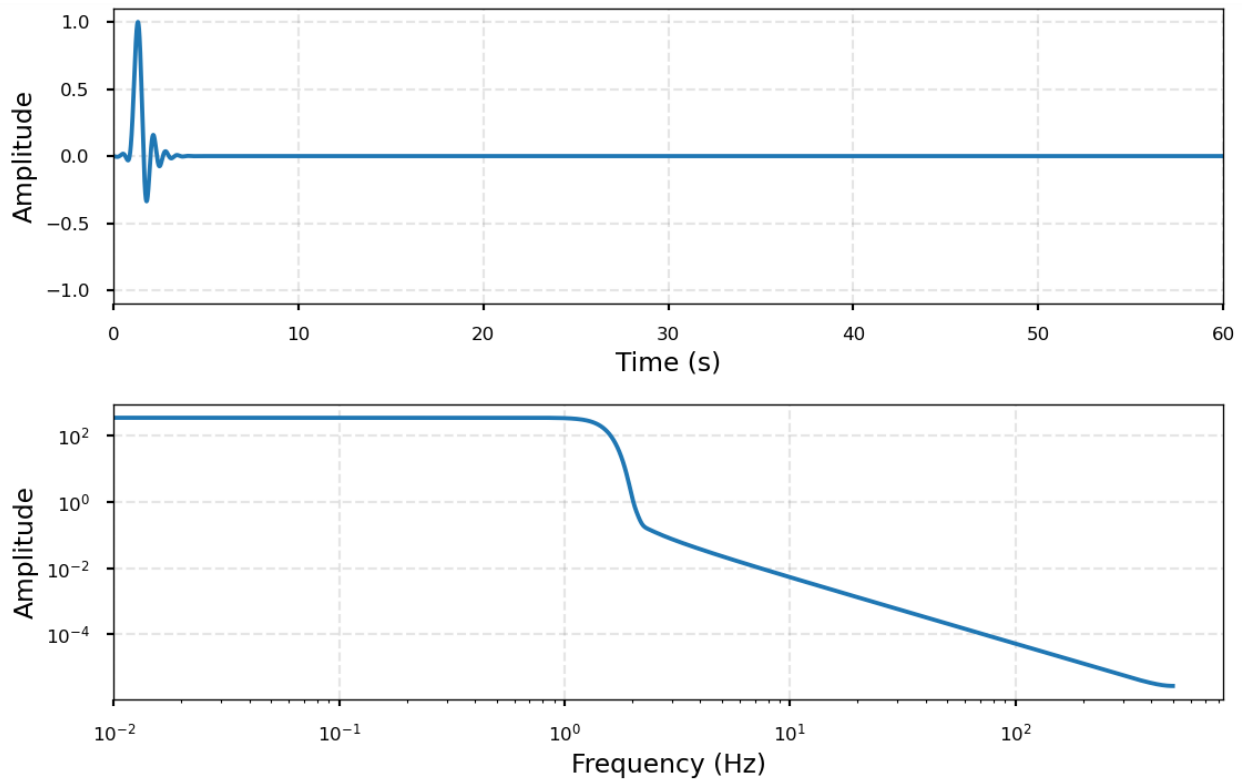


Figure 4-15: The low pass filter impulse used for Tehran simulations, with duration of four seconds, and the corresponding amplitude spectrum with the maximum target frequency of 2 Hz.

4-4-3-4 Receivers (teh.fsr)

For this study, I have utilized surface receivers that have been converted to the local coordinate system at the domain block. In this regard, for the final analysis, I extract the time series data at receivers located at the same place as the seismological stations used to record earthquakes (13) and seismic ambient noise (159) as well as 81 other stations along two cross sections all over the basin. As an example, the receiver locations for the H/V stations in local coordinates are shown in Figure 4-16. To obtain accurate coordinates, the latitude and longitude coordinates in the WGS84 global coordinate system are first adjusted relative to the reference point, which is the lower left corner of the simulation block. They are then rotated clockwise by an angle of 55.22 degrees, as the rotation angle mentioned in Section 4-4-2-2. After rotation, the coordinates are converted to the UTM coordinate system and shifted to 0,0 with respect to the lower left corner.

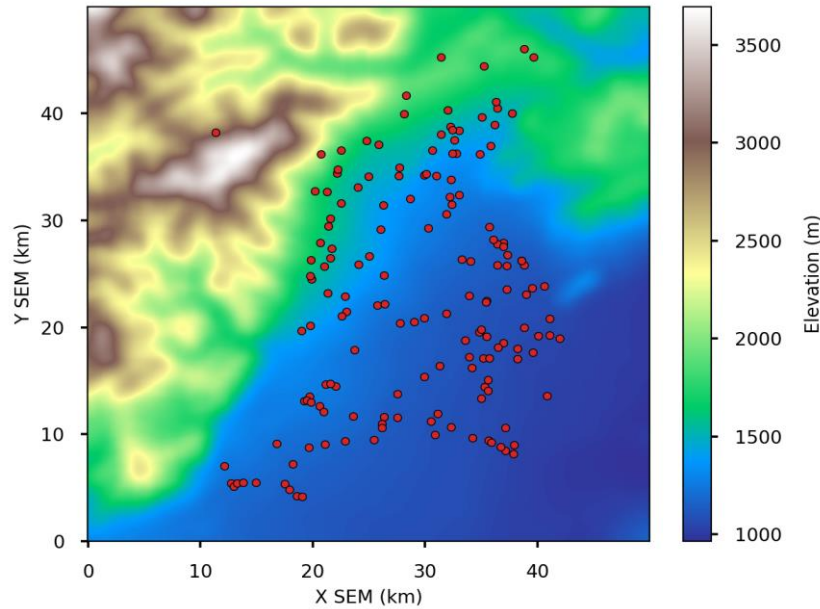


Figure 4-16: The locations of H/V stations' receivers represented on the elevation model map of Tehran in local coordinates.

4-5 Processing and results

After ensuring that all input files were correctly implemented, the main simulation was executed on the DAHU computing cluster. To take advantage of the parallel machine architecture, the mesh is divided into 64 slices that are distributed over 64 processors. The mesh contains 1310848 spectral elements with a polynomial degree of $N = 4$ to sample the wavefield; therefore, each spectral element contains 125 Gauss–Lobatto–Legendre points. Counting points on common spectral-element edges and corners only once, the mesh therefore contains a total of 86.5 million grid points. The homogenization length is equal to 82.8 meters and finally, the total memory consumption approximation is about 54 Gb while the calculation takes about 16 hours to compute seismograms with a duration of 60 seconds on 80,000 timesteps.

4-5-1 Numerical simulation snapshots

In numerical modeling, snapshots refer to a sequence of time-dependent steps of a simulation at discrete times. In other words, snapshots are a way to capture a particular state of a simulation at a given time that can be used for a variety of purposes, mostly for visualizing the behavior and the changes in a simulation's state over time.

In EFISPEC3D, snapshots are written to VTS files, a file format for storing structured grid data based on the XML, to represent complex 3D geometries. Figure 4-17 illustrates four snapshots taken at 3, 5, 10 and 20 seconds after the injection of a source time function. These snapshots depict the state of the simulation from the moment that the incident plane S wave hits the surface through the generation of diffracted waves at the basin edges.

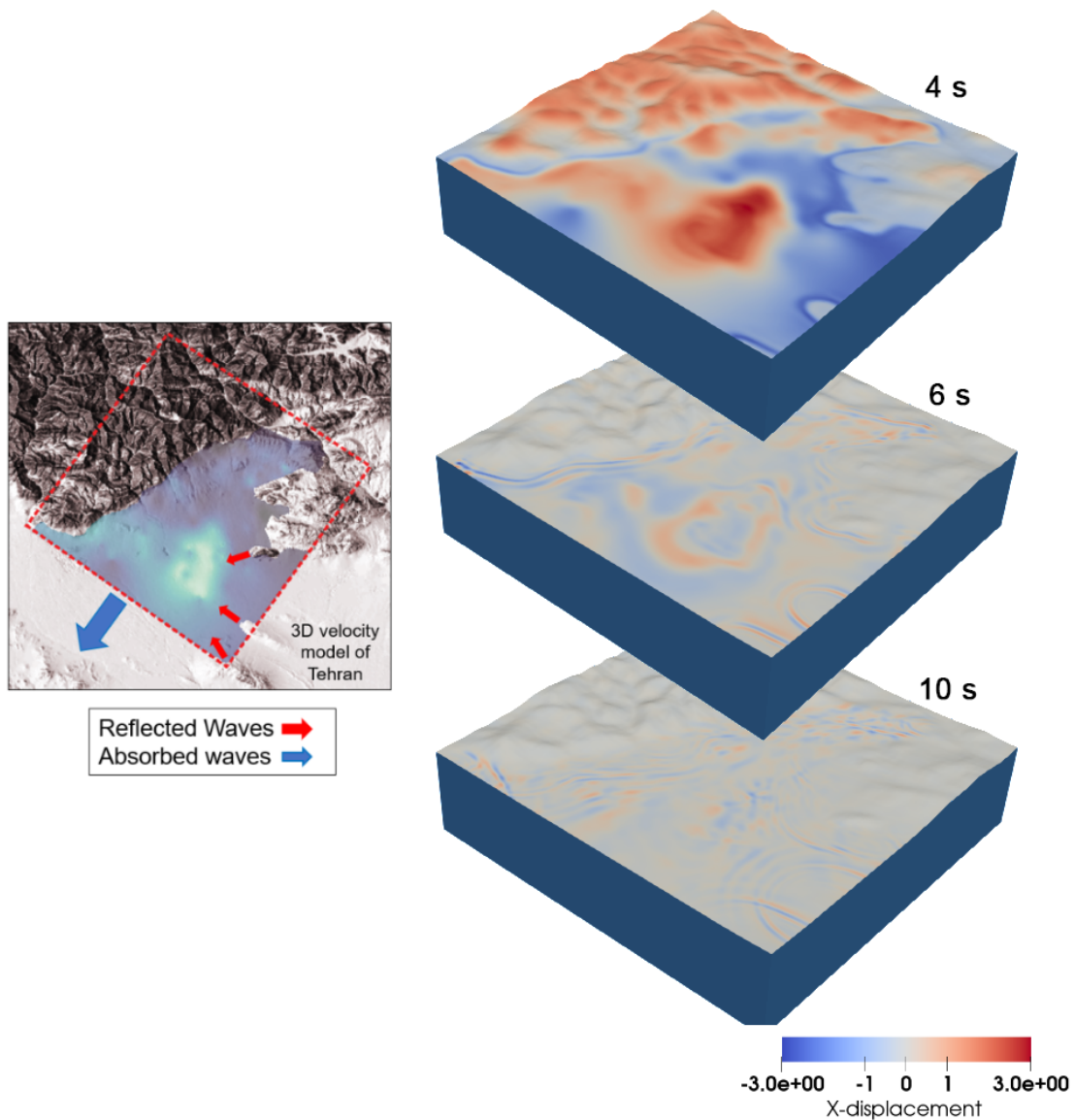


Figure 4-17: plot A to D represents the seismic wave propagation at four different time points: 3, 5, 10, and 20 seconds after the source was injected. The middle plot displays a 3D velocity structure of Tehran, with red arrows indicating diffracted waves at the basin edges, blue arrows indicating absorbed waves at the basin boundaries, and yellow arrows pointing waves trapped in the deeper parts of the basin.

4-5-2 Time-series cross-section

Besides capturing snapshots, it is possible to extract time-series data for each receiver location (Figure 4-18). These time-series data are saved in separate files, with file names corresponding to the line numbers in the receiver files. The data is stored in binary format by specific structure with 10 elements including the time and values for horizontal and vertical displacements (u_x , u_y , u_z), velocities (v_x , v_y , v_z), and accelerations (a_x , a_y , a_z) at each receiver location.

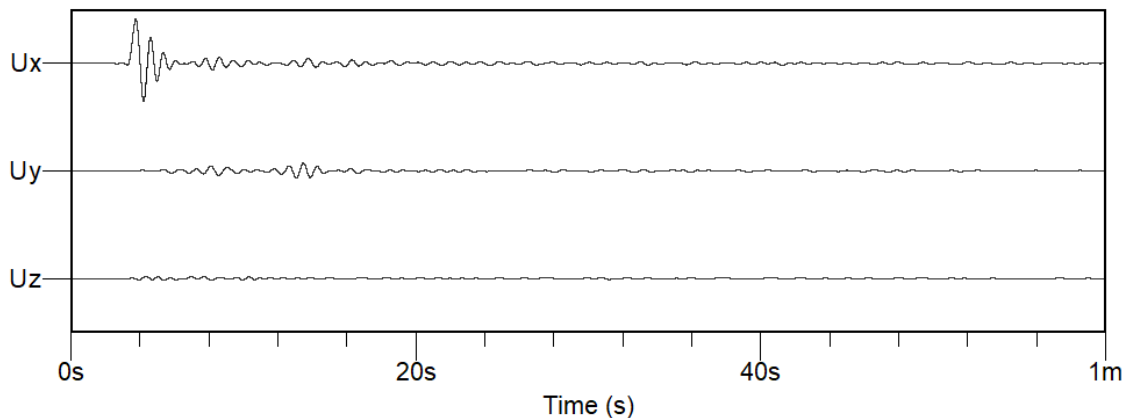


Figure 4-18: An example of time-series for displacement components.

In fact, the extraction of time-series along two cross-sections, introduced in chapter 3 (Figure 3-17), can provide more valuable information than single time-series. First of all, these cross sections can identify trends in the data to investigate how these trends correlate with variations in geophysical properties. In addition, they are capable of visualizing the three-dimensional site effect, such as the generation of diffracted surface waves along the cross-sections. Figure 4-19 illustrated time-series cross-sections alongside their corresponding geophysical cross-sections. As expected, for the northeast-southwest cross section the amplification and duration lengthening of the surface ground motion are evident from the middle of the basin where the seismic bedrock depth increases. This is caused by the generation of diffracted surfaces at the sediment-to-bedrock sloping interface that are efficiently trapped at the basin's center within the bowl-shaped region, especially evident in section BB' in Figure 4-19. Moreover, in the northern part, the occurrence of a local sub-basin results in locally trapped surface waves as evidenced in cross-section AA' in Figure 4-19.

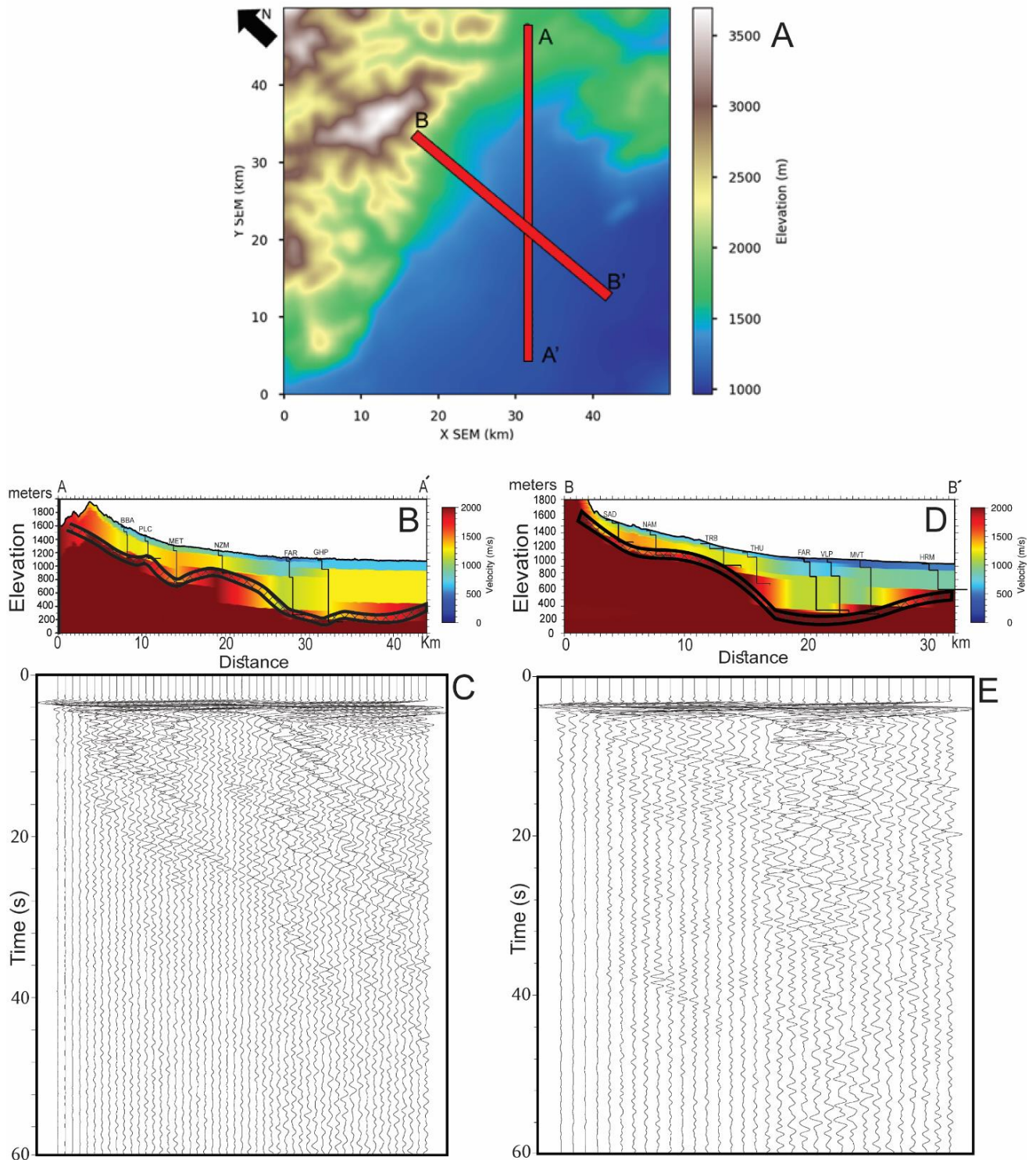


Figure 4-19: A) Tehran map with the location of two cross section AA' and BB'; B) AA' geological cross-section and C) corresponding velocity seismograms; D)BB' geological cross-section and E) corresponding seismograms.

Examining the other ground motion indicators than the time-series along the cross-section can give a deeper understanding about the characteristics of the seismic wave propagation. For instance, computing the Fourier amplitude spectrum along the entire length of the cross section can illustrate how the amplification varies from the northern to the southern region of the basin (Figure 4-20). Besides, it can also provide preliminary arguments regarding potential energy deficiency on the horizontal component in relation to the large number of H/V curves not exhibiting any peak (see Chapter 3, Figure 3-9). In this regard, if the flatness of the H/V curves were due to three-dimensional effects as observed in some studies (e.g. Uebayashi, 2003; Leroux et al., 2012), I should observe flat Fourier amplitude spectra in the numerical simulations. Fourier amplitude spectra along the two cross-sections in Figure 4-20 indicate that, in the northern and northeastern parts of the basin, ground motion is mostly amplified between 0.6 and 1.5 Hz, while in the southern and southwestern parts of the basin the amplification occurs between 0.3 and 0.5 Hz as a consequence of thicker geological materials. Along these two cross-sections, I do not see any “flat” amplitude spectra except for receivers on outcropping rock, which would not favor at first glance any 3D effects to explain the observed flat H/V curves.

However, it is difficult to make a conclusive statement, as the flatness of the experimental curves may be caused by other factors, such as the lack of significant velocity contrasts between sediments and bedrock, the lateral variation of shear-wave velocity not accounted for in the simplified 3D velocity model or the lack of energy in the seismic noise wavefield at the measurement time as outlined in Guillier et al. (2007).

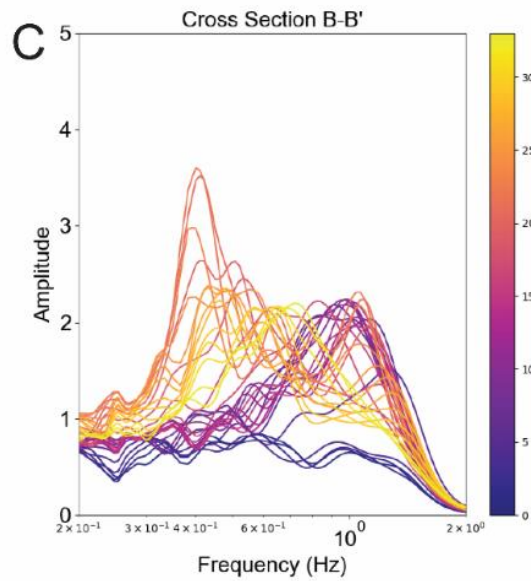
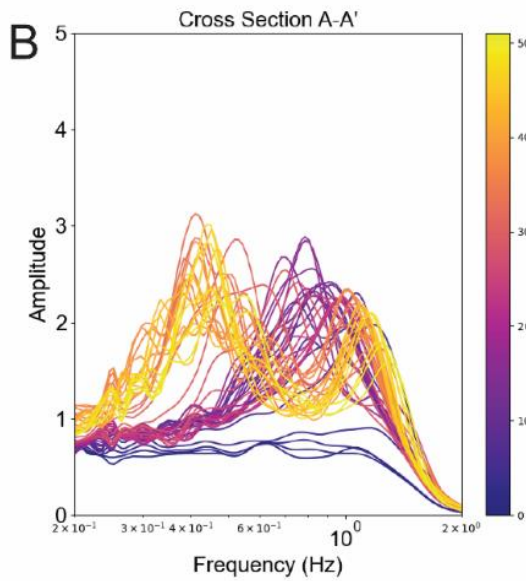
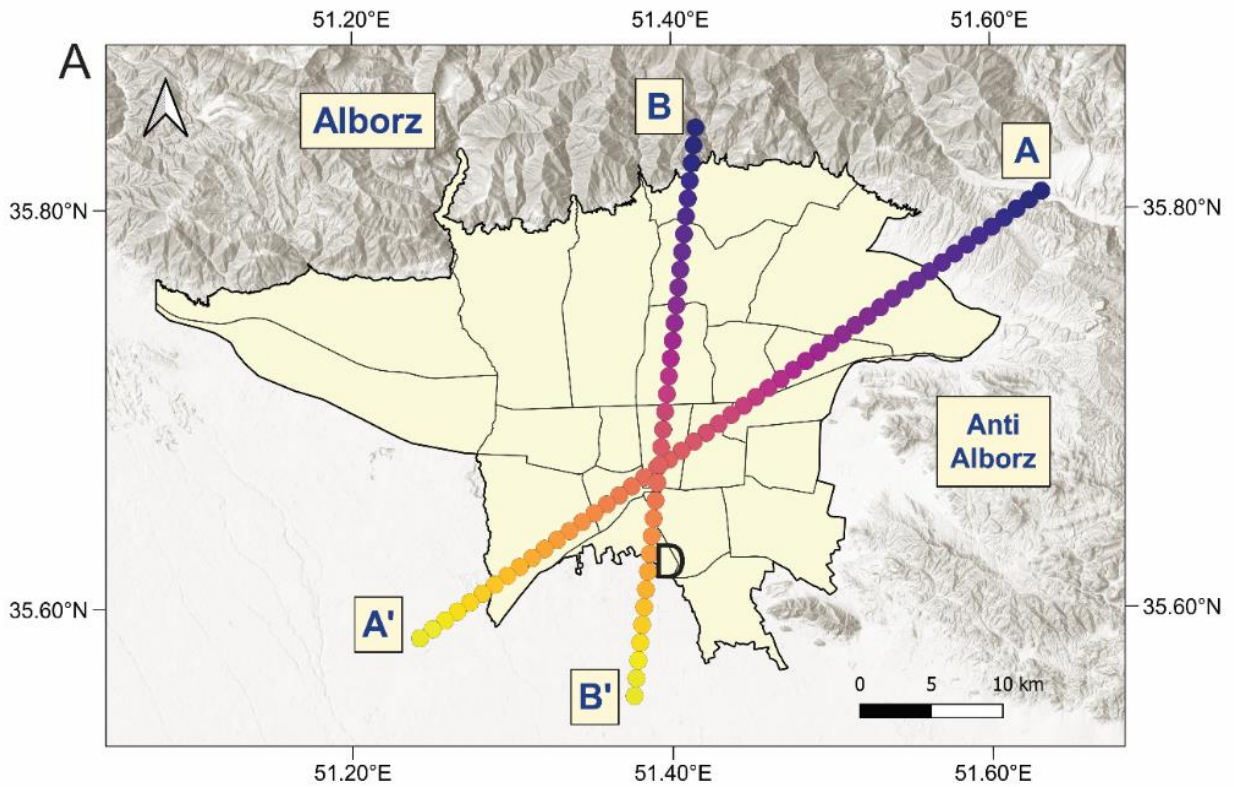


Figure 4-20: The Fourier amplitude spectrum for all time-series extracted on both cross sections. A: Map localization of the A-A' and B-B' cross sections. B: Fourier amplitude spectra for A-A'. C: Fourier amplitude spectra for B-B'.

4-5-3 Comparison between simulated and experimental f_0 's

The objective of this section is to focus on the comparison between synthetic and experimental fundamental resonance frequencies (f_0). The synthetic resonance frequencies were obtained by considering the peak of horizontal spectrum since there is almost zero energy in z component (Figure 4-18).

The relative differences between the fundamental resonance frequencies derived from synthetics ($F0_{sim}$) and experimental ones ($F0_{exp}$) are displayed in Figures 4-21. The relative average error is about -11% while the median error value is about -9% which outlines the overall ability of the 3D numerical simulations of ground motion to reproduce observed resonance frequencies. However, the negative bias indicates that our simulated fundamental frequencies are higher than the experimental one's. It can be explained by 1) the fact that the 3D structure model is constructed based on 1D wave propagation assumptions which is probably a strong assumption given the presence of large diffracted and trapped surface waves in the basin and 2) the negative bias introduced when simplifying the Vs profiles in the sediments (Figure 3-29).

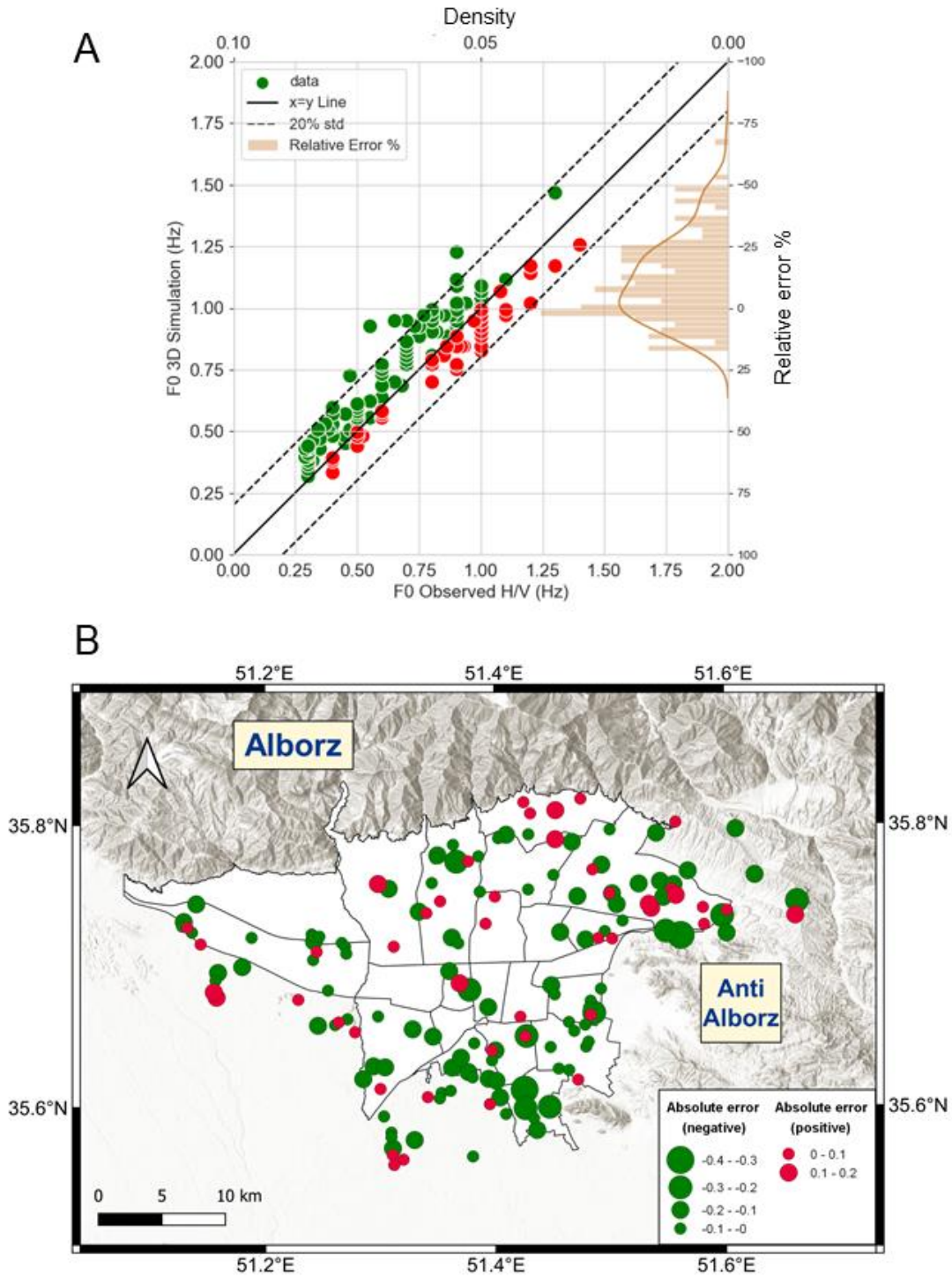


Figure 4-21: A: Scatter plot of f_0 extracted from 3D numerical simulation as a function of H/V peak frequencies observed in Tehran. The dash line represents the 20% standard deviation, the right panel represents density and histogram plot of relative error between the resonance frequencies derived from synthetics and experimental data. B: Spatial distribution of the absolute errors between observed and simulated frequencies.

4-5-4 Comparison between simulated and experimental amplifications (SSR's)

To assess the effectiveness and robustness of our 3D numerical simulation in the Tehran basin to predict site amplification, I compared the synthetic and experimental (Haghshenas, 2005) SSR curves. It involves computing SSRs from the simulated surface velocities. The Fourier amplitude spectrum for the experimental campaign (Haghshenas, 2005) was computed from the quadratic mean of the horizontal components using the entire signal and I use in this study the same approach and the same reference station (Haghshenas, 2005). It is worth noting that while selecting S-wave phases only is a common practice, this approach may suppress the diffracted surface waves arriving later from the edges of the ground in sedimentary basins, leading to an underestimation of amplification (Field, 1996; Haghshenas, 2005). First, I examined the obtained SSRs in three distinct basin regions in the north, the south-southwest and the southeast (Figure 4-22).

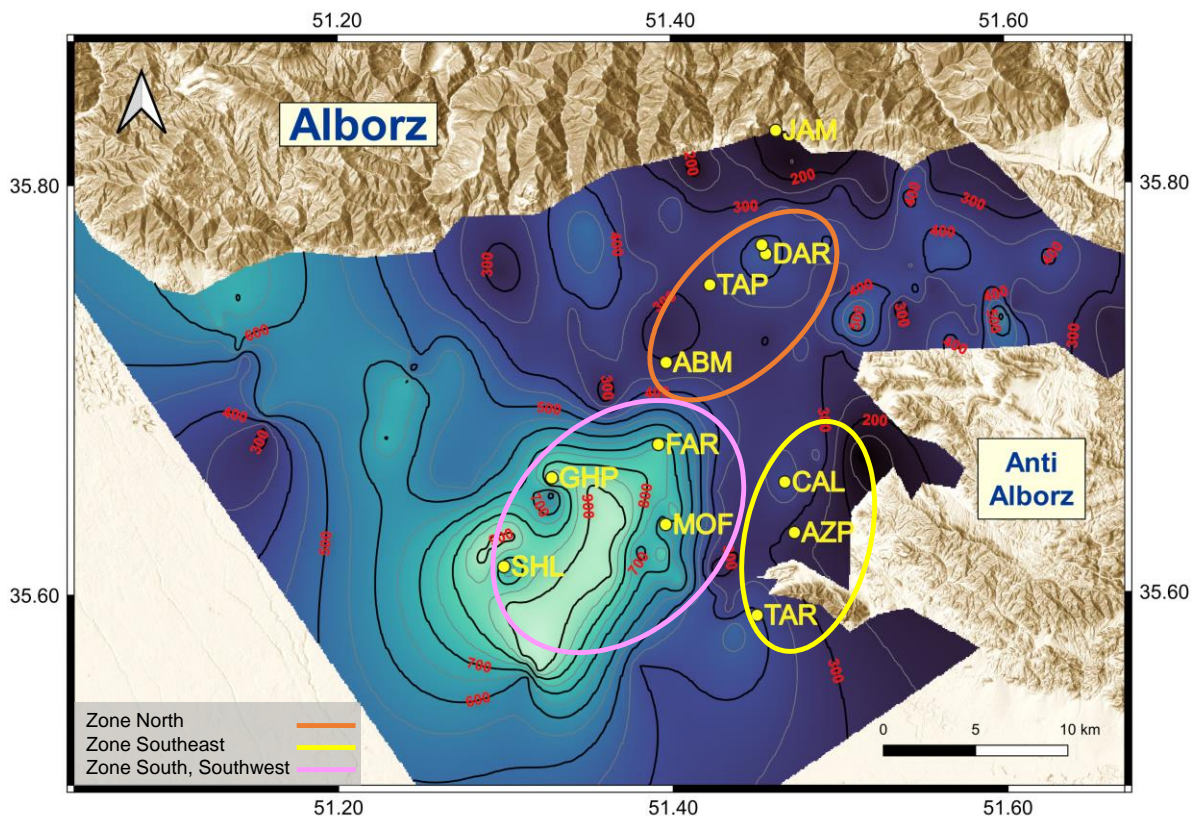


Figure 4-22: Different regions considered to compare observed and simulated SSR curves. Each region exhibits almost the same shape of SSR curves

4-5-4-1 Northern region

The northern region comprises four stations arranged in a north-south direction, namely DAR, SUD, TAP and ABM. The f_0 values extracted for these stations during the 2002 experiment were 0.69, 0.47, 0.45 and 0.3 Hz respectively while the f_0 derived from our seismic noise measurements is 0.9 Hz at DAR (Table 3-2).

Despite being located within a distance of merely seven hundred meters from each other, the experimental results reveal a peculiar dissimilarity in the spectral features between the DAR and SUD stations (Figure 4-23, A-B). In order to describe this heterogeneity, Haghshenas (2005) suggested the presence of softer lacustrine sediments that were deposited in tectonic depressions of this area. As depicted in Figure 4-23 (A and B), the ground motion synthetics provided almost equivalent results for both stations due to their proximity and exhibit satisfactory agreement with the peak frequency around 0.9 Hz (within 15%) and related amplification at DAR station, while underestimating the observed SSR between 0.3 and 0.6 Hz. This finding is consistent with the fact that the fundamental resonance frequency used at this site for the inversion of the 1D velocity model is 0.9 Hz, implying our 1D velocity model is not able to correctly reproduce actual amplification at low frequency.

For SUD, despite the resemblance in terms of the shape of the high-frequency between simulated and experimental SSR curves, still the actual SSR could not be reproduced at frequencies below 0.6 Hz. This is basically explained by the fact that the 1D Vs profile used to construct 3D velocity structure in this area is controlled by the 1D velocity profile inverted at DAR. The origin of this discrepancy is probably related to the complexity of the region, which can definitely not be explained by our simple 1D velocity structure.

Experimental results obtained from TAP station (Figure 4-23C) especially at low frequency, which is located in a highly tectonized region at the center of Tehran on a hilly topography within the crowded city center forest park, should be interpreted with caution, as the instrumental data are coming from the L22/C7227 short period sensor with frequency of 2.0 Hz and damping of 0.707. Similar to SUD, the shape of the high-frequency part of the curve is almost reproduced, although a notable difference in amplitude is observed between the experimental and simulated peak amplitudes at low frequency (Figure 4-23C).

The explanation of this discrepancy with the available information is not possible, particularly in the area where TAP is located where the available observed data for constructing the 3D structural model is very limited (Figure 3-9 for the distribution of observed data used to construct 3D velocity model).

For ABM at 0.3 Hz, experimental studies revealed a small amplification peak with a low amplitude just above two (Figure 4-23D). Despite the low amplitude, this peak was present in all earthquake data (Haghshenas, 2005).

Unfortunately, like station TAP, the available information around this station is very limited. Concerning the fact that the ABM is located at the edge of the sediment-to-bedrock transition zone within the basin, our model is just defined as an interpolation between the data in the north and south. Therefore, the exact shape of this transition close to ABM is not known exactly. The SSRs derived from ground motion synthetics are not consistent with the observed SSRs over the whole frequency range (Figure 4-23D).

4-5-4-2 Southern region

The southern section comprised four stations located in the south and the southwest parts of the basin, namely FAR, MOF, GHP, and SHL. The f_0 values extracted for these stations during the 2002 experiment were 0.45, 0.45, 0.26, and 0.27 Hz respectively.

The shapes of the SSR curves derived from the experimental data are fairly well reproduced over the whole frequency range by the SSRs derived from the synthetic data, particularly for the MOF site (Figure 4-24). The predicted amplifications are in the form of a plateau, with notably large amplifications between the resonance frequency peaks caused by diffracted surface waves as classically observed (e.g. Field, 1996; Cornou and Bard, 2003; Bindi et al., 2009; Maufroy et al., 2015; Theodulidis et al., 2018). However, I can note that the predicted amplifications are lower than the actual amplifications, except at GHP. These low amplifications may originate from average V_s in the sediments used in the wave propagation simulations being larger than the actual V_s , given that the inverted V_s show a decreasing velocity gradient from the northern to the southern parts of the basin (Figure 3-20) not considered in the calculation of average V_s . Other factors may also come into play, such as the V_s in the seismic bedrock or the quality factor, which will be discussed in a subsequent section.

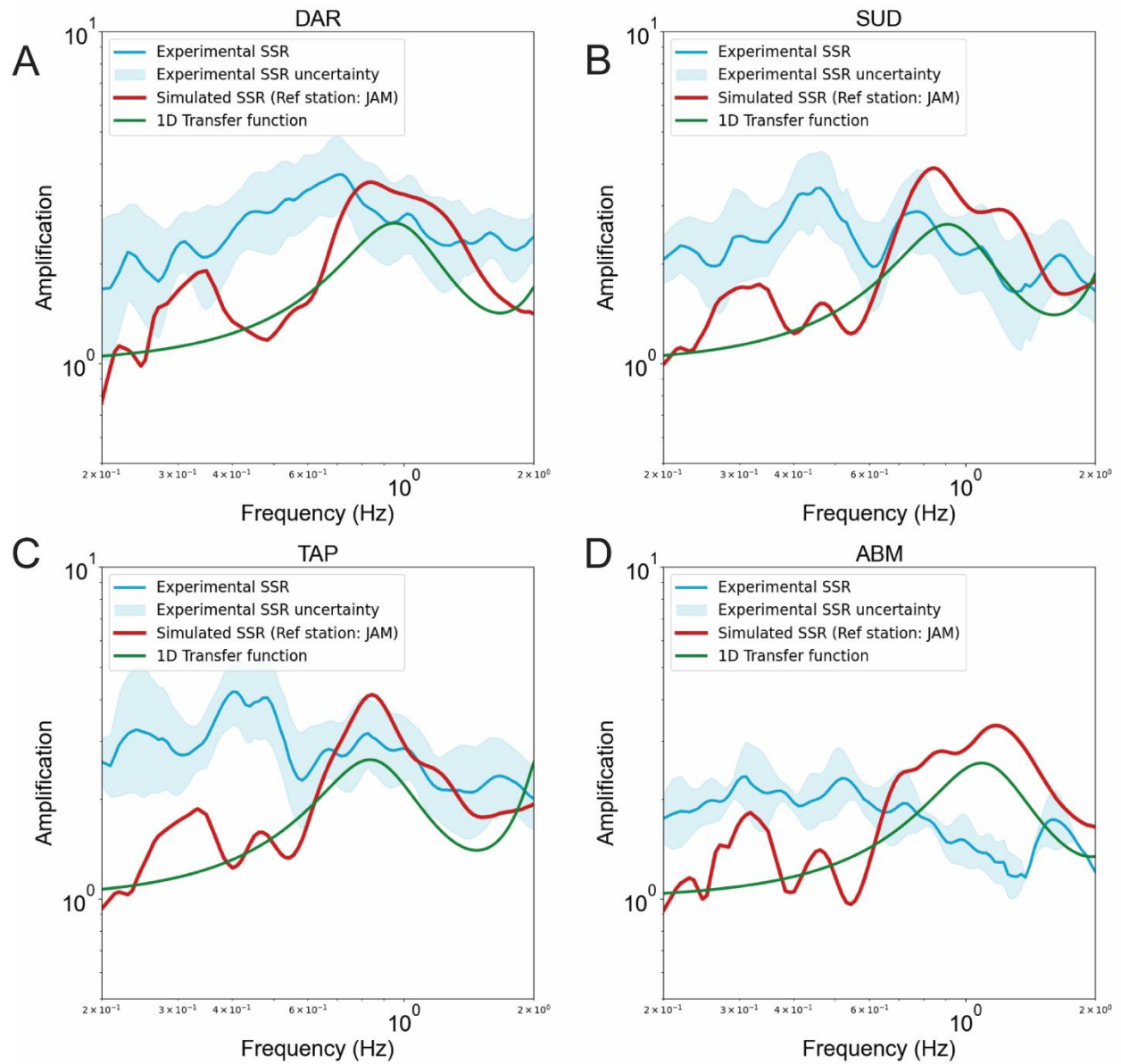


Figure 4-23: SSR derived from ground motion synthetics (red lines) and experimental earthquake data (blue lines) at four stations located in the north of Tehran’s basin. A: DAR station, B: SUD station, C: TAP station and D: ABM station. For all stations, the 1D SH transfer function is displayed in green lines.

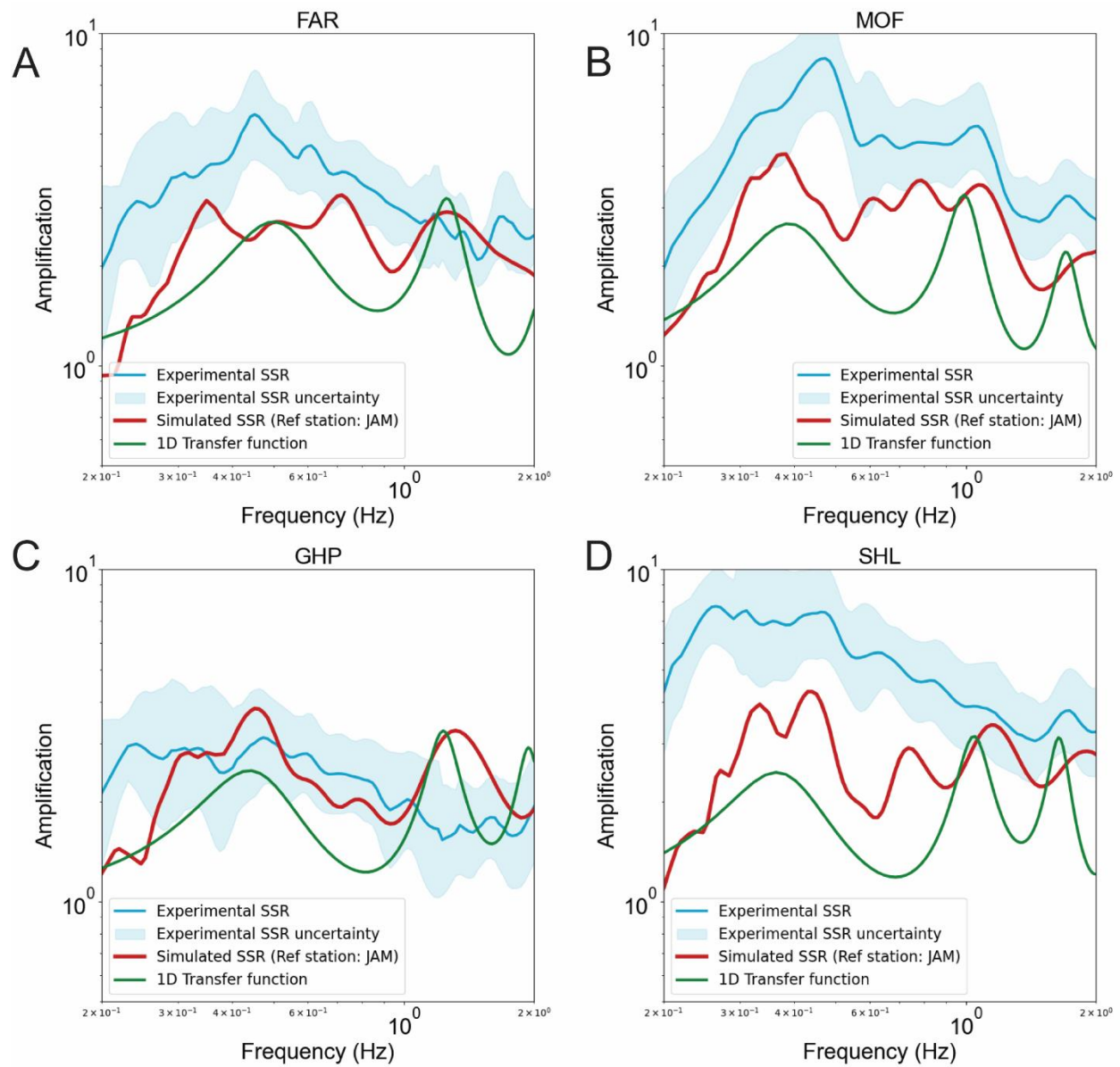


Figure 4-24: SSR derived from ground motion synthetics (red lines) and experimental earthquake data (blue lines) at four stations located in the south of Tehran's basin. A: FAR station, B: MOF station, C: GHP station and D: SHL station. For all stations, the 1D SH transfer function is displayed in green lines.

4-5-4-3 Southeastern region

Finally, the southeastern region consisted of three stations located in a southeast part of the basin, namely AZP, CAL, and TAR. The f_0 values extracted for these stations during the 2002 experiment were 5.4 (no peak below 2 Hz), 0.49, and 1.07 Hz respectively.

The reported resonance frequency at 0.49 Hz in the experimental SSR at CAL can be considered as a bump, given that the H/V from earthquakes from the 2002 experiment at this station shows a H/V peak frequency at 0.8 Hz (Figure 4-25B). I also observe this peak frequency with H/V noise campaign and use it to construct the 3D velocity structure model. This is the reason why SSR from ground motion synthetics indicates an amplification at about 0.8 Hz. The almost flat SSR curves at CAL obtained from earthquake recordings are not in agreement with those observed data (H/V on earthquake in 2005 or H/V on noise in this study). The absence of amplification in the experimental earthquake data could be attributed to the complex geometry of the basin edge leading to complex wave propagation not accounted for in our 3D model (Figure 4-25A and B).

At AZP which is located nearby CAL and closer to the basin edge, the SSR derived from synthetics also indicates an amplification at about 0.8 Hz, consistently with the V_s model used (Figure 4-25A). At this site however, the SSR from earthquake recordings is flat since the fundamental resonance frequency occurs at frequency higher than 2 Hz, which indicates that our 3D model is not able to capture the complexity (geometry and/or V_s) of the basin edge.

Station TAR exhibits a relatively clear peak around 1 Hz, which could be approximately retrieved through simulation. The SSRs from synthetics slightly overestimate the actual amplification, which could be due to the presence of more rigid alluviums at TAR station, situated near the mountains, compare to the V_s used in our simulation (Figure 4-25-C).

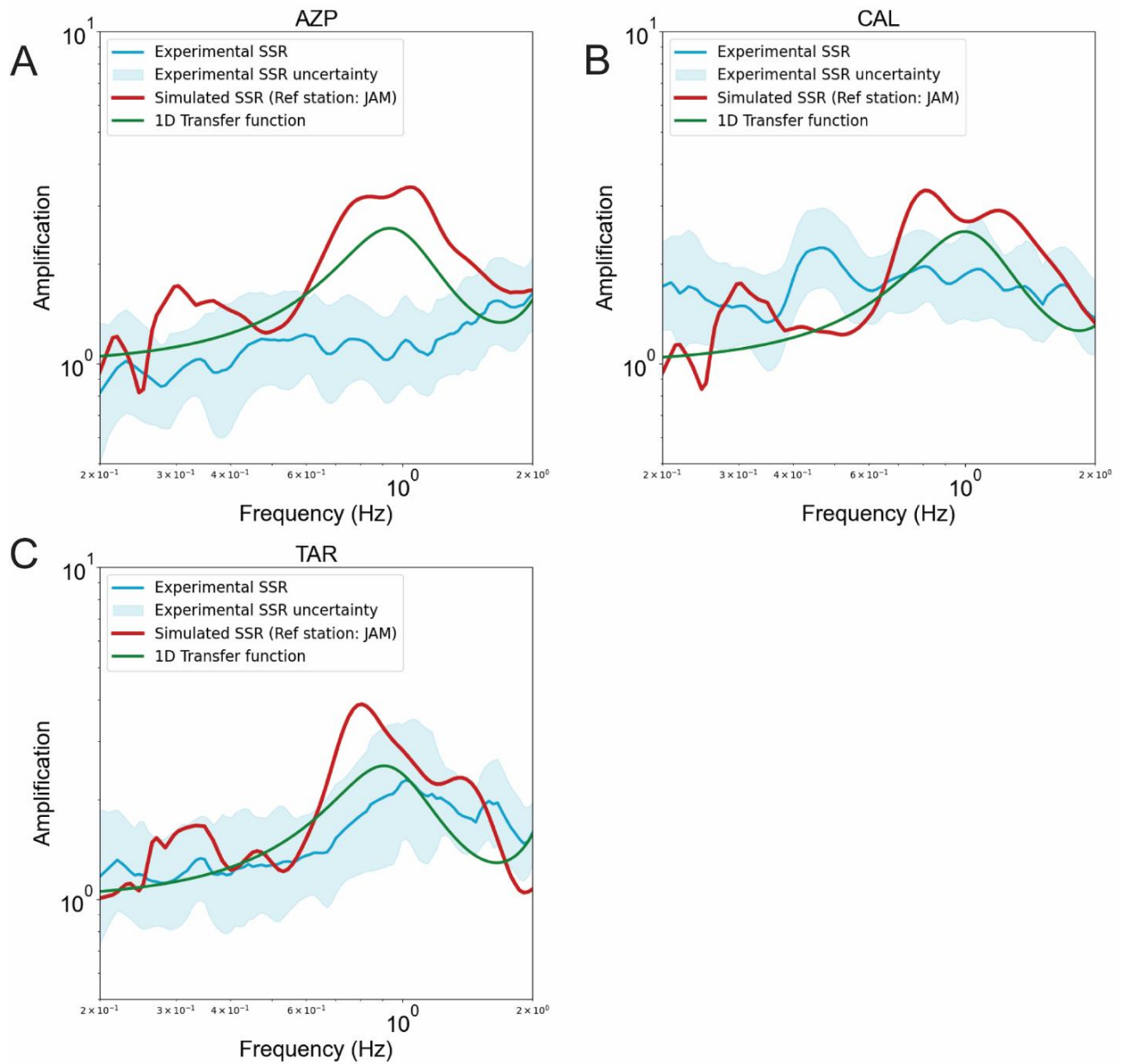


Figure 4-25: SSR derived from ground motion synthetics (red lines) and experimental earthquake data (blue lines) at four stations located in the in southeast zone. A: AZP station, B: CAL station and C: TAR station. For all stations, the 1D simulated response is displayed in green lines.

4-5-4-4 Conclusion

The discrepancies between the actual and simulated amplification at the fundamental resonance frequency are shown in Figure 4-26. While the amplifications are rather similar for the stations DAR and GHP stations located in the north and south of Tehran's basin, the experimental amplification are consistently higher than the simulated ones for all other stations, except for TAR station which is located very close the basin edge at southeast. This discrepancy is particularly pronounced for the stations located in the southern regions, reaching up a factor of two, and could be attributed to the higher average Vs used in the simulation compared to the actual Vs in the southern regions due to the gradual decrease of Vs from the northeast to the southwest as seen from Vs profiles inversion (Appendix C) or to the bedrock Vs or quality factors not large enough.

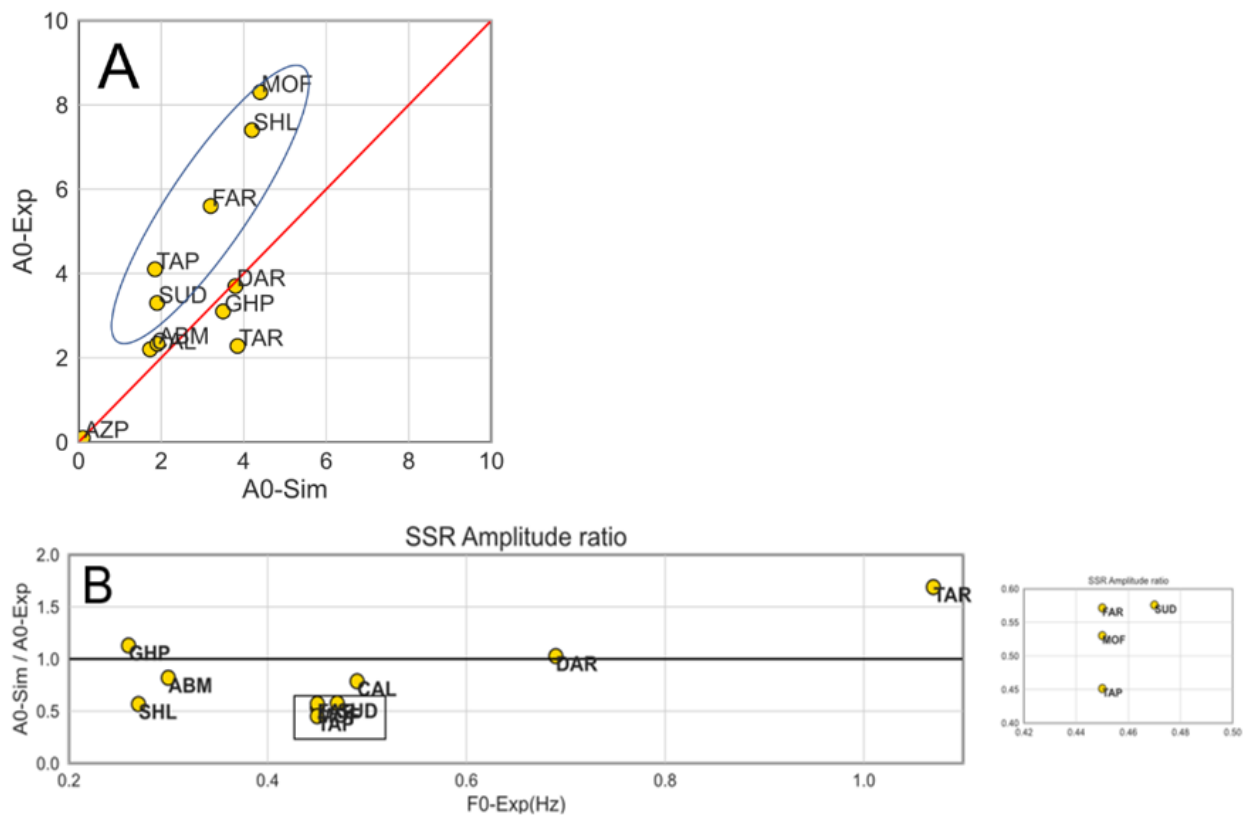


Figure 4-26: A: Amplification at the fundamental resonance frequency for the experimental and simulated SSR curves. B: ratio between simulated and experimental amplification at the fundamental resonance frequency as a function of experimental resonance frequency.

However, the shape of the SSR curves that are of the form of a plateau like typical of multidimensional site effects could be reproduced at the southern stations contrarily to the stations located in the northern region. In this region, our simulations are unable to capture the amplification observed at low frequency with earthquake recordings. Such discrepancies could be attributed to: i) limited available data for constructing the 3D model, ii) the inherent complexity of the central part of Tehran characterized by the presence of small and large faults, and iii) the short period sensors used for getting the experimental SSR that could also affect the results.

Interestingly also, SSRs derived from ground motion synthetics for the stations located in the north (Figure 4-23) and southeast (Figure 4-25) exhibit an amplification peak at 0.3 Hz, that will be discussed in the next sections.

4-5-5 Sensitivity analysis

In order to better understand the origin of the discrepancies between SSRs derived from synthetics and earthquake recordings, I investigate the impact of: (i) the reference station, (ii) the quality factor, and (iii) the bedrock S-wave velocity.

The choice of a reference rock site that is not impacted by any site effects due to topography or rock weathering is critical for site amplification studies (Steidl et al., 1996). Some rock sites may have their own (de)amplification (Chavez-Garcia et al., 1990) or topographical effect (Massa et al., 2014; Maufroy et al., 2018). The JAM station which I considered as the reference station as in Haghshenas (2005) is located in a small hut within Jamshidieh Park, positioned on the southern slope of Mount Touchal (Figure 4-27A), where the rock is composed of Eocene green Tuff which likely forms the bedrock in the northern part of the city. However, with an elevation of approximately 1800 m, the JAM station has an altitude difference of about 600 m compared to the southern stations such as SHL that could generate some topographical effects. The topographical effects would be at rather low frequency, given the dimensions of Mount Touchal (Haghshenas, 2005). Unfortunately, the raw data for the JAM station, as well as other seismological stations from the 2002 experiment, are not available any more, preventing us from conducting a precise examination of these effects in the earthquake recordings.

The quality factor that controls the damping of a seismic wave as it travels through a medium is another important parameter. In Tehran, I have no direct measurements of the quality factor in sediments and I used the rule of thumb value in our simulations (i.e. $Q_s = V_s/10$). Since the ground

motion amplification is proportional to the quality factor, it is critical to assess the impact of this parameter. Finally, the bedrock velocity controls the impedance contrast and consequently the site amplification.

Additionally, it is generally admitted that the Tertiary sediments can be assumed as rocky sites when some authors state that it is totally dependent of the Tertiary-older rocks impedance contrast (Nguyen et al., 2004; Guillier et al., 2005). This means that taking Tertiary sites as reference may sometimes lead to wrong interpretation, especially for SSR processing, and so the Tertiary sediment sites should be taken carefully to avoid any bad interpretation.

4-5-5-1 Impact of the reference station

In our SSR analyses, I used as a reference a receiver located at the same place as the reference station (JAM) used by Haghshenas (2005) during the 2002 seismological experiment. To determine the impact of using this specific station on the SSR curves, I computed the SSR using 17 other reference stations distributed on the topography (Figure 4-27A). The SSRs computed at all the stations are indicated in Appendix E.

The Fourier amplitude spectra calculated at the 18 reference stations are variable, as a consequence of topographical effects only (Figure 4-27B). Interestingly, station JAM is the only one with a spectral amplitude deficit at 0.3 Hz compared to the other stations. Consequently, the SSRs calculated at DAR and FAR stations (Figure 4-27C and D) using all the reference stations do not show an amplification peak at 0.3 Hz as pronounced as when using JAM. The choice of the JAM site as a reference rock site thus explains the amplifications at 0.3 Hz systematically observed in our SSR evaluations (Figure 4-23 and Figure 4-25). The choice of reference station also has a slight impact on the evaluation of the site's resonance frequency.

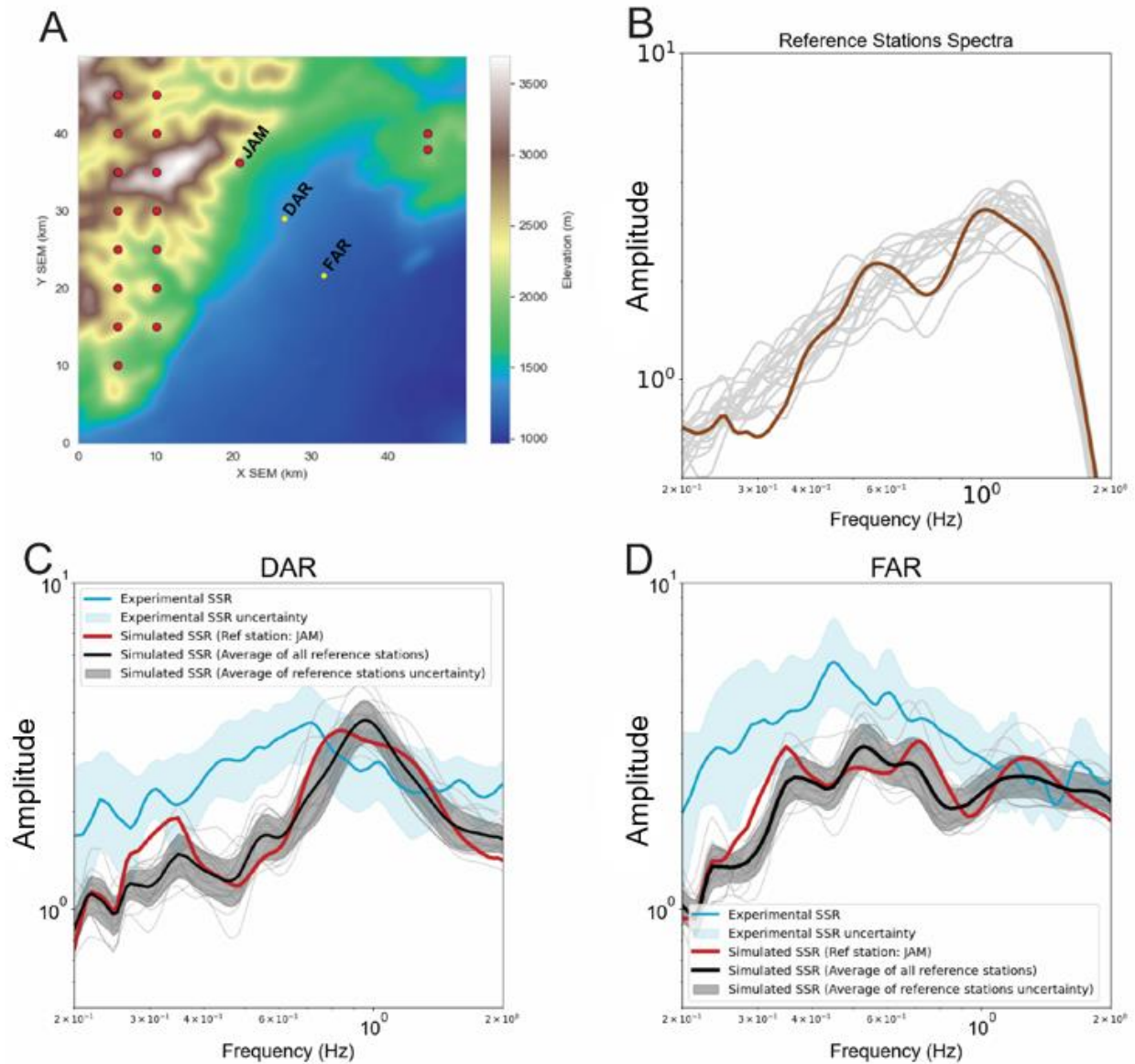


Figure 4-27: A: Location of reference JAM station and 17 other possible bedrock reference stations (red plain circles) and the location of DAR and FAR stations in yellow. B: The Fourier amplitude spectra of all reference stations (brown curve for JAM station and light grey curves for the 17 other sites) computed from the surface velocities. C: the experimental SSR (in blue) and simulated SSRs using the 17 reference stations (gray lines) for DAR station. The average SSR using all reference stations including JAM is shown in black while the SSR computed using JAM is indicated in red. D: the experimental SSR (in blue) and simulated SSR (in red) for FAR station. The average SSR using all reference stations including JAM is shown in black while the SSR computing using JAM is indicated in red.

4-5-5-2 The effect of the quality factor

In chapter 4, it is mentioned that wave attenuation in the Tehran basin has not been reliably studied in this work or in other study. Since this parameter describes how much energy is lost as seismic waves propagate through the subsurface, it can clearly affect the site response. Generally, the frequency dependent quality factor is calculated from the following equations for P and S waves.

$$Q_s(f) = \frac{-\pi f}{\ln \ln(10) c \beta} \quad \& \quad Q_p(f) = \frac{-\pi f}{\ln \ln(10) c \alpha} \quad (\text{eq. 4-46})$$

Where c is a constant and α, β are compressional and shear wave velocity. In the absence of detailed information about the subsurface structure to evaluate quality factors, it is common to use $Q_s = \frac{V_s}{10}$ and $Q_p = 2Q_s$, which was used in our simulations. However, it seems that the value of $\frac{V_s}{10}$ may be considered low for the alluvial part of Tehran basin (Zaferani et al., 2012), so I attempt to re-simulate the seismic ground motion in the basin using $Q_s = \frac{V_s}{5}$ and $Q_p = 2Q_s$. SSRs calculated with these new quality factors indicate that the predicted amplification over the whole frequency range increases by 1 to 3% (Figure 4-28). These results indicate that, the seismic response in the Tehran basin is not particularly sensitive to variations in Q , at least within the range of tested values.

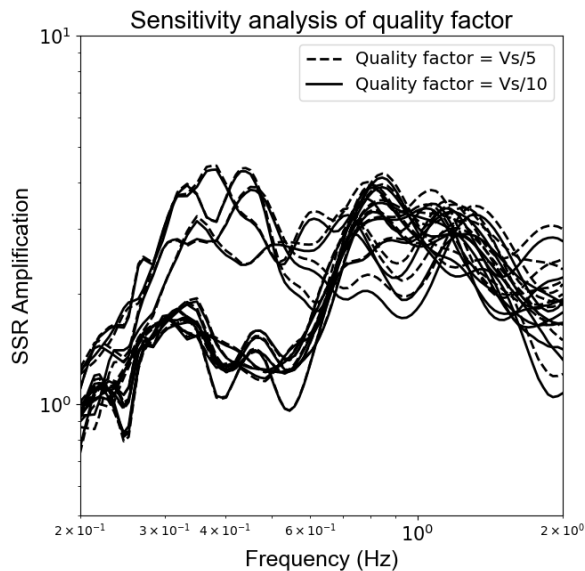


Figure 4-28: Testing the sensitivity of the SSR results to the quality factor (Q_s). The solid lines represent the simulation results using $Q_s = V_s/10$, while the dashed lines represent the results using $Q_s = V_s/5$. Note that $Q_p = 2Q_s$.

4-5-5-3 The effect of bedrock S-wave velocity

Impedance contrast plays a crucial role in controlling the amplification function, with larger contrasts resulting in larger amplification. In chapter 4, I reviewed the velocity models for the Alborz region below 5 km depth, where the range of shear wave velocity was around 3 to 3.2 km/s. However, these velocity estimates were primarily based on P-wave tomography and $\frac{V_p}{V_s}$ ratio assumption. Some other studies reported the values up to 6 km/s for V_p values. So, to investigate the effect of bedrock velocity, I simulate the seismic wave propagation using $V_s = 3.5$ km/s.

SSRs calculated with this new V_s value are shown in Appendix 5A. For the DAR and FAR stations (Figure 4-29), the new SSRs predict higher amplifications than previously, even leading to an SSR at FAR that is very consistent with the experimental SSR over a wide frequency range.

Moreover, the linear relationship (Pearson correlation coefficient) between the experimental SSR curve and the two simulated SSR curves with bedrock velocity of 3000 m/s and 3500 m/s is indicated in Table 4-3. The stations in south and southeast show higher coefficient value (negative change) when increasing V_s in the bedrock, i.e. the impedance contrast, indicating that the fit between the curves have been improved. On the contrary, the fit is found to worsen for stations located in the north. This leads to different observations:

- i) the possible existence of lateral variations in bedrock velocity, which is consistent with the geological conditions of Tehran. Indeed, the mountainous region is not homogeneous and is divided into two formations: The Tertiary Karaj Formation for the Alborz in north and the Cretaceous limestone with Paleozoic core for the Anti Alborz in southeast. Based on the lithology and age of the existing rocks (see Chapter 1), it can be inferred that the rocks constituting the bedrock in the south might have higher velocities. However, verifying this issue cannot be easily proven as tomography studies performed in Tehran so far have not enough resolution, and no boreholes have been drilled down to the bedrock in Tehran.
- ii) Any decrease of average V_s in sediments, especially in the south to be consistent with the gradual decrease of V_s from north to south, will automatically increase the impedance contrast, leading also to the same results.

- iii) Of course, a combination of both observations is also possible, with an increase in the bedrock velocity in relation with a decrease of the sediment S-wave velocity toward the south.

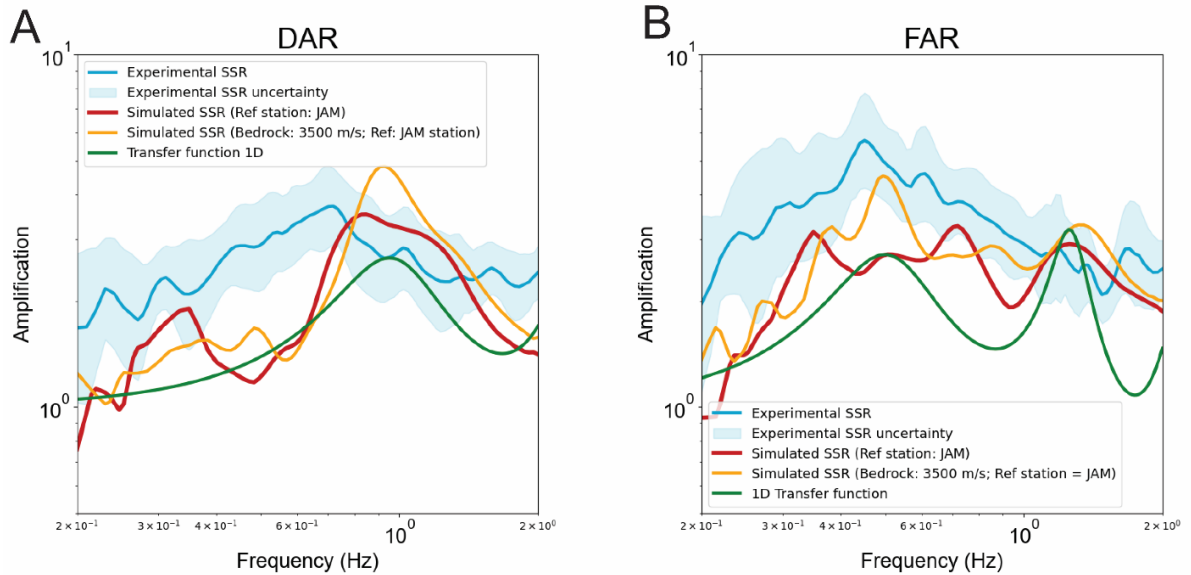


Figure 4-29: Testing the sensitivity of the SSR curves to change in the impedance contrast. the experimental SSR (in blue) and simulated SSR (in red), the simulated SSR with bedrock velocity of 3500 m/s (in yellow) and 1D transfer function (in green) for A: DAR station and B: FAR station.

Table 4-3: Pearson correlation coefficient between simulated SSR curves before and after the change of bedrock V_s . Negative change indicates that the results have improved following the bedrock velocity modification. The Pearson correlation coefficient ranges from -1 to +1, where -1 indicates a perfect negative correlation, and +1 indicates a perfect positive correlation.

Stations	Pearson correlation coefficient (Before bedrock change, $V_s=3000\text{m/s}$)	Pearson correlation coefficient (After bedrock change, $V_s=3500\text{m/s}$)	Change (before-after)
ABM	-0.7	-0.78	0.08
AZP	0.11	0.23	-0.12
CAL	0.24	0.26	-0.02
DAR	0.36	0.26	0.1
FAR	0.46	0.54	-0.08
GHP	0.09	0.1	-0.01
MOF	0.61	0.79	-0.18
SHL	0.24	0.12	0.12
SUD	-0.06	-0.21	0.15
TAP	-0.12	-0.24	0.12
TAR	0.68	0.81	-0.13

4-6 Discussion and conclusion

This chapter has presented the numerical simulation study aimed at a better understanding of the seismic wave propagation in the Tehran basin and the effects on surface ground motions. It should be noted that this numerical study has provided the first insights about prediction of ground motion in Tehran.

Using the open-source spectral-element code EFISPEC3D, I simulated ground motion based on the sedimentary basin model and compared it with real earthquake ground motion, as well as experimental H/V frequency peaks. The results in terms of fundamental resonance frequency demonstrate a promising correlation between real and simulated data. Meanwhile, the observation of significant trapped surface waves generated by 3D site effects in the time series cross-sections, suggested that the 3D geometry characteristics of the Tehran's basin should always be considered for an accurate ground motion estimation. Furthermore, analyzing the time series in the frequency domain (Fourier amplitude spectra) also reveals some insights about the site amplification variation from the north to the south of the basin. This observation highlights ground motion amplification along the entire north-south cross section, suggesting that the occurrence of experimental flat H/V curves cannot be straightforwardly linked to the 3D effect.

Following this, In the south and southwest, I have been able to reproduce the f_0 and the shape of site amplification (SSR) in the south and southwest of the basin, although predicted site amplifications are lower than actual ones.

However, in the north I am not able to reproduce the actual site amplification at low frequency, indicating that our 3D ground model is probably too simple to capture the complexity of the seismic wave propagation in this region.

Besides this, the failure to reproduce the amplification function in the north could potentially be attributed to the interpretation of geophysical data. First, I assumed 1D wave propagation when the observed Rayleigh and Love dispersion curves, even though these curves could be strongly biased by 3D effects. Moreover, it is less likely, but there is a possibility that I misinterpreted the modes in the inversion process. I might have inverted the higher modes as the fundamental mode, leading

to a shear wave velocity profile with a shallower bedrock depth (higher f_0) than its true structure. Finally, I assumed that the velocity variation in the sedimentary layers remains constant from north to south. However, while this may cause slight changes in the site amplification, it is not likely to impact f_0 significantly.

The main findings from the sensitivity analysis will be discussed below. I performed the sensitivity analysis for three different parameters that have the potential to impact the final results. First, the impact of reference stations was examined. The results revealed that using the JAM station as a reference had a significant influence on the SSR ratio results (curve's shape and f_0), especially at low frequency. However, since the JAM was used to calculate the experimental SSR ratios in Tehran, I draw our conclusions for numerical simulation using JAM as the reference station. Unfortunately, the data from the 2002 experiment are not available any more for re-processing the results and quantifying the influence of the reference station. Nevertheless, I am now aware about the potential impact of the reference stations on SSRs. To check the effect, I could perform a new seismological temporary measurement campaign at the location of one site in the north using different reference stations. Analyzing the effect of this change in the reference station will allow us to evaluate the reliability of the experimental SSRs derived by Haghshenas (2005) especially in the low frequency band. This will also certainly help to confirm or not the reliability of our 3D velocity model for the northern part of Teheran's basin.

Second, the influence of the quality factors was investigated. It turns out that changing the quality factor had no discernible effect on the final results.

Third, the impact of impedance contrast indicates that adjusting the bedrock S-wave velocity led to an improvement in the results by increasing the site amplification in the southern region. This observation allows us to draw two hypotheses: the first hypothesis suggests the presence of a lateral variation in bedrock S-wave velocity from the northern to the southern areas with higher values in south. The second hypothesis raises the question of whether the initial velocity used in our simulations may be suitable for the northern area but too high for the southern region because I assumed that the S-wave velocity in the sedimentary layers remains constant from north to south. Beside all of the aforementioned observations, the central finding of the present study is that for the first time the simulation allows us to directly explore the level of ground motion amplification in the Tehran basin. In fact, due to the limited number of stations in the 2005 experiment, I was

unable to thoroughly examine site effect indicators across the entire basin, particularly in the western areas of the city that have experienced significant population growth in recent years. To know the amplification function all over the basin, I calculated the SSR ratio at the H/V experimental measurements sites (the same points used for constructing the 3D velocity structure; Figure 3-17).

The Figure 4-30 shows the SSR curves at all H/V measurement sites. By dividing these curves into two groups based on fundamental resonance frequencies (below and above 0.5 Hz), it can be observed that the stations with f_0 below 0.5 Hz which are located mostly in the southern and western part of the city, exhibit a more pronounced three-dimensional site effects with amplification over a wide frequency band. This observation aligns with the findings in Figure 4-19, where the simulated time series demonstrates the generation of surface waves that contribute to increased amplification and duration lengthening.

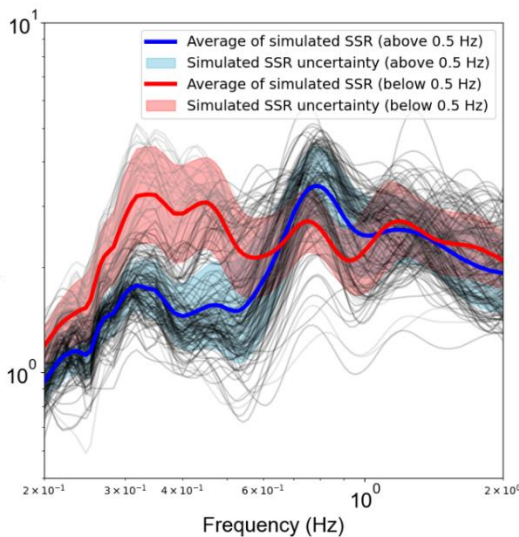
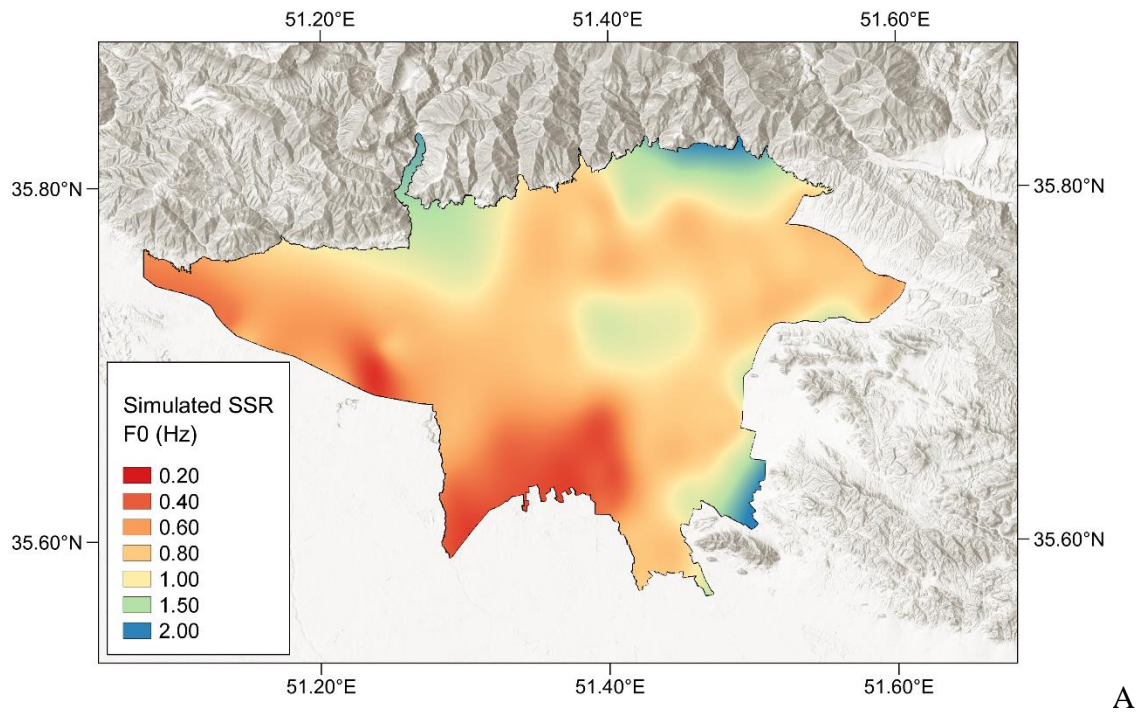
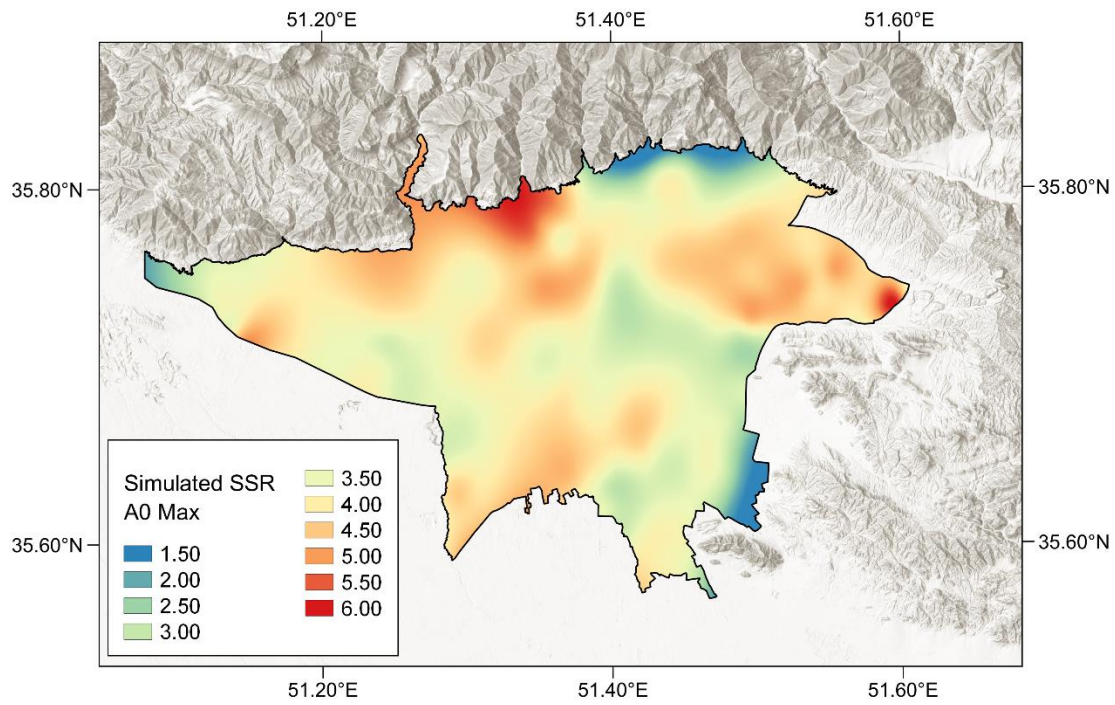


Figure 4-30: Simulated SSR at H/V experimental measurements location divided into two groups based on fundamental resonance frequencies. Results show that the sites with fundamental resonance frequency below 0.5 Hz located in the southern region exhibit significant 3D site effect.

After obtaining the SSR ratio at all H/V measurements location, I spatially interpolated the results to create simulated maps for f_0 and A_0 (amplification at the resonance frequency) in the Tehran basin. The interpolation was conducted using the kriging method with cubic interpolation. Figure 4-31 displays the resulting maps.



A



B

Figure 4-31: Interpolated results for f_0 (A) and A_0 (B) in Tehran basin from the simulated SSR at H/V sites.

The simulated f_0 map (Figure 4-31A) from SSR exhibits a consistent pattern with the bedrock depth map, which is logical considering that the bedrock depth map is derived based on the f_0 -depth relationship. It seems that most of the basin has a fundamental frequency between 0.5 to 1 Hz except some areas in south and south west. As expected, the area close to the basin border displays peaks above 1 Hz. The anomaly observed in the central region can be largely attributed to the limited available data for interpolation. However, it is not surprising to observe a resonance frequency peak above 1 Hz in accordance with the uplifting of bedrock depth in 3D velocity model (e.g. 2D cross sections in chapter 3).

The simulated A_0 map (Figure 4-31B) reveals more interesting findings. As anticipated, the areas located very close to the basin edge in the north and southeast exhibit the lowest amplitudes. In contrast, it can be observed significant A_0 values in the northern region, forming a west-east band. This high amplitude band aligns with the Evin-Tajrish-Niavaran depression (Chapter 1), a sub-zone characterized by a depression as described by Berberian in 1985. This depression has a bedrock depth of 400 meters, as opposed to the neighboring areas, which have depths of 200~300 meters (Figure 3-17; the 3D velocity structure model).

Furthermore, Figure 4-19 illustrates 2D cross-sections where these local anomalies in depth are evident in the northeast. These anomalies contribute to the generation of surface waves, which can lead to increased amplification. Finally, as expected, I observe other areas of high amplification in the southern part of the basin near the MOF and SHL stations.

Finally, it should be mentioned that this study identified some limitations and challenges, including the need for a more accurate 3D velocity structure model to increase the accuracy of results in this complex basin. Despite these limitations which will be discussed in the next part, the current numerical simulation provides valuable insights into the prediction of ground motion and highlights very well the variability of ground motion amplification in north and south of the basin

Chapter 5
Conclusion

5-1 General Conclusion

All seismic risk assessments carried out in Tehran have shown that the earthquake risk is extremely high. Despite the diverse fields in which these studies have been conducted, it is impossible to decrease casualties caused by earthquakes without considering the real site effects in a seismic risk assessment. Prior to our research, there were only one detailed site effect studies in Tehran conducted by Haghshenas (2005) which yielded some interesting results and raised interesting questions. The results revealed strong amplification particularly in the southern parts of the basin while the bandwidth of the amplification was very wide and started at a very low frequency for all parts of the basin. These results contradicted the initial assumption of site amplification in Tehran drawn from geotechnical drillings, which indicated high S-wave velocity values (exceeding 600–700 m/s) at shallow depths, suggested a resonance frequency greater than 1 Hz, and moderate amplification. In addition, the H/V method applied on seismic noise also yielded some surprising findings in Tehran, with many stations displaying flat curves, which could be misinterpreted as free from amplification effects.

In fact, the 2005 experiment's observations and discussions are insufficient to determine the cause of these effects. That study proposed multidimensional site effect as a reason for ground motion amplification over a wide frequency band and the possibility of a deep impedance contrast to explain the low fundamental frequency peak and the failure of the noise H/V method. The failure was just explained by assuming that the low impinging seismic noise energy at low frequency was insufficient to excite the basin.

In this regard, the creation of a three-dimensional velocity model for the city of Tehran via extensive geophysical, geotechnical and geological experiments and testing the model to predict real ground motion via numerical simulation is the only way to address the existing ambiguity generated by findings in 2005.

Therefore, the main objective of our study was divided into two parts. The first part was dedicated to creating the first 3D velocity structure model of Tehran. The integration of different methods (mainly passive noise-based methods) allowed to derive dispersion curves and ellipticities across a wide frequency range and then to generate 1D S-wave velocity profiles from the surface down to the seismic bedrock. In our study, the implementation of the RTBF method (Wathelet et al., 2018) enabled us to gather a large set of observational data, which includes dispersion curves

of both Rayleigh (fundamental and higher modes) and Love waves and the ellipticities of Rayleigh waves.

Despite the advantage of RTBF, the issue of flat H/V curves still persisted in the Tehran basin, resulting in two major challenges. First, it significantly reduced the amount of available observational H/V data and second, I had to ensure the reliability of the Rayleigh wave ellipticity extracted from seismic noise measurements close to the resonance frequency of the sites.

To address the first issue, I increased the number of measurements, which led to almost 600 single station measurements, compared to the 62 measurements in the 2005 studies. To address the second challenge, I developed a new method based on the RayDec method but for earthquakes, since seismic events can generate sufficient energy in the lower frequency domain. By comparing the Rayleigh wave ellipticity curves obtained from the earthquakes with corresponding curves from noise, the accuracy of the obtained ellipticities from noise measurements was verified.

Subsequently, the 3D velocity model of Tehran was constructed by utilizing the inversion results and the relationship between the fundamental frequency peak and depth. The following are the primary findings through the first part of the thesis.

- The observations simply indicated that the Tehran basin is not uniform, and there are variations in the bedrock depth from the north (northeast) to the south (southwest). The most significant variation was observed in the middle of the basin, where the deepening of the basin was evident from the results.
 - From the geotechnical data, the variation between the north and south indicate that the majority of the V_{s30} values were higher in the northern region, with an average over 600 m/s. In contrast, in the southern region, the V_{s30} values were lower, with an average of around 400 m/s.
 - From the dispersion curves, the fundamental mode (R0) of Rayleigh phase velocities clearly indicates for a given wavelength that there are higher phase velocities in the north and eastern parts of the basin comparing to the southern part
 - The fundamental resonance frequencies which are the most distinguishing parameters between the north and south regions, with the frequencies in the northern part mostly above 0.5 Hz, and those in the southern part predominantly below 0.5 Hz.

- The results also exhibit some activity mechanism of fault systems, such as the Lavizan fault although the accuracy was limited in the center of Tehran due to insufficient observational data. In this regard, it appears that there are still ongoing debates regarding the precision of the active faults map in Tehran, primarily due to the expansion of urban areas and the subsequent burial of geological traces (recent review by Solaymani Azad, 2023).

The second part of this thesis involves utilizing the 3D velocity structure of Tehran in a numerical simulation scheme to predict the variability of surface ground motion for long period earthquakes. In this part I used 3D SEM technique using EFISPEC3D code because of its efficiency and flexibility. I developed a numerical model that was capable of simulating frequencies up to 2 Hz while the model used a lowpass filtered Dirac impulse as a source time function, a S-plane wave excitation and involved a simplified description of the 3D subsoil structure that was obtained from the results of the first section. Because 3D numerical codes normally work with constant shear wave velocity for each layer, the simplification is required to replace the spatial heterogeneity in the layers with a single constant shear wave velocity value. To achieve a simplified model, I employed a two-step strategy: first, by removing the relatively thin superficial layer(s) and reducing the number of layers to two; and second, by calculating an average velocity per layer from all the V_s values estimated at the array sites. The simplified model was then utilized to simulate wave propagation within the medium.

The following are the primary findings through the second part of the thesis.

- Observations in terms of ground motion time series showed the generation of diffracted surface waves along the time series cross-section, particularly in the south, as an impact of the 3D site effect. Also, computing the Fourier amplitude spectrum along the cross section illustrates how the amplification varies from the northern to the southern regions of the basin. Based on this observation, it appears that the 3D site effect probably is not responsible for the flatness of the H/V curves.

- Comparison with experimental site amplification in terms of fundamental frequency, our numerical model shows a relatively good agreement with experimental resonance frequency with an average error of approximately 11%.
- As for the amplification values, comparing the SSR obtained from numerical simulation data with the SSR obtained from the temporary seismological data (Haghshenas, 2005), I found that our simulation was able to reproduce the shape of the site amplification in the southern region that exhibit a plateau-like shape typical of 2D/3D site effects. However, I noted that our simulation underestimated the amplification values.
- For the northern part it appears that our model is too simplistic to account for the ground structure heterogeneities, particularly near the complex central faults. The observational data in this area (near TAP or ABM stations) are also relatively low (due to flat H/V curves), which could lead to some misinterpretation of the velocity structure.
- The spatial variation of site amplification throughout Tehran also shows the largest amplification in the south and south west of the basin (at MOF and SHL stations) and the east west band in north of Tehran from the narrow valley of Hakimieh to the west.
- The sensitivity analysis of the simulation outlined that the impedance contrast is the most important parameter to adjust the amplification function. I examined this effect by increasing the bedrock S-wave velocity, and I found that such an increase led to site amplification in the southern region in better agreement with actual site amplification but worsen in the northern region, outlining the need for better refining the possible variation of bedrock and sediments S-wave velocity from north to south of the basin. According to all these observations and interpretations, I have made significant progress in assessing the local seismic hazard in Tehran. In comparison to Haghshenas (2005) study, I managed to construct the first 3D velocity model utilizing a relatively substantial dataset (although it may still be insufficient for a Metropolitan city of Tehran). This model opens up new possibilities for conducting large scale numerical simulation in Tehran basin and gives us a reasonable estimate of site response over the basin for the first time.

5-2 Perspectives and limitations

Although the current model may not be fully optimal, it still serves as a starting point for further development that can lead to more accurate ground motion simulation.

Below are some suggested short term topics to enhance the first part of the thesis:

- To obtain dispersion curves over a broader frequency range, especially at high frequencies, it is recommended to conduct MASW at all the presented stations. Due to constraints in time and resources, only 14 out of 33 stations had MASW measurements in current study.
- To obtain more useful H/V curves, it is possible to increase the measurement duration at sites exhibiting flat H/V curves stations or carry out new measurements at different locations based on the insights gained from the existing model.
- Given the city's relatively high seismicity and the absence of reliable earthquake monitoring within the city limits, another short-term study could be the installation of permanent or temporary seismological network in Tehran, that give us more insight into the complex structure of the basin and related site effects and also the impact of the reference station on measured site amplification. In fact, the current outcome of this thesis may serve as a tool for identifying optimal locations for permanent earthquake stations within Tehran.

Based on the second part of the text, some potential perspectives or areas of further research could include:

- To refine and improve the velocity model utilized in the simulation, I can explore several approaches. One strategy involves extending geophysical surveys and conducting gravimetry measurements on sediments and outcropping rock, which would provide much more data to create a more accurate description of the 3D subsoil structure. Looking ahead, a long-term perspective involves implementing very deep seismic profiling, which can yield highly accurate representations of shear wave velocities. This allows for the incorporation of additional layers and the accounting of local variations, leading to more precise ground motion predictions.

- Using the finite-size sources and rupture velocity models to perform parametric studies for earthquake scenarios that can also provide a more realistic representation of the seismic ground motions in Tehran.

References

- Abbassi, M.R., and Shabanian, E., 2023. Stress field evolution recorded by tectono stratigraphy of Quaternary deposits of the southern flank of the Central Alborz (Iran). (submitted.)
- Abbassi, M.R., Ghods A.R., 2020. Is WNW striking faults a seismic source threatening Tehran? in: The 19th Iranian Geophysical Conference. Tehran, Iran. pp.548–551.
- Abbassi, M.R., Mokhtari, H., 2020. Fault zones of Tehran (in Persian). Tehran Disaster Mitigation and Management Organization, Tehran, Iran. 169 p.
- Abbassi, A., Nasrabadi, A., Tatar, M., Yaminifard, F., Abbassi, M.R., Hatzfeld, D., Priestley, K., 2010. Crustal velocity structure in the southern edge of the Central Alborz (Iran). *J. Geodyn.* 49 (2), 68–78.
- Abbassi, M.R., Farbod, Y., 2009. Faulting and folding in quaternary deposits of Tehran's piedmont (Iran). *J. Asian Earth Sci.* 34-4, 522-531. <https://doi.org/10.1016/j.jseaes.2008.08.001>
- Abbassi, M.R., Shabanian, E., 1999. Evolution of the stress field in Tehran region during the quaternary, in: Proceeding of Third International Conference on Seismology and Earthquake Engineering (SEE-3) Tehran, Iran. pp. 67–84.
- Aki, K., Richards, P.G., 1980. *Quantitative Seismology, Theory and Methods*, Volume I: 557 Pages., 169 illustrations. Volume II: 373 Pages., 116 illustrations. Freeman, San Francisco.
- Aki K, Larner KL., 1970. Surface motion of a layered medium having an irregular interface due to incident plane SH waves. *Journal of Geophysical Research.* 75 933-954.
- Aki K., 1969. Analysis of the seismic coda of local earthquake as scattered waves. *J Geophys.* 74-2,615-631 <https://doi.org/10.1029/jb074i002p00615>
- Aki, K., 1957. Space and time spectra of stationary stochastic waves, with special reference to microtremors. *Bull. Earthq. Res. Inst.* 35, 415–457.
- Allen, M.B., Ghassemi, M.R., Shahrabi, M., Qorashi, M., 2003. Accommodation of late Cenozoic oblique shortening in the Alborz range, northern Iran. *J. Struct. Geol.* Vol 25-5, 659-672 [https://doi.org/10.1016/S0191-8141\(02\)00064-0](https://doi.org/10.1016/S0191-8141(02)00064-0)
- Ambraseys, N.N., Melville, C.P., 1982. *A History of Persian Earthquakes numerous illustrations.* Cambridge, London, New York, New Rochelle, Melbourne, Sydney: Cambridge University Press. 219 p.
- Amini Hosseini, K., Hosseini, M., Jafari, M.K., Hosseinioon, S., 2009. Recognition of vulnerable urban fabrics in earthquake zones: a case study of the Tehran metropolitan area. *J. Seismol. Earthq. Eng.* 10, 175–187.
- Anells, R.N., Arthurton, R.S., Bazley, R.A.B., Davies, R.G., Hamedi, M.A., Rahimzadeh, F., 1975. *Geological Map of the Qazvin-Rasht Quadrangle Map: Tehran*, Geological Survey of Iran, Map no. E3-E4, scale 1:250,000.
- Arai, H. and Tokimatsu, K. 2004. S-wave velocity profiling by inversion of microtremor H/V spectrum. *Bulletin of the Seismological Society of America*, 94(1) :53–63.
- Asadi, S., Rahimi, H., Fard, R.A., 2017. The imaging of the near-surface features using earthquakes and ambient noise in the Tehran region. *Near Surf. Geophys.* 15-2, 131-139. <https://doi.org/10.3997/1873-0604.2017005>
- Ashtari, M., Hatzfeld, D., Kamalian, N., 2005. Micro seismicity in the region of Tehran. *Tectonophysics* 395(3-4), 193-208 <https://doi.org/10.1016/j.tecto.2004.09.011>
- Asmussen, J.C., 1997. *Modal Analysis Based on the Random Decrement Technique - Application to Civil Engineering Structures.* PhD Thesis. Univ. of Aalborg, Aalborg, Denmark. 300 pages.

- Asten, M. W., Henstridge, J.D., 1984. Array estimators and the use of microseisms for reconnaissance of sedimentary basins. *Geophysics*, 49(11) :1828– 1837.
- Asten, M.W., 2006. On bias and noise in passive seismic data from finite circular array data processed using SPAC methods. *Geophysics* 71-6, 1ND, Z126. <https://doi.org/10.1190/1.2345054>
- Bachmanov, D.M., Trifonov, V.G., Hessami, K.T., Kozhurin, A.I., Ivanova, T.P., Rogozhin, E.A., Hademi, M.C., Jamali, F.H., 2004. Active faults in the Zagros and central Iran. *Tectonophysics* 380(3-4) 221-241. <https://doi.org/10.1016/j.tecto.2003.09.021>
- Bard, P.-Y., 2021. Physics-based site amplification prediction equation: a dream at reach?. 6th IASPEI/IAEE International Symposium: Effects of Surface Geology on Seismic Motion, Kyoto (on line), Japan. hal-03329430.
- Bard, P. Y., 2008. The H/V technique: capabilities and limitations based on the results of the SESAME project. *Bull Earthq Eng*, 6(1), 1-2.
- Bard, P.-Y. 1999. Microtremor measurements: a tool for site effect estimation. In preceding: Second International Symposium on the Effects of Surface Geology on seismic motion Yokohama, Japan Vol. 3, 1251-1279.
- Bard, P.-Y., & Bouchon, M., 1985. The two-dimensional resonance of sediment-filled valleys. *Bull. Seism. Soc. Am* 75(2), 519–541.
- Bard, P.- Y, & Bouchon, M., 1980b. The seismic response of sediment-filled valleys. Part II. The case of incident P and SV waves; *Bull. Seism. Soc. Am.* 70, 1921-1941.
- Bard, P.- Y. & Bouchon, M., 1980a. The seismic response of sediment-filled valleys. Part I. The case of incident SH waves, *Bull. Seism. Soc. Am.* 70,1263-1286.
- Bayasgalan, A., Jackson, J., Ritz, J.F., Carretier, S., 1999. “Forebergs”, flower structures, and the development of large intracontinental strike-slip faults: The Gurvan Bogd fault system in Mongolia. *J. Struct. Geol.* 21-10, 1285-1302. [https://doi.org/10.1016/S0191-8141\(99\)00064-4](https://doi.org/10.1016/S0191-8141(99)00064-4)
- Beauval, C., Bard, P.Y., Moczo, P., Kristek, J., 2003. Quantification of Frequency-Dependent Lengthening of Seismic Ground-Motion Duration due to Local Geology: Applications to the Volvi Area. *Bull. Earthq. Eng.* 93, 371–385. <https://doi.org/10.1785/0120010255>
- Berberian, M., Yeats, R.S., 2018. Tehran: An earthquake time bomb, in: *Tectonic Evolution, Collision, and Seismicity of Southwest Asia. In Honor of Manuel Berberian’s Forty-Five Years of Research Contributions At: GSA special papers 2017*, 84 p. [https://doi.org/10.1130/2016.2525\(04\)](https://doi.org/10.1130/2016.2525(04))
- Berberian, M., Yeats, R.S., 1999. Patterns of Historical Earthquake Rupture in the Iranian Plateau. *Bull. Seismol. Soc. Am.* 89-1, 120-139. <https://doi.org/10.1785/BSSA0890010120>
- Berberian, M., 1994. Natural Hazards and the First Earthquake Catalogue of Iran: Volume 1. *Historical Hazards in Iran Prior to 1900: UNESCO (IIEES) Publication during United Nations International Decade for Natural Disaster Reduction (IDNDR)*, 649 p.
- Berberian, M., Qorashi, B., Arzhang-ravesh, A., Mohajer-Ashjai, 1985. Recent tectonics, seismotectonics and earthquake fault hazard investigations in the greater Tehran region: contribution to the seismotectonics of Iran: Part V, Geological Survey of Iran, report 56, 316 pages.
- Bettig, B., Bard, P.Y., Scherbaum, F., Riepl, J., Cotton, F., Cornou, C., Hatzfeld, D., 2001. Analysis of dense array noise measurements using the modified spatial auto-correlation method (SPAC): Application to the Grenoble area. *Boll. di Geofis. Teor. ed Appl.* 42, 281-304.

- Bielak, J. and Xu, J., 1999. Earthquake ground motion and structural response in alluvial valleys. *Journal of Geotechnical and Geo environmental Engineering*, 125(5), 413–23.
- Bindi, D., Parolai, S., Cara, F., Di Giulio, G., Ferretti, G., Luzi, L., Monachesi, G., Pacor, F., and Rovelli, A., 2009. Site Amplifications Observed in the Gubbio Basin, Central Italy: Hints for Lateral Propagation Effects. *Bulletin of the Seismological Society of America*, Vol. 99, No. 2A, pp. 741–760. <https://doi.org/10.1785/0120080238>
- Bonilla, L. F., Liu, P.-C., Nielsen, S., 2006. 1D and 2D linear and non-linear site response in the Grenoble area. in: *Third International Symposium on the Effects of Surface Geology on Seismic Motion*. Grenoble, France.
- Boore, D.-M., 1970. Love waves in nonuniform waveguides: finite difference calculations. *J. Geophys. Res.*, 1970, 1512–27.
- Borcherdt, R.D, 1970. Effects of local geology on ground motion near San Francisco bay. *Bull. Seismol. Soc. Am.* 60-1, 29-61. <https://doi.org/10.1785/BSSA0600010029>
- Building and Housing Research Center (BHRC), 2016. Iranian code of practice for seismic resistant design of buildings, Standard No. 2800, 4th edition, Building and housing research center, Tehran, Iran.
- C.G.G (Compagnie Générale de Géophysique), 1965. Etude Géophysique par prospection électrique dans la région de Téhéran. Tehran, Iran, 500 p.
- Capon, J., 1969. High-Resolution Frequency-Wavenumber Spectrum Analysis. *Proc. IEEE* 57. <https://doi.org/10.1109/PROC.1969.7278>
- Chávez-García, F. J., Pedoti G., Hatzfeld D., and Bard P.-Y., (1990). An experimental study near Thessaloniki (Northern Greece). *Bull. Seism. Soc. Am.* 80, no. 4, 784–800.
- Chaljub, E., Maufroy, E., Moczo, P., Kristek, J., Hollender, F., Bard, P.-Y., Priolo, E., Klin, P., De Martin, F., Zhang, Z., Zhang, W., & Chen, X., 2015. 3-D numerical simulations of earthquake ground motion in sedimentary basins: testing accuracy through stringent models, *Geophys. J. Int.*, 201(1), 90-111.
- Chaljub, E., Moczo, P., Tsuno, S., Bard, P.Y. Käser, M., Stupazzini, M., and Kristekova, M., 2010. Quantitative comparison of four numerical predictions of 3D ground motion in the Grenoble Valley, France, *Bull. Seismol. Soc. Am.* 100, 1427–1455
- Chaljub, E., 2000. Modélisation numérique de la propagation d’ondes sismiques à l’échelle du globe. PhD thesis, Université Paris 7.
- Cheshomi, A., Ramezannejad, S.R., Fakher, A., 2018. Development of Tehran alluvium classification based on geological characteristics and geotechnical parameters. *JIRAEG*. 11, 65–79.
- Cornou, C., Bard, P.Y. 2003. Site-to-bedrock over 1D transfer function ratio: An indicator of the proportion of edge-generated surface waves? *Geophys. Res. Lett.* 30-9. <https://doi.org/10.1029/2002GL016593>
- Cox, B.R., Teague, D.P., 2016. Layering ratios: A systematic approach to the inversion of surface wave data in the absence of a priori information. *Geophys. J. Int.* 207-1, 422-438. <https://doi.org/10.1093/gji/ggw282>
- Cupillard, P., Delavaud, E., Burgos, G., Festa, G., Vilotte, J.-P., Capdeville, Y., and Montagner, J.-P., 2012. RegSEM: a versatile code based on the spectral element method to compute seismic wave propagation at the regional scale. *Geophys. J. Int.*, 188, 1203–20.
- Cushing, E.M., Hollender, F., Moiriat, D., Guyonnet-Benaize, C., Theodoulidis, N., Pons-Branchu, E., Sépulcre, S., Bard, P.Y., Cornou, C., Dechamp, A., Mariscal, A., Roumelioti, Z., 2020.

- Building a three-dimensional model of the active Plio-Quaternary basin of Argostoli (Cephalonia Island, Greece): An integrated geophysical and geological approach. *Eng. Geol.* 265. <https://doi.org/10.1016/j.enggeo.2019.105441>
- De Martin, F., Matsushima, Sh., Kawase, H., 2013 [Impact of geometric effects on near-surface green's functions](#). *Bull. Seism. Soc. Am.*, 103(6):3289–3304.
- De Martin, F. 2011. [Verification of a spectral-element method code for the Southern California Earthquake Center LOH.3 viscoelastic case](#). *Bull. Seism. Soc. Am.*, 101(6):2855–2865.
- De Martini, P.M., Hessami, K., Pantosti, D., D'Addezio, G., Alinaghi, H., Ghafory-Ashtiani, M., 1998. A geologic contribution to the evaluation of the seismic potential of the Kahrizak fault (Tehran, Iran). *Tectonophysics* 287, 187-199. [https://doi.org/10.1016/S0040-1951\(98\)80068-1](https://doi.org/10.1016/S0040-1951(98)80068-1)
- Dellenbach, J., 1964. Contribution à l'étude géologique de la région située à l'est de Teheran (Iran). PhD Thesis. Faculté de Science de l'Université de Strasbourg (France), 117 Pages.
- Di Giulio, G., Savvaidis, A., Ohrnberger, M., Wathelet, M., Cornou, C., Knapmeyer-Endrun, B., Renalier, F., Theodoulidis, N., Bard, P.Y., 2012. Exploring the model space and ranking a best class of models in surface-wave dispersion inversion: Application at European strong-motion sites. *Geophysics* 77-3, 1MG-Z74. <https://doi.org/10.1190/geo2011-0116.1>
- Djamour, Y., Hashemi, S., Sadiqi, M., Nankali, H., 2012. The GPS rate of tectonic movements along the northern Tehran with emphasis on the North Tehran fault: *Geosci. Geol. Surv. Iran* 84, 211–218.
- Engalenc, M., 1968. Contribution à la Géologie, Géomorphologie, Hydrogéologie de la Région de Tehran (Iran). Ph.D thesis. Univ. Of Montpellier, France. 250 p.
- Eurocode 8 (EC8), 2004. Design of structures for earthquake resistance—part 1: General rules, seismic actions and rules for buildings, European Committee for Standardization (CEN), EN 1998-1, <https://eurocodes.jrc.ec.europa.eu/> (last accessed April 2023).
- Fäh, D., F. Kind, and D. Giardini 2001. A theoretical investigation of average H/V ratios. *Geophysical Journal International*, 145(2) :535–549.
- Fäh, D., F. Kind, and D. Giardini., 2003. Inversion of local S-wave velocity structures from average H/V ratios, and their use for the estimation of site effects. *Journal of Seismology*, 7(4) :449–467.
- Fäh, D., Wathelet, M., Kristekova, M., Havenith, H., Endrun, B., Stamm, G., Poggi, V., Burjanek, J., Cornou, C. 2009. Using ellipticity information for site characterisation. D4, final report EC project number: 026130, NERIES JRA4 “Geotechnical Site Characterisation”, task B2.
- Fairchild, G.M., Lane, J.W., Voytek, E.B., LeBlanc, D.R., 2013. Bedrock topography of western Cape Cod, Massachusetts, based on bedrock altitudes from geologic borings and analysis of ambient seismic noise by the horizontal-to-vertical spectral-ratio method. *US Geological Survey Scientific Investigations Map*, 3233(1), 17.
- Fakher, A., Cheshomi, A., Khamechiyan, M., 2007. The addition of geotechnical properties to a geological classification of coarse-grained alluvium in a pediment zone. *Q. J. Eng. Geol. Hydrogeol.* 40, 163-174. <https://doi.org/10.1144/1470-9236/06-029>
- Fazlavi, M., 2015. Investigating the seismic characteristics of deep alluviums by array analysis of microtremor vibrations (Case study: Tehran). Ph.D Thesis. IIEES, Tehran, Iran, 171 p.
- Feghhi, K., 1999. Effect of active faults on groundwater table in Tehran region, in: *Proceedings of the 3rd International Conference on Seismology and Earthquake Engineering (SEE-3)*: pp. 127–137.

- Field, E.H., Clement, A.C., Jacob, K.H., Aharonian, V., Hough, S.E., Friberg, P.A., Babaian, T.O., Karapetian, S.S., Hovanessian, S.M. and H.A. Abramian, 1995. Earthquake site-response study in Giumri, Armenia, using ambient noise observation. *Bull. Seismol. Soc. Am.* 85-1, 349-353.
- Field, E.H., 1996. Spectral amplification in a sediment-filled valley exhibiting clear basin-edge-induced waves. *Bull. Earthq. Eng.*, 86(4), 991–1005. <https://doi.org/10.1785/BSSA0860040991>
- Firuzi, E., Ansari, A., Amini Hosseini, K., Rashidabadi, M., 2019. Probabilistic earthquake loss model for residential buildings in Tehran, Iran to quantify annualized earthquake loss. *Bull. Earthq. Eng.* 17, 2383–2406. <https://doi.org/10.1007/s10518-019-00561-z>
- Fookes, P.G., Knill, J.L., 1969. The application of engineering geology in the regional development of northern and central Iran. *Eng. Geol.* 3-2, 81-120. [https://doi.org/10.1016/0013-7952\(69\)90001-5](https://doi.org/10.1016/0013-7952(69)90001-5)
- Foti, S., Hollender, F., Garofalo, F., Albarello, D., Asten, M., Bard, P.Y., Comina, C., Cornou, C., Cox, B., Di Giulio, G., Forbriger, T., Hayashi, K., Lunedei, E., Martin, A., Mercerat, D., Ohrnberger, M., Poggi, V., Renalier, F., Sicilia, D., Socco, V., 2018. Guidelines for the good practice of surface wave analysis: a product of the InterPACIFIC project. *Bull. Earthq. Eng.* 16, 2367-2420 <https://doi.org/10.1007/s10518-017-0206-7>
- Furumura, T., and Kennett, B., 2005. Subduction zone guided waves and the heterogeneity structure of the subducted plate: intensity anomalies in northern Japan. *J. Geophys. Res.*, 110, <https://doi.org/10.129-2004JB003486>.
- Garofalo, F., Foti, S., Hollender, F., Bard, P.Y., Cornou, C., Cox, B.R., Ohrnberger, M., Sicilia, D., Asten, M., Di Giulio, G., Forbriger, T., Guillier, B., Hayashi, K., Martin, A., Matsushima, S., Mercerat, D., Poggi, V., Yamanaka, H., 2016a. InterPACIFIC project: Comparison of invasive and non-invasive methods for seismic site characterization. Part I: Intra-comparison of surface wave methods. *Soil Dyn. Earthq. Eng.* 82, 222-240 <https://doi.org/10.1016/j.soildyn.2015.12.010>
- Ghassemi, M.R., Fattahi, M., Landgraf, A., Ahmadi, M., Balato, P., and Tabatabaei, S.H., 2014. Kinematic links between the eastern Mosha fault and the North Tehran fault, Alborz range, northern Iran: Tectonophysics, v. 622, p. 81–95. <https://doi.org/10.1016/j.tecto.2014.03.007>.
- Giardini, D., Danciu, L., Erdik, M., Şeşetyan, K., Demircioğlu Tümsa, M.B., Akkar, S., Gülen, L., Zare, M., 2018. Seismic hazard map of the Middle East. *Bull. Earthq. Eng.* 16, 3567-3570. <https://doi.org/10.1007/s10518-018-0347-3>
- Gokhberg, A. and Fichtner, A., 2015. Full-waveform inversion on heterogeneous (HPC) systems. *Computers & Geosciences*, <https://doi.org/10.1016/j.cageo.2015.12.013>.
- Gorshkov, A., Mokhtari, M., Plotrovskaya, E.P., 2009. The Alborz region, identification of seismogenetic nodes with morphostructural zoning and pattern recognition. *JSEE* 11, 1–12.
- Gosar, A., Lenart, A., 2010. Mapping the thickness of sediments in the Ljubljana Moor basin (Slovenia) using microtremors. *Bull. Earthq. Eng.* 8, 501-518. <https://doi.org/10.1007/s10518-009-9115-8>
- GSI (Geological survey of Iran), 2010. 1:10000 geological map of Tehran. Iran.
- Guéguen, P., Cornou, C., Garambois, S. and Banton J., 2007. On the Limitation of the H/V Spectral Ratio Using Seismic Noise as an Exploration Tool: Application to the Grenoble Valley (France), a Small Apex Ratio Basin. *Pure and Applied Geophysics*. 164-1, 115-134. <https://doi.org/10.1007/s00024-006-0151-x>

- Guest, B., Axen, G.J., Lam, P.S., Hassanzadeh, J., 2006. Late Cenozoic shortening in the west-central Alborz Mountains, northern Iran, by combined conjugate strike-slip and thin-skinned deformation. *Geosphere*, 2,35-52. <https://doi.org/10.1130/GES00019.1>
- Guillier, B., Chatelain, J.L., Bonnefoy-Claudet, S., Haghshenas, E., 2007. Use of ambient noise: From spectral amplitude variability to H/V stability. *J. Earthq. Eng.* 11, 925-942. <https://doi.org/10.1080/13632460701457249>
- Guillier, B., Cornou, C., Kristek, J., Moczo, P., Bonnefoy-Claudet, S., Bard, P.Y., Fäh, D., 2006. Simulation of seismic ambient vibrations: does the H/V provide quantitative information in 2D-3D structures? In: Third international symposium on the effects of surface geology on seismic motion Grenoble, France. vol. 30.
- Haghshenas, E., Bard, P.Y., Theodulidis, N., Atakan, K., Cara, F., Cornou, C., Cultrera, G., Di Giulio, G., Dimitriu, P., Fäh, D., De Franco, R., Marcellini, A., Pagani, M., Rovelli, A., Savvaidis, A., Tenta, A., Vidal, S., Zacharopoulos, S., 2008. Empirical evaluation of microtremor H/V spectral ratio. *Bull. Earthq. Eng.* 6, 75-108. <https://doi.org/10.1007/s10518-007-9058-x>
- Haghshenas, E., 2005. Conditions géotechniques et aléa sismique local à Téhéran. PhD Thesis, Université Joseph Fourier - Grenoble I, Grenoble, France. 289 pages.
- Hallier, S., Chaljub, E., Bouchon, M., and Sekiguchi, H., 2008. Revisiting the basin-edge effect at Kobe during the 1995 Hyogo-Ken Nanbu earthquake. *Pure and app. geo.*, 165(9-10) :1751–1760.
- Hamzehloo, H., Vaccari, F., Panza, G.F., 2007. Towards a reliable seismic microzonation in Tehran, Iran. *Eng. Geol.* 93(1-2), 1-16. <https://doi.org/10.1016/j.enggeo.2007.05.001>
- Haskell, N.A., 1953. The dispersion of surface waves on multilayered media. *Bull. Seismol. Soc. Am.* 43. <https://doi.org/10.1785/bssa0430010017>
- Herrmann, R.B., 1973. Some aspects of band-pass filtering of surface waves. *Bull. Seismol. Soc. Am.* 63, 663-671. <https://doi.org/10.1785/bssa0630020663>
- Hessami, Kh. Jamali, F. Tabassin H, 2007. Major active faults of Iran. Map printed at IIEES, Tehran, Iran.
- Hobiger, M., Cornou, C., Wathelet, M., Di Giulio, G., Knapmeyer-Endrun, B., Renalier, F., Bard, P.Y., Savvaidis, A., Hailemikaël, S., Le Bihan, N., Ohrnberger, M., Theodoulidis, N., 2013. Ground structure imaging by inversions of Rayleigh wave ellipticity: Sensitivity analysis and application to European strong-motion sites. *Geophys. J. Int.* 192-1, 207-229. <https://doi.org/10.1093/gji/ggs005>
- Hobiger, M., 2011. Polarization of surface waves : characterization, inversion and application to seismic hazard assessment. PhD Thesis, Université Grenoble Alpes. 309 Pages.
- Hobiger, M., Bard, P.Y., Cornou, C., Le Bihan, N., 2009. Single station determination of Rayleigh wave ellipticity by using the random decrement technique (RayDec). *Geophys. Res. Lett.* 36(L14303). <https://doi.org/10.1029/2009GL038863>
- Hollingsworth, J., Nazari, H., Ritz, J.-F., Salamati, R., Talebian, M., Bahroudi, A., Walker, R., Rizza, M. and Jackson, J., 2010. Active tectonics of the East Alborz mountains, NE Iran; rupture of the left-lateral Astaneh fault system during the great 856AD Qumis earthquake. *Journal of Geophysical Research*, 115, B12313, <https://doi.org/10.1029/2009JB007185>
- Hourcade, B., 1982. The Anti-Alborz, a marginal space close to Tehran. *Rev. Geogr. Est.*, 22, 61-97. <https://doi.org/10.1029/Jb075I005P00933>

- Ibs-von Seht, M., Wohlenberg, J., 1999. Microtremor Measurements Used to Map Thickness of Soft Sediments. *Bull. Seismol. Soc. Am.* 89-1, 250-259. <https://doi.org/10.1785/bssa0890010250>
- Igel., H. 2017. Computational seismology, a practical introduction._Oxford university press, Oxford, 6DP, UK.
- Imtiaz, A., Cornou, C., Bard, P-Y., Hobiger, M., 2021. Diffracted wavefield decomposition and multidimensional site effects in the Argostoli valley, Greece. *Geophys. J. Int.* 224, 1849–1869. <https://doi.org/10.1093/gji/ggaa529>
- Irikura, K., 1986. Prediction of strong acceleration motions using empirical Green's functions., in: 7th Jap. Earthq. Eng. Symp., Tokyo, Japan, pp. 151–156.
- Jackson, J., Priestley, K., Allen, M., and Berberian, M., 2002, Active tectonics of the South Caspian Basin. *Geophysical Journal International*, v. 148, no. 2, p. 214–245. <https://doi.org/10.1046/j.1365-246X.2002.01588.x>
- Jafari, M.K., Kamalian, M., Sohrabi, A., Razmkhah, A., 2004. North of Tehran site effect microzonation, in: 13th World Conference on Earthquake Engineering. Vancouver, Canada. August 1-6, 2004. Paper No. 3423.
- Jafari, M.K., Razmkhah, A., Keshavarz-Bakhshayesh, M., Sohrabi, A., Pourazin, K., 2001b. Complementary Study of Seismic Microzonation: IIEES reports, Tehran, Iran (in Persian), 150 p.
- Jafari, M.K., Razmkhah, A., Pourazin, K., Keshavarz-Bakhshayesh, M., Sohrabi, A., 2001a. Study of Seismic Microzonation: North of Tehran. IIEES reports, Tehran, Iran. (in Persian), 200 Pages.
- Jalalhosseini, S.M., Zafarani, H., Zare, M., 2018. Time-dependent seismic hazard analysis for the Greater Tehran and surrounding areas. *J. Seismol.* 22, 187-215. <https://doi.org/10.1007/s10950-017-9699-4>
- JICA and CEST, 2000. The Study on Seismic Microzoning of the Greater Tehran Area in The Islamic Republic of Iran. Final Report. Japan International Cooperation Agency (JICA), Centre for Earthquake and Environmental Studies of Tehran (CEST) Tehran Municipality, Pacific Consultants International, OYO International.
- Karypis, G., & Kumar, V., 1998. A fast and high-quality multilevel scheme for partitioning irregular graphs. *SIAM Journal on Scientific Computing*, 20(1), 359-392. <https://doi.org/10.1137/S1064827595287997>
- Kato K., Aki K., and Takemura, M., 1995. Site amplification from coda waves: validation and application to S-wave site response. *Bull. Seism. Soc. Am.*, Vol. 85, No. 2, 467– 477.
- Kennet, B., 1983. Seismic wave propagation in stratified media. Canberra, Australia: ANU Press.
- Knill, J.L., Jones, K.S., 1968. Ground-water conditions in Greater Tehran. *Q. J. Eng. Geol.* 1, 181-194. <https://doi.org/10.1144/GSL.QJEG.1968.001.03.04>
- Komatitsch, D., Tsuboi, S., Tromp, J., 2005. The spectral-element method in seismology. *Seismic Earth: Array Analysis of Broadband Seismograms Geophysical Monograph Series 157* by the American Geophysical Union. <https://doi.org/10.1029/156GM13>
- Komatitsch, D., Liu, Q., Tromp, J., Suss, P., Stidham, C. & Shaw, J.H., 2004. Simulations of ground motion in the Los Angeles basin based upon the spectral-element method, *Bull. seism. Soc. Am.*, **94**, 187–206.

- Komatitsch, D. and Vilotte, J. P., 1998. The spectral element method: an effective tool to simulate the seismic response of 2D and 3D geological structures. *Bull. Seism. Soc. Am.*, 88, 368–92.
- Konno, K., Ohmachi, T., 1998. Ground-motion characteristics estimated from spectral ratio between horizontal and vertical components of microtremor. *Bull. Seismol. Soc. Am.* 88(1), 228-241. <https://doi.org/10.1785/bssa0880010228>
- Lacoss, R.T., Kelly, E.J., Toksöz, M.N., 1969. Estimation of seismic noise structure using arrays. *Geophysics* 34, 21-38. <https://doi.org/10.1190/1.1439995>
- Lebrun B., D. Hatzfeld et P.-Y. Bard, 2001. Site effect study in urban area: Experimental results in Grenoble (France). *Pure and Applied Geophysics*, **158-12**, 2543-2557.
- Le Roux, O., Cornou, C., Jongmans, D., and Schwartz, S. (2012). 1-D and 2-D resonances in an Alpine valley identified from ambient noise measurements and 3-D modelling. *Geophys. J. Int.*, 191(2), 579-590. <https://doi.org/10.1111/j.1365-246X.2012.05635.x>
- Ling, S., and H. Okada 1993. An extended use of the spatial autocorrelation method for the estimation of geological structure using microtremors. In : *Proc.89th Conf. SEGJ*. pp. 44–48.
- Lunedei, E., Albarello, D., 2009. On the seismic noise wavefield in a weakly dissipative layered Earth, *Geophysical Journal International*, Volume 177, Issue 3, Pages 1001–1014, <https://doi.org/10.1111/j.1365-246X.2008.04062.x>
- Maheri-Peyrov, M., Ghods, A., Donner, S., Akbarzadeh-Aghdam, M., Sobouti, F., Motaghi, K., Hassanzadeh, M., Mortezaejad, G., Talebian, M., Chen, L., 2020. Upper crustal structure of NW Iran revealed by regional 3-D Pg velocity tomography. *Geophysical Journal International* 222(2), 1093–1108. <https://doi.org/10.1093/gji/ggaa236>
- Malischewsky, P. G., Scherbaum, F., Lomnitz, C., Tuan, T. T., Wuttke, F., and Shamir, G., 2008. The domain of existence of prograde Rayleigh-wave particle motion for simple models. *Wave motion*, 45(4), 556-564 . <https://doi.org/10.1016/j.wavemoti.2007.11.004>
- Manakou, M. V., Raptakis, D.G., Chávez-García, F.J., Apostolidis, P.I., Pitilakis, K.D., 2010. 3D soil structure of the Mygdonian basin for site response analysis. *Soil Dyn. Earthq. Eng.* 30. <https://doi.org/10.1016/j.soildyn.2010.04.027>
- Maresca, R., Galluzzo, D., Del Pozzo, E., 2006. H/V Spectral Ratios and Array Techniques Applied to Ambient Noise Recorded in the Colfiorito Basin, Central Italy. *Bull. Earthq. Eng.*, Vol. 96, No. 2, pp. 490–505. <https://doi.org/10.1785/0120050057>
- Maufroy E, Chaljub E, Hollender F, Kristek J, Moczo P, Klin P, et al., 2015. Earthquake ground motion in the Mygdonian basin, Greece: the E2VP verification and validation of 3D numerical simulation up to 4 Hz. *Bull Seism Soc Am* V 2015;105:1398–418. <http://dx.doi.org/10.1785/0120140228>.
- Moczo, P., Kristek, J., and Galis, M. 2014. *The Finite Difference Modelling of Earthquake Motions*. Cambridge: Cambridge University Press.
- Molnar, S., Sirohey, A., Assaf, J., Bard, P.Y., Castellaro, S., Cornou, C., Cox, B., Guillier, B., Hassani, B., Kawase, H., Matsushima, S., Sánchez-Sesma, F.J., Yong, A., 2022. A review of the microtremor horizontal-to-vertical spectral ratio (MHVSR) method. *J. Seismol.* 26, 653-685. <https://doi.org/10.1007/s10950-021-10062-9>
- Nakamura, Y., 1989. Method for dynamic characteristics estimation of subsurface using microtremor on the ground surface. *Q. Rep. RTRI (railw. Tech. Res. Institute)* 30, 25-33.

- Nazari, H., Ritz, J.-F., Ghassemi, A., Bahar-Firuzi, K., Salamati, R., Shafei, A., Fonoudi M, 2011. Paleoearthquakes determination of magnitude ~6.5 on the North Tehran fault. *JSEE* 13, 159–166.
- Nazari, H., Ritz, J.-F., Salamati, R., Shahidi, A., Habibi, H., Ghorashi, M., Bavandpur, A.K., 2010. Distinguishing between fault scarps and shorelines: the question of the nature of the Kahrizak, North Rey and South Rey features in the Tehran plain (Iran). *Terra Nov.* 22. 227- 237. <https://doi.org/10.1111/j.1365-3121.2010.00938.x>
- Nazari, H., Ritz, J.F., Salamati, R., Shafei, A., Ghassemi, A., Michelot, J.L., Massault, M., Ghorashi, M., 2009. Morphological and palaeoseismological analysis along the Taleghan fault (Central Alborz, Iran). *Geophys. J. Int.* 178(2), 1028-1041. <https://doi.org/10.1111/j.1365-246X.2009.04173.x>
- Nemati, M., Hollingsworth, J., Zhan, Z., Bolourchi, M., Talebian, M., 2013. Microseismicity and seismotectonics of the South Caspian Lowlands, NE Iran, *Geophysical Journal International*, Volume 193, Issue 3, June 2013, Pages 1053–1070, <https://doi.org/10.1093/gji/ggs114>
- Nissen-Meyer, T., van Driel, M., Stähler, S. C., Hosseini, K., Hempel, S., Auer, L., Colombi, A., and Fournier, A. 2014. Axisem: broadband 3D seismic wavefields in axisymmetric media. *Solid Earth*, 5(1), 425–45.
- Nobile, M.S., Cazzaniga, P., Besozzi, D., Colombo, R., Mauri, G., Pasi, G., 2018. Fuzzy Self-Tuning PSO: a settings-free algorithm for global optimization. *Swarm Evol. Comput.* 39, 70–85.
- O’Neill, A., 2004. Shear Velocity Model Appraisal in Shallow Surface Wave Inversion. in : Symposium on the Application of Geophysics to Engineering and Environmental Problems 2004. P. 1544-1555. <https://doi.org/10.4133/1.2923300>
- Olsen, KB., 2000. Site amplification in the Los Angeles basin from three-dimensional modeling of ground motion. *Bull. Seism. Soc. Am.*, 90(6B): S77–S94.
- Panzer, F., Alber, J., Imperatori, W., Bergamo, P., Fäh, D., 2022. Reconstructing a 3D model from geophysical data for local amplification modelling: The study case of the upper Rhone valley, Switzerland, *Soil Dynamics and Earthquake Engineering*, Volume 155, 107163, ISSN 0267-7261. <https://doi.org/10.1016/j.soildyn.2022.107163>.
- Park, C.B., Miller, R.D., Xia, J., 1999. Multichannel analysis of surface waves. *Geophysics* 64(3), 800-817. <https://doi.org/10.1190/1.1444590>
- Parolai, S., Bard, P.Y., 2003. Evaluation of site effects by means of Joint Analysis of Sonogram and Standard Spectral Ratio (JASSSR). *J. Seismol.* 479-492. <https://doi.org/10.1023/B:JOSE.0000005723.52199.0e>
- Parsons, A.J., Abrahams, A.D., 2009. *Geomorphology of desert environments*. Springer Dordrecht. 831 p. <https://doi.org/10.1007/978-1-4020-5719-9>
- Pedrami, M., 1978. The timing, rate and nature of the late Quaternary tectonism in Iran. *Bull. Int. Union Quat. Res. Geological Survey of Iran (in Persian)*, 18 p.
- Perron, V., Laurendeau, A., Hollender, F., Bard, P.Y., Gélis, C., Traversa, P., Drouet, S., 2018. Selecting time windows of seismic phases and noise for engineering seismology applications: a versatile methodology and algorithm. *Bull. Earthq. Eng.* 16. <https://doi.org/10.1007/s10518-017-0131-9>
- Peter, D., Komatitsch, D., Luo, Y., Martin, R., Le Goff, N., Casarotti, E., Le Loher, P., Magnoni, F., Liu, Q., Blitz, C., Nissen-Meyer, T., Basini, P., and Tromp, J. 2011. Forward and adjoint simulations of seismic wave propagation on fully unstructured hexahedral meshes. *Geophys. J. Int.*, 186, 721–39.

- Pilz, M., Parolai, S., Leyton, F., Campos J. and Zschau, J. 2009. A comparison of site response techniques using earthquake data and ambient seismic noise analysis in the large urban areas of Santiago de Chile. *Geophys. J. Int.* (2009) 178, 713–728. <https://doi.org/10.1111/j.1365-246X.2009.04195.x>
- Poggi, V., Fäh, D., 2010. Estimating Rayleigh wave particle motion from three-component array analysis of ambient vibrations. *Geophys. J. Int.* 180(1), 251–267. <https://doi.org/10.1111/j.1365-246X.2009.04402.x>
- Priestley, K., Baker, C., Jackson, J., 1994. Implications of earthquake focal mechanism data for the active tectonics of the south Caspian Basin and surrounding regions, *Geophysical Journal International*, 118(1), 111–141. <https://doi.org/10.1111/j.1365-246X.1994.tb04679.x>
- Renalier, F., Jongmans, D., Campillo, M., Bard, P.Y., 2010. Shear wave velocity imaging of the Avignonet landslide (France) using ambient noise cross correlation. *J. Geophys. Res. Earth Surf.* 115(F3), pp.03032. <https://doi.org/10.1029/2009JF001538>
- Rezaei Far, M., Kissling, E., 2018. Compilation of a high-quality catalogue for M3.0+ seismicity in northern Iran region for the period of 2005–2017. *Geophys. J. Int.* 215(1), 118–132.
- Rieben, E.H., 1966. Geological observations on alluvial deposits in northern Iran. Geological Survey of Iran.
- Rieben, E.H., 1955. The Geology of Teheran Plain. *Am. J. Sci.* 253, 617–639. <https://doi.org/10.2475/ajs.253.11.617>
- Ritz, J.F., Nazari, H., Balescu, S., Lamothe, M., Salamati, R., Ghassemi, A., Shafei, A., Ghorashi, M., Saidi, A., 2012. Paleoearthquakes of the past 30,000 years along the North Tehran Fault (Iran). *J. Geophys. Res. Solid Earth* 117(B6), pp. B06305. <https://doi.org/10.1029/2012JB009147>
- Ritz, J.F., Nazari, H., Salamati, R., Shafeii, A., Solaymani, S., and Vernant, P., 2006. Active trans tension inside central Alborz: A new insight into the northern Iran–southern Caspian geodynamics. *Geology*, v. 34, p. 477– 480. <https://doi.org/10.1130/G22319.1>
- S.A.G.P. (Sir Alexander Gibbs and Partners), Unpublished Internal Report B.45, dated 20 July 1957, and B.58 dated 12 August 1957, filed at Sir Alexander Gibbs and Partners, London, and Ministry of Water and Power, Tehran.
- Sambridge, M., 1999a. Geophysical inversion with a neighbourhood algorithm - I. Searching a parameter space. *Geophys. J. Int.* 138(2)-479-494. <https://doi.org/10.1046/j.1365-246X.1999.00876.x>
- Sánchez-Sesma FJ, Crouse CB, 2015. Effects of site geology on seismic ground motion: early history. *Earthquake Eng Struct Dynam* 44:1099–1113. <https://doi.org/10.1002/eqe.2503>
- Satoh, T., Kawase, H., Matsushima, Sh., 2001. Differences Between Site Characteristics Obtained from Microtremors, S-waves, P-waves, and Cudas. *Bull. Seismol. Soc. Am*, 91, 2, pp. 313–334. <http://doi.org/10.1785/0119990149>
- Sawada, S. 1998. Phase characteristics on site amplification of layered ground with irregular interface. In Irikura, Kudo, Okada and Sasatani (eds); *The effect of surface geology on seismic motion*, Balkema, Rotterdam.
- Schuberth, G., *The spectral element method for seismic wave propagation: Theory, Implementation and Comparison to Finite Difference Methods* Ludwig-Maximilians-Universität München. 177 Pages.
- SCI (2016) Statistical Centre of Iran, vice-presidency for strategic planning and supervision, Tehran, national census of population and housing technical reports, sarshomri 2016 (1395),

- 2011 (1390), 2006 (1385), 1996 (1375), 1986 (1365), and 1976 (1355): Tehran, SCI, formerly, the plan and budget organization of the imperial government of Iran, statistical Centre. <http://www.amar.org.ir/Default.aspx?tabid=116>. Last accessed 28 Feb 2023.
- SESAME, 2004. Guidelines for the implementation of the H/V spectral ratio technique on ambient vibrations, measurements, processing and interpretation, European Commission-Research General Directorate Project No. EVG1-CT-2000-00026 SESAME, Report D23.12, https://www.earth-prints.org/bitstream/2122/8423/1/Del-D23-HV_User_Guidelines.pdf (last accessed April 2022).
- Shabani, E., Mirzaei, N., Haghshenas, E., Eskandari-Ghadi, M., 2011. Estimating shear-waves velocity structure by combining array methods and inversion of ellipticity curves at a site in south of Tehran. *J. Earth Sp. Phys.* 36(4)-No. 433127.
- Shabani, E., 2010. Optimization of spatial autocorrelation method in site characterization (case study: Tehran). Ph.D thesis, University of Tehran, Iran, 200 p.
- Shafiee, A., Azadi, A., 2007. Shear-wave velocity characteristics of geological units throughout Tehran City, Iran. *J. Asian Earth Sci.* 29(1), 105-115. <https://doi.org/10.1016/j.jseaes.2006.02.005>
- Shirzad, T., Naghavi, M., Afra, M., YaminiFard, F., 2019. Three-Dimensional P-Wave Velocity Structure of Tehran from Local Micro-Earthquake Tomography. *Pure Appl. Geophys.* 176, 4783-4796. <https://doi.org/10.1007/s00024-019-02269-2>
- Shirzad, T., Naghavi, M., Fard, F.Y., 2018. Shallow/upper crustal shear wave structure of the Tehran region (Central Alborz, Iran) from the inversion of Rayleigh wave dispersion measurements. *J. Seismol.* 22, 1409-1421. <https://doi.org/10.1007/s10950-018-9774-5>
- Shirzad, T., Shomali, Z.H., 2014. Shallow crustal radial anisotropy beneath the Tehran basin of Iran from seismic ambient noise tomography. *Phys. Earth Planet. Inter.* 231, 16-29. <https://doi.org/10.1016/j.pepi.2014.04.001>
- Shirzad, T., Shomali, Z.H., 2013. Shallow crustal structures of the Tehran basin in Iran resolved by ambient noise tomography. *Geophys. J. Int.* 196(2), 1162-1176. <https://doi.org/10.1093/gji/ggt449>
- Shomali, Z.H., Shirzad, T., 2015. Crustal structure of Damavand volcano, Iran, from ambient noise and earthquake tomography. *J Seismol* 19, 191–200. <https://doi.org/10.1007/s10950-014-9458-8>
- Silva, P., Goy, G.L., Zazo, C., Bardaji, T., 2003. Fault-generated mountain fronts in southeast Spain: geomorphologic assessment of tectonic and seismic activity. *Geomorphology* 50(1-3), 203-225. [https://doi.org/10.1016/S0169-555X\(02\)00215-5](https://doi.org/10.1016/S0169-555X(02)00215-5)
- Smerzini, C., Paolucci, R., Stupazzini, M., 2011. Comparison of 3D, 2D and 1D numerical approaches to predict long period earthquake ground motion in the Gubbio plain, Central Italy. *Bull. Earthq. Eng.* 9, 2007-2029. <https://doi.org/10.1007/s10518-011-9289-8>
- Socco, L.V., Foti, S., Boiero, D., 2010. Surface-wave analysis for building near-surface velocity models - Established approaches and new perspectives. *Geophysics* 75(5), ISO-Z116. <https://doi.org/10.1190/1.3479491>
- Socco, L. V., and Strobbia, C., 2004. Surface-wave method for near-surface characterization: A tutorial. *Near surface geophysics*, 2(4), 165-185. <https://doi.org/10.3997/1873-0604.2004015>
- Solaymani Azad, S., Ritz, J.F., Abbassi, M.R., 2011. Left-lateral active deformation along the Mosha-North Tehran fault system (Iran): Morphotectonics and paleoseismological investigations. *Tectonophysics* 497(1-4), 1-14. <https://doi.org/10.1016/j.tecto.2010.09.013>

- SoltaniMoghadam, S., Tatar, M., Komeazi, A., 2019. An improved 1-D crustal velocity model for the Central Alborz (Iran) using Particle Swarm Optimization algorithm. *Phys. Earth Planet. Inter.* 292, 87-99. <https://doi.org/10.1016/j.pepi.2019.05.009>
- Stacey, R. (1988). Improved transparent boundary formulations for the elastic wave equation, *Bull. Seismol. Soc. Am.* 78, 2089–2097.
- Stoecklin, J., 1974. Northern Iran: Alborz mountains. In: Spencer, A. (Ed.), *Mesozoic–Cenozoic Orogenic Belts: Data for Orogenic Studies*. *Geol. Soc. Spec. Publ.* 4, 13–234.
- Su, F., and Aki, K., 1995. Site amplification factors in central and Southern California determined from coda waves. *Bull. Seism. Soc. Am.*, Vol. 85, No.2, 452-466.
- Talebian, M., Copley, A.C., Fattahi, M., Ghorashi, M., Jackson, J.A., Nazari, H., Sloan, R.A., Walker, R.T., 2016. Active faulting within a megacity: The geometry and slip rate of the Pardisan thrust in central Tehran, Iran. *Geophys. J. Int.* 207(3), 1688-1699. <https://doi.org/10.1093/gji/ggw347>
- Tatar, M., Momeni, M., YaminiFard, F., 2015. Microseismicity and seismotectonics of the Garmsar area. *Geosci. Sci. c Q. Journal, Geol. Surv. Iran*, 24, 289–298.
- Tatar, M., Hatzfeld, D., Abbassi, A., Fard, F.Y., 2012. Microseismicity and seismotectonics around the Mosha fault (Central Alborz, Iran). *Tectonophysics* 544–545. <https://doi.org/10.1016/j.tecto.2012.03.033>
- Tatar, M., Jackson, J., Hatzfeld, D., Bergman, E., 2007. The 2004 May 28 Baladeh earthquake (M_w 6.2) in the Alborz, Iran: overthrusting the South Caspian Basin margin, partitioning of oblique convergence and the seismic hazard of Tehran, *Geophysical Journal International*, 170-1, Pages 249–261, <https://doi.org/10.1111/j.1365-246X.2007.03386.x>
- Tchalenko, J.S., 1975. Seismotectonic framework of the North Tehran Fault. *Tectonophysics* 9, 411-420. [https://doi.org/10.1016/0040-1951\(75\)90169-9](https://doi.org/10.1016/0040-1951(75)90169-9)
- Tchalenko, J.S., Berberian, M., Iranmanesh, H., Baily, M., Arsovsky, M., 1974. Tectonic framework of Tehran region. *Mater. study Seism. Iran; North-central Iran. Geol. Surv. Iran.* 29, 7–46.
- Thabet, M., 2019. Site-Specific Relationships between Bedrock Depth and HVSR Fundamental Resonance Frequency Using KiK-NET Data from Japan. *Pure Appl. Geophys.* 176, 4809-4831. <https://doi.org/10.1007/s00024-019-02256-7>
- Theodoulidis, N., G. Cultrera, C. Cornou, P.-Y. Bard, T. Boxberger, G. DiGiulio, A. Imtiaz, D. Kementzetidou, K. Makra, The Argostoli NERA Team, 2018. Basin effects on ground motion : the case of a high-resolution experiment in Cephalonia (Greece), *Bull. Earthq. Eng.* 16, 2, pp 529–560. <https://doi.org/10.1007/s10518-017-0225-4>
- Thomson, W.T., 1950. Transmission of elastic waves through a stratified solid medium. *J. Appl. Phys.* 21. <https://doi.org/10.1063/1.1699629>
- Uebayashi, H., Kawabe, H., Kamae, K., 2012. Reproduction of microseism H/V spectral features using a three-dimensional complex topographical model of the sediment-bedrock interface in the Osaka sedimentary basin. *Geophys. J. Int.* 189(2), 1060-1074. <https://doi.org/10.1111/j.1365-246X.2012.05408.x>
- Vasheghani Farahani, J., Zare, M., and Cichowicz, A., 2014. Microseismicity of Tehran region based on the data recorded in a local monitoring network, 2004–2010: Episodes, v. 37, no. 3, p. 206–217.
- Vernant, P., Nilforoushan, F., Chéry, J., Bayer, R., Djamour, Y., Masson, F., Nankali, H., Ritz, J.F., Sedighi, M., Tavakoli, F., 2004. Deciphering oblique shortening of central Alborz in Iran using geodetic data. *Earth Planet. Sci. Lett.* 223, v. 157(1), p. 381–398. <https://doi.org/10.1016/j.epsl.2004.04.017>

- Vernant, P., Nilforoushan, F., Hatzfeld, D., Abbassi, M., Vigny, C., Masson, F., Nankali, H., Martinod, J., Ashtiani, M., Bayer, R., Tavakoli, F., and Chéry, J., 2004. Present-day crustal deformation and plate kinematics in the Middle East constrained by GPS measurements in Iran and northern Oman. *Geophys. J. Int.* 157(1), 381–398. <https://doi.org/10.1111/j.1365-246X.2004.02222.x>
- Virieux, J., 1986. P–SV wave propagation in heterogeneous media: velocity–stress finite difference method. *Geophysics*, 51, 889–901.
- Vita-Finzi, C., 1969. Late quaternary alluvial chronology of Iran. *Geol. Rundschau* 58, 951–973.
- Wathelet, M., Chatelain, J.L., Cornou, C., Giulio, G. Di, Guillier, B., Ohrnberger, M., Savvaidis, A., 2020. Geopsy: A user-friendly open-source tool set for ambient vibration processing. *Seismol. Res. Lett.* 91(3), 1878-1889. <https://doi.org/10.1785/0220190360>
- Wathelet, M., Guillier, B., Roux, P., Cornou, C., Ohrnberger, M., 2018. Rayleigh wave three-component beamforming: Signed ellipticity assessment from high-resolution frequency-wavenumber processing of ambient vibration arrays. *Geophys. J. Int.* 215(1), 507-523. <https://doi.org/10.1093/gji/ggy286>
- Wathelet, M., 2008. An improved neighborhood algorithm: Parameter conditions and dynamic scaling. *Geophys. Res. Lett.* 35, L09301 <https://doi.org/10.1029/2008GL033256>
- Wathelet, M., Jongmans, D., Ohrnberger, M. and Bonnefoy-Claudet, S., 2008. Array performances for ambient vibrations on a shallow structure and consequences over Vs inversion, *J. Seismol.*, 12, 1-19. <https://doi.org/10.1007/s10950-007-9067-x>
- Wathelet, M., Jongmans, D., Ohrnberger, M., 2004. Surface-wave inversion using a direct search algorithm and its application to ambient vibration measurements. *Near Surf. Geophys.* 2(4), 211-221. <https://doi.org/10.3997/1873-0604.2004018>
- Woods, J., Lintz, P., 1973. Plane waves at small arrays. *Geophysics*, 38(6) :1023–1041.
- Yamanaka, H., and Ishida, H., 1996. Application of genetic algorithms to an inversion of surface-wave dispersion data. *Bulletin of the Seismological Society of America*, 86(2) :436–444.
- Zafarani, H., Vahidifard, H., Ansari, A., 2013. Prediction of broadband ground-motion time histories: The case of Tehran, Iran. *Earthq. Spectra* 29(2), 633-660. <https://doi.org/10.1193/1.4000150>
- Zeng, Y., 2006. Scattered surface wave energy in the seismic coda. *Pure Appl. Geophys.* 163, 533-548. <https://doi.org/10.1007/s00024-005-0025-7>
- Zhou, Y., Dahlen, F.A., Nolet, G., 2004. Three-dimensional sensitivity kernels for surface wave observables. *Geophys. J. Int.* 158(1), 142-168. <https://doi.org/10.1111/j.1365-246X.2004.02324.x>
- Zienkiewicz, O. C., Taylor, R. L., and Zhu, J. Z., 2013. *The Finite Element Method: Its Basis and Fundamentals*. 7th Edn. Volume 1. Cambridge-Elsevier.
- Zor, E., Özalaybey, S., Karaaslan, A., Tapirdamaz, M.C., Özalaybey, S.Ç., Tarancioğlu, A., Erkan, B., 2010. Shear wave velocity structure of the Izmit Bay area (Turkey) estimated from active-passive array surface wave and single-station microtremor methods. *Geophys. J. Int.* 182. <https://doi.org/10.1111/j.1365-246X.2010.04710.x>

Appendix A:

Figure A1- JICA soil columns from JICA and CEST (2000)

The JICA's ground model for Tehran classifies the soil into 4 types: C for Clay, CS for Clay and Sand, S for Sand and G for Gravelly soil, based on soil condition and average N-STP values up to the engineering bedrock. The Tehran's ground model is composed of 41 soil columns, the deepest soil column is model #1 which is located in south of Tehran (see the location of other soil columns in Figure 4) while the model #41, located in the northern part of Tehran, corresponds to rocky site.

Model No.	Depth (GL-m)																									
	5	10	15	20	25	30	35	40	45	50	55	60	65	70	75	80	85	90	95	100	110	120	130	140	150	
1	C1	C1	C1	C1	C1	C1	C3	C3	C3	C3	C3	C3	C3	C3	C3	C3	C3	C3	C3	C3	C3	C3	C3	C3	C3	C4
2	C1	C1	C2	C2	C2	C2	C3	C3	C3	C3	C3	C3	C3	C3	C3	C3	C3	C3	C3	C3	C3	C3	C3	C3	C3	C4
3	C1	C1	CS1	CS1	CS1	CS1	CS3	CS3	CS3	CS3	C3	C3	C3	C3	C3	C3	C3	C3	C3	C3	C3	C3	C3	C3	C3	C4
4	C1	C1	C2	C3	C3	C3	C3	C3	C3	C3	C3	C3	C3	C3	C3	C3	C3	C3	C4							
5	C1	C1	C1	C1	C1	C1	C2	C2	C2	C2	C3	C3	C3	C3	C3	C3	C3	C3	C3	C3	C3	C3	C3	C3	C3	C4
6	C2	C2	C2	C2	C2	C2	C3	C3	C3	C3	C3	C3	C3	C3	C3	C3	C2	C2	C2	C2	C2	C2	C2	C2	C2	C4
7	C1	C1	C2	C3	C3	C3	C4												C4							
8	C1	C1	C2	C2	C2	C2	C2	C2	C2	C2	C2	C2	C2	C2	C2	C2	C2	C4								
9	C2	C2	CS2	CS2	CS2	CS2	C3	C3	C3	C3	C2	C2	C2	C2	C4											C4
10	C1	C1	CS2	CS2	CS2	CS2	C3	C3	C3	C3	C2	C2	C2	C2	C4											C4
11	C2	C2	C3	C3	C3	C3	CS3	CS3	CS3	CS3	C2	C2	C2	C2	C4											C4
12	C2	C2	C2	C2	C2	C2	C2	C2	C2	C2	C4															C4
13	C2	C2	C2	C2	C2	C2	CS3	CS3	CS3	CS3	CS4															C4
14	C2	C2	C2	C2	C2	C2	CS2	CS2	CS2	CS2	CS4															C4
15	CS1	CS1	C2	C2	C2	C2	CS3	CS3	CS3	CS3	CS3															C4
16	C2	C2	C2	C2	C2	C2	CS3	CS3	CS3	CS3	CS4															C4
17	C2	C2	CS1	CS1	CS1	CS1	CS3	CS3	CS3	CS3	CS3															C4
18	G2	G2	CS1	CS1	CS1	CS1	G3	G3	G3	G3	G3															G4
19	C3	C3	C3	C3	C3	C3	G3	G3	G3	G3	G3															G4
20	C2	C2	C3	C3	C3	C3	CS3	CS3	CS3	CS3	CS3															C4
21	CS2	CS2	CS3															C4								
22	C1	C1	C1	C1	C1	C1	C4																			C4
23	C2	C2	C2	C2	C2	C2	C4																			C4
24	CS2	CS2	CS2	CS2	CS2	CS2	CS4																			C4
25	C1	C1	CS2	CS2	CS2	CS2	CS4																			C4
26	CS1	CS1	CS3	CS3	CS3	CS3	CS3																			C4
27	G2	G2	G4	G4	G4	G3	G3																			G4
28	C2	C2	G3	G3	G3	G3	G4																			G4
29	S3	S3	S3	S3	S3	S3	G4																			G4
30	S3	S3	G3	G3	G3	G3	G4																			G4
31	G3	G3	G3	G3	G3	G3	G4																			G4
32	G2	G2	G3	G3	G3	G4																				G4
33	G3	G3	G3	G3	G3	G4																				G4
34	G3	G3	G3	G4																						G4
35	S3	S3	S3	G4																						G4
36	CS3	CS3	CS3	G4																						G4
37	C1	C1	C1	G4																						G4
38	C2	C2	C2	G4																						G4
39	G3	G3	G3	G4																						G4
40	Pre-Miocene																									G4
41	Rock																									G4

Clay	C1	C2	C3	C4
Average N Value	15	35	75	100
Sand and Clay	CS1	CS2	CS3	CS4
Average N Value	15	35	75	100
Sand	S1	S2	S3	S4
Average N Value	15	35	75	100
Gravel	G1	G2	G3	G4
Average N Value	15	35	75	100

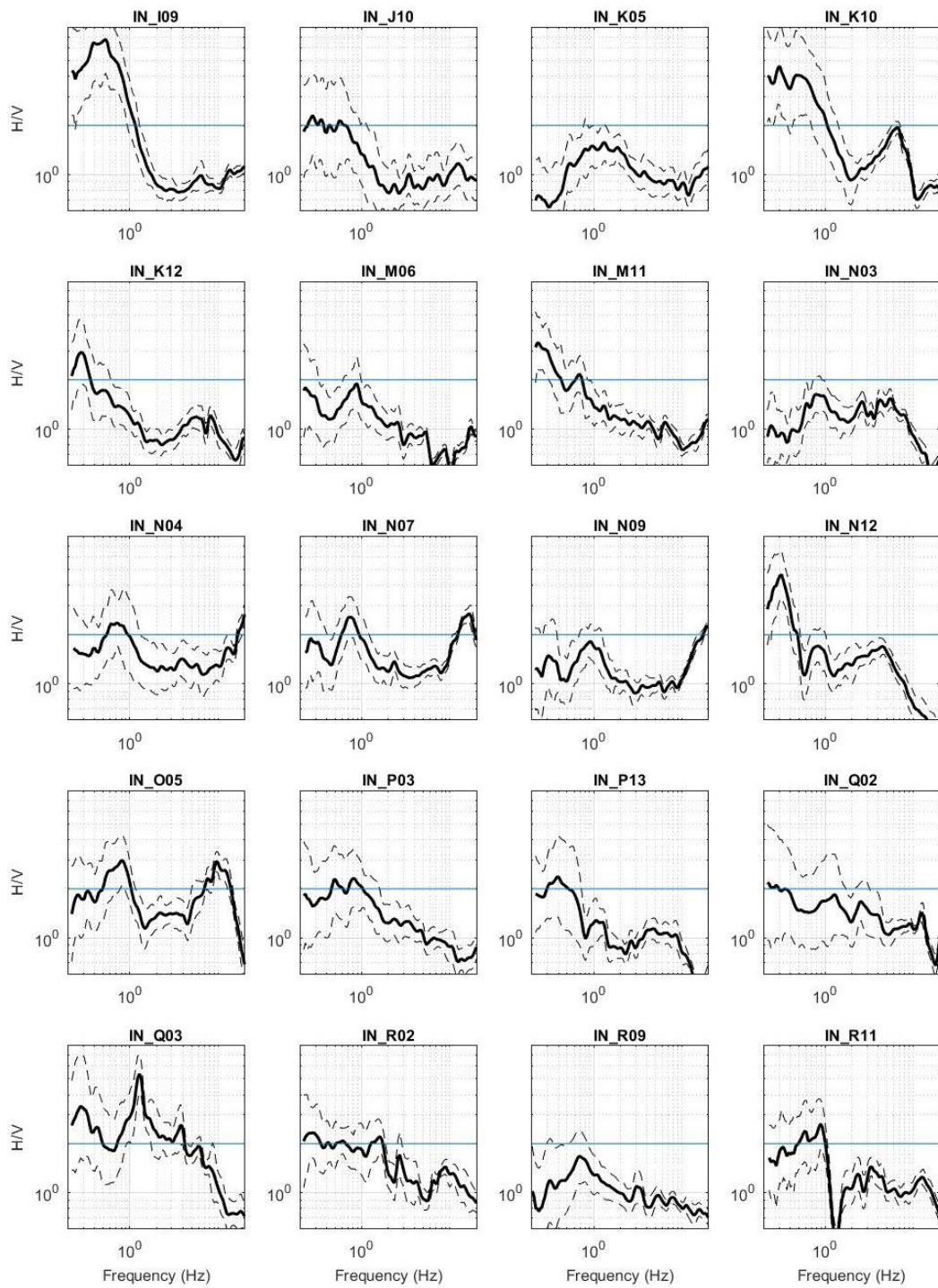
Appendix B:

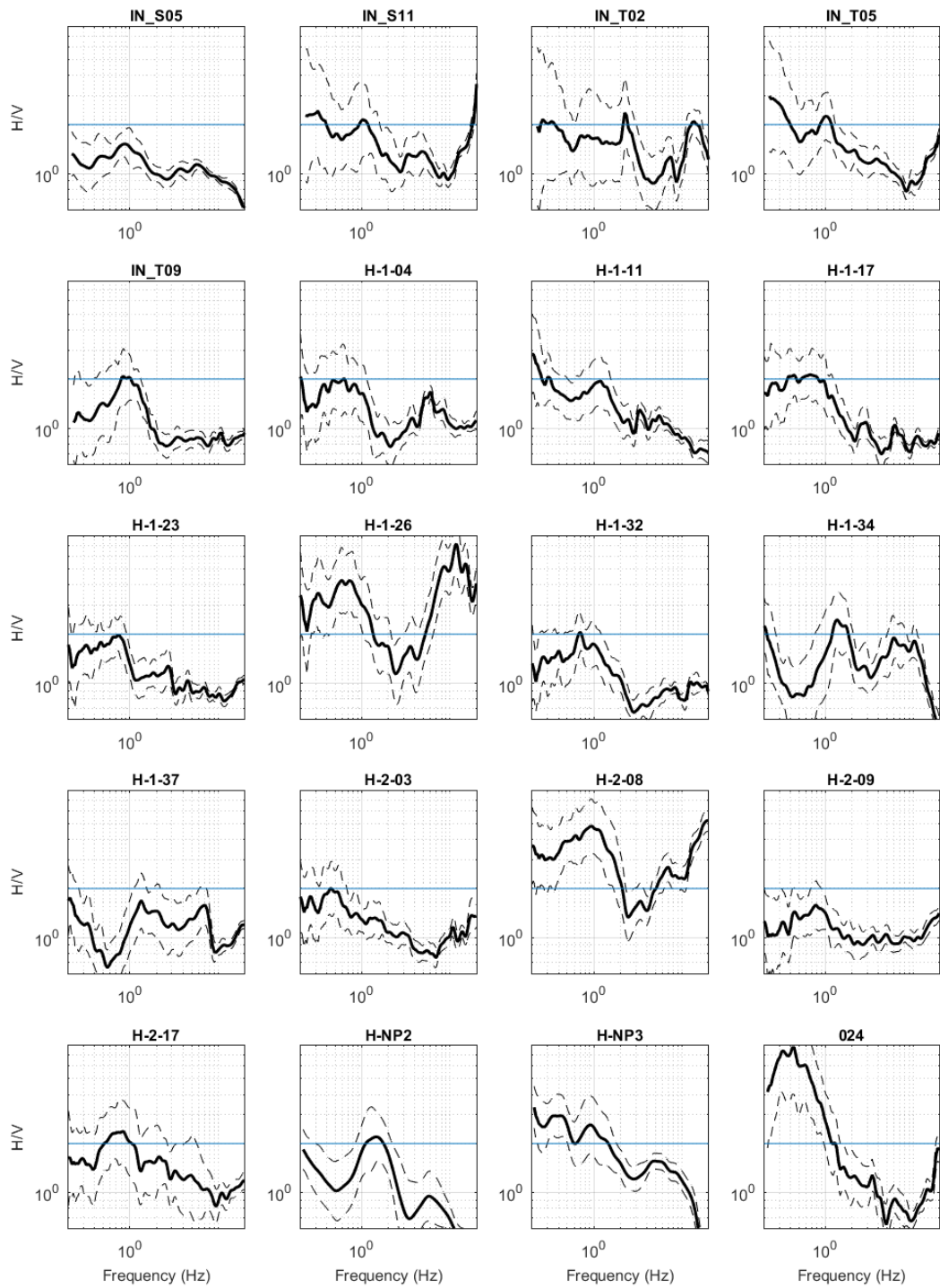
Table 1. names, geographical locations of H/V measurements and H/V peak frequency (f_0)

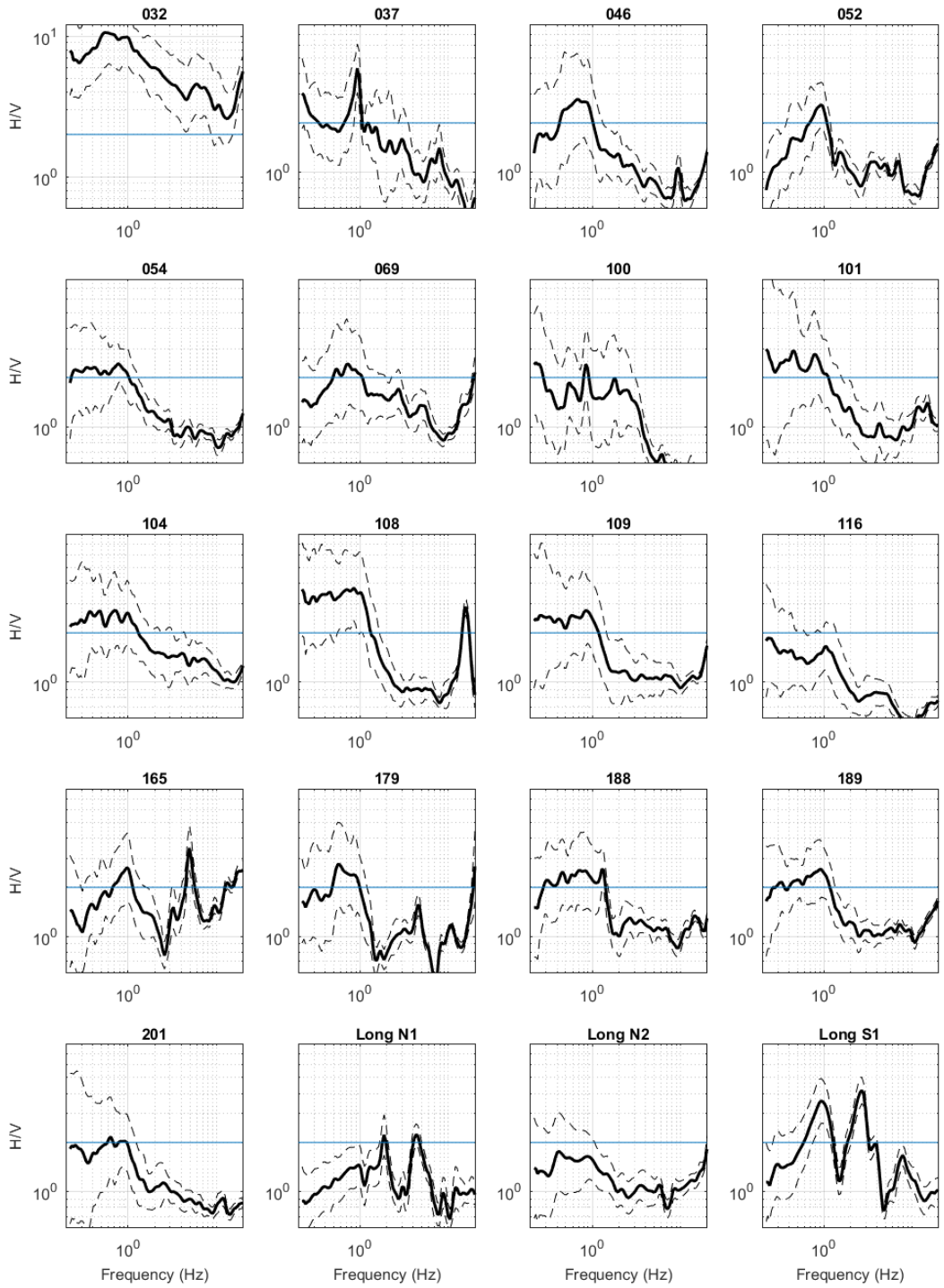
Number	Name	Lat.	Long.	f_0 (Hz)	Number	Name	Lat.	Long.	f_0 (Hz)
1	I09	35.68279	51.25459	0.5	41	32	35.75876	51.34513	0.65
2	J10	35.66241	51.27151	0.55	42	37	35.77753	51.38575	0.9
3	K05	35.75822	51.29834	1.2	43	46	35.7385	51.33372	0.75
4	K10	35.66434	51.29807	0.5	44	52	35.65805	51.47813	0.9
5	K12	35.62832	51.30404	0.3	45	54	35.66654	51.48603	0.8
6	M06	35.73742	51.34029	0.9	46	69	35.77132	51.49278	0.7
7	M11	35.64997	51.34581	0.3	47	100	35.81123	51.4565	0.9
8	N03	35.7858	51.3637	0.8	48	101	35.78754	51.46724	0.8
9	N04	35.77381	51.36648	0.7	49	104	35.77403	51.37676	1
10	N07	35.72006	51.36242	0.8	50	108	35.72424	51.49551	0.8
11	N09	35.68775	51.36905	0.9	51	109	35.71837	51.47879	0.8
12	N12	35.62796	51.36232	0.3	52	116	35.71933	51.48993	1
13	O05	35.75245	51.38694	0.8	53	165	35.78946	51.45267	1
14	P03	35.79278	51.40997	0.8	54	179	35.71374	51.31183	0.8
15	P13	35.60671	51.40391	0.4	55	188	35.61912	51.47183	1.2
16	Q02	35.80786	51.431	1.2	56	189	35.67014	51.48154	0.9
17	Q03	35.79301	51.42934	1.1	57	201	35.77616	51.34851	1
18	R02	35.81006	51.45298	1.3	58	LongN1	35.81808	51.47481	1.5
19	R09	35.67957	51.45172	0.9	59	LongN2	35.78786	51.38405	1
20	R11	35.64228	51.44798	0.9	60	LongS1	35.61854	51.40078	0.9
21	S05	35.74912	51.47178	0.8	61	LongS2	35.59206	51.43334	0.4
22	S11	35.64248	51.47891	1	62	D1_1	35.7165	51.26665	0.5
23	T02	35.806	51.49704	1.7	63	D1_4	35.70884	51.27058	0.5
24	T05	35.75123	51.49976	1	64	D1_14	35.66022	51.26385	0.6
25	T09	35.68347	51.49193	1	65	D1_15	35.65834	51.26062	0.55
26	H-1-04	35.72278	51.60152	0.6	66	D1_21	35.71378	51.26956	0.5
27	H-1-11	35.74054	51.53601	1.1	67	D2_3	35.72259	51.24048	0.55
28	H-1-17	35.74826	51.54651	0.9	68	D2_4	35.72103	51.2472	0.6
29	H-1-23	35.75726	51.55556	0.7	69	D2-2-4-2	35.688	51.21471	0.6
30	H-1-26	35.76417	51.62621	0.7	70	D2-2-4-4	35.69734	51.20328	0.5
31	H-1-32	35.79369	51.54065	0.7	71	D2_5	35.72129	51.24216	0.55
32	H-1-34	35.79657	51.60973	1.3	72	D2_6	35.71764	51.24252	0.5
33	H-1-37	35.80148	51.55746	1.2	73	D2_8	35.71017	51.24473	0.6
34	H-2-03	35.73506	51.59775	0.45	74	D2_9	35.70444	51.24172	0.4
35	H-2-08	35.74957	51.55747	1	75	D2_16	35.67627	51.22872	0.5
36	H-2-09	35.72439	51.54853	0.8	76	D2_18	35.6579	51.24584	0.45
37	H-2-17	35.75787	51.52525	0.8	77	D3-07	35.73156	51.12926	0.4
38	H-NP2	35.73523	51.66132	1.4	78	D3-11	35.7441	51.14015	0.4
39	H-NP3	35.74543	51.66298	0.9	79	D3-19	35.72826	51.12789	1.5
40	24	35.68305	51.37767	0.4	80	D3-20	35.7274	51.13241	1.5

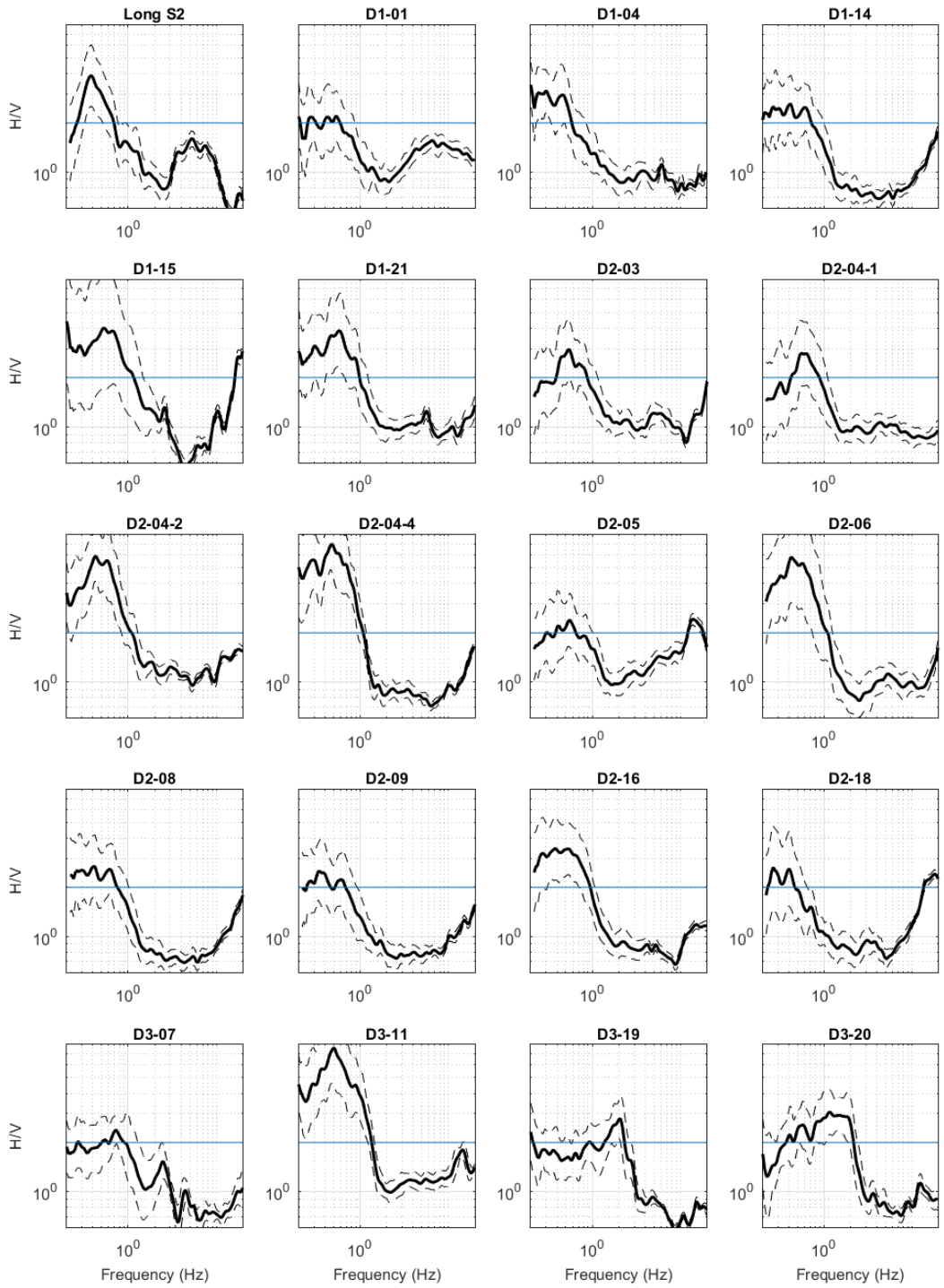
Number	Name	Lat.	Long.	F0 (Hz)	Number	Name	Lat.	Long.	F0 (Hz)
81	D3-21	35.7239	51.13635	0.45	121	SDT	35.77837	51.35008	0.6±0.1
82	D3-25	35.71562	51.14382	0.8	122	SHR	35.61225	51.42521	0.55±0.1
83	D3-33	35.72025	51.18823	0.5	123	SKH	35.72123	51.56161	0.9±0.15
84	D3-45	35.6996	51.18004	0.5	124	THR	35.74337	51.53394	0.9±0.15
85	D3-49	35.69549	51.15893	0.5	125	TOS	35.69637	51.36003	0.85±0.1
86	D3-50	35.68994	51.15681	0.5	126	TRB	35.72987	51.39184	1.08±0.1
87	D3-52	35.68172	51.15525	1	127	VLP	35.64518	51.38158	0.32±0.05
88	D3-Extra	35.67792	51.15769	0.5	128	sta01	35.613	51.3	0.4
89	D4-2	35.61156	51.36093	0.3	129	sta02	35.62	51.285	0.32
90	D4-6	35.58205	51.30941	0.3	130	sta05	35.6	51.447	0.77
91	D4-8	35.61007	51.35308	0.3	131	sta08	35.627	51.455	1
92	D4-9	35.60712	51.3411	0.4	132	sta11	35.629	51.294	0.29
93	D4-12	35.56289	51.31977	0.5	133	sta13	35.58358	51.436	0.7
94	D4-13	35.55913	51.31173	0.5	134	sta14	35.602	51.395	0.52
95	D4-15	35.56609	51.31052	1.2	135	sta15	35.599	51.426	0.73
96	D4-16	35.57086	51.31067	0.3	136	sta16	35.595	51.409	0.68
97	D4-17	35.59354	51.30299	0.3	137	sta17	35.626	51.464	1
98	D4-18	35.60623	51.35151	0.3	138	sta20	35.64	51.397	0.4
99	D4-21	35.57676	51.32958	0.3	139	sta21	35.754	51.554	0.92
100	D4-23	35.57882	51.30939	0.3	140	sta22	35.741	51.581	0.93
101	D4-26	35.62478	51.3764	0.3	141	sta23	35.749	51.4	1
102	BBA	35.76694	51.56798	0.6±0.05	142	sta24	35.633	51.397	0.47
103	BSP	35.65022	51.4271	0.65±0.1	143	sta26	35.768	51.485	0.86
104	DAR	35.76419	51.45101	0.7±0.05	144	sta27	35.751	51.502	0.82
105	ELM	35.74327	51.50602	0.7±0.1	145	sta31	35.739	51.602	1
106	FAR	35.67075	51.39387	0.38±0.05	156	sta32	35.729	51.582	0.9
107	GHP	35.65518	51.32815	0.35±0.05	147	sta41	35.675	51.483	0.88
108	HRM	35.56497	51.3802	0.65±0.15	148	sta42	35.665	51.483	0.97
109	JNT	35.75478	51.30763	0.9±0.15	149	sta43	35.646	51.481	1
110	KHJ	35.65316	51.27801	0.6±0.05	150	sta44	35.646	51.481	0.94
111	KHV	35.65367	51.46861	0.9±0.1	151	sta45	35.66	51.464	0.82
112	MET	35.73168	51.511	0.6±0.1	152	sta46	35.65	51.426	0.4
113	MVT	35.62104	51.38009	0.35±0.05	153	sta47	35.64	51.4	0.37
114	NAM	35.79034	51.40304	0.9±0.2	154	sta48	35.62	51.394	0.34
115	NZM	35.72366	51.45673	0.9±0.15	155	sta49	35.719	51.502	1
116	OZG	35.79624	51.50016	0.9±0.1	156	sta55	35.754	51.429	0.88
117	PLC	35.7596	51.54383	0.75±0.1	157	sta56	35.716	51.368	0.87
118	PRD	35.74578	51.35234	0.85±0.1	158	sta60	35.66385	51.42184	0.8
119	PRZ	35.68605	51.44876	0.8±0.1	159	sta62	35.635	51.37	0.29
120	SAD	35.8158	51.4252	1.1±0.1					

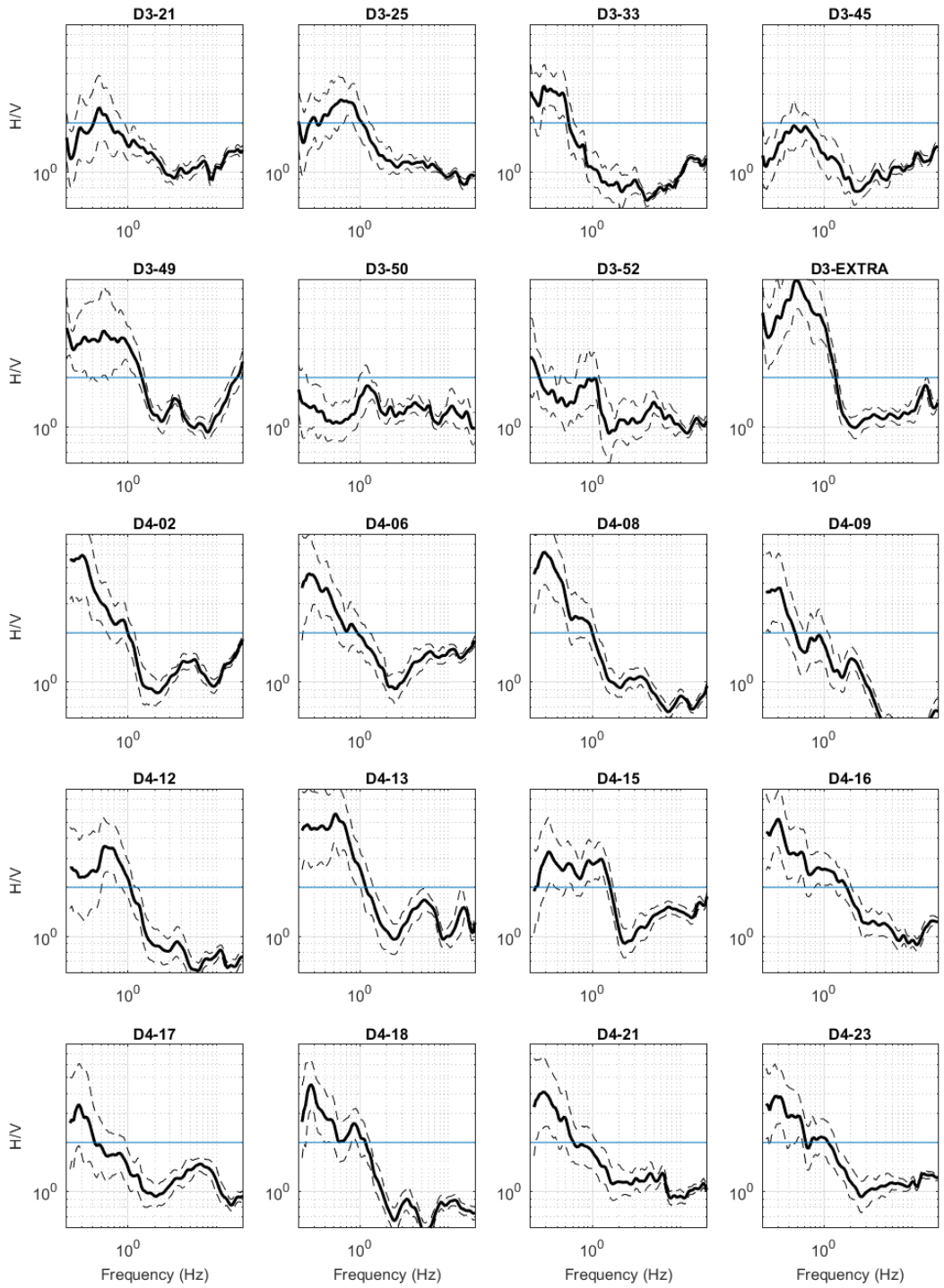
Figure B. H/V curves used to extract H/V peak frequency. Average H/V curve with its uncertainty are indicated by black and dashed lines, respectively. The blue line indicates an amplitude of H/V of 2. The H/V curves from the 2002 experimental campaign are available in Haghshenas (2005).

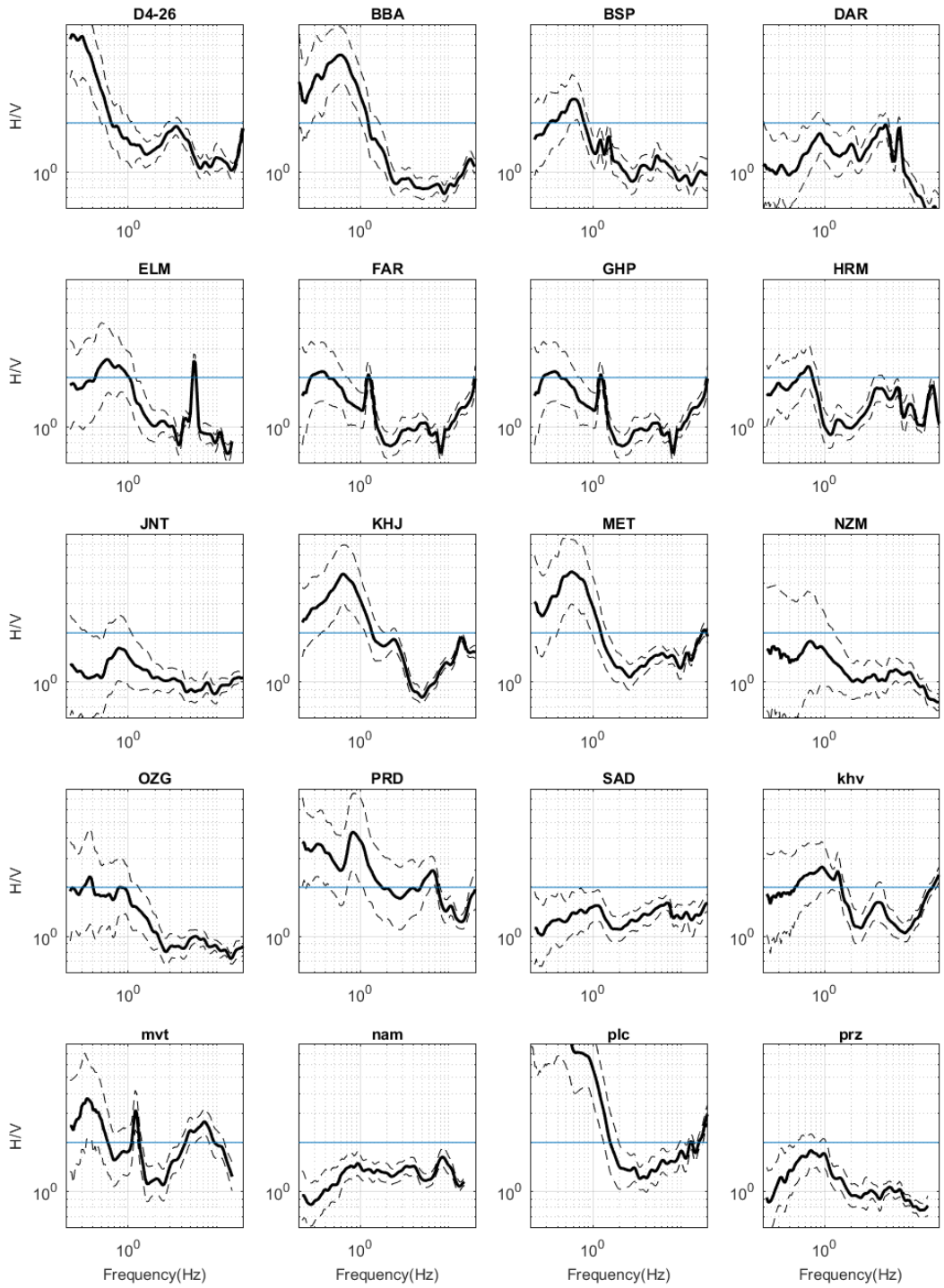


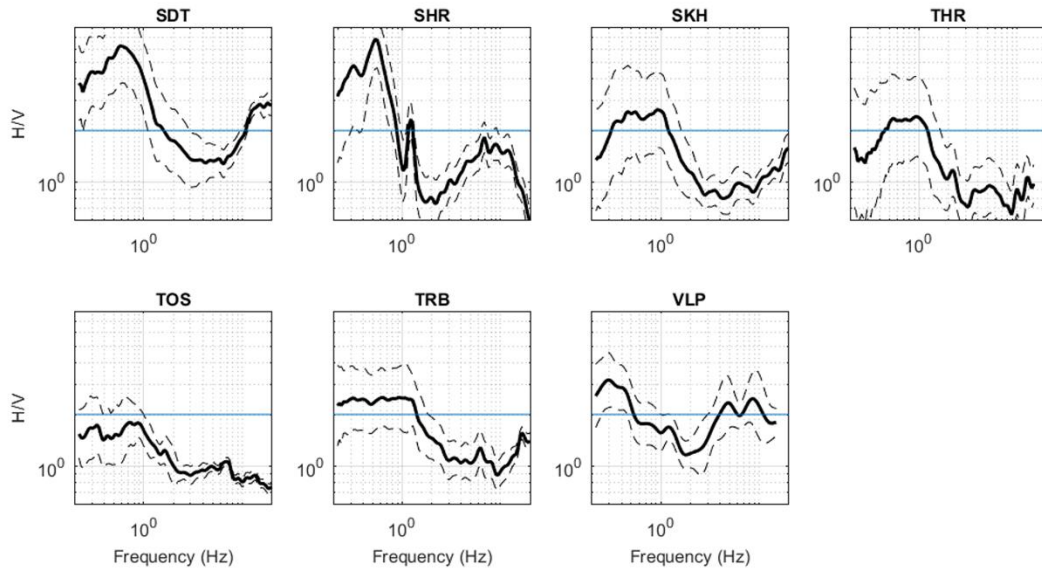












Appendix C:

Extraction of Rayleigh wave ellipticity from coda of earthquakes

I applied the RayDec method algorithm to earthquake coda data (RaydecC).

Coda parts are selected following Perron et al. (2018) from $(T_{coda} = 4.6(T_S - T_p) + T_0)$ to T_{end} where T_p and T_s indicates the P and S wave time arrival, T_{coda} the starting time of the coda and T_{end} corresponds to the time for which 95% of the cumulative energy (evaluated on the three components) between T_p and the end of the record is reached. Figure 1 indicates an example of coda selection for 4.9 Mw earthquake (recorded at 18:36:36, 05-04-2002 occurring 610 km far from the DAR station).

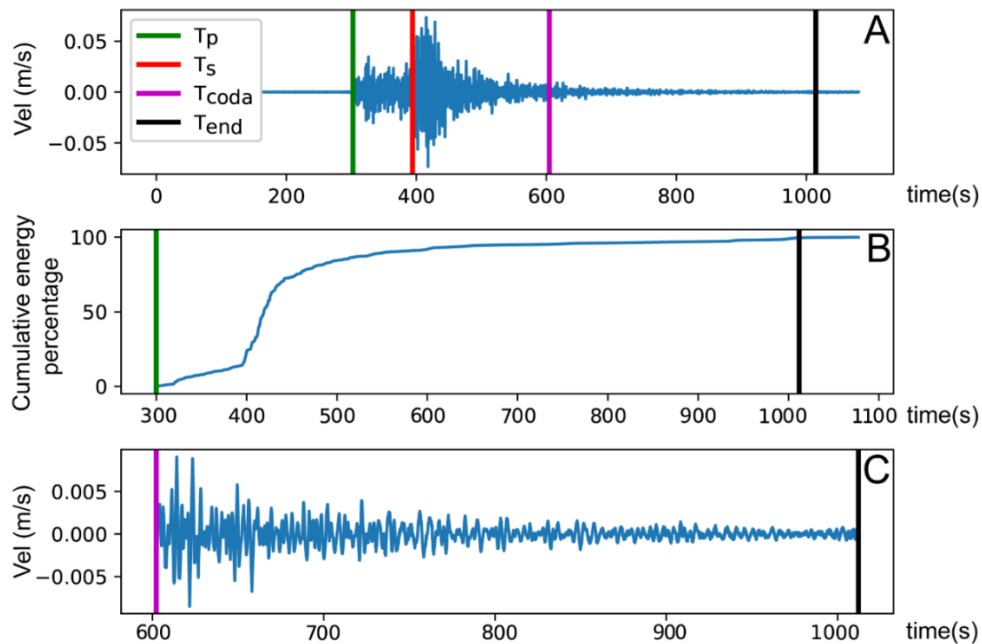


Figure C1: The 4.9 Mw recorded event at station DAR (18:36:36, 05-04-2002; lat: 32.069N, long: 56.369W, 610 km far from the DAR station)

For the application of the RayDec method (Hobiger et al., 2009), I consider a minimum window duration of 60 seconds for the coda part, which leads to consider only regional earthquakes. The

average ellipticity of Rayleigh wave is then obtained after averaging ellipticities obtained for various earthquakes.

The ellipticity obtained for one earthquake event, all events and the resulting average RayDecC curve is shown for 1 seismological station from the 2002 seismological network in Figure 2. The number of events was 64.

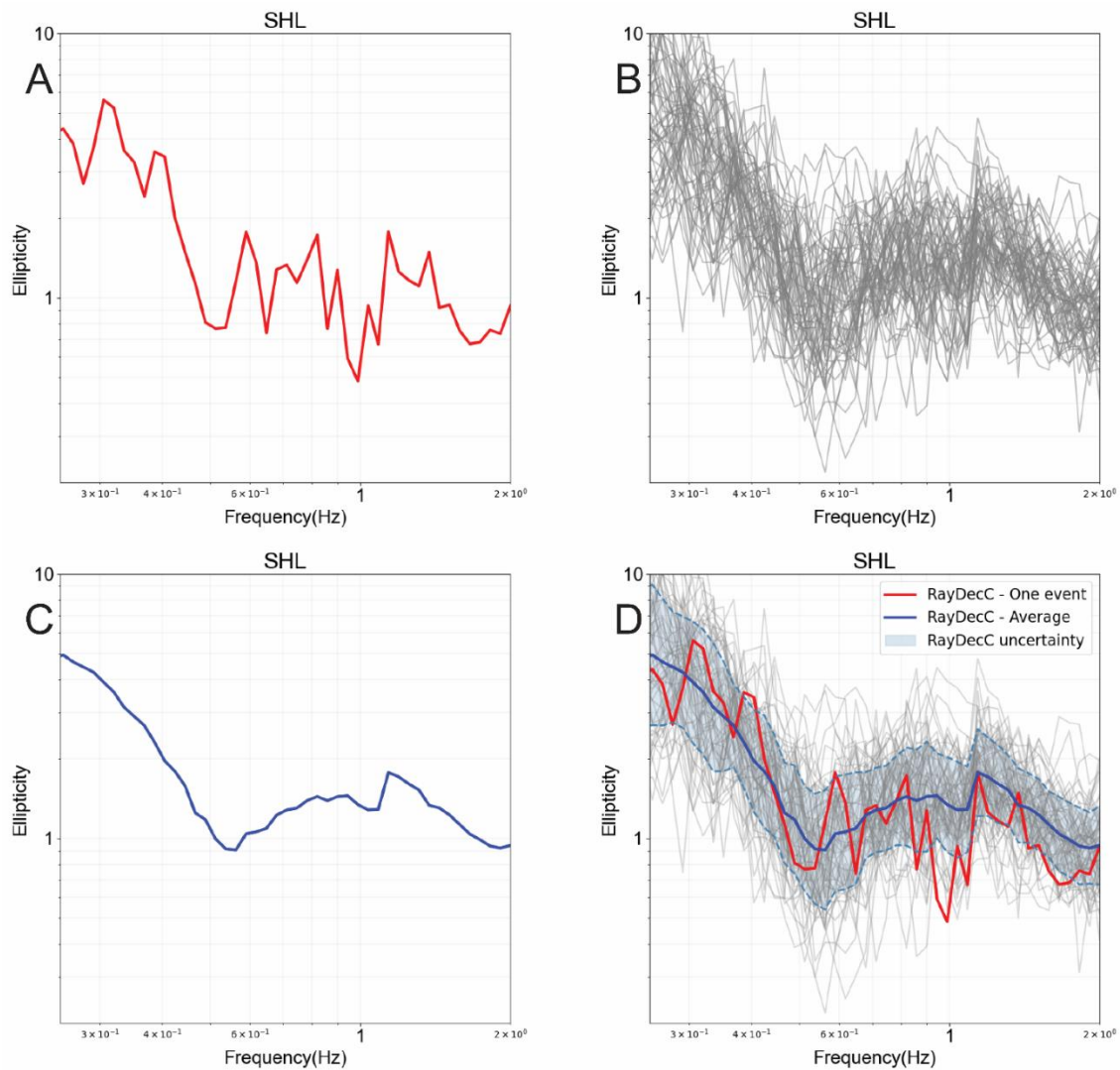


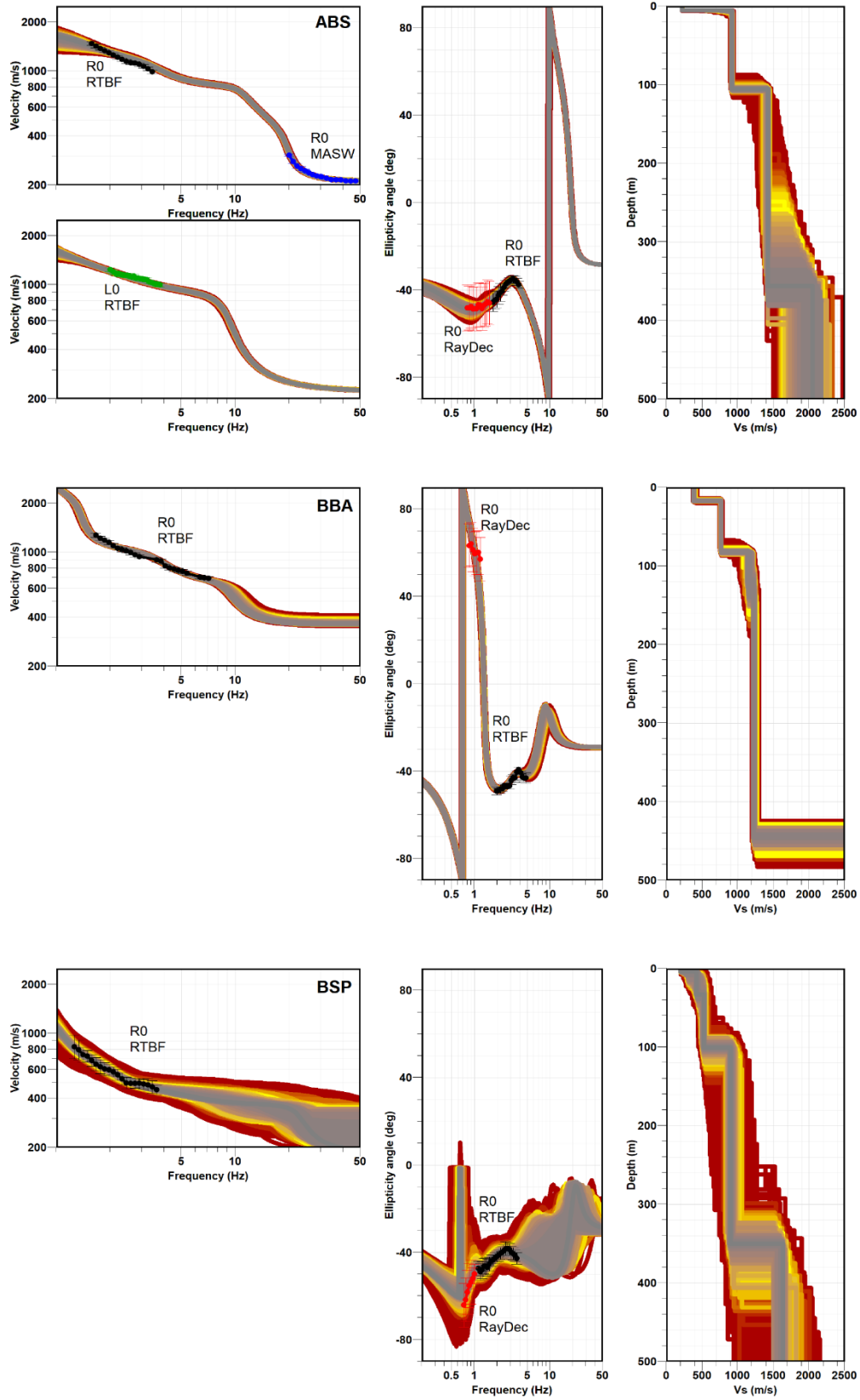
Figure C2: Calculated ellipticity for a-one event, b- all event c- average of all events and d- comparing one event and the average uncertainty.

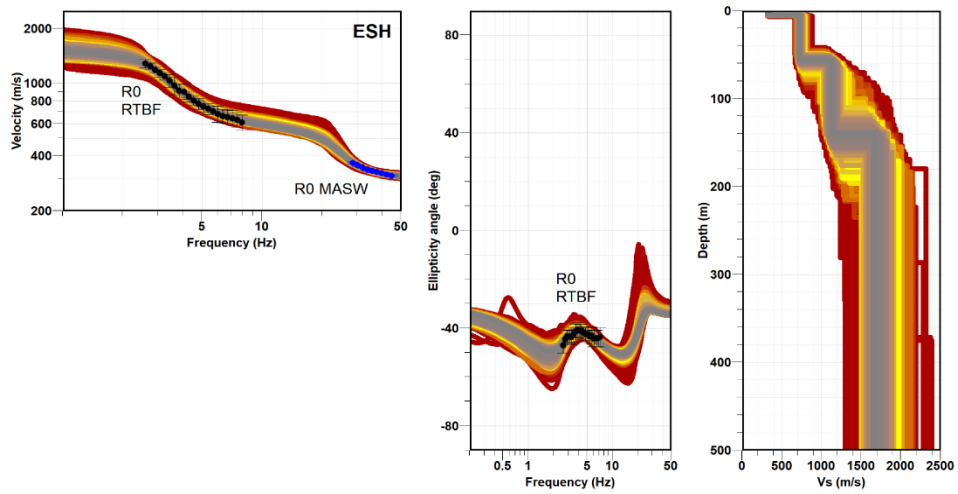
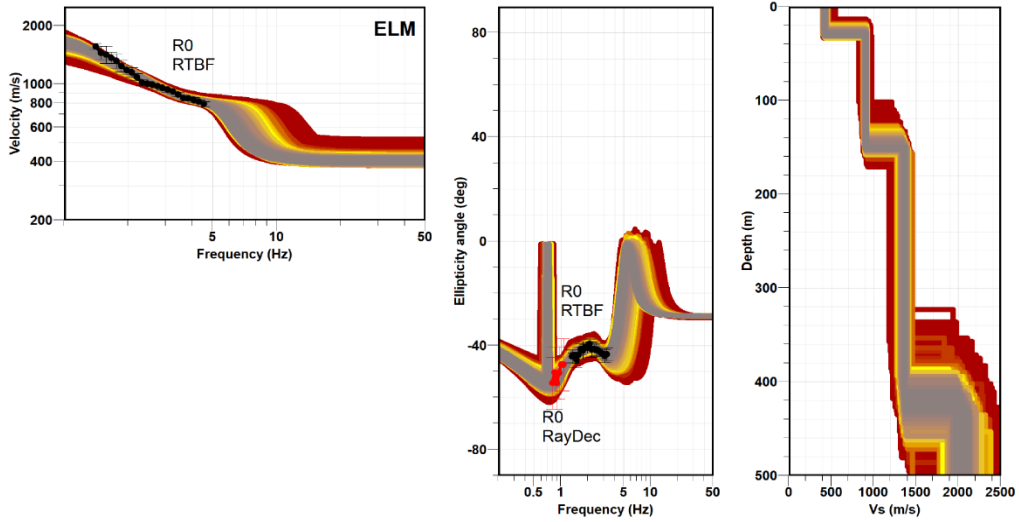
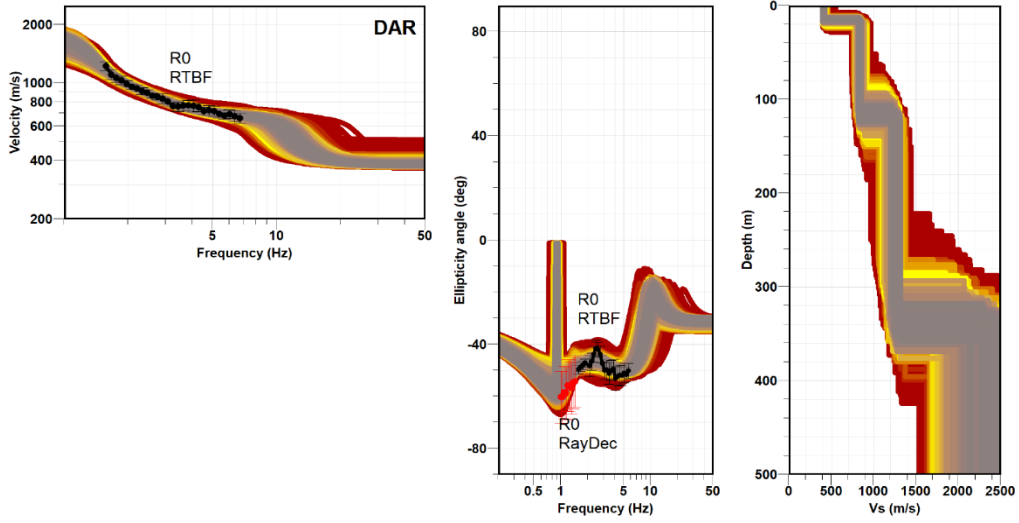
Appendix D:

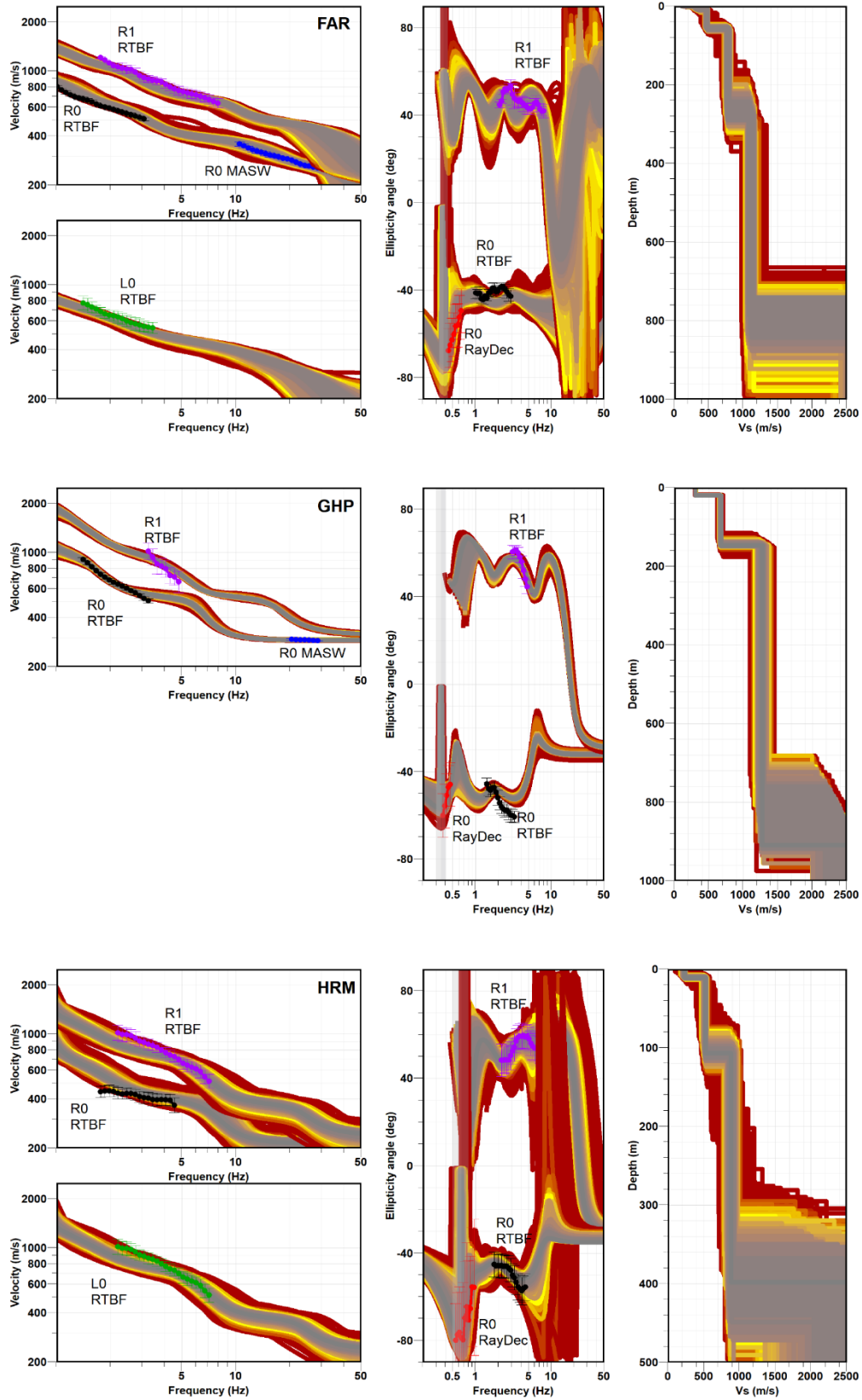
Inversion results

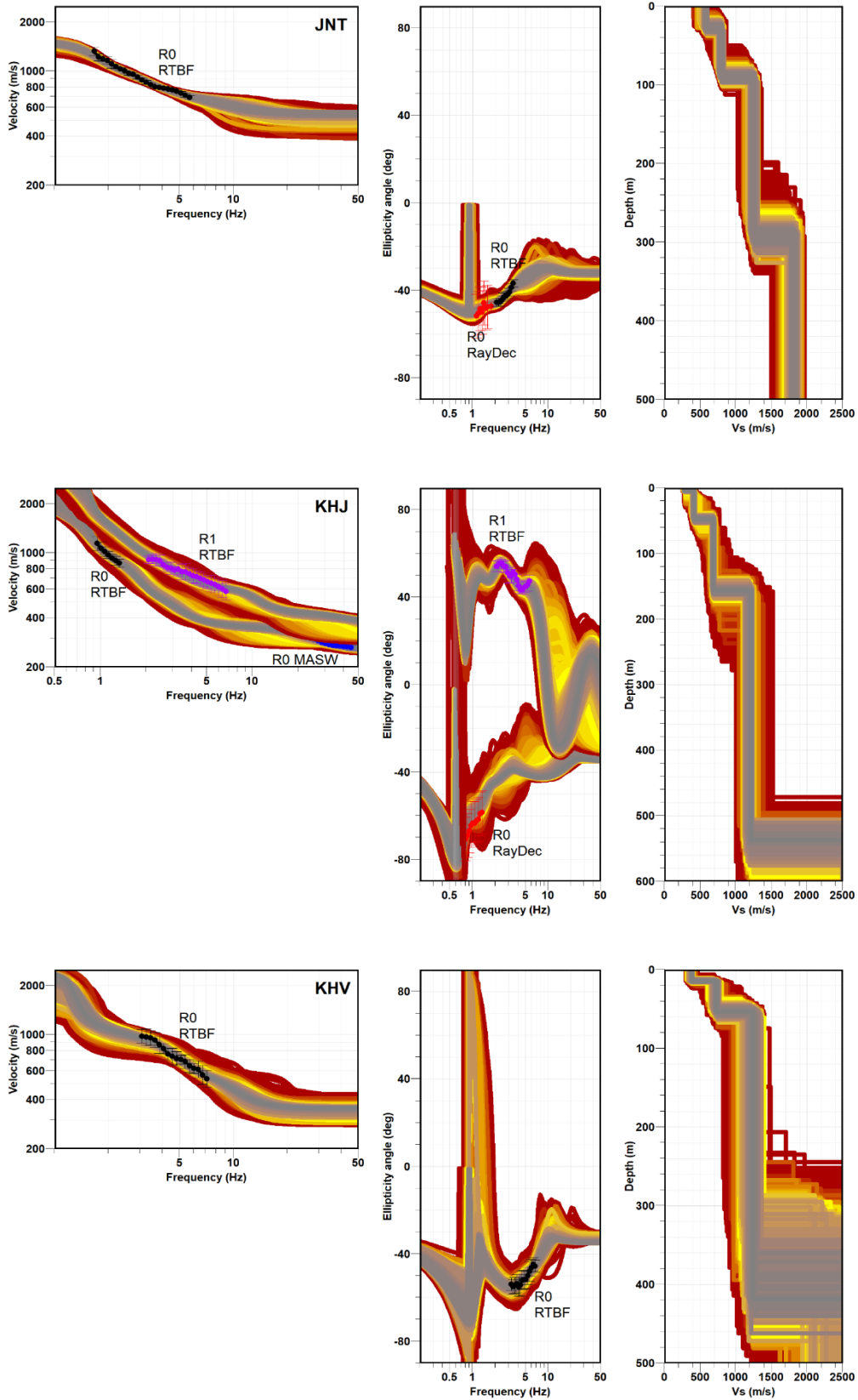
Inversion results for the 33 array measurements used in the paper.

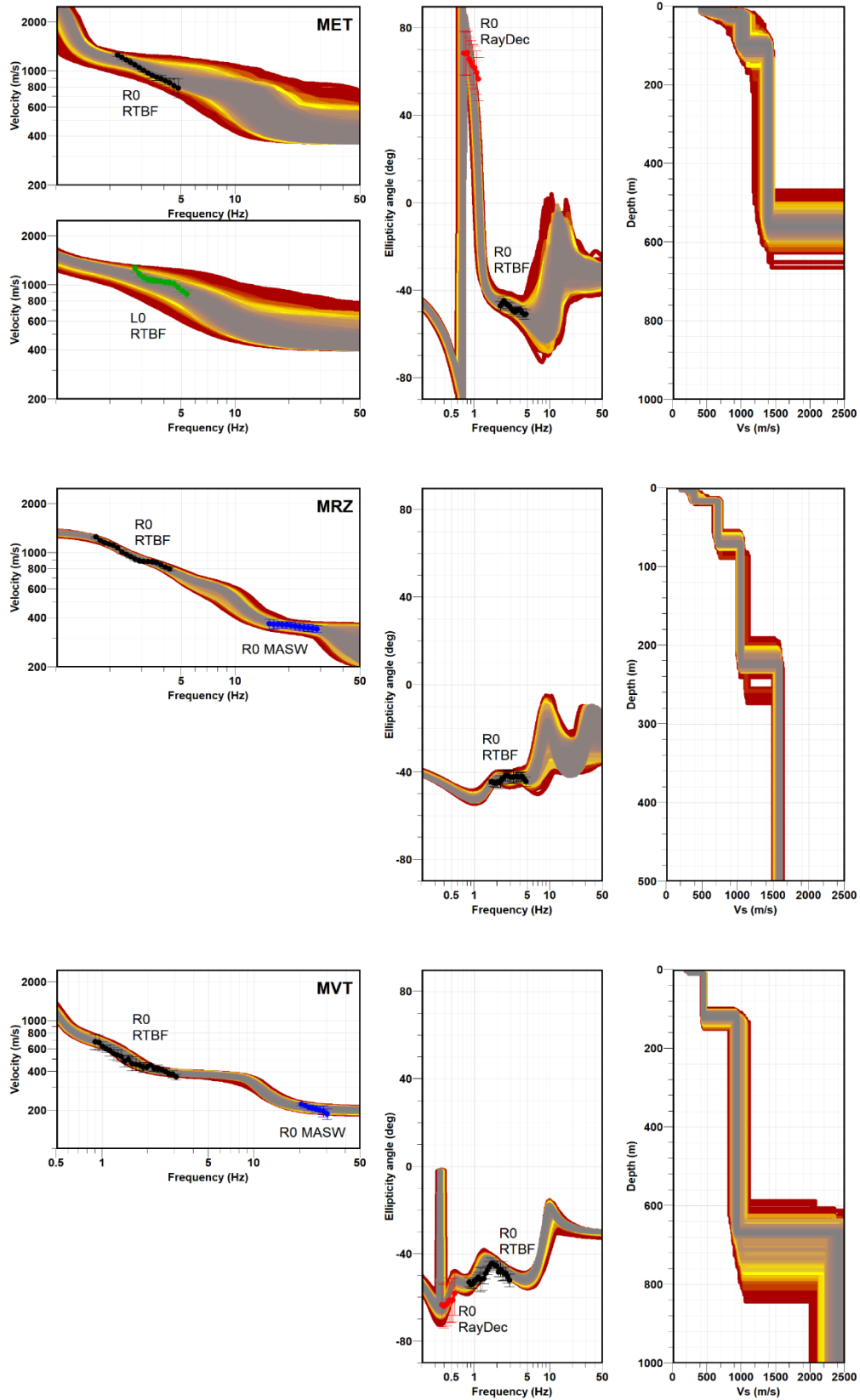
Black curves: R0 DC from RTBF processing and related ellipticity curve. Purple curves: R1 DC from RTBF processing and related ellipticity curve. Green curves: L0 DC from RTBF processing. Blue curves: R0 DC from MASW processing. Red curves: used R0 ellipticity angle curves extracted using RayDec method.

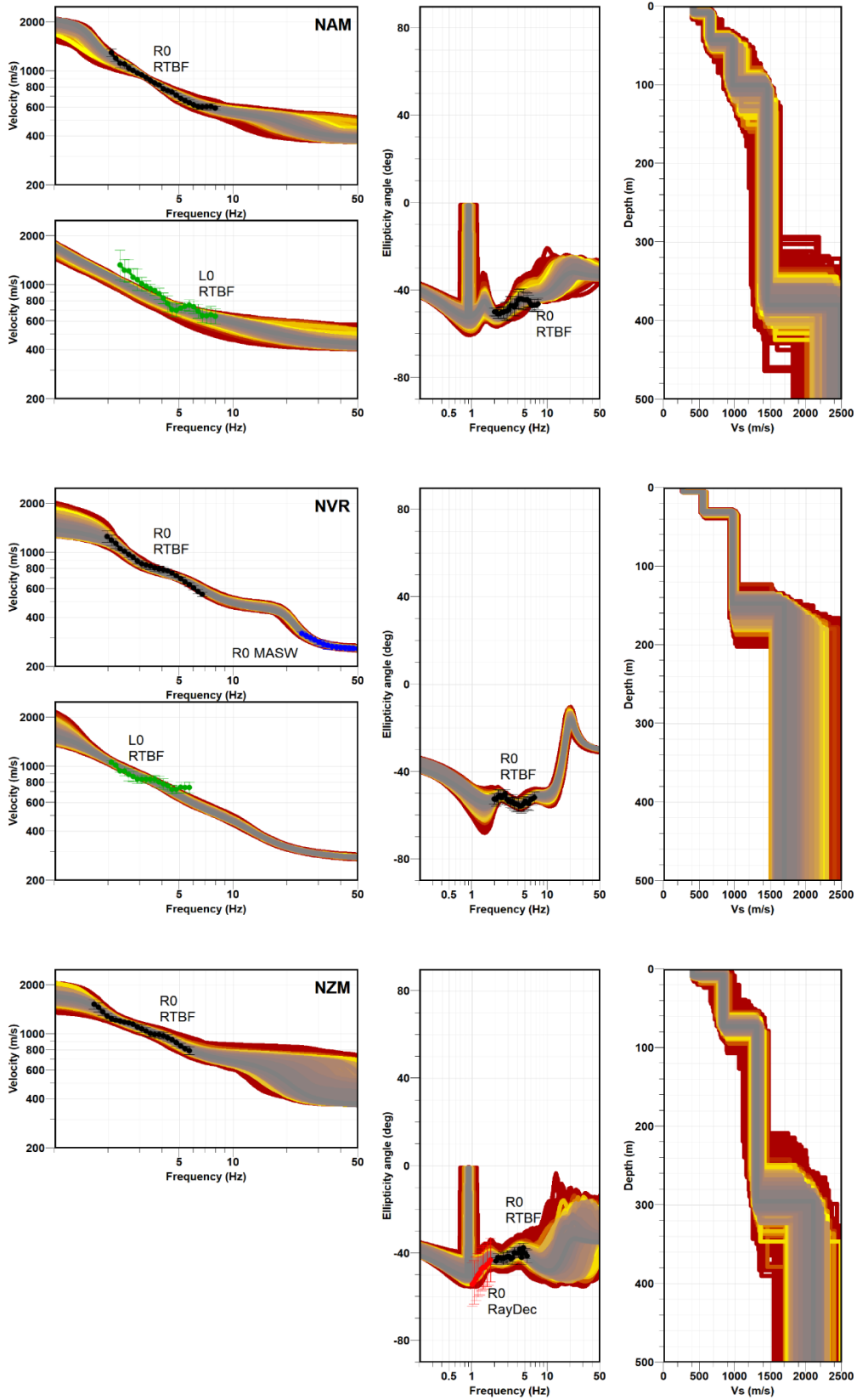


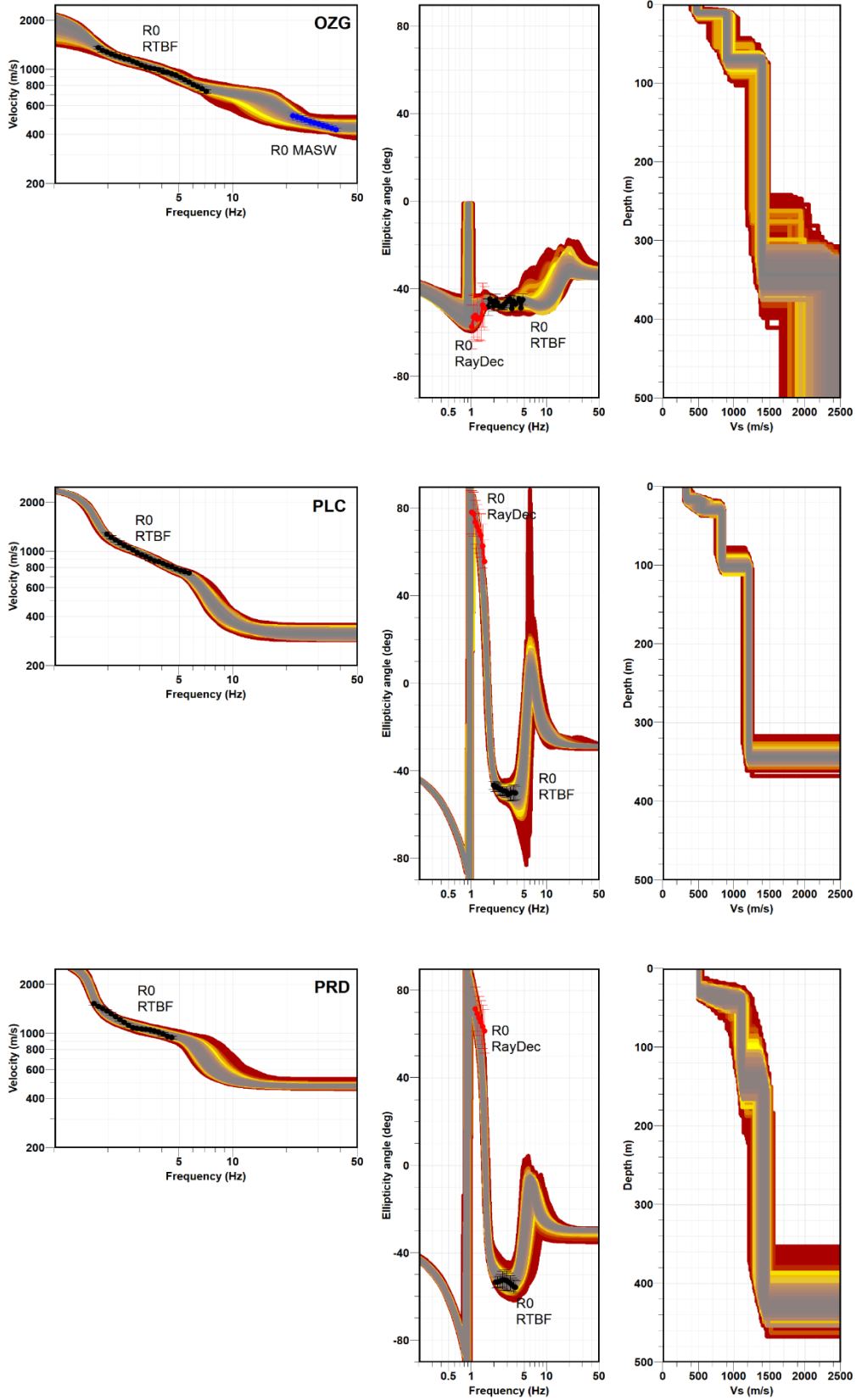


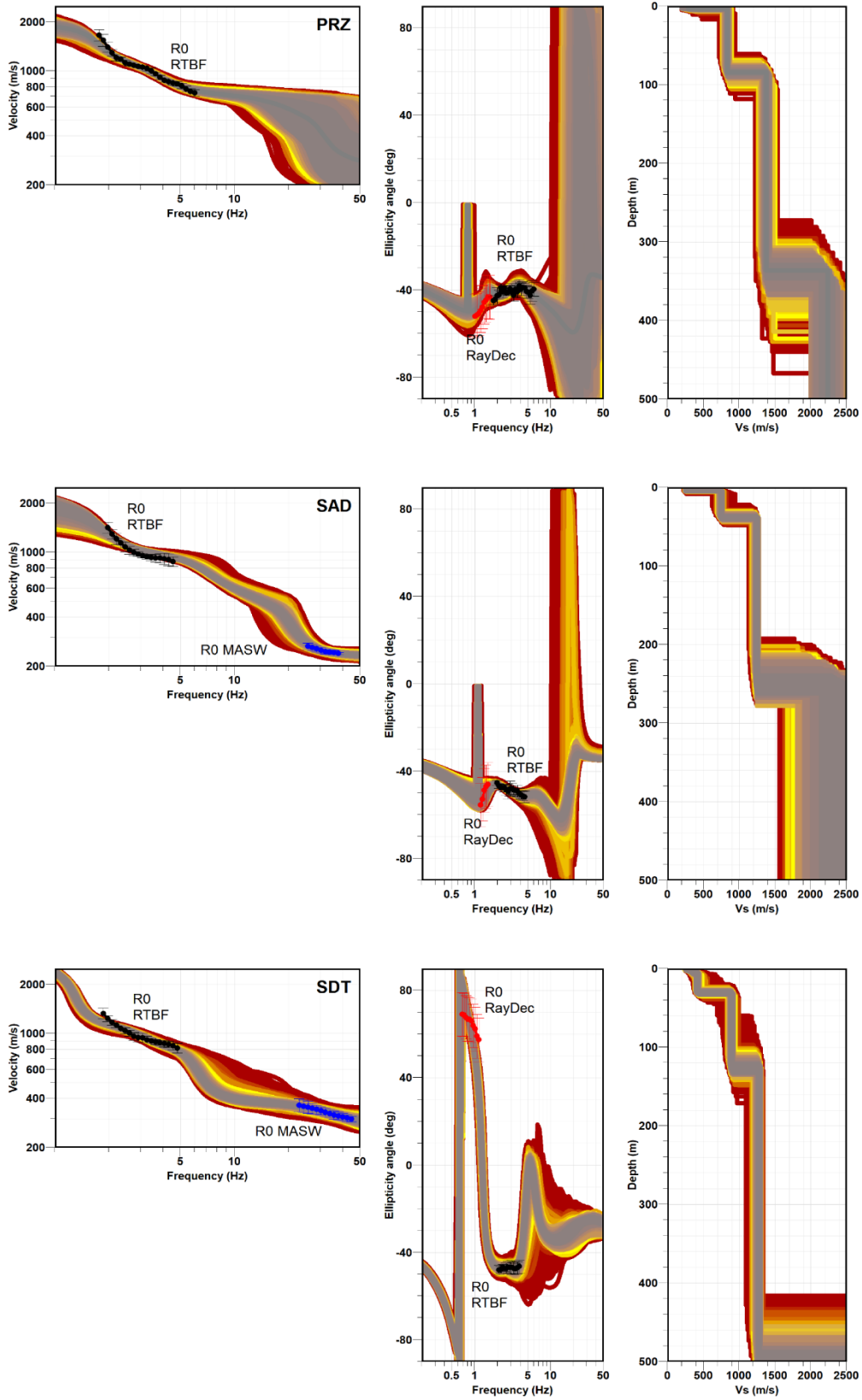


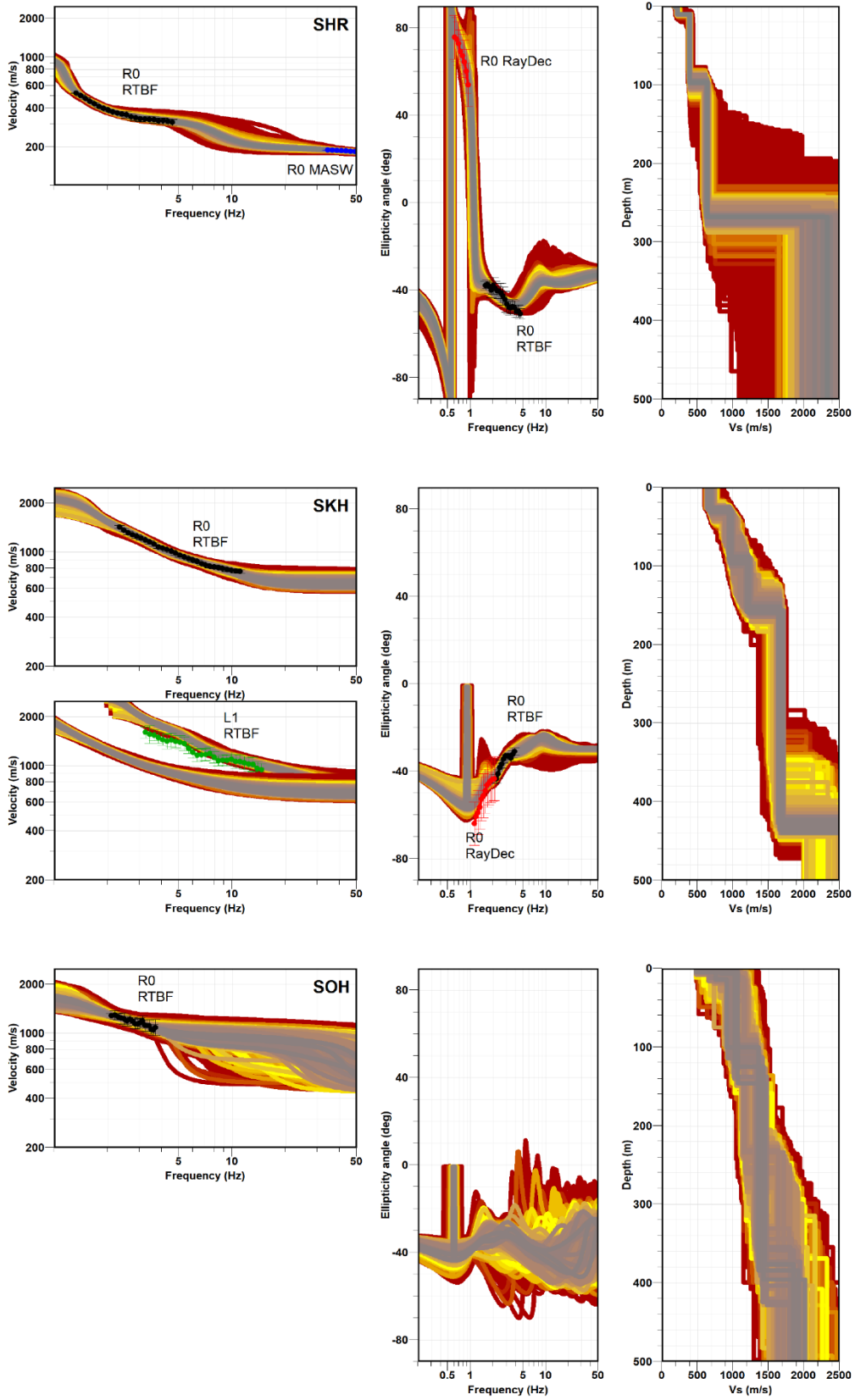


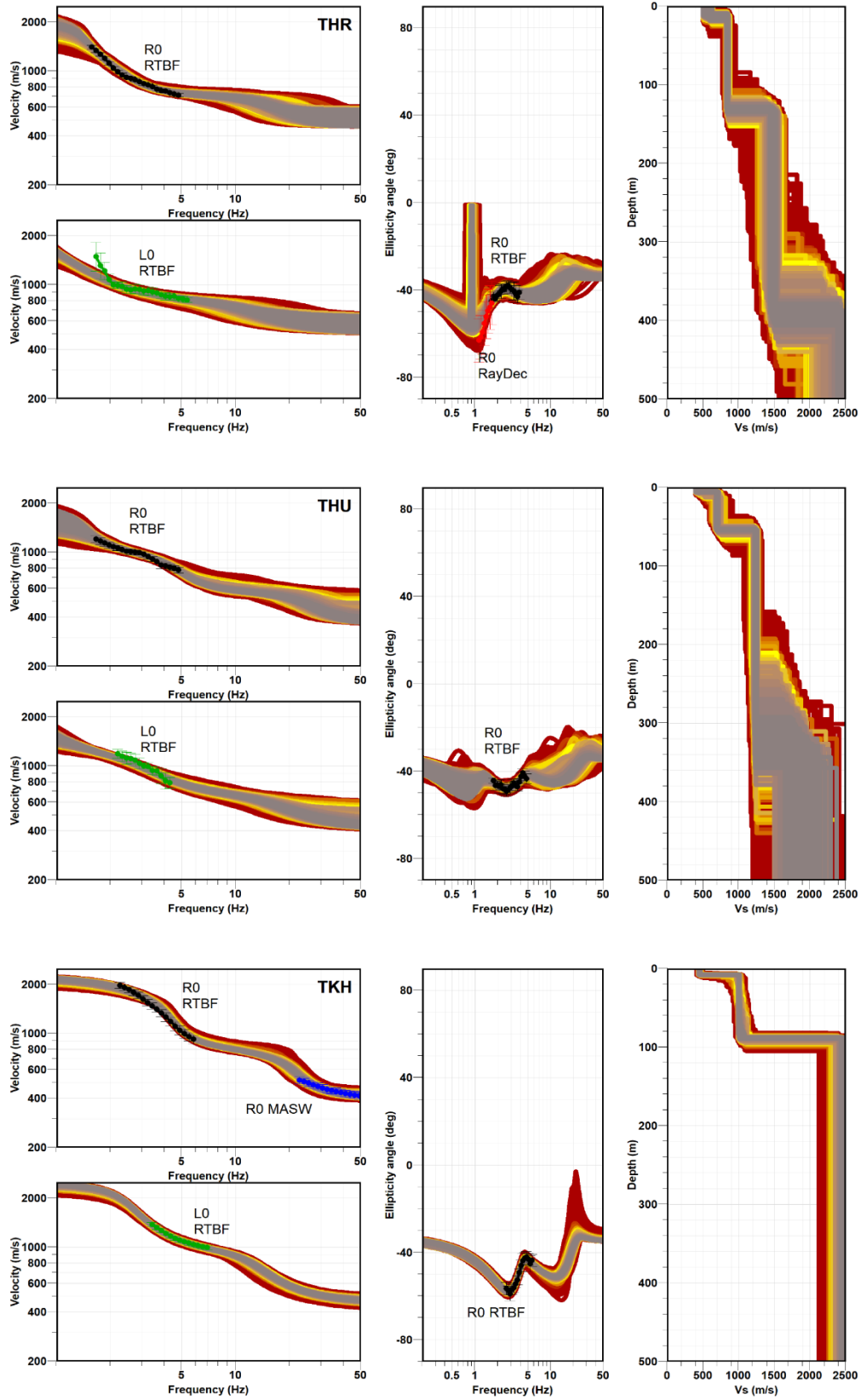


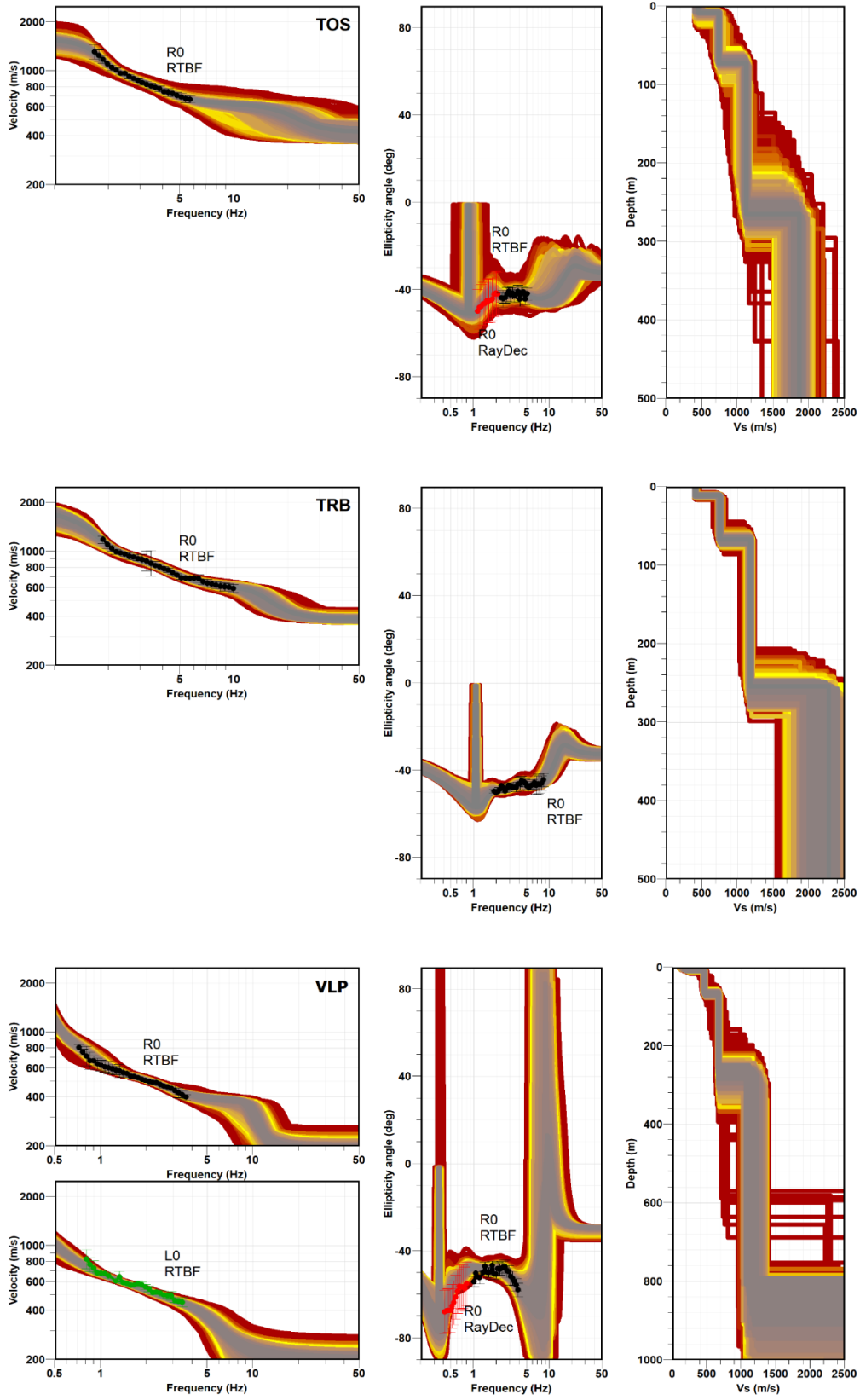












Appendix E:

Simulation results

Comparison between the simulation the experimental SSR results obtained from 11 stations located on sedimentary deposits during the temporary network measurements carried out in 2002. Light blue curves: Experimental SSR. Red curves: Simulated SSR. Yellow curves: Simulated SSR with different bedrock velocity. Dark blue curves: (The average of) Simulated SSR with different reference station. Green curves: 1D Transfer function.

